

EXPERIMENTAL INVESTIGATION AND NUMERICAL ANALYSIS OF  
MICROCHANNEL HEATSINKS FOR PHASED ARRAY RADAR COOLING  
APPLICATIONS

A THESIS SUBMITTED TO  
THE GRADUATE SCHOOL OF NATURAL AND APPLIED SCIENCES  
OF  
MIDDLE EAST TECHNICAL UNIVERSITY

BY

EMRAH ALPSAN

IN PARTIAL FULFILLMENT OF THE REQUIREMENTS  
FOR  
THE DEGREE OF MASTER OF SCIENCE  
IN  
MECHANICAL ENGINEERING

MAY 2008

Approval of the thesis:

**EXPERIMENTAL INVESTIGATION AND NUMERICAL ANALYSIS OF  
MICROCHANNEL HEATSINKS FOR PHASED ARRAY RADAR  
COOLING APPLICATIONS**

submitted by **EMRAH ALPSAN** in partial fulfillment of the requirements for the  
degree of **Master of Science in Mechanical Engineering Department, Middle  
East Technical University** by,

Prof. Dr. Canan ÖZGEN  
Dean, Graduate School of **Natural and Applied Sciences**

Prof. Dr. S. Kemal İDER  
Head of Department, **Mechanical Engineering**

Prof. Dr. M. Haluk AKSEL  
Supervisor, **Mechanical Engineering Dept, METU**

Asst. Prof. Dr. Cüneyt SERT  
Co-Supervisor, **Mechanical Engineering Dept., METU**

**Examining Committee members:**

Prof. Dr. Kahraman ALBAYRAK  
Mechanical Engineering Dept., METU

Prof. Dr. M. Haluk AKSEL  
Mechanical Engineering Dept., METU

Asst. Prof. Dr. Cüneyt SERT  
Mechanical Engineering Dept., METU

Asst. Prof. Dr. İlker TARI  
Mechanical Engineering Dept., METU

M. Sc. Uğur Etiz  
Design Leader, ASELSAN

**Date: 02.05.2008**

**I hereby declare that all information in this document has been obtained and presented in accordance with academic rules and ethical conduct. I also declare that, as required by these rules and conduct, I have fully cited and referenced all material and results that are not original to this work.**

Name, Last name : Emrah Alpsan

Signature :

## **ABSTRACT**

### **EXPERIMENTAL INVESTIGATION AND NUMERICAL ANALYSIS OF MICROCHANNEL HEATSINKS FOR PHASED ARRAY RADAR COOLING APPLICATIONS**

Alpsan, Emrah

M. Sc., Department of Mechanical Engineering

Supervisor: Prof. Dr. M. Haluk Aksel

Co-Supervisor: Asst. Prof. Dr. Cüneyt Sert

May 2008, 177 pages

Experimental measurements and numerical simulations have been performed on copper and aluminum microchannel heatsinks of 300, 420, 500, and 900  $\mu\text{m}$  channel widths. The heatsinks have been designed specifically for use with T/R (transmit/receive) module cooling applications of military phased array radars. An analytical calculation was also performed to aid in the design methodology.

A chip carrier mounted with attenuators was used to simulate the localized heat load of actual T/R modules. Distilled water was used as the coolant with flow rates ranging from 0.50 lpm (liters per minute) to 1.00 lpm. Local heat fluxes as high as  $100 \text{ W/cm}^2$  were tested. Temperature measurements were taken by thermistors on the heat load surface and by J-type thermocouples in the water and air regions. Pressure measurements were taken by pressure transducers at the heatsink inlet and outlet regions. A digital output flow meter was used to record the coolant flow rate. All experimental measurements were recorded via a digital data logger.

Experimental results showed that copper specimens were significantly superior to aluminum specimens in terms of cooling performance, as expected due to their difference in thermal conductivity. The thermally best performing specimen, the 300  $\mu\text{m}$  copper specimen, yielded a maximum temperature rise of 26.1  $^{\circ}\text{C}$  between the heat load and coolant inlet, at a coolant flow rate of 1.00 lpm and local heat flux of 100  $\text{W}/\text{cm}^2$ , leading to a thermal resistance of 0.63  $^{\circ}\text{C}/\text{W}$ . The pressure drop measured across the heatsink under these conditions was 0.030 bar. The experimental results regarding thermal performance were observed to be consistent when compared to similar studies in the literature. Results for pressure drop, however, showed significant departure. This was attributed to the geometrical differences in the heatsinks between studies compared.

Numerical simulations were carried out using the commercial Computational Fluid Dynamics (CFD) software FLUENT<sup>®</sup>. Effects of thermal interface layers and heat spreading due to the localized heat load were investigated. Simulation results for temperature were seen to agree fairly well with experimental data as long as thermal interface layers were accounted for. The simple analytical calculation for temperature, based on the classical fin approach, deviated greatly from experimental results due to the thermal interface and heat spreading effects not being included in the calculation. The analytical calculation for pressure drop, based on conventional theory for developing flow, coincided perfectly with the numerical results. The numerical and analytical results for pressure drop also agreed well with experimental results.

The present study showed that the T/R modules of military phased array radars, dissipating as high as 100  $\text{W}/\text{cm}^2$  locally, could be cooled within the limits of the harsh environmental conditions required of military applications with moderate pressure drops.

**Keywords:** Microchannel, Heatsink, Electronics Cooling, Phased Array Radar Cooling, CFD

## ÖZ

### FAZ DİZİLİ RADAR SOĞUTMASI UYGULAMALARINA YÖNELİK MİKROKANALLI ISI ALICILAR ÜZERİNDE DENEYSEL ARAŞTIRMA VE SAYISAL ANALİZ

ALPSAN, Emrah

Yüksek Lisans, Makina Mühendisliği Bölümü

Tez Yöneticisi: Prof. Dr. M. Haluk AKSEL

Ortak Tez Yöneticisi : Yrd. Doç. Dr. Cüneyt SERT

Mayıs 2008, 177 sayfa

300, 420, 500 ve 900  $\mu\text{m}$  kanal genişliğine sahip alüminyum ve bakırdan mikrokanailli ısı alıcılar üzerinde deneysel ölçümler ve sayısal simülasyonlar yapılmıştır. Isı alıcılar özgül olarak askeri faz dizili radarların A/G (alma/gönderme) modüllerinin soğutulmasına dair uygulamalara yönelik tasarlanmıştır. Tasarım yöntemine katkı sağlamak adına analitik hesaplama da yapılmıştır.

Gerçek A/G modüllerinin bölgesel ısı yükünü simüle etmek için elektronik zayıflatıcılarla donatılmış bir çip taşıyıcısı kullanılmıştır. Soğutucu sıvı olarak arıtılmış su kullanılmıştır. Soğutucu debisi dakikada 0.50 ila 1.00 litre arasında değiştirilmiştir. 100  $\text{W}/\text{cm}^2$  değerine kadar çıkan bölgesel ısı akıları test edilmiştir. Sıcaklık ölçümleri ısı yükü yüzeyinde termistörlerle, sıvı ve hava bölgelerinde ise J-tipi ısı çiftleriyle alınmıştır. Basınç ölçümleri ise ısı alıcıların giriş ve çıkışlarında, dijital basınç ölçerlerle alınmıştır. Soğutucu debisi dijital debimetre ile ölçülmüştür. Tüm deneysel ölçümler bir dijital veri kayıt cihazına kaydedilmiştir.

Deneysel ölçümler, ısı iletkenlik katsayılarında fark nedeniyle beklendiği üzere, bakır numunelerin alüminyum numunelere göre soğutma performansı yönünden üstün olduğunu göstermiştir. En iyi soğutma performansına sahip 300 µm bakır numunesinde, dakikada 1.00 litre soğutucu debisi ve 100 W/cm<sup>2</sup> bölgesel ısı yükünde, ısı yükü ile soğutucu girişi arasında en çok 26.1 °C sıcaklık artışı gerçekleşmiştir. Bu ölçüm 0.63 °C/W ısı dirence denk gelmektedir. Bu koşullar altında ısı alıcı üzerinden ölçülen basınç kaybı 0.030 bar olmuştur. Isıl performansa dair deneysel sonuçların literatürdeki benzer çalışmalarla tutarlı olduğu gözlenmiştir. Basınç kaybına dair sonuçlar ise ciddi sapma göstermiştir. Bu sapma, karşılaştırma yapılan çalışmalardaki ısı alıcı geometrilerinin farklı olmasına mal edilmiştir.

Sayısal simülasyonlar, ticari hesaplamalı akışkanlar dinamiği (HAD) yazılımı FLUENT® ile gerçekleştirilmiştir. Isıl ara yüz katmanlarının etkileri ve bölgesel ısı yükünün yayılımından kaynaklanan etkiler incelenmiştir. Isıl ara yüz katmanları hesaba katıldığı sürece, sıcaklık için alınan simülasyon sonuçlarının deneysel sonuçlarla makul ölçüde tutarlı olduğu görülmüştür. Klasik fin yaklaşımına dayalı analitik hesap sonucu bulunan sıcaklıklar ise, ısıl ara yüz katmanı ve ısı yayılımı etkilerini dahil etmediğinden, deneysel sonuçlara göre büyük sapma göstermiştir. Klasik gelişen akış teorisine göre yapılan analitik hesap sonucu bulunan basınç kaybı değerleri sayısal sonuçlarla bire bir çakışmıştır. Analitik hesap ve sayısal modelleme ile bulunan basınç kaybı değerleri deneysel sonuçlarla da tutarlıdır.

Yapılan çalışma, askeri faz dizili radarların A/G modüllerinin, 100 W/cm<sup>2</sup> bölgesel ısı akısına kadar, askeri uygulamaların gerektirdiği zorlayıcı çevre koşullarının sınırları dahilinde ve makul basınç kayıplarıyla soğutulabileceğini göstermiştir.

Anahtar kelimeler: Mikrokanal, Isı Alıcı, Elektronik Soğutma, Faz Dizili Radar Soğutması, HAD

## ACKNOWLEDGEMENTS

The author would like to express his sincere thanks to his supervisor, Prof. Dr. M. Haluk Aksel, and to his co-supervisor, Asst. Prof. Dr. Cüneyt Sert, for their continuous guidance, support, and encouragement throughout the course of this thesis. The author would also like to thank Prof. Dr. Kahraman Albayrak and Asst. Prof. Dr. İlker Tarı for their valuable comments and suggestions on the contents of this thesis.

The author would like to thank his colleagues and superiors at ASELSAN, specifically Mr. Fuat Savaş for his support during the preliminary production phases, Mr. İnanç Altungüneş for his help in the electronics aspects of this study, and most of all, Mr. Uğur Etiz for encouraging the author to study microchannel flow and heat transfer and by gaining the support of ASELSAN with his personal efforts, thus making the experimental part of this study possible. This work could not have been finalized without their support and contributions.

The author would also like to acknowledge Asst. Prof. Dr. Ünver Özkol for his indirect but substantial role in this thesis in inspiring the author to work in the field of experimental fluid dynamics. His guidance and mentoring during his years at ASELSAN are valued greatly by the author.

## TABLE OF CONTENTS

PLAGIARISM .....	iii
ABSTRACT .....	iv
ÖZ .....	vi
ACKNOWLEDGEMENTS .....	viii
TABLE OF CONTENTS.....	ix
LIST OF TABLES .....	xii
LIST OF FIGURES.....	xiii
LIST OF SYMBOLS.....	xviii
CHAPTERS	
1. INTRODUCTION.....	1
1.1 Miniaturization and Microchannels .....	1
1.2 Electronics Cooling Technologies .....	2
1.3 Motivation .....	7
1.4 Present Study.....	8
2. AN OVERVIEW OF THEORETICAL BACKGROUND APPLICABLE TO MICROCHANNEL FLOW AND HEAT TRANSFER .....	9
2.1 Fundamental Theoretical Background on Channel Flow and Heat Transfer.	9
2.1.1 <i>Governing Equations</i> .....	9
2.1.2 <i>Flow in Closed Conduits</i> .....	12
2.1.2.1 <i>Geometrical Considerations</i> .....	12
2.1.2.2 <i>Pressure Drop</i> .....	13
2.1.2.3 <i>Entrance Effects</i> .....	15
2.1.2.4 <i>Turbulence Effects</i> .....	16
2.1.2.5 <i>Minor Losses</i> .....	17
2.1.3 <i>Heat Transfer in Closed Conduits</i> .....	20
2.1.3.1 <i>Developing Flow</i> .....	22
2.1.3.2 <i>Turbulence Effects</i> .....	23

2.1.3.3 <i>Thermal Performance of Liquid Cooled Heatsinks</i> .....	24
2.1.3.4 <i>Heat Transfer from Extended Surfaces</i> .....	25
2.2 Characteristics of Flow and Heat Transfer in Microchannels.....	27
2.2.1 <i>Newtonian Framework</i> .....	29
2.2.2 <i>Continuum Approximation</i> .....	30
2.2.3 <i>Thermodynamic Equilibrium</i> .....	30
3. AN OVERVIEW OF CURRENT LITERATURE RELATED TO FLOW AND HEAT TRANSFER IN MICROCHANNELS .....	34
3.1 Experimental Work on Microchannel Flow and Heat Transfer: A Bibliographical Perspective.....	34
3.2 Analytical and Numerical Studies on Microchannel Flow and Heat Transfer .....	47
3.3 Microchannel Cooling Applications and Application Oriented Studies .....	55
4. EXPERIMENTAL PROCEDURE AND RESULTS .....	59
4.1 Design and Manufacturing of the Microchannel Heatsinks.....	59
4.1.1 <i>The Preliminary Specimen</i> .....	60
4.1.2 <i>The Test Specimens</i> .....	64
4.2 The Experimental Setup.....	70
4.2.1 <i>Components of the Experimental Setup</i> .....	70
4.2.2 <i>Measurements and Results</i> .....	77
4.2.3 <i>Evaluation of Results</i> .....	85
5. NUMERICAL ANALYSES AND RESULTS .....	87
5.1 The Computational Model .....	87
5.2 Boundary Conditions and Solver Settings .....	92
5.3 Numerical Simulation Results.....	95
5.3.1 <i>Numerical Results for Pressure Drop and Temperature Rise</i> .....	96
5.3.2 <i>CFD Results on Flow Characteristics</i> .....	99
5.3.3 <i>Heat Loss</i> .....	103
5.3.4 <i>Effect of Thermal Interface Layer</i> .....	104
5.3.5 <i>Effect of Localized Heat Load</i> .....	104
6. DISCUSSION AND COMPARISON OF RESULTS .....	108

6.1 Comparison of Maximum Temperature Rise Results .....	108
6.2 Comparison of Average Temperature Rise Results .....	110
6.3 Comparison of Pressure Drop Results .....	112
6.4 Thermal Performance .....	113
6.5 Comparison with Similar Studies in the Literature .....	114
7. CONCLUSION .....	117
7.1 Agreement of Experimental, Numerical, and Analytical Results .....	117
7.2 Effect of Thermal Interface Layer and Localized Heat Sources .....	118
7.3 Critic of The Experimental Setup.....	119
7.4 Thermal Performance .....	120
7.5 Future Work .....	121
REFERENCES.....	122
APPENDICES	
A. RELATIONS OF VECTOR CALCULUS AND TENSOR NOTATION.....	131
B. TECHNICAL DRAWINGS - PRELIMINARY SPECIMEN .....	133
C. TECHNICAL DRAWINGS - TEST SPECIMENS .....	135
D. SAMPLE ANALYTICAL CALCULATION .....	141
E. PHOTOGRAPHS OF TEST SPECIMEN BODY AND CAP .....	147
F. MICROSCOPE VIEWS OF TEST CHANNELS .....	153
G. EXPERIMENTAL RESULTS .....	157
H. EXPERIMENTAL RESULTS AT STEADY STATE CONDITIONS .....	169
I. HEAT LOSS CALCULATION.....	173
J. NUMERICAL ANALYSIS RESULTS .....	176

## LIST OF TABLES

Table 2.1: Nusselt number in the developing laminar region .....	23
Table 4.1: Analytical calculation results .....	66
Table 4.2: Design parameters of the test specimens .....	68
Table 4.3: Cooling system components .....	74
Table 4.4: Measurement instruments of the experimental setup .....	77
Table 4.5: Test parameter combinations .....	79
Table 4.6: Pressure drop across heatsinks .....	83
Table 5.1: Mesh statistics .....	88
Table 5.2: Boundary condition specifications .....	94
Table 5.3: Volume specifications .....	94
Table 5.4: Solver settings .....	94
Table 5.5: Simulation parameters .....	96
Table D.1: Properties of water and ethylene glycol at 300K.....	141
Table D.2: Calculated flow parameters .....	143
Table D.3 Calculated parameters for copper specimens .....	145
Table D.4 Calculated parameters for aluminum specimens .....	145
Table H.1: Pressure readings .....	169
Table H.2: Temperature readings @ 0.50 lpm coolant flow rate .....	170
Table H.3: Temperature readings @ 0.75 lpm coolant flow rate .....	171
Table H.4: Temperature readings @ 1.00 lpm coolant flow rate.....	172
Table I.1: Heat loss* @ 0.50 lpm coolant flow rate .....	173
Table I.2: Heat loss* @ 0.75 lpm coolant flow rate .....	174
Table I.3: Heat loss* @ 1.00 lpm coolant flow rate .....	175
Table J.1: Numerical analysis results @ 0.2 mm thermal interface material thickness .....	176
Table J.2: Numerical analysis results @ 0.3 mm thermal interface material thickness .....	177

## LIST OF FIGURES

Figure 1.1: Trends in increasing power density and categorization of cooling methods employed by INTEL [5] .....	3
Figure 1.2: A heatsink-fan assembly (left) and various heat pipe configurations (right) .....	4
Figure 1.3: Liquid cooling system schematics (left) and example of a liquid cooled heat sink mounted on a PCB .....	4
Figure 1.4: Schematics of liquid heatsink (left), minichannel heatsink (center), microchannel heatsink (right) [6] .....	5
Figure 1.5: Localized spray cooling (left) and system level spray cooling (right) [7] .....	6
Figure 1.6: Schematic representation of thermoelectric cooling (left), thermoelectric modules (right) [8] .....	6
Figure 2.1: Side designation in definitions of aspect ratio and hydraulic diameter .....	13
Figure 2.2: Regions of minor loss in a typical microchannel heatsink [14] .....	18
Figure 2.3: $K_e$ and $K_c$ for laminar channel flow [17] .....	19
Figure 2.4: Fin geometrical parameters .....	27
Figure 4.1: Heatsink dimensions - 1 .....	61
Figure 4.2: Heatsink dimensions - 2 .....	61
Figure 4.3: Parts of the microchannel heatsink assembly .....	62
Figure 4.4: The joined structure with pipe adaptors added .....	63
Figure 4.5: Main dimensions of the heatsink and cap .....	65
Figure 4.6: Specimen 1 and its cap .....	67
Figure 4.7: Microscope view of specimen 1 .....	68
Figure 4.8: Test specimens after brazing .....	69
Figure 4.9: Configuration of fluid inlet and outlets .....	69
Figure 4.10: Heat load carrier .....	71

Figure 4.11: Effective heat load area .....	71
Figure 4.12: The heat load carrier mounted on the heatsink .....	72
Figure 4.13: The test specimen in its protective casing .....	73
Figure 4.14: Pressure transducers at fluid inlet and outlets .....	75
Figure 4.15: Schematic representation of the experimental setup .....	76
Figure 4.16: The experimental setup .....	76
Figure 4.17: Temperature sensor enumeration convention .....	78
Figure 4.18: Maximum temperature rise of copper specimens at 1 lpm coolant flow rate .....	81
Figure 4.19: Maximum temperature rise of aluminum specimens at 1 lpm coolant flow rate .....	82
Figure 4.20: Maximum temperature rise of copper specimens at 100 W/cm <sup>2</sup> local heat flux .....	82
Figure 4.21: Maximum temperature rise of aluminum specimens at 100 W/cm <sup>2</sup> local heat flux .....	83
Figure 4.22: Pressure drop of copper specimens .....	84
Figure 4.23: Pressure drop of aluminum specimens .....	84
Figure 5.1: Model of the test specimens in GAMBIT® .....	87
Figure 5.2: General view of the mesh on solid surfaces .....	89
Figure 5.3: View of the mesh on outer surfaces of the heatsink .....	89
Figure 5.4: Close-up view of the mesh on outer surfaces of the heatsink .....	90
Figure 5.5: View of the mesh on outer surfaces of the heat load carrier .....	90
Figure 5.6: Transition of the mesh from the channels to coolant inlet-outlet regions .....	91
Figure 5.7: Transition of the mesh within the coolant inlet-outlet regions to smaller densities .....	91
Figure 5.8: Mesh zones shown along central section .....	92
Figure 5.9: Effect of local heat flux on maximum temperature rise – 300 µm specimens .....	97
Figure 5.10: Effect of coolant flow rate on maximum temperature rise – 300 µm specimens .....	98

Figure 5.11 Effect of coolant flow rate on pressure drop and maximum channel velocity for the 300 $\mu\text{m}$ specimens .....	98
Figure 5.12 Effect of channel width on pressure drop and maximum channel velocity for the constant coolant flow rate of 1 lpm .....	99
Figure 5.13 Velocity contours in (m/s) along horizontal mid-section .....	100
Figure 5.14 Pressure contours in (Pa) along horizontal mid-section .....	101
Figure 5.15 Velocity contours in (m/s) along vertical mid-section .....	102
Figure 5.17 Temperature contours in (K) along external surfaces.....	103
Figure 5.18 Temperature contours in (K) along vertical normal mid-section, with 0.3 mm TI .....	104
Figure 5.19 Temperature contours in (K) along vertical normal mid-section, without TI, with homogenous heat load .....	105
Figure 5.20 Temperature contours along heatsink surfaces, without TI, with localized heat load (K) .....	106
Figure 5.21 Temperature contours on heatsink surfaces, without TI, with homogenous heat load (K) .....	106
Figure 5.22 Temperature contours along heat load carrier, without TI, with localized heat load (K) .....	107
Figure 6.1: Comparison of maximum temperature rise for copper specimens ....	109
Figure 6.2: Comparison of maximum temperature rise for aluminum specimens .....	109
Figure 6.3: Comparison of average temperature rise for copper specimens .....	110
Figure 6.4: Comparison of average temperature rise for aluminum specimens...	111
Figure 6.5: Comparison of pressure drop at 1 lpm coolant flow rate .....	112
Figure B.1: Microchannel heatsink assembly .....	133
Figure B.2: Inlet - outlet parts .....	133
Figure B.3: Cover plate .....	134
Figure B.4: Heatsink body .....	134
Figure C.1: 300 $\mu\text{m}$ heatsink body dimensions .....	135
Figure C.2: 300 $\mu\text{m}$ channel dimensions .....	136

Figure C.3: 420 $\mu\text{m}$ channel dimensions .....	136
Figure C.4: 420 $\mu\text{m}$ heatsink body dimensions .....	137
Figure C.5: 500 $\mu\text{m}$ heatsink body dimensions .....	138
Figure C.6: 500 $\mu\text{m}$ channel dimensions .....	139
Figure C.7: 900 $\mu\text{m}$ channel dimensions .....	139
Figure C.8: 900 $\mu\text{m}$ heatsink body dimensions .....	140
Figure D.1: Geometrical parameters .....	144
Figure E.1: AL 300 $\mu\text{m}$ specimen .....	147
Figure E.2: AL 420 $\mu\text{m}$ specimen .....	147
Figure E.3: AL 500 $\mu\text{m}$ specimen .....	148
Figure E.4: AL 900 $\mu\text{m}$ specimen .....	148
Figure E.5: AL cap – top view .....	149
Figure E.6: AL cap – bottom view .....	149
Figure E.7: CU 300 $\mu\text{m}$ specimen .....	150
Figure E.8: CU 420 $\mu\text{m}$ specimen .....	150
Figure E.9: CU 500 $\mu\text{m}$ specimen .....	151
Figure E.10: CU 420 $\mu\text{m}$ specimen .....	151
Figure E.11: CU cap – top view .....	152
Figure E.12: CU cap – bottom view.....	152
Figure F.1: AL 300 $\mu\text{m}$ specimen .....	153
Figure F.2: AL 420 $\mu\text{m}$ specimen .....	153
Figure F.3: AL 500 $\mu\text{m}$ specimen .....	154
Figure F.4: AL 900 $\mu\text{m}$ specimen .....	154
Figure F.5: CU 300 $\mu\text{m}$ specimen .....	155
Figure F.6: CU 420 $\mu\text{m}$ specimen .....	155
Figure F.7: CU 500 $\mu\text{m}$ specimen .....	156
Figure F.8: CU 420 $\mu\text{m}$ specimen .....	156
Figure G.1: Flow data – 300 $\mu\text{m}$ CU specimen.....	157
Figure G.2: Air and coolant temperature data – 300 $\mu\text{m}$ CU specimen .....	157
Figure G.3: Heat load carrier temperature data – 300 $\mu\text{m}$ CU specimen .....	158
Figure G.4: Flow data – 300 $\mu\text{m}$ AL specimen .....	158

Figure G.5: Air and coolant temperature data – 300 $\mu\text{m}$ AL specimen .....	159
Figure G.6: Heat load carrier temperature data – 300 $\mu\text{m}$ AL specimen .....	159
Figure G.7: Flow data – 420 $\mu\text{m}$ CU specimen .....	160
Figure G.8: Air and coolant temperature data – 420 $\mu\text{m}$ CU specimen .....	160
Figure G.9: Heat load carrier temperature data – 420 $\mu\text{m}$ CU specimen .....	161
Figure G.10: Flow data – 420 $\mu\text{m}$ AL specimen .....	161
Figure G.11: Air and coolant temperature data – 420 $\mu\text{m}$ AL specimen .....	162
Figure G.12: Heat load carrier temperature data – 420 $\mu\text{m}$ AL specimen .....	162
Figure G.13: Flow data – 500 $\mu\text{m}$ CU specimen .....	163
Figure G.14: Air and coolant temperature data – 500 $\mu\text{m}$ CU specimen .....	163
Figure G.15: Heat load carrier temperature data – 500 $\mu\text{m}$ CU specimen .....	164
Figure G.16: Flow data – 500 $\mu\text{m}$ AL specimen .....	164
Figure G.17: Air and coolant temperature data – 500 $\mu\text{m}$ AL specimen .....	165
Figure G.18: Heat load carrier temperature data – 500 $\mu\text{m}$ AL specimen .....	165
Figure G.19: Flow data – 900 $\mu\text{m}$ CU specimen .....	166
Figure G.20: Air and coolant temperature data – 900 $\mu\text{m}$ CU specimen .....	166
Figure G.21: Heat load carrier temperature data – 900 $\mu\text{m}$ CU specimen .....	167
Figure G.22: Flow data – 900 $\mu\text{m}$ AL specimen .....	167
Figure G.23: Air and coolant temperature data – 900 $\mu\text{m}$ AL specimen .....	168
Figure G.24: Heat load carrier temperature data – 900 $\mu\text{m}$ AL specimen .....	168

## LIST OF SYMBOLS

$c_p$	: Specific heat at constant pressure
$f$	: Friction factor
$f_{app}$	: Apparent friction factor
$\mathbf{g}$	: Gravitational acceleration vector
$h$	: Convection heat transfer coefficient
$h_{ave}$	: Average convection heat transfer coefficient
$k$	: Conduction heat transfer coefficient
$\dot{m}$	: Coolant mass flow rate
$m_m$	: Molecular mass
$p$	: Pressure
$q$	: Rate of heat transfer
$q_f$	: Rate of heat transfer between fin and coolant
$q_{max}$	: Maximum possible rate of heat transfer between fin and coolant
$q_t$	: Rate of total heat transfer between heatsink and coolant
$q_s''$	: Channel wall surface heat flux
$t$	: Time
$t_f$	: Fin thickness
$u_{fluid}$	: Fluid free flow velocity
$u_m$	: Mean velocity
$u_{mc}$	: Mean channel velocity
$u_{mp}$	: Mean plenum velocity
$u_{wall}$	: Fluid velocity at the wall
$w$	: Fin width
$x$	: Distance along channel from inlet
$x_i$	: Position tensor
$A_c$	: Fin cross sectional area
$A_{ch}$	: Channel flow area

$A_f$	: Fin surface area
$A_{flow}$	: Flow area
$A_{ht}$	: Heat transfer area
$A_p$	: Plenum flow area
$A_t$	: Fin total area
$C_D$	: Smallest channel dimension
$D_h$	: Hydraulic diameter
$K(x)$	: Pressure defect in hydrodynamically developing flow region
$K(\infty)$	: Pressure defect in hydrodynamically fully developed flow region
$K_{90}$	: Pressure loss coefficient of 90° bends
$K_c$	: Pressure loss coefficient of sudden contraction
$K_e$	: Pressure loss coefficient of sudden expansion
$K_L$	: Pressure loss coefficient
$L$	: Fin length
$L_c$	: Corrected fin length
$L_{ch}$	: Channel length
$L_h$	: Hydrodynamic development length
$L_s$	: Slip length
$L_t$	: Thermal development length
$N$	: Number of fins
$Nu$	: Nusselt number
$Nu_{ave}$	: Average Nusselt number
$P$	: Heat power input
$Po$	: Poiseuille number
$Pr$	: Prandtl number
$P_w$	: Wetted perimeter
$Q$	: Coolant inlet volumetric flow rate
$Q_{inlet}$	: Coolant inlet volumetric flow rate
$R_{HS}$	: Heatsink thermal resistance
$Re$	: Reynolds number
$Re_{ch}$	: Channel Reynolds number

$Re_{le}$	: Laminar equivalent Reynolds number
$T$	: Temperature field
$T_b$	: Heatsink base temperature
$T_i$	: Fluid inlet temperature
$T_m$	: Fluid mean temperature
$T_o$	: Fluid outlet temperature
$T_s$	: Surface temperature
$TI_t$	: Thermal interface layer thickness
$V$	: Velocity
$\mathbf{V}$	: Velocity vector
$V_{ch}$	: Channel flow velocity
$V_{inlet}$	: Coolant inlet velocity
$V_{max}$	: Maximum channel velocity
$W_c$	: Channel width
$\alpha_c$	: Channel aspect ratio
$\delta_{ij}$	: Kronecker delta
$\Delta T$	: Temperature difference
$\Delta T_{LMTD}$	: Log Mean Temperature Difference
$\Delta p$	: Pressure difference
$\Delta p_f$	: Fitting pressure difference
$\varepsilon$	: molecular energy scale
$\theta_b$	: Base temperature rise
$\mu$	: Dynamic viscosity
$\eta_f$	: Fin efficiency
$\eta_o$	: Overall fin efficiency
$\rho$	: Density
$\sigma$	: characteristic length
$\tau$	: molecular length scale

## CHAPTER 1

### INTRODUCTION

This introductory chapter aims at presenting the need of understanding microchannel flow and heat transfer from an electronics cooling point of view, in conjunction with the global trends in cooling technologies and the requirements of the national defense industry.

#### 1.1 Miniaturization and Microchannels

The concept of miniaturization may be said to form the basis of a relatively young field of technology, *MicroElectroMechanical Systems* (MEMS). When Richard P. Feynman referred to his anticipation of a trend towards miniaturization in his talk titled “There’s Plenty of Room at the Bottom”, delivered at the annual meeting of the American Physical Society in 1959, he made a striking remark: “In the year 2000, when they look back at this age, they will wonder why it was not until the year 1960 that anybody began to seriously move in this direction.” [1]

It was not until two decades after Feynman’s famous speech that Tuckerman and Pease first made use of miniaturization for the purposes of heat removal, within the scope of a Ph.D. study in 1981. Their publication titled “High Performance Heat Sinking for VLSI” [2] is credited as the first study on microchannel heat transfer. Their pioneering work has motivated many researchers to focus on the topic and microchannel flow has been recognized as a high performance heat removal tool ever since. Presently, modeling and experimental investigation of microchannel flow and heat transfer are rapidly maturing, although conflicts

among researchers as to how microscale flows should be modeled and discrepancies between experimental results remain.

Their extremely high heat transfer capability is the primary point of interest of microchannels for this thesis. Besides heat related applications, microscale fluid flow also finds important applications in MEMS. Microducts are used in infrared detectors, diode lasers, and miniature gas chromatographs; micropumps are used for inkjet printing, environmental testing, and electronics cooling; microturbines are being developed as miniature energy generators and microvalves [3]. Chemical and biological applications such as microreactors and lab-on-a-chip devices are also many.

As is evident from the diversity of application areas, the study of flow and heat transfer in microchannels is very important for the technology of today and the near future, as developments are following the trend of miniaturization in all fields.

## **1.2 Electronics Cooling Technologies**

Following the invention of the chip, methods for cooling of electronics have improved and sophisticated at an ever increasing pace in conjunction with the rapid development of the electronics industry. The importance of cooling for electronic components is that high temperatures not only decrease their lifetime by accelerating failure mechanisms in materials, but they also reduce the overall reliability of the assembly by accelerating failure mechanisms in connections and interfaces [4]. The evident trend in the development of integrated circuits is that the sizes are getting smaller while the heat dissipation quantities are getting larger. To meet the rapidly rising heat densities, methods of thermal engineering applied to the cooling of electronics have evolved from primitive, passive structures to advanced systems. The power dissipation trend of INTEL processor chips, shown in Fig. 1.1, is representative of the silicon industry in general [5].

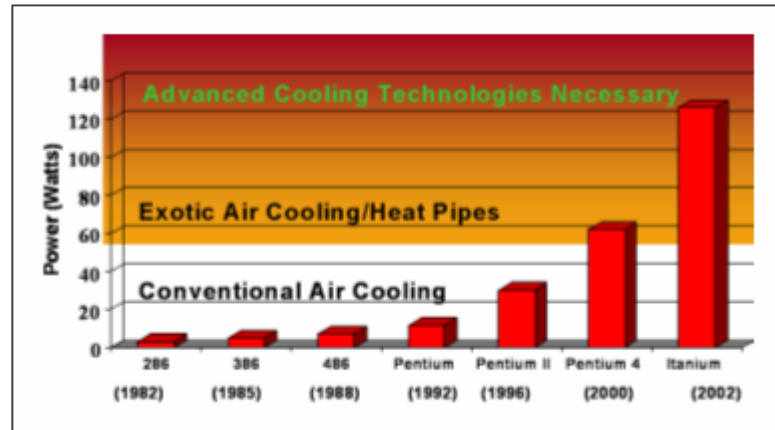


Figure 1.1: Trends in increasing power density and categorization of cooling methods employed by INTEL [5]

The categorization of cooling methods employed by INTEL given in the figure below shows that conventional cooling methods have become insufficient by the year 2000. Conventional air cooling methods refer to making use of natural or forced convection together with heat spreaders or heat sinks. As long as the heat dissipation of the chips to be cooled is moderate, it is preferable to use a simple heatsink design that can provide adequate cooling with natural convection. For higher heat fluxes, natural convection is not sufficient and fans must be used to obtain higher heat removal rates associated with forced convection.

When conventional air cooling methods do not suffice, enhanced cooling tools such as fan-heatsink assemblies or heat pipes must be used. Fan-heatsink assemblies are commonly used in personal computers to cool high performance processors, while heat pipes are commonly used in laptop computers where space is a major limitation. Fan-heatsink assemblies are, in fact, an extension of forced cooling methods where the heatsink is designed to achieve maximum cooling performance with the air flow due to the fan attached to it. Heat pipes, on the other hand, are structures that attain extraordinarily high thermal conductivity, enabling the heat dissipated by the chips to be carried effectively to an appropriate location for cooling.

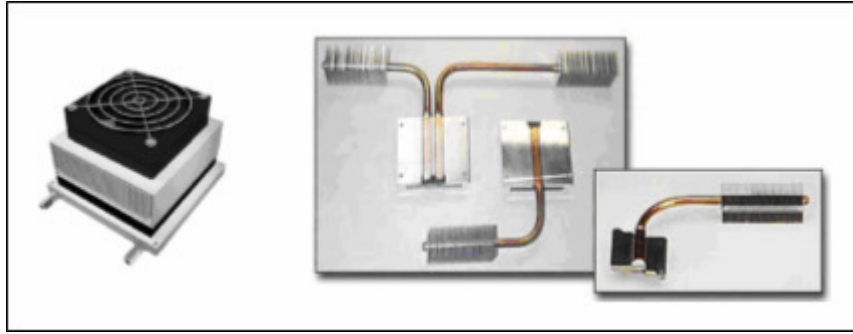


Figure 1.2: A heatsink-fan assembly (left) and various heat pipe configurations (right)

When the limits of extended air cooling methods fall short of accommodating the rising heat densities to be cooled, advanced cooling technologies must be employed to achieve the high cooling performance required. The first milestone in advanced cooling is to utilize a coolant liquid instead of air. The heat removal capacity of liquids (eg. water) is much higher compared to that of air, however, use of a liquid cooling system involves major changes in design compared to air cooling. To avoid damage to the electronics, the coolant must be totally isolated. A heat exchanger must be employed to serve as a medium of heat exchange between the coolant and the surrounding atmosphere. A pump must be used in place of the fan, heatsinks must be replaced by cold plates, or liquid cooled heatsinks, to generate a heat path between the chip and the coolant.

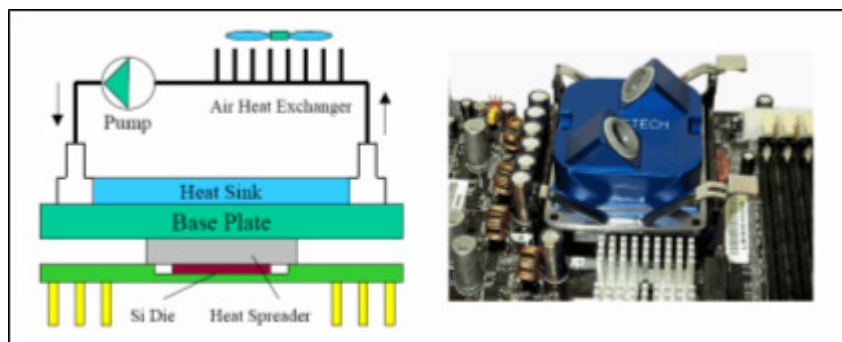


Figure 1.3: Liquid cooling system schematics (left) and example of a liquid cooled heat sink mounted on a PCB

The cooling capabilities of liquid systems are wide ranging, depending on the coolant used, the performance of the heat exchanger, the pumping power, and the thermal interface between the heat source and the coolant. Conventional liquid cooling utilizes simple liquid heatsink geometries, commonly of rectangular cross section. The cooling method is characterized by the geometry of the heatsink. The cooling capacity of the system increases as the channel size decreases, leading to the categorization of "conventional liquid cooling", "minichannel liquid cooling", and "microchannel liquid cooling".



Figure 1.4: Schematics of liquid heatsink (left), minichannel heatsink (center), microchannel heatsink (right) [6]

Liquid cooling by means of conventional, minichannel, or microchannel liquid heatsinks is appropriate for the cooling of most high heat flux applications. Many supercomputers of recent years employ minichannel liquid cooling, while microchannel liquid cooling is used most commonly in military radar applications. In certain applications, where highly localized heat sources can not be cooled sufficiently by channel cooling, spray cooling is employed. In this method, an atomizer (or nozzle) converts the liquid flow into a spray that impinges directly on the surface to be cooled. Dielectric coolants are used to avoid damage to the electronics. Because the coolant and heat source are brought into direct contact, the thermal path is more effective and higher cooling capacities may be achieved. Spray cooling may be designed to cool local hot spots in a system using a few nozzles, or to cool larger areas using a set of nozzles.

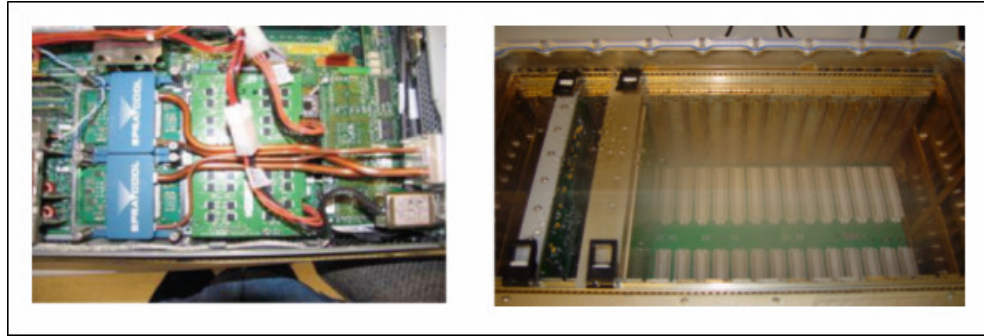


Figure 1.5: Localized spray cooling (left) and system level spray cooling (right) [7]

A final method worth mentioning among advanced cooling technologies is thermoelectric cooling. The Peltier effect, achieved by using a series of P and N type semiconductors, causes a finite temperature difference between the two surfaces of a thermoelectric cooler when a voltage is applied. The cold side of the thermoelectric cooler is attached to the surface to be cooled, while the hot side must be cooled by another cooling system (such as a heatsink and a fan) to achieve as low a temperature as possible at the heat source. The temperature difference between the cold side and hot side of high performance thermoelectric coolers may exceed 100°C. In this way, very low temperatures at the heat source may be obtained. The drawback of this technique is that yet another cooling method must be employed for the hot side, and the electric power requirements of thermoelectric modules are high.

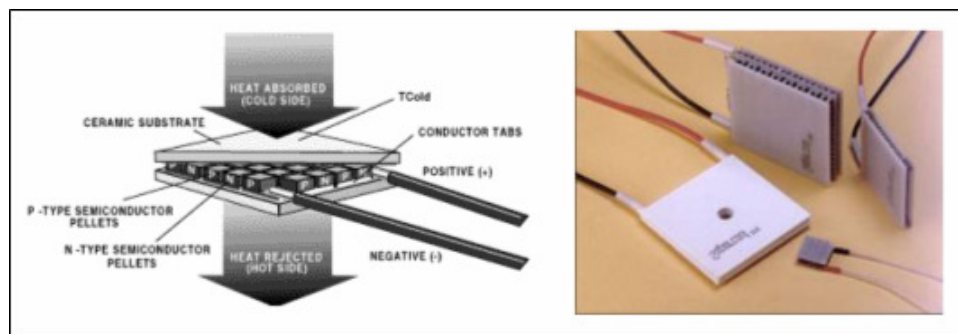


Figure 1.6: Schematic representation of thermoelectric cooling (left), thermoelectric modules (right) [8]

### 1.3 Motivation

The requirements of electronics cooling are much more critical in military electronic applications when compared to commercial applications such as personal computers, laptops and communication equipment. This is due to two reasons in conjunction. Firstly, the heat dissipation rates in military applications are usually higher; and secondly, military electronics is required to function reliably in harsh environments. The typical operating temperature specification for military equipment is the  $-30\text{ }^{\circ}\text{C}$  /  $+55\text{ }^{\circ}\text{C}$  range. Usually, the lower bound causes no problems in terms of functionality or reliability. There are, however, occasional cases in which the system must be heated to a particular temperature before beginning operation. In such instances, a heater must be employed, which is a relatively simple design consideration. It is the upper bound of  $+55\text{ }^{\circ}\text{C}$  that challenges the thermal engineer in the design of thermal management systems for military electronics. Although upper limits given by manufacturers for the operating temperature of some electronic components rate as high as  $+150\text{ }^{\circ}\text{C}$ , it is desirable to keep the surfaces of most components under the  $+85\text{ }^{\circ}\text{C}$  level. For integrated circuits, and many other electronic components, the heat dissipated by the component causes a significant temperature rise. When heat fluxes are large, that is, when large amounts of heat are dissipated by small components, such as in high performance chips, the temperature rise of the component may be as high as  $20\text{ }^{\circ}\text{C}$  or higher.

Cooling strategies for electronic components that are to comply with military operational specifications must be designed to keep the temperature rise of the component very small. The methods of cooling required at the component level may vary from conventional air cooling to advanced cooling methods such as microchannel liquid cooling and spray cooling. The selection of the cooling method is primarily based on the maximum heat flux associated with the device or component of interest. For military applications, it is common practice to employ conventional liquid cooling for heat fluxes in the order of tens of  $\text{W}/\text{cm}^2$ . When the maximum heat flux to be cooled approaches or exceeds  $100\text{ W}/\text{cm}^2$ , microchannel

liquid cooling becomes necessary. Such high heat fluxes are frequently encountered in the microwave modules of phased array radars.

#### **1.4 Present Study**

This study focuses on the experimental characterization and numerical analyses of a set of liquid cooled microchannel heat sinks designed for high performance radar cooling applications. The primary aim of the work is to apprehend the limits of the heat removal capability of microchannel heat sinks applicable to the cooling of high performance transmit/receive (T/R) modules in phased array systems in terms of temperature rise vs. surface heat flux. The goal is to be able to cool a surface heat flux of  $100 \text{ W/cm}^2$  with a moderate temperature rise (temperature difference between the hot surface and coolant inlet). The set of microchannel heat sinks consists of two material alternatives (copper and aluminum), and four channel width alternatives (300-420-500-900  $\mu\text{m}$ ). The surface area of the microchannel heatsinks, 23 mm x 61.5 mm, is selected to represent the surface area of a typical compact T/R module. The constant channel depth of 4 mm is selected to represent typical applications while satisfying size constraints and manufacturing limitations. The base thickness of 1 mm is selected due to limitations imposed by manufacturing processes while keeping in mind the thermal resistance of the base and spreading of heat along the base. An experimental setup is constructed to pump and cool the coolant fluid, to supply the high heat loads required to represent a T/R module, and to take flow rate and temperature measurements.

The secondary aim of this work is to state whether or not – and how accurately – microchannel flow and heat transfer can be simulated using commercial software. The set of microchannel heatsinks are modeled using FLUENT and the simulation results are compared with the experimental measurements.

## CHAPTER 2

### AN OVERVIEW OF THEORETICAL BACKGROUND APPLICABLE TO MICROCHANNEL FLOW AND HEAT TRANSFER

This chapter has been included to introduce channel flow concepts and methods of calculation for various flow parameters. Characteristics specific to microchannel flow and heat transfer have also been presented.

#### 2.1 Fundamental Theoretical Background on Channel Flow and Heat Transfer

This section is intended to provide a general overview of the theory of flow and heat transfer, beginning from the conservation laws. Relations for pressure drop and heat transfer calculations for channel flow are presented, and considerations specific to microchannel flow are discussed. For formulations that vary with channel cross sectional shape, the discussion is limited to expressions for rectangular cross sections due to the relevance with the present study.

##### 2.1.1 Governing Equations

Flow and heat transfer is governed by three fundamental conservation laws of physics: conservation of mass, conservation of momentum, and conservation of energy. The general form of the conservation of mass, also known as the continuity equation, is

$$\frac{\partial \rho}{\partial t} + \nabla \cdot (\rho \mathbf{V}) = 0 \quad (2.1)$$

where  $\rho$  is the density of the fluid,  $t$  refers to time, and  $V$  is the velocity vector.

The general form of the conservation of momentum, or Navier-Stokes equations, is

$$\rho \frac{DV}{Dt} = \rho \mathbf{g} - \nabla p + \frac{\partial}{\partial x_j} \left[ \mu \left( \frac{\partial v_i}{\partial x_j} + \frac{\partial v_j}{\partial x_i} \right) + \delta_{ij} \lambda \nabla \cdot (\mathbf{V}) \right] \quad (2.2)$$

where  $\mathbf{g}$  is the gravitational acceleration vector,  $p$  is the pressure field,  $\mu$  is the dynamic viscosity,  $\lambda$  is a viscosity parameter assumed to be equal to  $-(2/3)\mu$  and variables in tensor notation are as defined in Appendix A.

The general form of the conservation of energy, or the first law of thermodynamics, is

$$\rho \frac{Dh}{Dt} = \frac{Dp}{Dt} + \nabla \cdot (k \nabla T) + \phi \quad (2.3)$$

where  $h$  is the enthalpy,  $k$  is the thermal conductivity,  $T$  is the temperature field, and  $\phi$  is given by

$$\begin{aligned} \phi = & \mu \left[ 2 \left( \frac{\partial u}{\partial x} \right)^2 + 2 \left( \frac{\partial v}{\partial y} \right)^2 + 2 \left( \frac{\partial w}{\partial z} \right)^2 + \left( \frac{\partial v}{\partial x} + \frac{\partial u}{\partial y} \right)^2 + \left( \frac{\partial w}{\partial y} + \frac{\partial v}{\partial z} \right)^2 + \left( \frac{\partial u}{\partial z} + \frac{\partial w}{\partial x} \right)^2 \right] \\ & + \lambda \left( \frac{\partial u}{\partial x} + \frac{\partial v}{\partial y} + \frac{\partial w}{\partial z} \right)^2 \end{aligned}$$

For convenience, the relations above have been expressed in compact form. A review of tensor notation and relations of calculus are given in Appendix A.

The conservation equations may be greatly simplified by assuming steady, incompressible flow, as is the case for the flows of consideration in the present study. The continuity equation for steady and incompressible flow reduces to,

$$\nabla \cdot \mathbf{V} = 0 \quad (2.4)$$

or, in expanded form,

$$\rho \left( \frac{\partial u}{\partial x} + \frac{\partial v}{\partial y} + \frac{\partial w}{\partial z} \right) = 0 \quad (2.5)$$

where  $u$ ,  $v$ , and  $w$  are the three components of the velocity vector in the three general orthogonal directions  $x$ ,  $y$ , and  $z$ .

For channel flow, body forces may be neglected and viscosity may often be assumed to be constant. With these additional simplifications, the Navier-Stokes equations for steady and incompressible flow reduce to

$$\rho (\mathbf{V} \cdot \nabla \mathbf{V}) = -\nabla p + \mu \nabla^2 \mathbf{V} \quad (2.6)$$

or, in expanded form,

$$\rho \left( u \frac{\partial u}{\partial x} + v \frac{\partial u}{\partial y} + w \frac{\partial u}{\partial z} \right) = -\frac{\partial p}{\partial x} + \mu \left( \frac{\partial^2 u}{\partial x^2} + \frac{\partial^2 u}{\partial y^2} + \frac{\partial^2 u}{\partial z^2} \right) \quad (2.7a)$$

$$\rho \left( u \frac{\partial v}{\partial x} + v \frac{\partial v}{\partial y} + w \frac{\partial v}{\partial z} \right) = -\frac{\partial p}{\partial y} + \mu \left( \frac{\partial^2 v}{\partial x^2} + \frac{\partial^2 v}{\partial y^2} + \frac{\partial^2 v}{\partial z^2} \right) \quad (2.7b)$$

$$\rho \left( u \frac{\partial w}{\partial x} + v \frac{\partial w}{\partial y} + w \frac{\partial w}{\partial z} \right) = -\frac{\partial p}{\partial z} + \mu \left( \frac{\partial^2 w}{\partial x^2} + \frac{\partial^2 w}{\partial y^2} + \frac{\partial^2 w}{\partial z^2} \right) \quad (2.7c)$$

Similarly, the conservation of energy equation for steady and incompressible flow, with the additional simplifying assumption of constant thermal conductivity, reduces to

$$\rho c_p (\mathbf{V} \cdot \nabla \mathbf{V}) = k \nabla^2 T \quad (2.8)$$

or, in expanded form,

$$\rho c_p \left( u \frac{\partial T}{\partial x} + v \frac{\partial T}{\partial y} + w \frac{\partial T}{\partial z} \right) = k \left( \frac{\partial^2 T}{\partial x^2} + \frac{\partial^2 T}{\partial y^2} + \frac{\partial^2 T}{\partial z^2} \right) \quad (2.9)$$

where  $T$  is the temperature and  $c_p$  is the specific heat under constant pressure.

The five equations defining the conservation laws, presented above, provide a complete mathematical description of the flow of incompressible Newtonian fluids for the five unknowns of  $u$ ,  $v$ ,  $w$ ,  $p$ , and  $T$ . A more detailed discussion of these equations may be found in [9].

### ***2.1.2 Flow in Closed Conduits***

Due to the countless applications of flows in closed conduits such as channels and pipes, a full understanding of such flows is very important. From a thermal engineering point of view, the most important parameters associated with channel and pipe flows are the pressure drop and rate of heat transfer, as these define the power input required to drive the flow and the thermal performance of the system.

#### ***2.1.2.1 Geometrical Considerations***

A well established background for calculations regarding the pressure drop and heat transfer in channels is available in the literature. Two important geometrical

parameters for channel flows that are frequently encountered in such calculations are the aspect ratio,  $\alpha$ , and the hydraulic diameter,  $D_h$ , defined as follows for a channel of rectangular cross section with a short side of  $a$  and a long side of  $b$ , shown in Fig. 2.1.

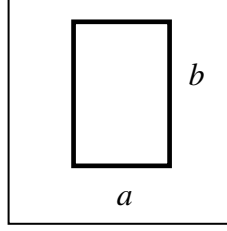


Figure 2.1: Side designation in definitions of aspect ratio and hydraulic diameter

$$\alpha = \frac{b}{a} \quad (2.10)$$

$$D_h = \frac{4A_{ch}}{P_w} \quad (2.11)$$

where  $A_{ch}$  is the cross sectional area and  $P_w$  is the wetted perimeter

$$A_{ch} = ab \quad (2.12)$$

$$P_w = 2(a + b) \quad (2.13)$$

### 2.1.2.2 Pressure Drop

The frictional pressure drop over a length  $L_{ch}$  of the channel is given by

$$\Delta p = 4f \frac{L_{ch}}{D_h} \frac{\rho u_m^2}{2} \quad (2.14)$$

where  $f$  is the Fanning friction factor and  $u_m$  is the mean flow velocity.

The Reynolds number,  $Re$ , for channel flow is defined as

$$Re = \rho u_m \frac{D_h}{\mu} \quad (2.15)$$

The Poiseuille number,  $Po$ , is defined as the product of the Reynolds number and the friction factor

$$Po = fRe \quad (2.16)$$

For fully developed laminar flow, the Poiseuille number is a constant depending on the channel aspect ratio,  $\alpha$ , for rectangular channels. The constant value may be calculated using the following relation due to Shah and London [10]

$$Po = 24 \left( 1 - 1.3553\alpha + 1.9467\alpha^2 - 1.7012\alpha^3 + 0.9564\alpha^4 - 0.2357\alpha^5 \right) \quad (2.17)$$

where the aspect ratio,  $\alpha$ , is this time the ratio of the smaller side of the channel to the larger side so that its value does not exceed unity.

The Poiseuille number calculated using the relation above ranges from 14.23 for an aspect ratio of 1, indicating a square channel, to the limiting value of 24 for infinite aspect ratio, indicating an infinitely slender channel. For a given aspect ratio and Reynolds number, the Poiseuille number calculated as such may be used to obtain the friction factor, and the pressure drop across a finite length of the channel may thus be calculated.

The onset of transition to turbulence in channel flow occurs at  $Re > 2300$ , so that the above methodology for pressure calculations is valid only for smaller Reynolds numbers. For flows in microchannels, the hydraulic diameter is always very small

and the flow velocity is not very large so that the Reynolds number is almost always under the critical value of 2300. Consequently, microchannel flow is almost always laminar [11] and the relations limited to laminar flow may be used.

### 2.1.2.3 Entrance Effects

For cases in which entrance effects are important, such as flow in short channels, the apparent friction factor,  $f_{app}$ , is used to account for the pressure drop due to friction and developing flow effects. The modified pressure drop over a length  $x$  from the entrance is then

$$\Delta p = 4 f_{app} \frac{x}{D_h} \frac{\rho u_m^2}{2} \quad (2.18)$$

The difference between the apparent friction factor over a length  $x$  and fully developed friction factor  $f$  is expressed in terms of an incremental pressure defect  $K(x)$

$$K(x) = (f_{app} - f) \frac{4x}{D_h} \quad (2.19)$$

The total pressure drop over a length  $x$  from the entrance is then

$$\Delta p = \frac{2 (f_{app} Re) \mu u_m x}{D_h^2} = \frac{2 (f Re) \mu u_m x}{D_h^2} + K(x) \frac{\rho u_m^2}{2} \quad (2.20)$$

The length of the hydrodynamic developing region,  $L_h$ , is commonly accepted to be related to the hydraulic diameter and Reynolds number as follows:

$$\frac{L_h}{D_h} = 0.05 Re \quad (2.21)$$

For  $x > L_h$ , that is, when the length of the channel considered includes the whole entrance length, the incremental pressure defect attains a constant value  $K(\infty)$  known as *Hagenbach's factor*. An equation for *Hagenbach's factor* valid for rectangular channels, based on aspect ratio, is given by Steinke and Kandlikar [12]:

$$K(\infty) = 0.6796 + 1.2197\alpha + 3.3089\alpha^2 - 9.5921\alpha^3 + 8.9089\alpha^4 - 2.9959\alpha^5 \quad (2.22)$$

#### 2.1.2.4 Turbulence Effects

For cases where turbulence has to be taken into account, a number of correlations with comparable accuracies are available for the friction factor. The relation recommended by Kandlikar et al. [13] is that presented by Philips [14], which is valid for both developing and fully developed turbulent flow,

$$f_{app} = A Re_{le}^B \quad (2.23)$$

where

$$A = 0.0929 + \frac{1.01612}{\frac{x}{D_h}} \quad (2.24)$$

$$B = -0.268 - \frac{0.3293}{\frac{x}{D_h}} \quad (2.25)$$

and  $Re_{le}$  is the “laminar-equivalent Reynolds number”, based on a modified hydraulic diameter, given by Jones [15]

$$Re_{le} = \frac{\rho u_m \left[ \frac{2}{3} + \frac{11}{24} \left( \frac{1}{\alpha} \right) \left( 2 - \frac{1}{\alpha} \right) \right] D_h}{\mu} \quad (2.26)$$

where the product of the expression in the square brackets and  $D_h$  is termed the “laminar-equivalent hydraulic diameter”.

#### **2.1.2.5 Minor Losses**

Referring to the relations above, the frictional pressure drop across a channel may be calculated for all modes of flow, ie., for developing laminar, fully developed laminar, developing turbulent, and fully turbulent flow. However, for a microchannel heatsink, pressure drop is not limited to the frictional pressure drop across the channels. Typically, flow enters the microchannels through inlet and outlet plenums, which are commonly incorporated with a 90° bend. The flow thus encounters a 90° change in direction during entrance to the inlet plenum, a sudden contraction during entrance to the channels from the inlet plenum, a sudden expansion during the entrance to the outlet plenum from the channels, and finally, another 90° change in direction while leaving the outlet plenum. Drops in pressure due to such changes in the flow geometry are termed *minor losses*. A sketch of the regions of minor loss in a typical microchannel heatsink, also representative of the heatsinks of the present study, is given by Philips [14] in Fig. 2.2. The sketch also includes the regions of flow separation leading to pressure losses. Referring to the numbered sections in the figure, the minor losses may be defined as follows:

0-1: 90° bend at entry

1-2: sudden contraction in flow area between the inlet plenum and channel entrance

3-4: sudden expansion in flow area between the channel exit and outlet plenum

4-5: 90° bend at exit

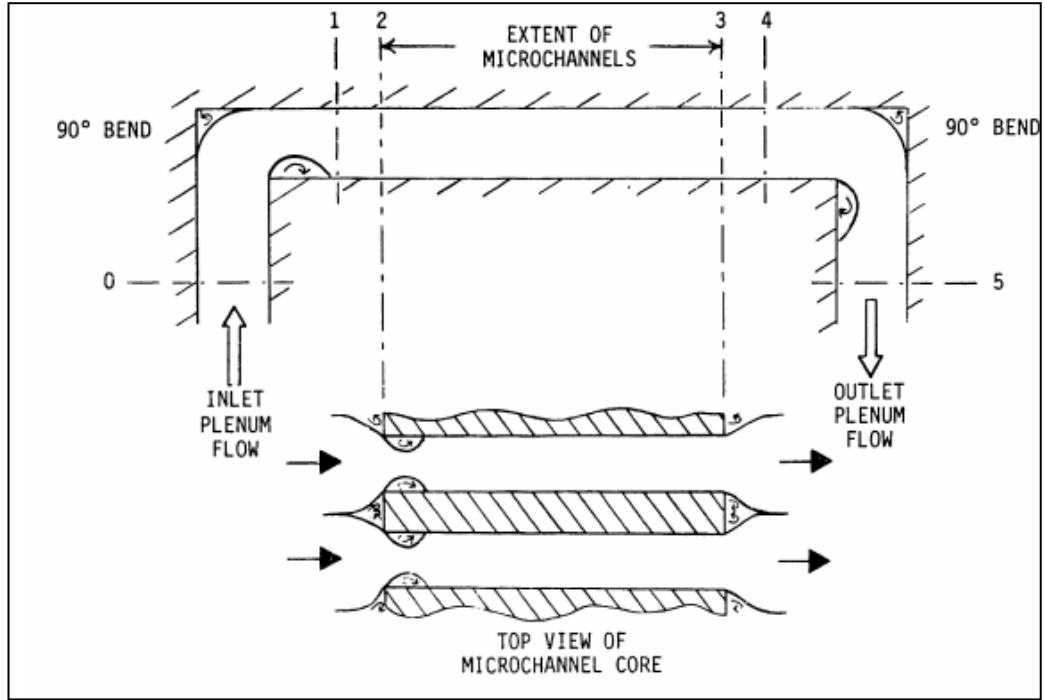


Figure 2.2: Regions of minor loss in a typical microchannel heatsink [14]

The most common method to determine minor pressure drops is to specify the loss coefficient,  $K_L$  [16]. The pressure loss is related to the loss coefficient as

$$\Delta p = K_L \frac{1}{2} \rho V^2 \quad (2.27)$$

For rectangular channels, the loss coefficients for sudden contraction ( $K_c$ ) and sudden expansion ( $K_e$ ) are given by Kays and London [17], based on the flow area ratio and Reynolds number, as shown in Fig. 2.3. The loss coefficient for 90° bends,  $K_{90}$ , is commonly taken to be 1.1 [16]. Having determined the loss coefficients, the total pressure drop across the microchannel heatsink of Fig. 2.2 may be calculated:

$$\Delta p = \frac{1}{2} \rho u_{mp}^2 K_{90} + \frac{1}{2} \rho u_{mc}^2 K_c + 4 \left( f_{app} \right) \frac{L_{ch}}{2D_h} + \frac{1}{2} \rho u_{mc}^2 K_e + \frac{1}{2} \rho u_{mp}^2 K_{90} \quad (2.28)$$

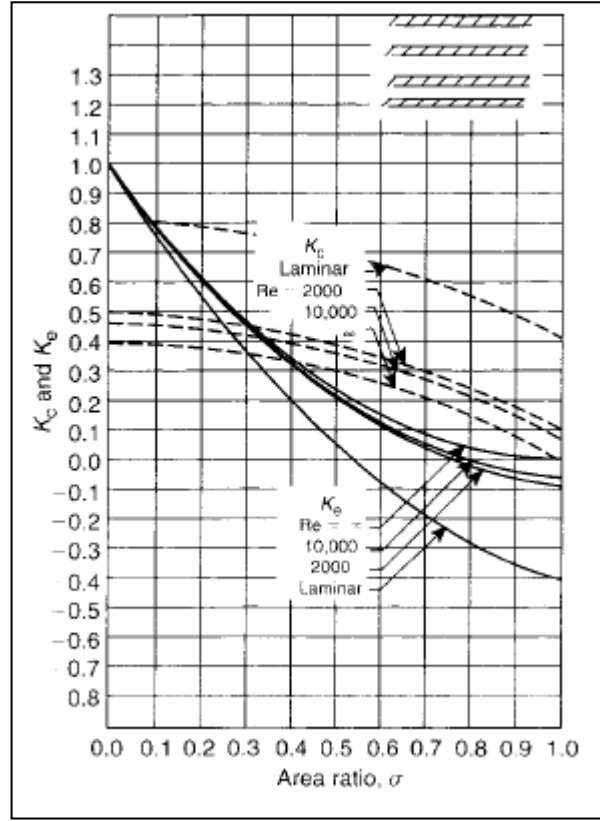


Figure 2.3:  $K_c$  and  $K_e$  for laminar channel flow [17]

where  $u_{mp}$  is the mean velocity of the flow in the inlet and outlet plenums, which are assumed to be identical, and  $u_{mc}$  is the mean velocity of the flow inside the microchannels. Recognizing that the ratio of these velocities is the inverse of the ratio of the plenum and channel flow areas, and making use of the relation for the apparent friction factor, the total pressure drop may be rewritten as

$$\Delta p = \frac{1}{2} \rho u_m^2 \left[ \left( \frac{A_c}{A_p} \right)^2 2 K_{90} + (K_c + K_e) + \frac{4fL_{ch}}{D_h} + K(x) \right] \quad (2.29)$$

where  $u_m$  is the mean channel flow velocity,  $A_{ch}$  is the channel flow area, and  $A_p$  is the plenum flow area. As long as the channel length exceeds the hydrodynamic entrance length ( $L_{ch} > L_h$ ),  $K(x)$  may be replaced with  $K(\infty)$ .

### 2.1.3 Heat Transfer in Closed Conduits

The convective heat transfer to or from the channel walls from or to the fluid is given by Newton's law of cooling:

$$q = h_{ave} (A_{ht}) (T_s - T_m) \quad (2.30)$$

where  $q$  is the rate of heat transfer,  $h_{ave}$  is the average convective heat transfer coefficient,  $A_{ht}$  is the total heat transfer area,  $T_s$  is the channel wall inner surface temperature, and  $T_m$  is the fluid mean temperature.

The heat transfer can be more accurately described using a log mean temperature difference, especially if the wall surface temperature is not constant:

$$\Delta T_{LMTD} = \frac{(T_s - T_i) - (T_s - T_o)}{\ln \left( \frac{T_s - T_i}{T_s - T_o} \right)} \quad (2.31)$$

where  $T_i$  is the fluid inlet temperature and  $T_o$  is the fluid outlet temperature.

The channel wall surface heat flux can be defined as the rate of heat transferred to or from the channel wall from or to the fluid per unit heat transfer area,

$$q_s'' = h_{ave} (T_s - T_m) \quad (2.32)$$

or

$$q_s'' = h_{ave} \Delta T_{LMTD} \quad (2.33)$$

where

$$q_s'' = \frac{q}{A_{ht}} \quad (2.34)$$

Alternatively, the rate of heat transfer may be expressed by means of an energy balance between the channel inlet and outlet

$$q = \dot{m} c_p (T_o - T_i) \quad (2.35)$$

where  $\dot{m}$  is the mass flow rate and  $c_p$  is the specific heat under constant pressure. Heat transfer between the fluid and channel walls is characterized by the Nusselt number, Nu, given by

$$Nu = \frac{hD_h}{k} \quad (2.36)$$

where  $k$  is the thermal conductivity of the fluid and  $h$  is the local convective heat transfer coefficient.

Theoretical analysis reveals that, for fully developed laminar flow under constant wall temperature, constant wall heat flux, or circumferentially constant wall temperature and axially uniform heat flux conditions, the Nusselt number is constant [18]. These three boundary conditions are commonly designated as follows

*T*-Boundary Condition: constant wall temperature

*H1*-Boundary Condition: circumferentially constant wall temperature, axially uniform heat flux

*H2*-Boundary Condition: constant wall heat flux

For rectangular channels, the Nusselt number for each of these three boundary conditions is given by the relations below [13].

$$Nu_T = 7.541 \left( 1 - 2.610\alpha + 4.970\alpha^2 - 5.119\alpha^3 + 2.702\alpha^4 - 0.548\alpha^5 \right) \quad (2.37a)$$

$$Nu_{HI} = 8.235 \left( 1 - 2.0421\alpha + 3.0853\alpha^2 - 2.4765\alpha^3 + 1.0578\alpha^4 - 0.1861\alpha^5 \right) \quad (2.37b)$$

$$Nu_{H2} = 8.235 \left( 1 - 10.6044\alpha + 61.1755\alpha^2 - 155.1803\alpha^3 + 176.9203\alpha^4 - 72.923\alpha^5 \right) \quad (2.37c)$$

### ***2.1.3.1 Developing Flow***

The thermal entry length, which is often not negligible in microchannel applications, is expressed as follows for duct flow

$$\frac{L_t}{D_h} = cRePr \quad (2.38)$$

where  $L_t$  is the thermal entry length,  $c$  is a constant that may be taken to be 0.1 for rectangular channels [13], and the Prandtl number,  $Pr$ , a measure of the ratio of momentum to thermal diffusion, is defined as

$$Pr = \frac{c_p \mu}{k} \quad (2.39)$$

For rectangular channels under the four side heating condition, the Nusselt number in the developing laminar flow region is given in Table 2.1 derived by Kandlikar [13] based on the work of Philips [14].

Table 2.1: Nusselt number in the developing laminar region ( $\alpha_c$  defined as width/thickness)

$x^*$	$\alpha_c \leq 0.1^*$	$Nu_{c,4}$				$\alpha_c \geq 10^{**}$
		$\alpha_c = 0.25$	$\alpha_c = 0.333$	$\alpha_c = 0.5$	$\alpha_c = 1.0$	
0.0001	31.4	26.7	27.0	23.7	25.2	31.6
0.0025	11.9	10.4	9.9	9.2	8.9	11.2
0.005	10	8.44	8.02	7.46	7.1	9.0
0.00556	9.8	8.18	7.76	7.23	6.86	8.8
0.00625	9.5	7.92	7.5	6.96	6.6	8.5
0.00714	9.3	7.63	7.22	6.68	6.32	8.2
0.00833	9.1	7.32	6.92	6.37	6.02	7.9
0.01	8.8	7	6.57	6.05	5.69	7.49
0.0125	8.6	6.63	6.21	5.7	5.33	7.2
0.0167	8.5	6.26	5.82	5.28	4.91	6.7
0.025	8.4	5.87	5.39	4.84	4.45	6.2
0.033	8.3	5.77	5.17	4.61	4.18	5.9
0.05	8.25	5.62	5.00	4.38	3.91	5.55
0.1	8.24	5.45	4.85	4.22	3.71	5.4
1	8.23	5.35	4.77	4.11	3.6	5.38

$x^* = x/(Re Pr D_h)$ ; \* – parallel plates, both sides heated; \*\* – parallel plates, one side heated.

### 2.1.3.2 Turbulence Effects

For flows involving turbulence, the following equations for the Nusselt number are suggested by Philips [14] for thermally developing turbulent flow

$$Nu = 0.0214 \left[ 1 + \left( \frac{D_h}{x} \right)^{\frac{2}{3}} \right] [Re^{0.8} - 100] Pr^{0.4} \text{ for } 0.5 < Pr < 1.5 \quad (2.40a)$$

$$Nu = 0.012 \left[ 1 + \left( \frac{D_h}{x} \right)^{\frac{2}{3}} \right] [Re^{0.87} - 280] Pr^{0.4} \text{ for } 1.5 < Pr < 500 \quad (2.40b)$$

In the above relations, the term  $\left( \frac{D_h}{x} \right)^{\frac{2}{3}}$  drops asymptotically to unity as  $x$  increases. Therefore, for fully developed turbulent flow, these relations reduce to

$$Nu = 0,0428 \left[ Re^{0,8} - 100 \right] Pr^{0,4} \text{ for } 0,5 < Pr < 1,5 \quad (2.41a)$$

$$Nu = 0,024 \left[ Re^{0,87} - 280 \right] Pr^{0,4} \text{ for } 1,5 < Pr < 500 \quad (2.41b)$$

Correlations for the Nusselt number in all modes of flow for rectangular channels have been presented. Correlations for the friction factor had been presented previously. Using these relations, the pressure drop and heat transfer across rectangular channels may be calculated. Although a number of researchers argue that in microchannels, correlations developed for conventional sized channels (such as those presented thus far) are no longer valid, it is widely accepted, based on more recent studies, that these correlations may be used with confidence for flow and heat transfer in microchannels.

### ***2.1.3.3 Thermal Performance of Liquid Cooled Heatsinks***

Although the friction factor and convective heat transfer coefficient are representative of the hydraulic and thermal characteristics of channel flow, the thermohydraulic performance of a heatsink is commonly characterized by the pressure drop and the concept of thermal resistance. The thermal resistance of a heatsink, commonly given in °C/W, is defined as the temperature rise between the heatsink base and the coolant fluid caused by unit heat power applied to the heatsink base.,

$$R_{HS} = \frac{T_b - T_i}{q} = \frac{\theta_b}{q} \quad (2.42)$$

where  $T_b$  is the heatsink base temperature,  $T_i$  is the coolant fluid inlet temperature, and  $q$  is the heat load applied to the base of the heatsink. The coolant fluid inlet temperature is commonly taken to be the temperature at the inlet to the heatsink.

The thermal resistance concept is important in electronics cooling applications because it can be used to calculate the heatsink base temperature, which usually must be kept under a certain limit, when the heat load and coolant fluid inlet temperature are known. Because the temperature rise in the definition of thermal resistance depends on the convective heat transfer coefficient, which is determined by the Nusselt number, which is a function of aspect ratio and/or Reynolds number, the value of thermal resistance depends on the coolant flow rate and channel geometry. The friction factor, thus the pressure drop, is also a function of the Reynolds number, thus the coolant flow rate and channel geometry. The coolant flow rate, therefore, has a great impact on both the cooling performance of the heatsink and the pumping power required to drive the flow for a particular channel geometry. Finding a compromise between cooling performance and pumping power is often a challenge in electronics cooling applications. Commonly, the maximum allowable thermal resistance for a heatsink to provide sufficient cooling is determined as a first step, and a suitable design is selected from a set of flow rate/channel geometry pairs that satisfy the thermal resistance requirement.

#### ***2.1.3.4 Heat Transfer from Extended Surfaces***

For fins of uniform cross sectional area, such as the channel walls of rectangular microchannels heatsinks, a straightforward calculation methodology that takes into account the fin array effect is available [18]. When it is desired to relate the heat transferred between a heatsink and its coolant to the temperature rise between the heatsink base and coolant ( $\theta_b$ ), the concept of fin efficiency,  $\eta_f$ , is commonly used. Fin efficiency is defined as the ratio of the actual heat transfer between the fin and coolant to the amount of heat that would be transferred if all surfaces of the fin were at the constant base temperature:

$$\eta_f = \frac{q_f}{q_{\max}} = \frac{q_f}{hA_f \theta_b} \quad (2.43)$$

where  $q_f$  is the heat transferred between the fin and coolant,  $h$  is the convection heat transfer coefficient, and  $A_f$  is the surface area of the fin. The fin efficiency for rectangular fins is given as [18]:

$$\eta_f = \frac{\tanh(mL_c)}{mL_c} \quad (2.44)$$

where  $L_c$  is the characteristic length of the fin, based on the length,  $L$ , and thickness,  $t_f$ , of the fin

$$L_c = L + \frac{t_f}{2} \quad (2.45)$$

and  $m$  is defined as

$$m = \sqrt{\frac{hP_w}{kA_c}} \quad (2.46)$$

where  $h$  is the convection heat transfer coefficient,  $P_w$  is the fin perimeter,  $k$  is the thermal conductivity of the fin material, and  $A_c$  is the cross sectional area of the fin. The geometrical parameters are illustrated in Fig. 2.4

For an array of fins, which is representative of a microchannel heatsink, an overall surface efficiency,  $\eta_o$ , characterizes the overall efficiency of all surfaces of the heatsink:

$$\eta_o = \frac{q_t}{q_{\max}} = \frac{q_t}{hA_t \theta_b} \quad (2.47)$$

where  $q_t$  is the actual heat transferred between the heatsink and coolant through  $A_t$ , the total surface area of the heatsink exposed to the coolant. The overall surface efficiency is given by:

$$\eta_o = 1 - \frac{NA_f}{A_t} (1 - \eta_f) \quad (2.48)$$

After the overall surface efficiency is calculated, the temperature rise of the heatsink base with respect to the coolant temperature may readily be obtained:

$$\theta_b = \frac{q_t}{\eta_o} h A_t \quad (2.49)$$

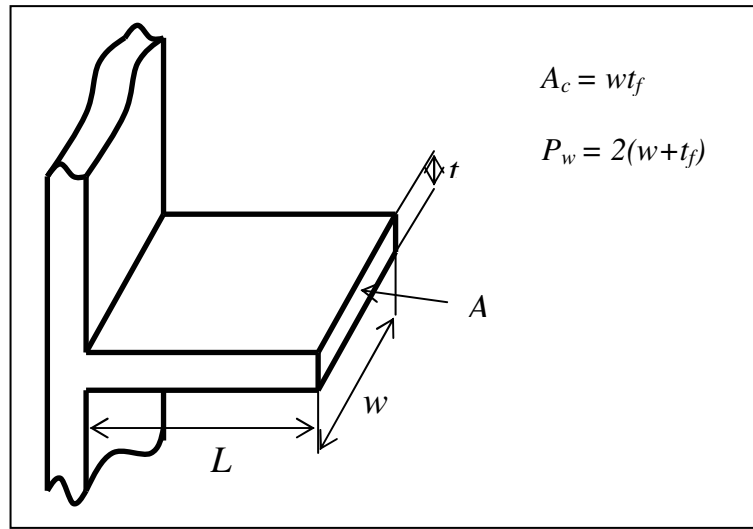


Figure 2.4: Fin geometrical parameters

## 2.2 Characteristics of Flow and Heat Transfer in Microchannels

Before proceeding with the characteristics of microchannel flow and heat transfer, it is appropriate to introduce a definition for the term “microchannel”. The scope of the term is among the topics of debate between researchers in the field. Mehendale *et al.* [19] used the following classification based on manufacturing techniques required to obtain various ranges of channel dimensions, “ $C_D$ ” being the smallest channel dimension:

$1\ \mu\text{m} < C_D < 100\ \mu\text{m}$	: Microchannels
$100\ \mu\text{m} < C_D < 1\ \text{mm}$	: Minichannels
$1\ \text{mm} < C_D < 6\ \text{mm}$	: Compact passages
$6\ \text{mm} < C_D$	: Conventional passages

Kandlikar and Grande [20] adopted a different classification based on the rarefaction effect of gases in various ranges of channel dimensions, “ $C_D$ ” being the smallest channel dimension:

$1\ \mu\text{m} < C_D < 10\ \mu\text{m}$	: Transitional Microchannels
$10\ \mu\text{m} < C_D < 200\ \mu\text{m}$	: Microchannels
$200\ \mu\text{m} < C_D < 3\ \text{mm}$	: Minichannels
$3\ \text{mm} < C_D$	: Conventional passages

A simpler classification was proposed by Obot [21] based on the hydraulic diameter rather than the smallest channel dimension. Obot classified channels of hydraulic diameter under 1 mm ( $D_h < 1\ \text{mm}$ ) as microchannels, which was also adopted by many other researchers such as Bahrami [22,23] and Bayraktar [24]. This definition is considered to be more appropriate for the purposes of this thesis as the classification proposed by Kandlikar and Grande is based on the behavior of gas flows – which is outside the scope of this study, and the classification proposed by Mehendale is based on manufacturing processes – which are expected to change and/or improve in the future. The definition adopted by Obot is more convenient as it is based on the channel geometry alone and that it makes use of the hydraulic diameter concept, which is the primary representative dimension for internal flow geometry.

When researchers began to study flow and heat transfer in geometries that may be defined as microchannels by any of the classifications given above, many observed that the experimental results did not agree well with conventional flow and heat transfer theory. Discrepancies with conventional analytical predictions and

correlations were reported for friction factor observations, transition to turbulence, and heat transfer characteristics. Among these flow properties, transition to turbulence has consistently been reported by researchers to be earlier for microscale flows than predicted by conventional theory. However, experimental results for friction factor and calculated Nusselt number are observed to be inconsistent with each other. A number of researchers have reported friction factors that are significantly higher than predicted by conventional theory, while others have reported friction factors that are significantly lower than predicted by conventional theory. A similar trend is observed for heat transfer characteristics based on the calculated Nusselt number. The nature of these discrepancies is a matter of debate between researchers. It is observed that some researchers claim that the discrepancies are due to microscale flow effects while some researchers argue that the conflicts are due to uncertainties and inaccuracies in measurements. It is also observed, however, that the results of more recent studies are more consistent with conventional theory predictions in comparison with the results of earlier studies.

What is meant by conventional flow and heat transfer theory is the continuum description of the flow based on the principles of conservation of mass, momentum and energy, and the second law of thermodynamics. The set of partial differential equations resulting from these principles are the Navier-Stokes and Fourier equations. There are three fundamental assumptions that need to be satisfied for these equations to remain valid [25]:

### ***2.2.1 Newtonian Framework***

The Navier-Stokes equations are based on a Newtonian framework that assumes the fluid motion is non-relativistic [25]. The implication of this condition is that the characteristic velocity has to be much smaller than the speed of light, which is met by almost all flows, including those at the microscale.

### 2.2.2 Continuum Approximation

The Navier-Stokes equations are based on the assumption that the fluid is infinitely divisible. In other words, local flow properties such as density, pressure, velocity, and shear stress can be defined as averages computed over flow elements that are sufficiently large compared to the microscopic structure of the fluid, but small enough in comparison to the macroscopic gradients to allow the use of differential calculus to describe the variation of flow properties [25]. This approximation is almost always satisfied, the exception being flows where the spatial length scale is comparable to the mean distance between molecules, such as in nanodevices and in shock waves that are extremely thin relative to the molecular separation distance [3].

### 2.2.3 Thermodynamic Equilibrium

The Navier-Stokes equations are also based on the approximation that all flow properties are in local thermodynamic equilibrium, implying that the macroscopic quantities within the fluid have sufficient time to adjust to their surroundings [25]. For the flow adjacent to the wall, this requires an infinitely high frequency of collisions between the fluid and the solid surface [3]. Validity of this condition leads to the ideal no-slip/no-temperature-jump boundary conditions at the wall. However, since the infinite collision frequency is not possible to physically attain, there will always be a finite velocity slip and temperature jump at the wall. For both liquids and gases, the linear Navier boundary condition empirically relates the tangential velocity slip at the wall to the local shear:

$$\Delta u|_w = u_{fluid} - u_{wall} = L_s \left[ \frac{\partial u}{\partial y} \right]_w \quad (2.50)$$

In the above expression,  $L_s$  is the constant slip length and the partial derivative is the strain rate computed at the wall. In most practical applications, the slip length is so small that the no-slip condition holds [3].

To summarize the implications of the above conditions, it may be said that the Newtonian framework condition holds for all practical applications. For gas flows, thermodynamic equilibrium does not hold for many microscale flows, and wall slip/temperature jump phenomena are observed. Various boundary conditions that accommodate such flow behavior at the wall have been proposed by a number of researchers including Deissler [26], Beşkök [27], Xue and Fan [28], Jie *et al.* [29], and Lockerby *et al.* [30]. These boundary conditions have been implemented in numerical gas flow models with success. For gas flows in which the flow geometry is so small that the molecular diameter becomes comparable to the mean distance between molecules, the continuum approximation also breaks down such that the Navier-Stokes equations become invalid. In such cases, successful modeling may be achieved using the Burnett equations, or, when necessary, direct molecular modeling. It may be said that microscale gas flows are well understood due to the kinetic theory of gases, and modeling at all scales is possible.

For liquid flows, it may be said that the continuum approximation is always valid for practical applications. Also, the flow is sufficiently close to thermodynamic equilibrium such that the slip length is so small that the no-slip/no-temperature-jump boundary condition holds for most flows. However, the conditions under which the no-slip boundary condition becomes inaccurate or the point at which the stress-strain relation or the heat flux-temperature gradient relation fails to be linear, is not well known [3]. It has been shown by Loose and Hess [31] that non-Newtonian behavior begins when the strain rate exceeds twice the molecular frequency scale:

$$\frac{\partial u}{\partial y} \geq 2\tau^{-1} \quad (2.51)$$

where  $\tau$  is the molecular length scale, and is given by:

$$\tau = \sqrt{\frac{m_m \sigma^2}{\varepsilon}} \quad (2.52)$$

where  $m_m$  is the molecular mass, and  $\sigma$  and  $\varepsilon$  are, respectively, the characteristic length and energy scale for the molecules. For ordinary liquids such as water, this time scale is extremely small and the threshold shear rate for the onset of non-Newtonian behavior is, therefore, extraordinarily high. For high molecular weight polymers, on the other hand,  $m$  and  $\sigma$  are both many orders of magnitude higher than their respective values for water, and the linear stress-strain relation breaks down at realistic values of the shear rate [3].

Although rare, examples where slip flow in liquids occurs are corner flows and extrusion of polymer melts from capillary tubes [3]. It has been observed by Israelvichli [32] and Gee et al. [33] that slip occurs in liquids only when the flow scale is smaller than 0.1  $\mu\text{m}$ .

It is evident from the above discussion that for the flow of conventional liquids - such as water - in practical geometries - such as those on the order of tens or hundreds of microns - flow behavior such as deviation from continuum, slip flow, or non-Newtonian effects is not expected. However, surface effects are much more important for all microscale flows when compared to conventional scale flows, even though the continuum approximation, no-slip boundary conditions, and Newtonian behavior relations hold. For a flow domain with a characteristic length of 1 m, the surface area/volume ratio is  $1 \text{ m}^{-1}$ , while that for a microscale flow domain with a characteristic length of 1  $\mu\text{m}$  is  $10^{-6} \text{ m}^{-1}$ . This dramatic increase implies that surface effects dominate in microscale flows. For conventional manufacturing techniques suitable for manufacturing microchannels, the surface roughness becomes comparable to the channel dimensions such that the surface roughness may introduce a viscosity effect. Que *et al.* proposed a Roughness-

Viscous Model (RVM) [34] to accommodate for such effects. Surface roughness effects were also investigated by Kleinstreuer [35] using a thin Porous Medium Layer (PML) on the walls. It is suggested by Kleinstreuer that the viscosity effect due to surface roughness is among the possible reasons for discrepancies in experimental results for liquid flows. Based on a similar argument, entrance and exit effects are also considered to be possible causes of discrepancies. Considering the conflicts in heat transfer rate measurements, Kleinstreuer pointed out the drastic increase of viscous dissipation with decreasing channel dimensions to be the cause.

As a concluding statement, the characteristics of flow and heat transfer at the microscale that separate them from macroscale flows may be summarized as follows:

- i. Friction factors that are observed to be significantly higher or lower than those predicted by conventional theory.
- ii. Nusselt numbers that are observed to be significantly higher or lower than those predicted by conventional theory.
- iii. Earlier transition to turbulence, in terms of the Reynolds number.
- iv. Enhanced surface effects such as the viscosity effect of surface roughness, and viscous dissipation.

## **CHAPTER 3**

### **AN OVERVIEW OF CURRENT LITERATURE RELATED TO FLOW AND HEAT TRANSFER IN MICROCHANNELS**

This chapter is devoted to selected observations from the survey of literature on flow and heat transfer in microchannels. For convenience, the material is presented in three separate sections for experimental studies, analytical and numerical studies, and application oriented studies.

#### **3.1 Experimental Work on Microchannel Flow and Heat Transfer: A Bibliographical Perspective**

Attention was first drawn to the study of microchannel flow as a method of advanced cooling by the pioneering work of Tuckerman and Pease [2] in 1981. Various aspects of flow and heat transfer in microgeometries have since been widely studied experimentally. Following the work of numerous investigators, significant conflicts have been observed among results. Although recent studies are generally more consistent with theoretical predictions and also with each other, conflicts still remain between researchers as to how experimental results should be interpreted. In this section, important aspects of selected experimental studies are presented. In consistence with the observation of Kandlikar and Grande [20] that active research on establishing microchannel thermal hydraulic performance has started in the late 1990s, the survey of literature is presented with an emphasis on more recent studies.

In 1981, Tuckerman and Pease [2] experimented on a series of parallel rectangular microchannels of 50  $\mu\text{m}$  width and 300  $\mu\text{m}$  height, with 50  $\mu\text{m}$  wall thickness,

machined in a 1 cm x 1 cm silicon wafer. They made use of thin film WS<sub>2</sub> resistors to supply 790 W/cm<sup>2</sup> heat flux to the silicon heatsink. They pumped water through the microchannel at a flow rate of 0.52 lpm (liters per minute) at a pressure drop of 2.2 bar. They measured the temperature of the heat sink to be 71 °C above the water inlet temperature for these values, and calculated the thermal resistance of the microchannel heatsink to be 0.09 °C/W. It is widely recognized that the results of this study demonstrates that laminar flow in microchannels has higher heat extraction abilities than turbulent flow in conventional sized channels [36].

In the following years, before 1994, a number of similar studies by researchers such as Missagia et al. [37], Riddle et al. [38], Peng and Weng [39], Rahman and Gui [40], were performed with water in rectangular channels. The hydraulic diameters of the channels in these studies ranged from 90 μm to 500 μm. These researchers reported various discrepancies between theoretical predictions and their experimental results, for both Nusselt number and friction factor. Interest in microchannel studies increased following the comprehensive work by Wang and Peng [41] in 1994. In their study, Wang and Peng obtained measurements leading to friction factor and Nusselt number for deionized water in stainless steel tubes with a fixed channel height of 0.7 mm and channel widths of 0.2, 0.4, 0.6 and 0.8 mm. They observed that the Nusselt number was lower than the theoretical value for laminar flow, and exhibited dependence with the Reynolds number. In the turbulent regime, they report that the Nusselt number is almost a third of the values predicted by Colburn's correlation and that transition to turbulence begins at the critical Reynolds number of 700, which is much lower than the widely accepted value of 2300 for internal flow in the case of conventional flow passages. They also observed that friction factors departed significantly from theoretical predictions in the laminar regime. They attributed the conflicts between theoretical predictions and their measurements to the early onset of transition to turbulence. Although this work has been referenced by many researchers and is recognized as one of the milestones in the experimental investigation of microchannel flow and heat transfer, it is argued by Hetsroni et al. in a recent review paper that “these

results do not agree with those reported by others (in proceeding studies) and are probably incorrect” [42].

In 1995, Peng and Peterson [43] experimented on a water-methanol mixture in stainless steel rectangular channels of hydraulic diameter ranging from 133  $\mu\text{m}$  to 367  $\mu\text{m}$ . They observed an inconsistent increase or decrease in friction factor compared to theory and attributed this behavior to the early onset of transition to turbulence, which they observed to occur at Reynolds numbers of 400 for larger channels and 70 for the smaller channels. They developed correlations for Nusselt number and friction factor. They attributed the conflicts between the results of Wang and Peng discussed above to the reduction of fluid viscosity along the channels due to a significant increase in temperature. They concluded from their results that transition zone and heat transfer characteristics in the laminar and transition regimes were influenced by liquid temperature, velocity, Reynolds number, and microchannel size.

In 1998, based on a series of experiments of distilled water in copper microtubes of diameters ranging from 102  $\mu\text{m}$  to 1.09 mm in the turbulent regime, Adams et al. [44] proposed a modification to the Gnielinski correlation to match their experimental results for the Nusselt number, which were underpredicted by the original equation. A year later, the same study group repeated the experiments in non-circular channels of 1.13 mm hydraulic diameter and observed that the experimental Nusselt number values were well predicted by the Gnielinski equation. They therefore concluded that standard correlations for Nusselt number could be applied to channels of  $D_h \geq 1.2$  mm in the turbulent regime [45].

In 1999, Sabry [46] proposed as a possible physical explanation for the deviation of friction and heat transfer coefficients from conventional values. He stated that the wall shear stress, particularly high in microchannels, could give to the flow a greater tendency to separate over roughness elements. The flow would then be

separated from the wall by a thin film of gas playing the role of a heat insulator, which would act to reduce the Nusselt number from predicted values.

Again in 1999, Mala and Li [47] experimented with deionized water in fused silica and stainless steel tubes of diameters ranging from 50  $\mu\text{m}$  to 254  $\mu\text{m}$ , at Reynolds numbers up to 2500. They used a precision pump to drive the flow, a 0.1  $\mu\text{m}$  filter ahead of the pump, a flow meter for flow rate measurements and pressure transducers at inlet and exits for pressure drop measurements. Their results indicate significant departure of flow characteristics from the predictions of conventional theory for microtubes of smaller diameter. For diameters above 150  $\mu\text{m}$ , experimental results are in rough agreement with theory. Two interesting observations are:

- 1- For low Reynolds numbers, pressure gradients are well predicted by Poiseuille flow theory, but as the Reynolds number increases, there is a significant increase in pressure drop than that predicted. The friction factor is, therefore, also higher.
- 2- For the same flow rate and diameter, a fused silica microtube requires a higher pressure drop than a stainless steel microtube, although roughness values are the same.

They conclude that the higher pressure gradient measured may be due to early transition to turbulence or surface roughness, and that the roughness increases the momentum transfer in the boundary layer near the wall. They propose a roughness viscosity,  $\mu_R$ , to account for the additional momentum transfer (RVM – Roughness Viscosity Model). Based on the curves predicted by their RVM to be in excellent agreement with their data, they state that their proposed RVM may be used to interpret flow characteristics in microtubes. A year later, the same researchers repeated the experiments with the same experimental setup on trapezoidal silicon microchannels of hydraulic diameter ranging from 51  $\mu\text{m}$  to 169  $\mu\text{m}$  and obtained consistent results, then consequently extended their RVM to trapezoidal channels [48].

Contrary to previous researchers, Xu et al. in 2000 [49] experimented with water in aluminum and silicon microchannels of hydraulic diameters ranging from 30  $\mu\text{m}$  to 344  $\mu\text{m}$  at Reynolds numbers ranging from 20 to 4000, and observed that experimental friction factor results agreed fairly well with conventional theory in the laminar regime for hydraulic diameters greater than 100  $\mu\text{m}$ . They used an electronic balance for flow rate measurements and pressure transducers at the inlet and outlet chambers for pressure measurements. They included entrance and exit pressure losses in their pressure calculations. They observed an early transition to turbulence at the critical Reynolds number of 1500. They stated that the deviations in the results of previous literature might be due to dimensional errors rather than microscale effects.

The study by Pfund et al. in 2000 [50] differs from the experimental studies reported until that date in the literature in that pressure measurements are taken within the channels itself by using pressure taps and transition to turbulence is observed by flow visualization. The authors experimented with water in high aspect ratio channels with a fixed width of 1cm and heights ranging from 128  $\mu\text{m}$  to 521  $\mu\text{m}$  at Reynolds numbers ranging from 60 to 3450. After considering experimental uncertainties and systematic errors, significant differences remained between their results and theoretical predictions. Early transition to turbulence was also observed. They concluded that their results suggest the presence of microscale effects at low aspect ratios and low Reynolds number flows, but added that more data must be collected to make a firm conclusion. They put forward that due to the importance of the measurement of channel dimensions, there is a possibility that the available experimental data contains slight errors that become magnified during the data analysis process.

In 2002, Qu and Mudawar [51] studied the pressure drop and heat transfer characteristics of deionized water in an array of rectangular microchannels of hydraulic diameters ranging from 231  $\mu\text{m}$  to 713  $\mu\text{m}$  at Reynolds numbers ranging from 139 to 1672. The microchannels were machined in copper to form a

microchannel heatsink. The researchers used a gear pump to drive the flow and incorporated a 15  $\mu\text{m}$  filter. They used cartridge heaters to supply heat fluxes up to 200  $\text{W}/\text{cm}^2$ . They took temperature and pressure measurements from the inlet and outlet plenums using K-type thermocouples and pressure transducers. They also performed 3-D numerical modeling of the flow and heat transfer based on the Navier-Stokes and energy equations assuming steady flow and heat transfer, laminar flow, incompressible fluid, negligible radiation and natural convection of air, and constant solid and water properties except for water viscosity. They employed a variable temperature dependent water viscosity based on mean temperature. Their experimentally measured pressure drop and temperature values showed good agreement with the corresponding analysis results. They also did not observe any signs of early transition to turbulence. They thus concluded that conventional Navier-Stokes and energy equations adequately predict pressure drop and heat transfer characteristics of microchannel heatsinks and recommended the use of conventional equations for practical cooling applications involving microchannels.

In the same year, Gao et al. [52] investigated scale effects on hydrodynamics and heat transfer in 2-D mini and microchannels using deionized water in brass microchannels with heights ranging from 0.1 mm to 1 mm. They used an adjustable top to change the height of the microchannel only, while ensuring that all other parameters such as secondary dimensions, wall roughness etc. remained perfectly constant for all measurements. They used a pump with a 1  $\mu\text{m}$  filter to drive the flow and four 250 W electric cartridges to supply the heat load required. Their results showed that while the friction factor was consistent with the theoretical value in the laminar region, plots of Nusselt number departed from theory for channel heights under 500  $\mu\text{m}$ , the magnitude of departure increasing as channel height was decreased. They concluded that physical interpretation of the results was very difficult and that further experiments must be made.

The study by Sinton and Li [53] in 2003 differs from the work of previous researchers in that they used state-of-the-art flow visualization techniques to obtain the velocity profile of dyed aqueous solutions in fused silica capillaries of 102  $\mu\text{m}$  and 205  $\mu\text{m}$  internal diameter. They used a syringe pump to drive the flow and a setup based on the reflection of ultraviolet laser beams to visualize the flow. They concluded that their results compared favorably to analytical solutions.

Again in 2003, Yang et al. [54] experimented on the friction characteristics of water and R-134a in tubes of internal diameter ranging from 173  $\mu\text{m}$  to 4.01 mm. They used a gear pump with a 25  $\mu\text{m}$  filter to drive the flow, a positive displacement flow meter for flow rate measurements, and a differential pressure transducer to measure the pressure drop between inlet and outlet plenums. They included entrance and exit effects in their pressure drop calculations. They observed transition to turbulence starting at Reynolds numbers of approximately 1200 and increasing up to 3800 with decreasing tube diameter, while their measurements of friction factors for both water and R134a agreed well with the Poiseuille equation for laminar flow and the Blasius correlation for turbulent flow. They concluded from their results that conventional correlations for large tubes may be used to estimate flow in microtubes.

In another study in 2003, Wu and Cheng [55] experimented on the flow of deionized water in trapezoidal microchannels machined in silicon wafers, with hydraulic diameters ranging from 25.9  $\mu\text{m}$  to 291  $\mu\text{m}$  and with varying aspect ratios. They used compressed nitrogen gas to drive the flow, an electronic balance to measure the flow rate, and pressure transducers located in the inlet and outlet reservoirs to measure the pressure drop. Their data for friction factor exhibited  $\pm 11\%$  error in comparison with the analytical solution of the Navier-Stokes equations by Ma and Peterson [56], and, based on this result, judged that the Navier-Stokes equations are valid for the laminar flow of deionized water in smooth, trapezoidal microchannels with hydraulic diameters as small as 25.9  $\mu\text{m}$ . For hydraulic diameters between 103.4  $\mu\text{m}$  and 291  $\mu\text{m}$ , they observed the onset of

transition to turbulence at Reynolds numbers in the range of 1500 to 2000, suggesting early transition to turbulence. They emphasized that cross-sectional shape had a great effect on friction factor.

In 2004, Lelea et al. [57] experimented on the flow and heat transfer of distilled water in stainless steel tubes of 0.1, 0.3 and 0.5 mm diameter in the laminar regime, with Reynolds numbers up to 800. They used a micropump with a 2  $\mu\text{m}$  filter to drive the flow, a counter flow heat exchanger to control the temperature of the water, a digital balance to measure flow rate, joule heating to provide the heat source, K-type thermocouples and pressure transducers to measure the temperature and pressure at the inlet and outlet plenums. They included the pressure losses due to acceleration, contraction and expansion in their pressure drop calculations. To compare their experimental results, they solved the set of one dimensional continuity, momentum, and energy equations using the finite volume method, taking into account the variation of water viscosity with temperature. They concluded from their results that both friction factor and Nusselt number are in good agreement with conventional theories for the laminar regime.

In 2005, Lee et al. [58] investigated the flow and heat transfer characteristics of deionized water in rectangular microchannels of hydraulic diameter ranging from 194  $\mu\text{m}$  to 534  $\mu\text{m}$ , machined in copper, at Reynolds numbers ranging from 300 to 3500. They used pressurized nitrogen gas to drive the flow, cartridge heaters to supply a maximum heat load of 800W, T-type thermocouples to measure the temperature and a differential pressure transducer to measure the pressure difference between the inlet and outlet. They compared their experimental results against numerical results from the literature and a computational solution on FLUENT. They concluded that the numerical and computational results were in good agreement with the experimental results, and emphasized that such approaches can be employed with confidence to predict heat transfer in microchannels, as long as the entrance and boundary conditions are selected appropriately. They drew attention to the possibility of error in comparing the

results of experimental work with conventional correlations that do not comply with the boundary conditions of the experiments, such as comparing measurements on non-circular channels against correlations that are developed for circular channels or failing to account for inlet and outlet effects. In a similar study, Reynaud et al. [59] conducted experiments on water in channels of thicknesses ranging from 300  $\mu\text{m}$  to 1.12 mm. They also compared their results with a computational simulation using FLUENT and obtained results that are consistent with the conclusions of Lee et al. They attributed the minor deviations between the experimental data and CFD results to macroscopic effects, such as viscous dissipation and entry effects, and imperfections of the experimental apparatus.

Again in 2005, Kohl et al. [60] experimented on the flow of water in silicon microchannels of rectangular cross section with hydraulic diameters ranging from 25  $\mu\text{m}$  to 100  $\mu\text{m}$  at Reynolds numbers ranging from 4.9 to 2068. The importance of this study is that, unlike most of the studies in the literature, the researchers obtained pressure measurements inside the channels using pressure taps, similar to the study of Pfund et al. in 2000, mentioned previously. Contrary to the results of Pfund et al., the measurements of Kohl et al. showed overall agreement with analytically predicted values and they did not observe early transition to turbulence. They attributed the discrepancies of the results of previous researchers to the effects of developing flow in the entrance region, which do not cause error when pressure measurements are taken inside the channels. They reached the conclusion that the analytical results of Shah and London [10] can be used to predict pressure drop for water in channels with hydraulic diameter as small as 25  $\mu\text{m}$ .

Another important study from 2005 is the work of Zhang et al. [61], which is very similar to the present study in many aspects. In their experimental investigation of the heat removal capacity of a liquid cooled microchannel heatsink intended for electronic packages, Zhang et al. experimented on deionized water in rectangular channels of 380  $\mu\text{m}$  hydraulic diameter. The importance of this study is in that it is

among the very few studies that aim at determining the heat removal characteristics of microchannel heatsinks as a method of electronics cooling, an aim shared by the present study. The dimensions of the channels, 0.21 mm wide by 2 mm high, are also of the same order of magnitude as the smallest channels used in the present study. The dimensions of the heatsink, 15x12.2x50 mm, are also very close to the heatsink dimensions in the present study. An FCBGA package is employed as a realistic source of heat and a carrier of temperature sensors. A gear pump with a 10  $\mu\text{m}$  filter is used to drive the flow, a compact fin-tube heat exchanger is used to control the liquid temperature, pressure transducers and T-type thermocouples are employed at the liquid inlet and exits to measure pressure drop and temperature rise. Experimental results reveal that a heat flux of 189  $\text{W}/\text{cm}^2$  can be cooled with such a heatsink at a water flow rate of 1 lpm with a temperature rise of 60  $^{\circ}\text{C}$  between the coolant and heat source. The thermal resistance values calculated for the heatsink range from 0.32  $^{\circ}\text{C}/\text{W}$  to 0.59  $^{\circ}\text{C}/\text{W}$ . The experimental results are shown to be in good agreement with the values of thermal resistance and pressure drop predicted by conventional correlations.

In 2006, Celata et al. [62] investigated the flow characteristics of deionized water in glass microtubes of internal diameter ranging from 70  $\mu\text{m}$  to 326  $\mu\text{m}$  at Reynolds numbers ranging from 50 to 3000. They used a gear pump with a 10  $\mu\text{m}$  filter to drive the flow, and pressure transducers and K-type thermocouples at the inlet and outlet regions to measure pressure drop and temperature rise. They observed a definite adherence of experimental results to the Hagen-Poiseuille law for all diameters for Reynolds numbers above 300. They did not anticipate any early transition to turbulence, noting that the onset was seen at Reynolds numbers above 2000. Experimenting on both smooth and roughened tubes, they observed that the rough channels did not show any deviation from the classical prediction. They thus concluded that wall roughness had no significant effect on laminar flow.

Again in 2006, Steinke et al. [63] experimented on the flow and heat transfer characteristics of deionized water in silicon microchannels of rectangular cross

section of 133  $\mu\text{m}$  hydraulic diameter at Reynolds numbers ranging from 61 to 324. A gear pump with a 1  $\mu\text{m}$  filter was used to drive the flow, a rotameter type flow meter was used to measure the flow rate, and pressure transducers were placed at the inlet and exit plenums to measure pressure drop. Six temperature resistor sensors are placed under the inlet and exit plenums and along the channel length for accurate temperature measurements. A resistive electric heater, formed by thin film deposition, is used as the heat source. For the maximum dissipated heat flux of  $54.9 \text{ W/cm}^2$ , a temperature rise of  $23.5 \text{ }^\circ\text{C}$  was measured between the liquid inlet and the heat source at a mass flow rate of  $1262 \text{ kg/m}^3$ . The thermal resistance calculated for these values is  $0.15 \text{ }^\circ\text{C/W}$ . A comparison of experimental results with analytical solutions or conventional predictions was not attempted, apart from the apparent friction factor, which was in good agreement with laminar flow predictions.

Another important study from 2006, by Li and Olsen [64], involved microscopic particle image velocimetry in square polydimethylsiloxane (PDMS) microchannels of hydraulic diameter ranging from 200  $\mu\text{m}$  to 640  $\mu\text{m}$ . The working fluid was deionized water mixed with fluorescent seed particles, and the Reynolds number ranged from 200 to 3971. Velocity measurements in the laminar region are compared against the analytical solution of White [9] for rectangular pipe flow. The experimental results were observed to deviate from the analytical laminar solution before a transition to turbulence is anticipated. No evidence of early transition to turbulence was observed. In the fully turbulent region, observed to occur at Reynolds numbers above 2600, results were compared to the experimental results of Schlichting [65] for turbulent duct flow. Larger channels showed good agreement while the smaller channels of 200 and 320  $\mu\text{m}$  showed significant deviations. The authors did not arrive at a general conclusion as to the general compatibility of their results with conventional predictions and analytical solutions.

In 2007, Li et al. [66] performed experimental and numerical research on flow and heat transfer in microtubes of hydraulic diameter ranging from 50  $\mu\text{m}$  to 1570  $\mu\text{m}$  with distilled water at Reynolds numbers ranging from 20 to 2400. They used smooth silica tubes and rough stainless steel tubes. They employed compressed nitrogen to drive the flow, resistive heaters as the heat load, a mass balance to measure the flow rate, T-type thermocouples to measure temperature difference and pressure transducers to measure pressure loss between the inlet and exit of the tubes. They solved the 2-D Navier-Stokes equations with the finite volume method. Their experimental data revealed that the friction factor was well predicted by conventional theory for smooth tubes, but for rough tubes, friction factors were higher than predicted. The measurements leading to heat transfer coefficients showed deviation from conventional predictions, especially at Reynolds numbers under 100. The researchers attributed this behavior to the effect of axial conduction along the tubes. They concluded that no phenomena suggested inadequacy of the Navier-Stokes equations to describe the flow, and that deviation of the friction factor from conventional predictions was caused by geometrical factors only.

Again in 2007, Hrnjak and Tu [67] performed direct pressure measurements on rectangular microchannels of hydraulic diameter ranging from 69.5  $\mu\text{m}$  to 304.7  $\mu\text{m}$  with R134a at Reynolds numbers ranging from 112 to 9180. They used a vacuum pump with a 10  $\mu\text{m}$  filter to drive the flow, T-type thermocouples to measure the temperature drop, and pressure transducers to measure the pressure drop across the channels. They also used two pressure taps to obtain direct pressure measurements at the channel inlet and outlet sections. Measurements of laminar friction factor and the observed critical Reynolds number for the onset of transition to turbulence agreed well with conventional predictions, however, the friction factors in the turbulent region were considerably larger than predicted by the Churchill equations. This was attributed to the effect of roughness being more important in the turbulent regime.

In another direct pressure measurement study in 2007 by Costaschuk et al. [68], flow of water in rectangular aluminum microchannels of 169  $\mu\text{m}$  hydraulic diameter was studied. The flow was driven by pressurized nitrogen with a 7  $\mu\text{m}$  filter, a mass balance was used for flow rate measurements, and T-type thermocouples were used to measure inlet and outlet temperatures. The pressure distribution along the channels was measured by pressure taps, which were more densely packed near the inlet to study the entry region. Experimentally obtained laminar friction factor and critical Reynolds number agreed well with theoretical predictions, and the turbulent friction factor agreed well with the Haaland equation. In all calculations, the temperature dependence of water density and viscosity were taken into account, as viscous heating caused a rise of temperature between the inlet and outlet. The researchers concluded that experimental friction factors were in excellent agreement with conventional theory.

In the same year, Mishan et al. [69] extended the trend towards direct measurements by incorporating infra red temperature measurement techniques. They experimented on water flow and heat transfer in rectangular microchannels of 440  $\mu\text{m}$  hydraulic diameter at Reynolds numbers ranging from 30-600. 16 such channels were machined in aluminum to form a 14 mm by 20 mm microchannel heatsink. The flow was driven by a gear pump with a 10 $\mu\text{m}$  filter, flow rate was measured by a precision flow meter, and the heat load was supplied by a serpentine pattern electric heater attached to the heatsink by chemical vapor deposition. Pressure measurements were taken inside the channels using pressure taps, and temperature measurements were taken with an infrared thermal camera over the sapphire glass cover of the heatsink. A maximum heat flux of 17  $\text{W}/\text{cm}^2$  was cooled with a temperature rise of 27  $^{\circ}\text{C}$  between the water inlet and the heater surface, at a mass flux of 194  $\text{kg}/\text{m}^2\text{s}$  and 1 kPa pressure drop. Upon comparing their data with conventional analytical solutions and correlations, the researchers concluded that, including the entrance effects, conventional theory is applicable for water flow through microchannels.

### **3.2 Analytical and Numerical Studies on Microchannel Flow and Heat Transfer**

This section is devoted to studies employing various analytical and numerical techniques to obtain solutions of flow and heat transfer in microgeometries. The studies presented have been selected to provide examples to as many different methods of solution as possible. The more recent and comprehensive studies have been considered.

In 2002, Zhao and Lu [70] performed a comparative study employing both analytical and numerical methods on the heat transfer characteristics of forced convection across a microchannel heatsink. They assumed the bottom surface of the heat sink to satisfy either a constant temperature or constant heat flux boundary condition. They assumed the top surface to be insulated. They also assumed the length of the channels to be much larger than the channel width and channel wall thickness so that the analysis could be focused on a single channel. The fluid and solid temperatures were averaged over the channel width to reduce the problem to a two dimensional domain. Heat and fluid flow were assumed to be fully developed and properties such as thermal conductivity, density and viscosity, were taken to be temperature independent. One of two analytical methods employed was the fin approach, in which the problem was reduced to a one dimensional steady state conduction problem with an internal heat source, where fluid temperature was assumed to be constant along the height of the channel wall. This assumption was relaxed in the alternative analytical method, employing the porous medium model, which assumes a porous region in the fluid domain near the channel walls to capture surface effects. The analytical approaches were verified using a numerical solution of the full two dimensional momentum and energy equations. The ADI finite difference scheme was employed in the numerical solution. Results revealed that heat transfer was significantly overestimated by the fin approach due to the assumption of constant fluid properties, while the analytical solution based on the porous layer model was in excellent agreement

with the numerical solution. The authors concluded from their results that the effect of heat transfer boundary conditions, namely, constant heat flux versus constant temperature, on the overall Nusselt number of a microchannel heatsink was very small.

In 2003, Koo and Kleinstreuer [35] performed a computational analysis of microfluidics effects concerning channel entrance, wall slip, non-Newtonian behavior, surface roughness, viscous dissipation, and turbulence on friction factor. They used an extension of the Navier-Stokes equations as the governing equations. They employed the Low Reynolds Number (LRN)  $k$ - $\omega$  model to investigate turbulence effects, and a Porous Layer Model (PLM) similar to that of Zhao and Lu [70] to investigate the effect of surface roughness on the friction factor, pressure gradient, and flow structure. They discretized their governing equations using a central differencing scheme except for the convective terms, which were discretized using a higher order upwind scheme. They used MATLAB and a commercial code to obtain solutions. Their results showed that the entrance effect should be taken into account for microfluidic systems, that non-Newtonian fluid effects are expected to be important for polymeric liquids and particle suspension flows, that wall slip effects are negligible for liquid flows in micro conduits, that surface roughness effects depend on the Reynolds number and cross sectional configurations, and that turbulence effects become very important for Reynolds numbers above 1000. They also concluded, following a comparison of their numerical results with various experimental results available in the literature (such as Mala and Li [47]), that conventional theory, selectively augmented with the LRN  $k$ - $\omega$  turbulence model and/or the PML model, could readily predict benchmark experimental results for liquid flows in microconduits.

In 2003, Belhardj et al. [71] employed the Transmission Line Matrix (TLM) technique to model an array of microchannels for the cooling of microprocessors. In TLM, the physical problem of heat flow is represented as a sequence of voltage pulses traveling through a three dimensional network of transmission lines.

Temperature is replaced with voltage and heat flow is replaced with current, while physical properties such as heat capacity and density are replaced with relations involving resistances and impedances. The authors state that the explicit nature of TLM, coupled with its unconditional stability feature, provides advantages in the modeling of heat diffusion compared to other techniques. In their study, Belhardj et al. considered a 2 mm thick silicon die with a surface area of 20 mm x 20 mm. They assumed a uniform heat flux of  $100 \text{ W/cm}^2$  generated on the top surface of the die, cooled by microchannels of various depths and widths on the backside of the die. They solved the heat flow along the microchannel using an iterative finite volume method with their TLM technique, assuming the material properties to be independent of temperature. They verified their model against the analytical solution of Smy et al. [72]. Their results showed a temperature rise of  $30^\circ\text{C}$  for a single channel and  $20^\circ\text{C}$  for seven channels along the channel length for  $100 \text{ W/cm}^2$  heat load. The optimum channel width was given to be 1.8 mm, while the remaining channel dimensions, flow rate, and coolant are not specified. The authors concluded that the TLM technique is a powerful modeling tool for the given heat transfer problem.

In 2004, Kucaba-Pietal [73] studied the applicability of the micropolar fluid theory to modeling flow in microchannels, depending on the geometrical properties of the flow field. Micropolar fluid theory is an extension of the Navier-Stokes approach, which augments classical continuum fluid mechanics by incorporating the effects of microrotation of fluid molecules. If the characteristic geometrical linear dimension of the flow field becomes appropriately large, the equations describing micropolar fluid flow can be transformed into the Navier-Stokes equations. In his study, Kucaba-Pietal aimed to obtain the limiting value of microchannel hydraulic diameter below which micropolar effects are important and can not be neglected. The analytical solution of plane Poiseuille flow based on the micropolar fluid theory was first compared against a numerical solution with the molecular dynamics method to verify that the analytical solution was valid for channel widths not smaller than ten times the molecular diameter. The analytical results

revealed that the volume flow rate calculated using the micropolar fluid theory was smaller than the flow rate calculated using the classical Newtonian model under a limiting value of channel hydraulic diameter, the difference increasing with decreasing hydraulic diameter. The limiting hydraulic diameter was established as a value depending on the rheological properties of the fluid that can be expressed through a set of non-dimensional microstructure parameters.

In the same year, Koo and Kleinstreuer [74] investigated the effect of viscous dissipation on the temperature field and friction factor in microtubes and microchannels using numerical simulation. The governing equations were derived from the Navier-Stokes and energy equations. Both one dimensional and three dimensional approaches were considered. The one dimensional approach was limited to the solution of the energy equation, while the three dimensional approach involved solution of the full governing equations assuming hydraulically fully developed flow and constant fluid properties, except for viscosity, which was assumed to vary only with the mean flow temperature. Central differencing was employed, except for the convection term, which was discretized using a first order upwind scheme. Solution was carried out with MATLAB using the simple explicit method. Three working fluids, water, methanol, and isopropanol, were considered. The solution for isopropanol was compared with the experimental results by Judy et al. [75] to verify the model, and a close agreement was observed. A comparison between the one dimensional and three dimensional solutions revealed that the one dimensional solution was applicable only for thermally fully developed flow where entrance effects are negligible. It was concluded from the numerical results that the effect of viscous dissipation depended on the channel geometry and Reynolds number, and that viscous dissipation should be considered in order to obtain accurate friction factor measurements for flows in microconduits. An analytical solution of the generalized transport equations, incorporating a Porous Medium Layer model (PML), was also performed by the same authors in the same year [76]. This analytical model was verified with the

experimental measurements of Guo and Li [77], and consistent results regarding entrance and viscous dissipation effects were obtained.

In another important study of 2004, Gamrat et al. [78] performed two and three dimensional numerical simulations of a rectangular microchannel heatsink using FLUENT. They modeled the experimental setup of Gao et al. [52], in which the microchannel height ranged from 0.1 mm to 1 mm and the working fluid was deionized water. Symmetry allowed the system to be represented by half of the geometry. Coupled conduction and convection was modeled using the Navier-Stokes equations simplified with the assumptions of incompressible fluid, laminar flow, constant solid and fluid properties, and negligible buoyancy, radiation and viscous heating. The simplified assumptions allowed the temperature field to be solved after the converged solution for the flow field was obtained. The hydraulic boundary conditions were uniform velocity profile at the inlet and fully developed flow at the exit, while the thermal boundary conditions were constant heat flux at the heater surface and free convection of the heatsink with the surrounding air assumed to be at 300 K with a heat transfer coefficient of  $10 \text{ W/m}^2\text{K}$ . For the three dimensional simulation, the optimized mesh generated in GAMBIT contained  $2.7 \times 10^6$  cells. A second order upwind finite volume method was employed for space discretization in FLUENT. The simulation results were checked with the correlation of Bejan and Sciubba [79] for laminar simultaneously thermally and hydraulically developing flow along a two dimensional channel with symmetrical uniform heat flux surfaces, and excellent agreement was observed. A comparison with the experimental results on the modeled system, however, revealed that the wall temperature was underestimated and the Nusselt number was overestimated by the numerical model. The deviation was small for the largest channel of 1 mm height (10-20% for Nusselt number), but large for the smaller channel of 0.3 mm height (40-80% for Nusselt number). The deviations were attributed to the simplifications in the numerical model. The authors also concluded from their numerical results that there was no size effect on heat transfer when the channel

height was reduced from 1 mm to 0.1 mm, leaving the related experimental observations of reduced Nusselt number with reduced channel height unexplained.

In 2005, Bahrami and Jovanovich [22] proposed a compact, approximate model to predict the pressure drop of fully developed, laminar flow in microchannels of various cross sections. The authors used the simplifying assumptions of two dimensional flow conditions, constant cross sectional area and perimeter, incompressible flow with constant properties, negligible body forces, negligible rarefaction effects, and negligible surface effects to reduce the Navier-Stokes equations to the simplified momentum equation known as the Poisson equation. They obtained exact analytical solutions of the Poisson number for rectangular, circular, annular, elliptic, and triangular cross-sections, and approximate solutions for trapezoidal and regular polygon cross-sections. They compared their results against the experimental results of Gao et al. [52], Wu and Cheng [55], and Lee et al. [58] and concluded that their model showed good agreement.

Again in 2005, Kulkarni and Das [80] conducted an analytical and numerical study aimed at cooling a silicon chip of dimensions  $600\text{ }\mu\text{m} \times 600\text{ }\mu\text{m} \times 60\text{ }\mu\text{m}$  with an air cooled heatsink. The chip had a thermal design power of 3.9 mW and a maximum junction temperature of  $80\text{ }^{\circ}\text{C}$ . The heatsink analyzed was a standard Intel Pentium heatsink with 10 microchannels of  $189\text{ }\mu\text{m}$  width and  $1534\text{ }\mu\text{m}$  height machined in aluminum. A conduction analysis was performed for the heatsink using the fin theory with the energy equation, taking into account the heat spreading resistance, interface resistances, radiation, and transient effects. The heat transfer coefficient due to natural convection was calculated using a conventional correlation for laminar flow over a flat fin surface. The heatsink was also modeled numerically using FLUENT with 10,000 cells for the two dimensional case, and 65,000 cells for the three dimensional case. Based on the numerical results, the authors concluded that their analytical model slightly underestimated the heat removed by the heatsink due to the simplifying assumptions.

In another study of 2005, Koo et al. [81] performed numerical analysis of boiling convection in an integrated multilayer microchannel heatsink for electronic circuit architectures. The channels considered were 700  $\mu\text{m}$  wide and 300  $\mu\text{m}$  deep with water as the coolant. Assuming that the flow in each channel was distributed uniformly with the same flow rate, and that the generated heat flux only varied along the length of the channels, they limited their analysis to the numerical solution of the time and space averaged one dimensional energy equation using the finite volume method. To close their governing equation, they used conventional relations to specify the convective heat transfer coefficients and pressure drop. The channel walls were assumed to be adiabatic and water properties were incorporated using thermodynamic property correlations to account for their dependence on temperature and pressure. The total electric circuit area was taken to be 4  $\text{cm}^2$  with a total power generation of 150 W. The water inlet temperature was fixed at 70  $^{\circ}\text{C}$  and the exit pressure was fixed at 0.3 bar. The numerical results for these conditions predicted the maximum circuit junction temperature to be 85  $^{\circ}\text{C}$  at a flow rate of 15 ml/min. A comparison of the numerical simulations was not attempted, and it was stated by the authors that experimental data on boiling convection in microchannels were needed to verify the model.

In 2006, Bahrami et al. [23] conducted a theoretical analysis of the pressure drop in rough microtubes. They based their analysis on the concept of frictional resistance, and arrived at the friction factor by manipulating theoretical expressions for the effective frictional resistance in rough microtubes, assuming a Gaussian distribution of the roughness. They assumed fully developed and laminar flow with constant fluid properties, neglecting effects such as rarefaction, compressibility, and wall slip. They compared the predictions of their analytical model against the experimental results of Mala and Li [47] and Li et al. [82] for deionized water, and concluded that the predictions of their model remained within the uncertainties of the experimental data.

In the same year, Lee and Garimella [83] performed three dimensional numerical simulations on thermally developing flow and heat transfer in rectangular microchannels using FLUENT, and proposed a set of correlations based on their results. The channels they considered had hydraulic diameters ranging from 200  $\mu\text{m}$  to 364  $\mu\text{m}$  with aspect ratios ranging from 1 to 10. In their simulation, they considered only a single channel, and modeled only a quarter of the channel due to axial symmetry. They specified a constant heat flux of  $50 \text{ W/cm}^2$  on all four walls of the channel. They assumed a fully developed velocity profile at the channel entrance at a temperature of 300 K. They used a maximum of 400,000 grid cells. Based on their results, they developed correlations for the local and average Nusselt numbers. They compared their correlations against Nusselt number calculations based on experimental data on microchannels [58] and also against numerically obtained values for conventional channels [84]. Both comparisons showed very good agreement, and the authors concluded that their proposed correlations allowed accurate predictions of the thermal performance of microchannel heatsinks.

In another study of 2006, Herwig and Mahulikar [85] investigated the effect of varying fluid properties on flow and heat transfer in microchannels through numerical simulations using the CFD software CFX. Observing that Reynolds numbers are small, and axial temperature gradients are large while cross sectional temperature differences are small in microchannel flows, they emphasized the importance of taking into account the variation of viscosity and coefficient of thermal conductivity with temperature. For a hydraulic diameter of 100  $\mu\text{m}$ , they conducted numerical simulations for both constant and variable property cases at channel wall heat fluxes ranging from  $-30$  to  $30 \text{ W/cm}^2$ . They concluded from their results for the Nusselt number that variable property effects that are often of minor importance in pipe and channel flows through macro sized conduits, have a strong influence in flows through microgeometries.

### 3.3 Microchannel Cooling Applications and Application Oriented Studies

This section is intended to provide a general overview of current trends in phased array radar cooling methods and the use of microchannel heatsinks as an advanced method of electronics cooling. Selected application-oriented academic work, industrial applications, and related reviews are briefly presented.

A review of a number of high performance thermal management solutions for military electronic systems, with an emphasis on phased array radar systems, is given by Price [86]. Various methods of air cooling and liquid cooling, including two phase applications, are included. The structure of phased array radar antennas and the effects of the thermal layers in the heat dissipating modules of such radars are described by Wilson [87]. A temperature rise of 107 °C between the coolant liquid and the heat dissipating junction, due to the thermal resistance of all the layers in the device, is predicted for a heat flux of 100 W/cm<sup>2</sup>. The design concepts and architecture of such a radar, with microchannel cooled T/R modules dissipating a maximum of 500 W, is given by Revankar et al. [88].

The thermal performance of a liquid cooled microchannel heatsink integrated with a power multichip module has been studied by Gillot and Schaeffer [89]. In their study, two high power chips, Siemens V IGBT of 11 mm x 11 mm surface area, were directly brazed on a 51 mm x 18 mm copper piece in which microchannels were machined. Four modules, incorporating two such chips each, were used for experimental testing. The microchannels were 200 µm wide and 2 mm deep, separated by channel walls of 200 µm thickness. The power dissipation per chip reached 300 W at a coolant (40% glycol-water) flow rate of 0.26 l/s. Calculations based on experimental measurements revealed a thermal resistance of 0.08 K/W. The thermal performance of the microchannel heatsink was represented by its ability cool a heat flux of 350 W/cm<sup>2</sup> with a temperature rise of 35 °C between the coolant entrance and the chip surface, at a coolant flow rate of 0.26 l/s.

For an application involving the refrigeration of a tank of water, Chein and Chen [90] studied the performance of a thermoelectric cooler integrated with a microchannel heatsink. Water in a tank of 1.18 L was cooled by a 40mm by 40mm thermoelectric module with a cooling rate of 51.4 W, the hot side of which was in turn cooled by a silicon microchannel heatsink with trapezoidal channels of hydraulic diameter ranging from 65  $\mu\text{m}$  to 150  $\mu\text{m}$ . In their experiments, the tank of water was at an initial temperature of 25  $^{\circ}\text{C}$  and the coolant flow rate ranged from 289 to 10702 ml/hr. The coolant was deionized water, also at 25  $^{\circ}\text{C}$ . Results showed the minimum refrigerated water temperature to be 10  $^{\circ}\text{C}$ , indicating a temperature drop of 15  $^{\circ}\text{C}$ . The thermal performance of the microchannel heatsink was characterized by a minimum thermal resistance of 1.68 K/W for the smallest channel hydraulic diameter.

A liquid cooled microchannel heatsink, with a channel flow area of 0.2 mm x 30 mm, was employed by Hirshfeld et al. [91] for the cooling of accelerator targets. An electron gun, capable of providing up to 20 kW heating power with heat fluxes above 5  $\text{kW}/\text{cm}^2$ , was used as the heat source in their experiments. Deionized water was used as the coolant. Experimental results showed that, at a flow rate of 4.2 lpm, a heat flux of 1500  $\text{W}/\text{cm}^2$  could be removed at an accelerator target temperature of over 100  $^{\circ}\text{C}$  with heatsink temperatures exceeding 400  $^{\circ}\text{C}$ , indicating boiling of the coolant.

The performance of liquid cooled microchannel and minichannel heatsinks, in both single phase and two phase flow conditions, for cooling IGBT (Insulated Gate Bipolar Transistor) components was studied by Gillot et al. [92]. The single phase heatsink had rectangular microchannels of 182  $\mu\text{m}$  hydraulic diameter machined in copper while the two phase heatsink had circular minichannels of 2 mm diameter, also machined in copper. The experimental results for the single phase case showed that, for a coolant (40% glycol - water) flow rate of 260 ml/s, a component heat flux of 370  $\text{W}/\text{cm}^2$  could be cooled at a temperature rise of 40  $^{\circ}\text{C}$  between the coolant inlet and component surface. For the two phase case with minichannels, a

maximum of  $240 \text{ W/cm}^2$  could be dissipated at a flow rate of 216 ml/min with the same temperature rise. The thermal performance of the rectangular microchannel heatsink in single phase flow was characterized by a thermal resistance ranging from 0.09 to 0.11 K/W.

The performance of microchannel heatsinks for cooling microspacecraft electronic components was studied by Birur et al. [93]. An electric heater with a footprint area of  $3.5 \text{ cm}^2$ , typical of microspacecraft electronic components, was attached to a silicon heatsink with microchannels of hydraulic diameter ranging from  $50 \text{ }\mu\text{m}$  to  $67 \text{ }\mu\text{m}$  for testing. At a maximum deionized water flow rate of 25 ml/min, the temperature rise between the coolant inlet and the heatsink was measured to be  $30 \text{ }^\circ\text{C}$  at a heat flux of  $25 \text{ W/cm}^2$ .

In the 2004 Intel Technology Journal [5], the need for the use of liquid cooled microchannel heatsinks is emphasized and an experimental study to verify the performance of a microchannel heatsink for cooling an Intel microprocessor is presented. The experimental study was performed on a chip attached to a silicon heatsink, with channel widths ranging from  $61 \text{ }\mu\text{m}$  to  $300 \text{ }\mu\text{m}$ , mounted on a motherboard. Using water as the coolant with 110 ml/min flow rate, a thermal resistance as small as 0.22 K/W was obtained between the chip junction and the coolant inlet, for a total chip power of 70 W.

A number of patents involving liquid cooled microchannel heatsinks are available. These include a diamond heatsink with  $150 \text{ }\mu\text{m}$  channel width designed for the cooling of power amplifier chips [94], a microchannel heatsink assembly with  $100 \text{ }\mu\text{m}$  channel width designed for integrated circuit cooling [95], another microchannel heatsink assembly with  $50 \text{ }\mu\text{m}$  channel width designed for supercomputer applications [96], and a monolithic microchannel heatsink with  $150 \text{ }\mu\text{m}$  channel width designed for the cooling of laser diode arrays [97]. All heatsinks are designed for water as the coolant. A patent with a more direct relevance to the present study is that by a leading military technology firm, Raytheon [98], in

which a liquid cooled microchannel cold plate is proposed for the cooling of phased array radar modules. The design incorporates a porous metallic substrate to provide a thermal performance equivalent to an array of microchannels with channel widths under 265  $\mu\text{m}$ .

## **CHAPTER 4**

### **EXPERIMENTAL PROCEDURE AND RESULTS**

This chapter is devoted to a thorough presentation of all the aspects of the procedure followed in designing and constructing the experimental setup, including preliminary stages and various difficulties encountered. The experimental results are given concisely at the end of the chapter, detailed test results are reported in the Appendix.

#### **4.1 Design and Manufacturing of the Microchannel Heatsinks**

The first step of the work leading to a set of experimental results on the thermal performance of microchannel heatsinks was to investigate the manufacturing methods suitable for such geometries. Preliminary research revealed that common methods available for manufacturing channels having widths on the order of hundreds of microns were laser machining, electrodischarge machining (EDM), microsawing, and chemical etching. Laser machining offers high accuracy, but the channel depth that can be machined is limited to a few microns. EDM is a conventional machining method that can be applied easily to microgeometries by employing fine wire, and aspect ratios up to 15 can be machined with good accuracy. Microsawing is a purely mechanical process that is typically employed in silicon micromachining. Chemical etching is commonly employed together with lithographic techniques and is also typically applied in the silicon industry.

In order to select the most appropriate manufacturing method, various design parameters such as channel geometry and material, and applicability of the method within Turkey was considered. For military applications that require rugged

designs, the heatsink material would preferably be a metal with high thermal conductivity, such as aluminum or copper. Because chemical etching and microsawing are not commonly employed with metals, and because they are not commonly available in Turkey, these methods were dismissed. Laser machining was also dismissed due to the channel depth restriction imposed by this method, as the channels would preferably have a depth on the order of a few millimeters to provide a large surface area for heat transfer and a high aspect ratio to achieve better heat transfer coefficients. Consequently, EDM was chosen as the manufacturing method since it allowed channel widths as small as 300 microns with channel depths as large as 5mm to be machined with good accuracy. Another reason for choosing EDM was that it is a conventional machining method employed commonly in machine shops around Turkey, and also in ASELSAN, allowing for the heatsink designs of this study to be manufactured locally.

#### ***4.1.1 The Preliminary Specimen***

Once the manufacturing method was decided upon, a preliminary specimen was designed so that the possible difficulties in manufacturing could be observed and the actual test specimens could be redesigned accordingly. The preliminary specimen was aimed to be manufactured making use of solely the manufacturing capabilities available within ASELSAN. The available EDM machine and wire imposed a minimum channel width of 300 $\mu$ m and a maximum channel depth of 4mm. These values were carried directly into the design, and a microchannel heatsink with 72 channels of 300 $\mu$ m width and 4mm depth, separated by walls of 300 $\mu$ m thickness, was designed. A simple cover plate for the heatsink and identical inlet and outlet parts to provide axial flow into and out of the heatsink through available pipes, were also designed. Dimensions of these parts are given in Fig.4.1 and Fig. 4.2. Detailed technical drawings may be found in Appendix B.

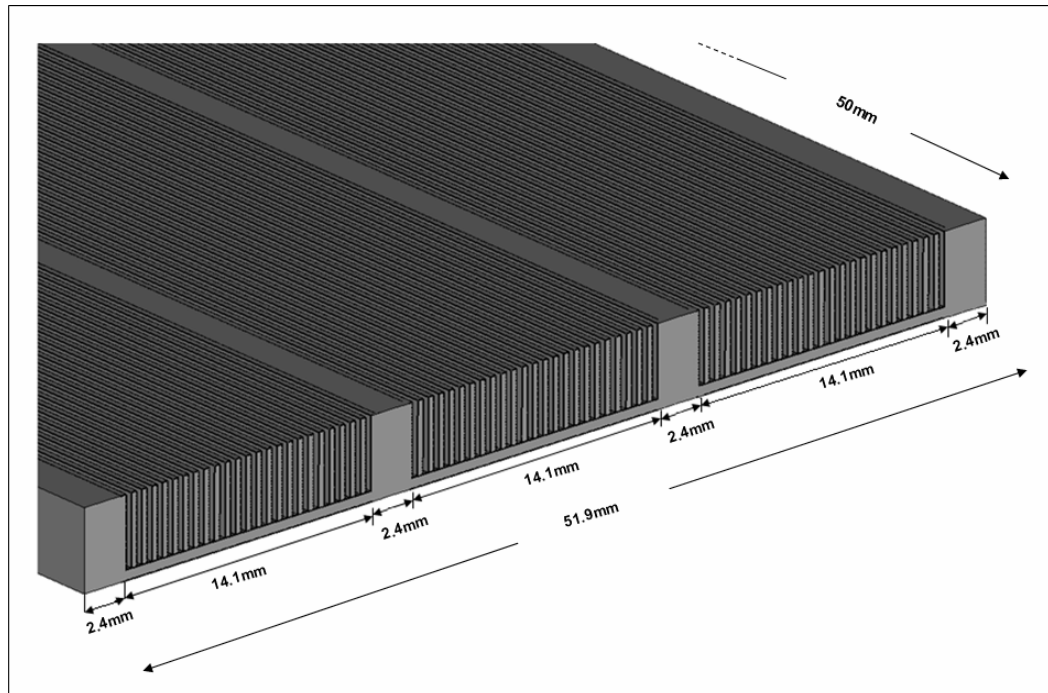


Figure 4.1: Heatsink dimensions - 1

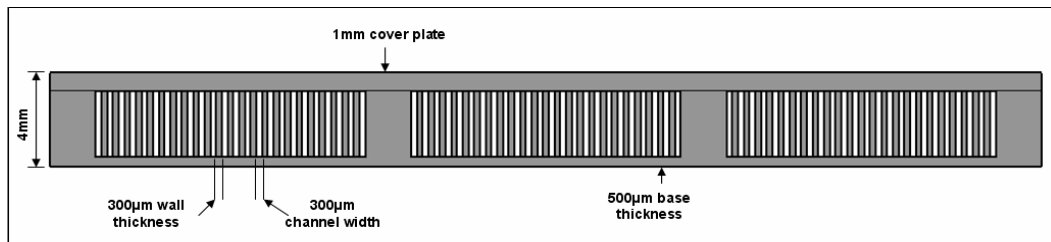


Figure 4.2: Heatsink dimensions - 2

The parts shown were manufactured from copper. No problems were encountered during the manufacturing of the parts, shown in Fig. 4.3, however, joining the parts in a durable and leak-proof fashion proved to be a challenge. For use in a military radar application, the final product must be resistant to failure in harsh environments involving shock and vibration. Joining the parts using adhesives or using silicon to seal the mating sections, therefore, are not appropriate methods, considering the intended application of the heatsinks. The most reliable joining method is brazing, in which the mating parts are brought together and exposed to

very high temperatures in the presence of a compatible filler material so that the filler penetrates into the mating interface and bonds with both mating parts when cooled. The filler to be used and the temperature to which the parts are to be exposed depend on the material of the mating parts. For copper, typical brazing temperatures exceed 1000 °C, while aluminum is typically brazed at temperatures near 600 °C. These temperatures are given for the torch brazing method, currently employed at ASELSAN. In torch brazing, the parts to be joined are heated using a high temperature torch while the filler material is applied simultaneously. The parts are then placed in a water bath to allow for the filler material to harden. Once brazed, the mating parts bond so well that they act essentially like a single part in terms of both strength and thermal conductivity.

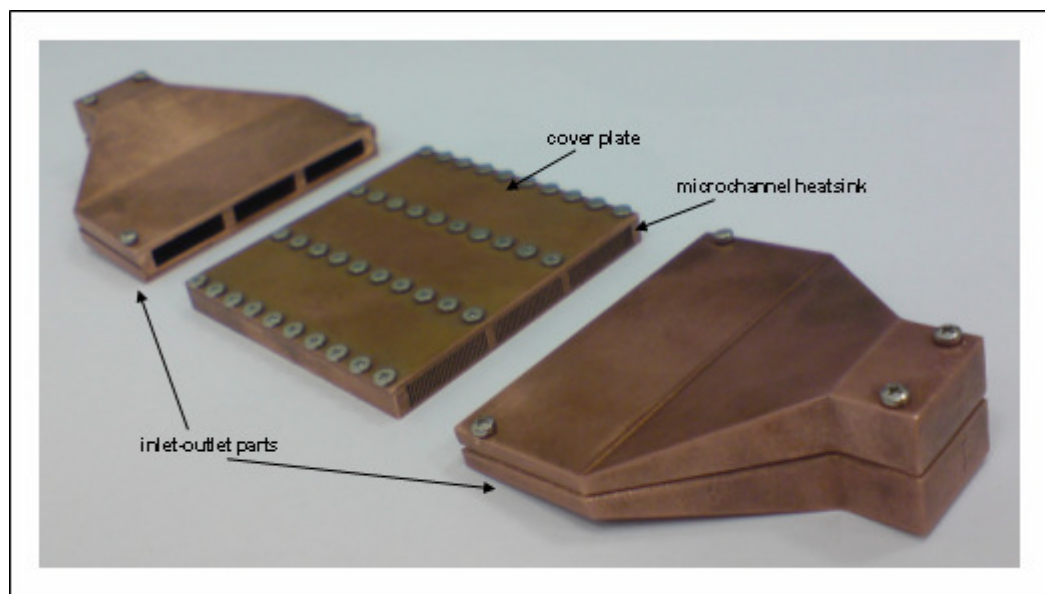


Figure 4.3: Parts of the microchannel heatsink assembly

The disadvantage of the design of the preliminary specimen was that brazing the inlet and outlet parts to the microchannel heatsink, or brazing the cover plate to the microchannel heatsink, carried the risk of the filler material penetrating too much through the mating interface and blocking the microchannels. Therefore, only the two halves of the inlet and outlet parts were brazed while the remaining mating

sections were soldered. Although soldering provided satisfactory sealing of the mating interfaces, the joined structure would not be appropriate for use in a military application subject to vibration. The joined structure, with pipe adaptors added to the inlet and outlet parts, is shown in Fig. 4.4.

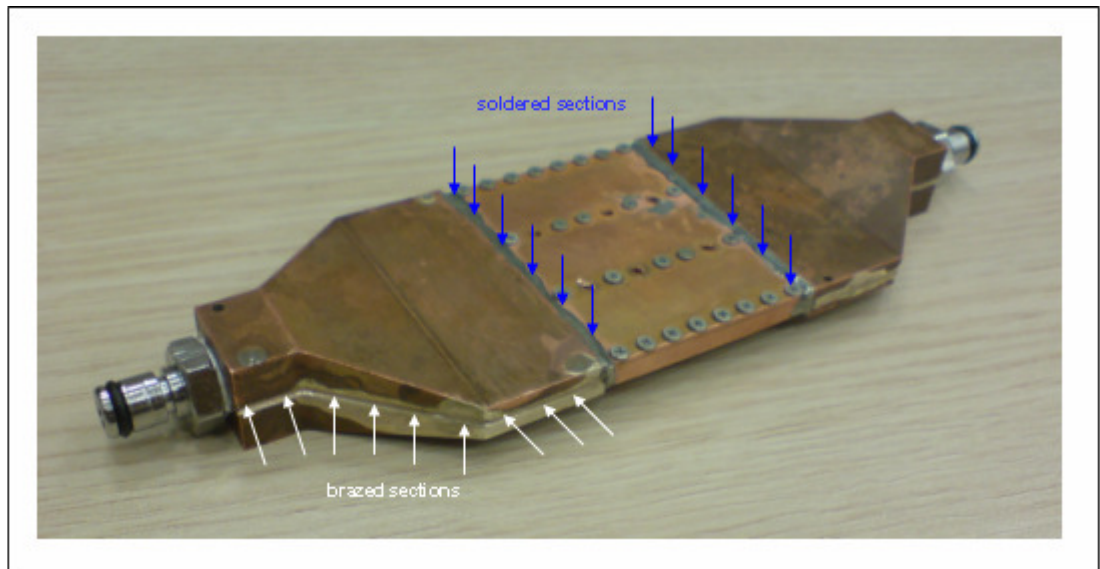


Figure 4.4: The joined structure with pipe adaptors added

Inspection of the resulting heatsink assembly and the experience gained during the manufacturing process of the preliminary specimen revealed the following:

- The parts should be redesigned to ease the brazing process
- The parts should be redesigned so that all mating surfaces can be brazed together without the risk of channel blockage due to over-penetration of the filler material
- The inlet and outlet parts should be redesigned to allow for a more compact design
- The heatsink assembly should be redesigned to consist of as few parts as possible

Another factor that was taken into account while designing the test specimens, in addition to the observations above, was that the heatsink base area of the preliminary specimen was too large for a typical T/R module. The reason for this was to ease the joining processes, as smaller parts posed greater difficulty, and to allow for a very firm contact between the heatsink and the cover plate through multiple rows of screws. The assembly and joining procedure, however, showed that such a precaution was unnecessary and that a more compact design could be handled just as well. The preliminary specimen served solely as a tool to gain experience in the design and production of a microchannel heatsink assembly. Only a pressure drop test, to gain a preliminary understanding of the flow, was conducted on this specimen to determine the appropriate pump to be used with the test specimens.

#### ***4.1.2 The Test Specimens***

Utmost care has been taken to relate this study to actual electronics cooling applications that are likely to be encountered in the near future within the scope of ASELSAN phased array radar projects. The microchannel heatsinks to be tested have therefore been designed to comply with the dimensions of the transmit/receive modules (T/R modules) currently employed in an ASELSAN phased array radar project. Because the T/R modules are part of a confidential, military project, information regarding these modules has not been included in this text. It may be stated, however, that the set of microchannel heatsinks tested, excluding the preliminary specimen, are compatible with the dimensions and mechanical constraints of the T/R modules used in the mentioned ASELSAN project. In consistence with the observations given in the previous section regarding design improvements, the test specimen assemblies have been designed to consist of two parts, with inlet and outlet parts implemented into the cap. The main dimensions of the test specimen heat sink and cap are given in Fig. 4.5. Detailed technical drawings of these parts are given in Appendix C.

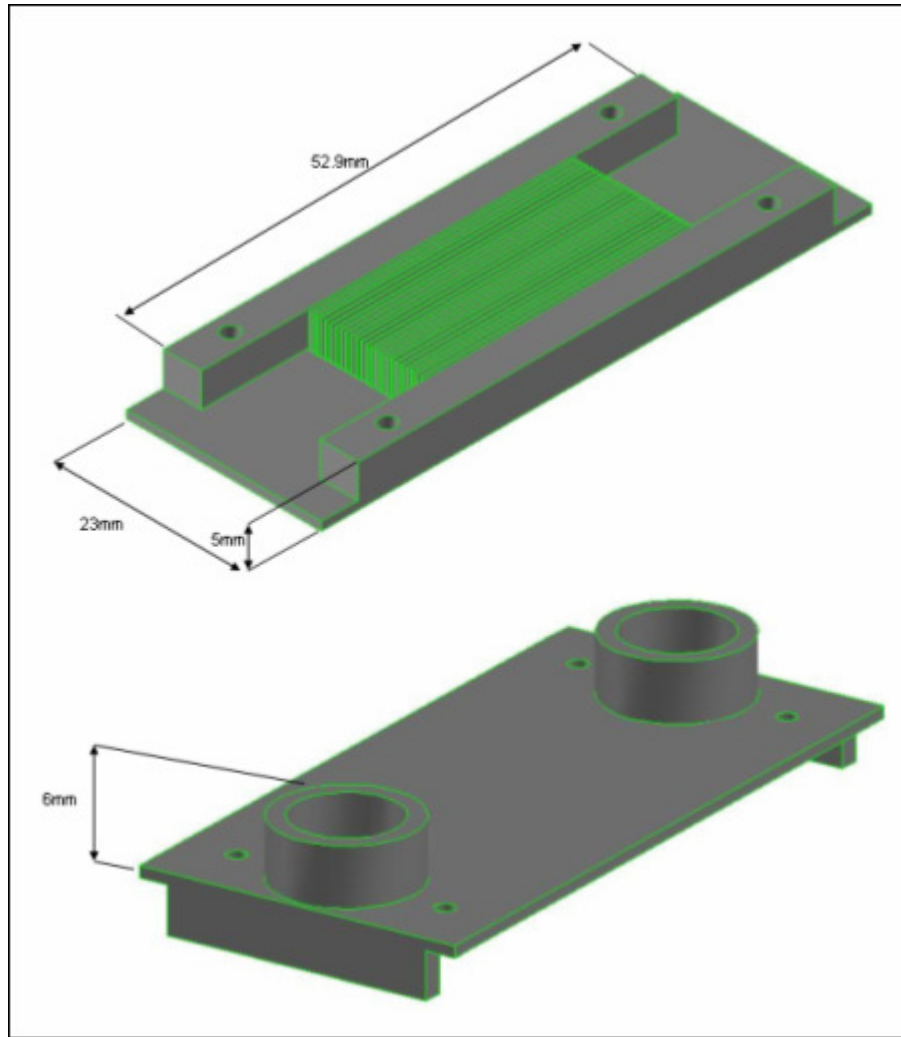


Figure 4.5: Main dimensions of the heatsink and cap

Only the main dimensions are given in Fig. 4.5. The small protrusions along the length of the heatsink base and along the width of the cap are intended to ease the brazing process. The minimum microchannel width has been selected to be  $300\text{ }\mu\text{m}$  due to manufacturing constraints associated with EDM. For performance comparison purposes, four microchannel widths –  $300$ ,  $420$ ,  $500$ ,  $900\text{ }\mu\text{m}$  – have been considered. The channel wall thickness of  $300\text{ }\mu\text{m}$ , channel height of  $4\text{ mm}$ , and heatsink base thickness of  $1\text{ mm}$  have been kept constant to minimize the geometrical variables. A thorough analytical calculation has been performed based on the chosen dimensions to confirm their applicability and to aid in the selection

of the pump and heat exchanger. The calculation methodology employed is that outlined in Section 2.1. A sample calculation is given for the 300  $\mu\text{m}$  copper specimen in Appendix D. The analytical calculation results for the heatsink pressure drop,  $\Delta p$ , and average heatsink base temperature rise,  $\theta_b$  (average temperature difference between the heatsink base and heatsink coolant inlet), for all specimens is given in Table 4.1.

Table 4.1: Analytical calculation results

Channel Width ( $\mu\text{m}$ )	Material	$\Delta p$ (kPa)	$\theta_b$ ( $^{\circ}\text{C}$ )
300	CU	2.64	11.9
	AL	2.64	15.3
420	CU	1.31	16.0
	AL	1.31	20.0
500	CU	0.94	18.9
	AL	0.94	23.3
900	CU	0.39	33.6
	AL	0.39	39.4

The same set of microchannel widths has been considered for two material alternatives, copper and aluminum, in order to assess the effect of heatsink material on thermal performance. A total of eight test specimens have therefore been defined, with design parameters summarized in Table 4.2. It is seen from Table 4.2 that specimens 4 and 8, of 900  $\mu\text{m}$  channel width, have a hydraulic diameter of over 1 mm, falling into the minichannel category. These specimens have been included to allow for a comparison between microchannels and minichannels in terms of thermal performance.

Because the EDM machine available at ASELSAN was not suitable for machining aluminum, unlike the preliminary specimen, the test specimens had to be manufactured commercially. Due to time constraints and hesitation of local companies to bid for small quantities of production in non-conventional dimensions, the manufacturing of the parts was done by a company abroad

specializing in advanced electronics cooling products, MEZZO Tech. (USA). It may be stated with confidence, however, that manufacturing of such parts is possible within Turkey, as long as either a long delivery time is permissible or the quantity of parts is large.

Upon arrival of the parts, the microchannel heatsinks were photographed under a microscope. Photographs of the parts may be found in Appendix E, and microscope views are given in Appendix F. The photographs of Specimen 1 and one of the copper caps are presented in Fig. 4.6, and the microscope view of Specimen 1 is presented in Fig. 4.7 as samples.

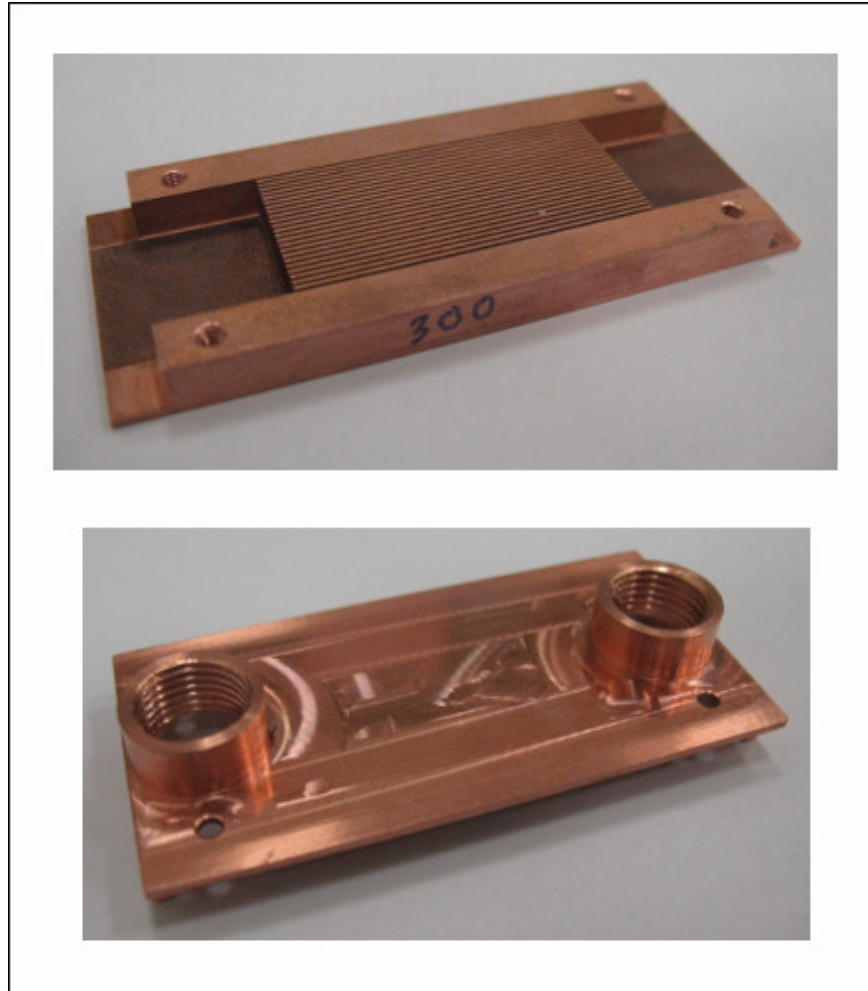


Figure 4.6: Specimen 1 and its cap

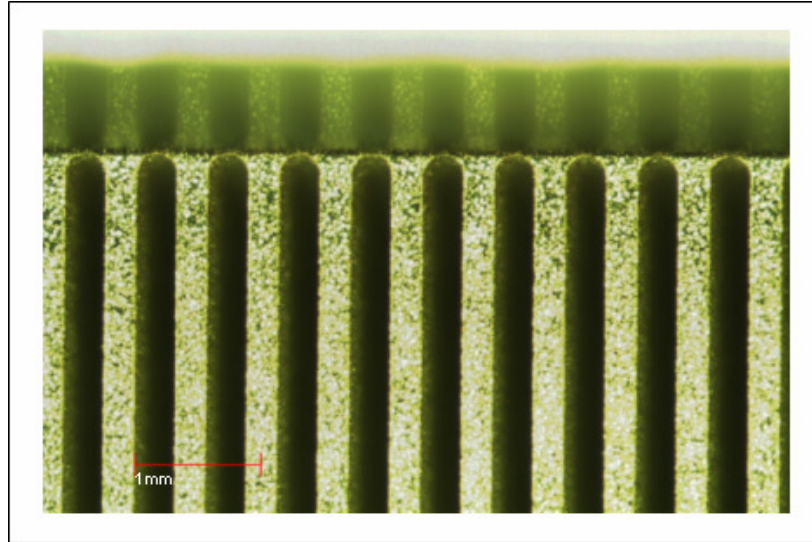


Figure 4.7: Microscope view of specimen 1

Table 4.2: Design parameters of the test specimens

SPECIMEN	CHANNEL WIDTH	CHANNEL HEIGHT	ASPECT RATIO	HYDRAULIC DIAMETER	# OF CHANNELS	MATERIAL
1	300 $\mu\text{m}$	4 mm	13.33	558 $\mu\text{m}$	24	COPPER
2	420 $\mu\text{m}$	4 mm	9.52	760 $\mu\text{m}$	20	COPPER
3	500 $\mu\text{m}$	4 mm	8.00	888 $\mu\text{m}$	18	COPPER
4	900 $\mu\text{m}$	4 mm	4.44	1469 $\mu\text{m}$	12	COPPER
5	300 $\mu\text{m}$	4 mm	13.33	558 $\mu\text{m}$	24	ALUMINUM
6	420 $\mu\text{m}$	4 mm	9.52	760 $\mu\text{m}$	20	ALUMINUM
7	500 $\mu\text{m}$	4 mm	8.00	888 $\mu\text{m}$	18	ALUMINUM
8	900 $\mu\text{m}$	4 mm	4.44	1469 $\mu\text{m}$	12	ALUMINUM

Each microchannel test specimen and cap pair, such as the 300  $\mu\text{m}$  copper pair shown in Fig. 4.6, were brazed together to form a monolithic test specimen consisting of a microchannel cold plate covered by a flat plate housing inlet and outlet sections, with perfectly sealed and mechanically strong mating interfaces. The inlet and outlet sections were then threaded to allow for the insertion of quick disconnect fluid connectors. The fluid connectors were screwed to the test specimens with a hardening sealant to ensure a leak-free and strong connection.

All eight test specimens resulting from the brazing of the microchannel cold plates and caps are shown in Fig. 4.8. The 500  $\mu\text{m}$  copper test specimen with its fluid connectors is shown in Fig. 4.9 to illustrate the configuration of the fluid inlet and outlets.

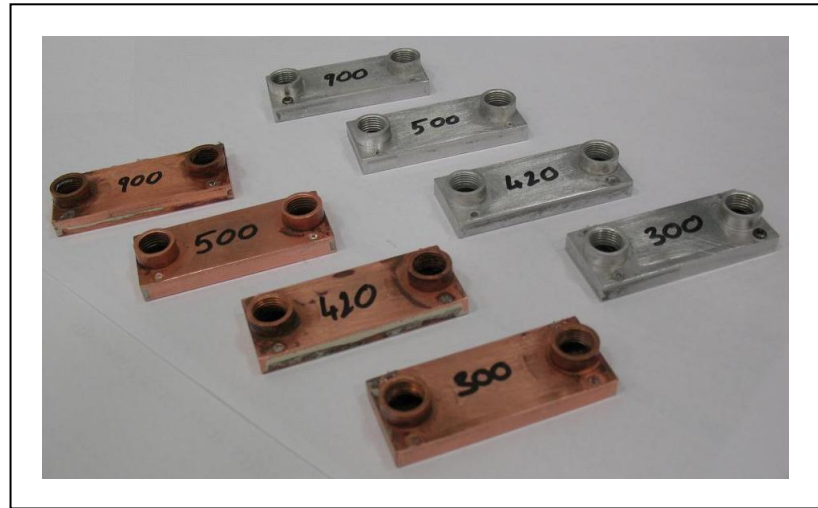


Figure 4.8: Test specimens after brazing



Figure 4.9: Configuration of fluid inlet and outlets

## 4.2 The Experimental Setup

The experimental setup was designed to simulate a typical liquid cooling system. In addition to the flow of coolant circulating in a closed loop, the system required a sophisticated measurement facility to record data such as pressure, temperature, and flow rate. Another important requirement was a heat source to represent the heat load on the heatsink. All the components required by the system, and the construction of the setup, are described in the following subsections.

### 4.2.1 Components of the Experimental Setup

One of the most critical components of the setup was the heat load carrier. In order to simulate an active electronic device requiring cooling, such as the T/R modules of a phased array radar, a high heat flux had to be supplied to the microchannel heatsink base. This was achieved by means of a gold coated copper-tungsten (CuTg) carrier of 0.5 mm thickness, housing 72 attenuators. Attenuators are passive electric components that are used to manipulate voltage and current in circuits. They are resistive elements, and thus, dissipate heat. Each attenuator placed on the heat load carrier has a surface area of  $0.76 \text{ mm}^2$  and can dissipate a maximum of 1.8 W. In addition to the attenuators, the heat load carrier also contains four temperature sensors to allow for direct measurements of the carrier temperature as close as possible to the attenuators. A schematic drawing of the heat load carrier is shown in Fig. 4.10. Each group of attenuators seen in Fig. 4.10 contains 24 attenuators, so that the total number of attenuators sums up to 72. The total effective heat load area, illustrated in Fig. 4.11, is  $63 \text{ mm}^2$ . The temperature sensors, NTC (negative temperature coefficient) thermistors, are distributed evenly among the groups of attenuators to provide a means of measuring the mean carrier temperature. Thermistors are very suitable for temperature measurements on chip carriers due to their high accuracy and very fast response due to their small size. Both accuracy and size of the temperature sensing elements are very important in the present study as the performance of the heatsink is determined by calculations

based on temperature measurements taken directly on the carrier, and the sensors must be very small to provide a reliable measurement of temperature on the active heat load area.

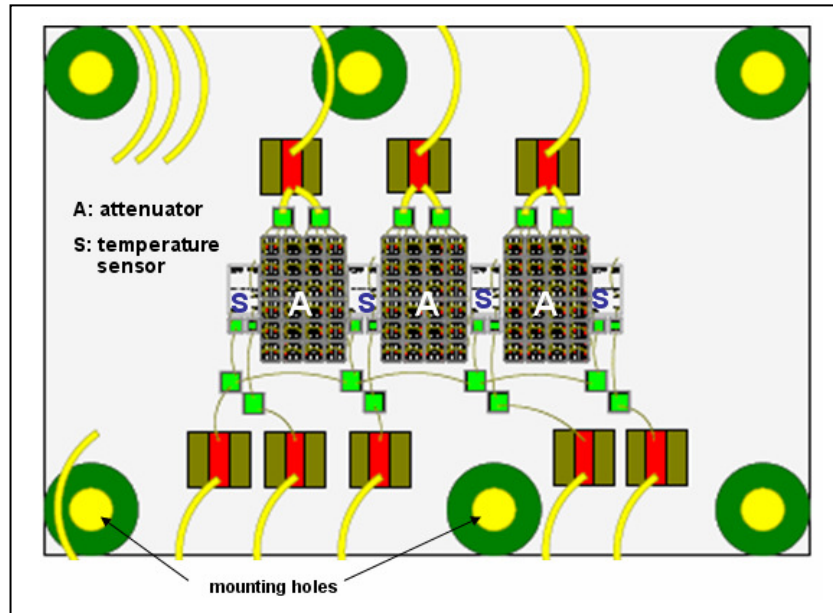


Figure 4.10: Heat load carrier

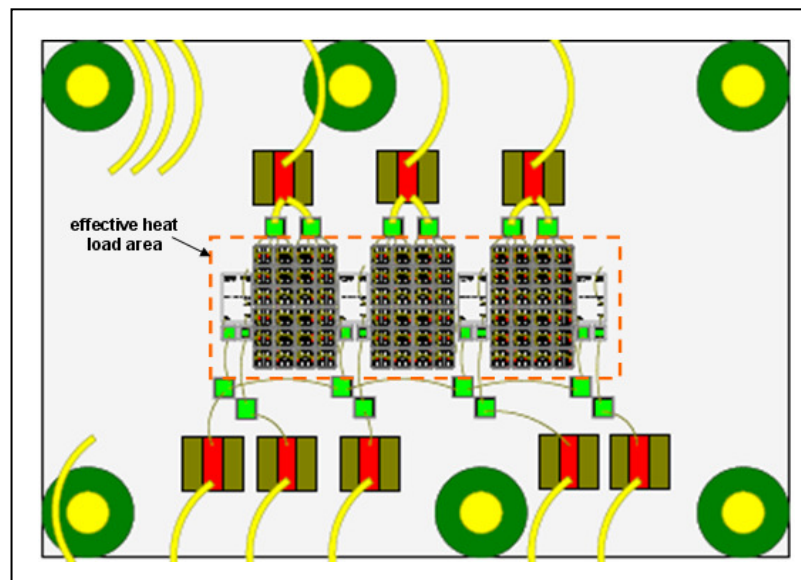


Figure 4.11: Effective heat load area

The heat load carrier was mounted onto the base of each microchannel heatsink using six M2 screws. A layer of thermal interface material, Thermagon© T-flex®, with a thermal conductivity of  $k = 3\text{W/mK}$ , was placed between the carrier and the heatsink base to reduce thermal interface resistance. The thickness of the thermal interface material layer was found to be 0.2mm after fastening of the screws, by measuring the total thickness of the test specimen after the mounting of the heat load carrier, and subtracting from this value the thickness of the heat load carrier alone.

To protect the heat load carrier, and also to form a confined volume of air to thermally insulate the test specimen from surrounding air, a transparent, protective casing was used. The heat load carrier mounted onto the heatsink is shown in Fig. 4.12, and the test specimen in its protective casing is shown in Fig. 4.13.

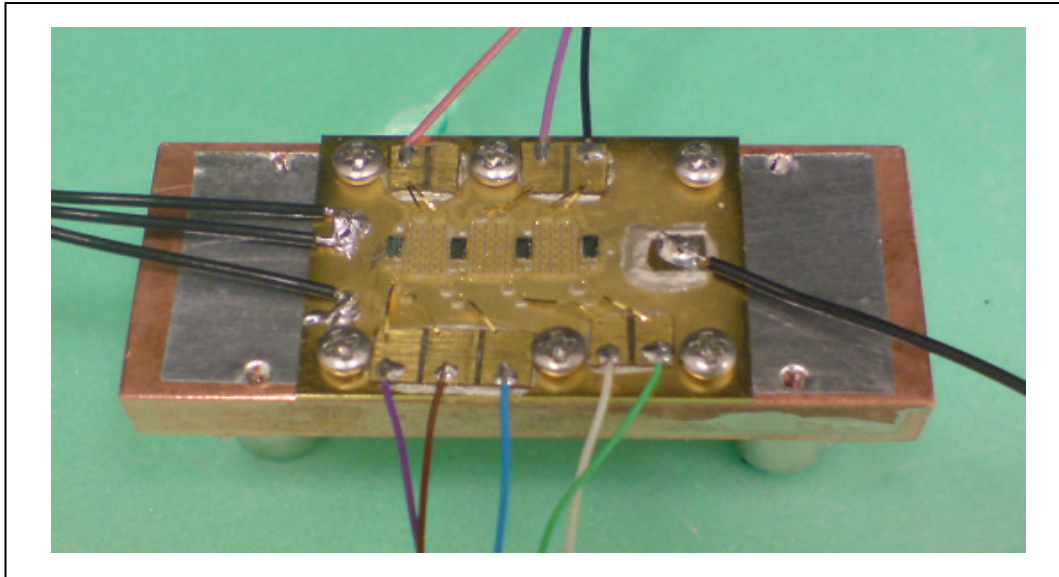


Figure 4.12: The heat load carrier mounted on the heatsink

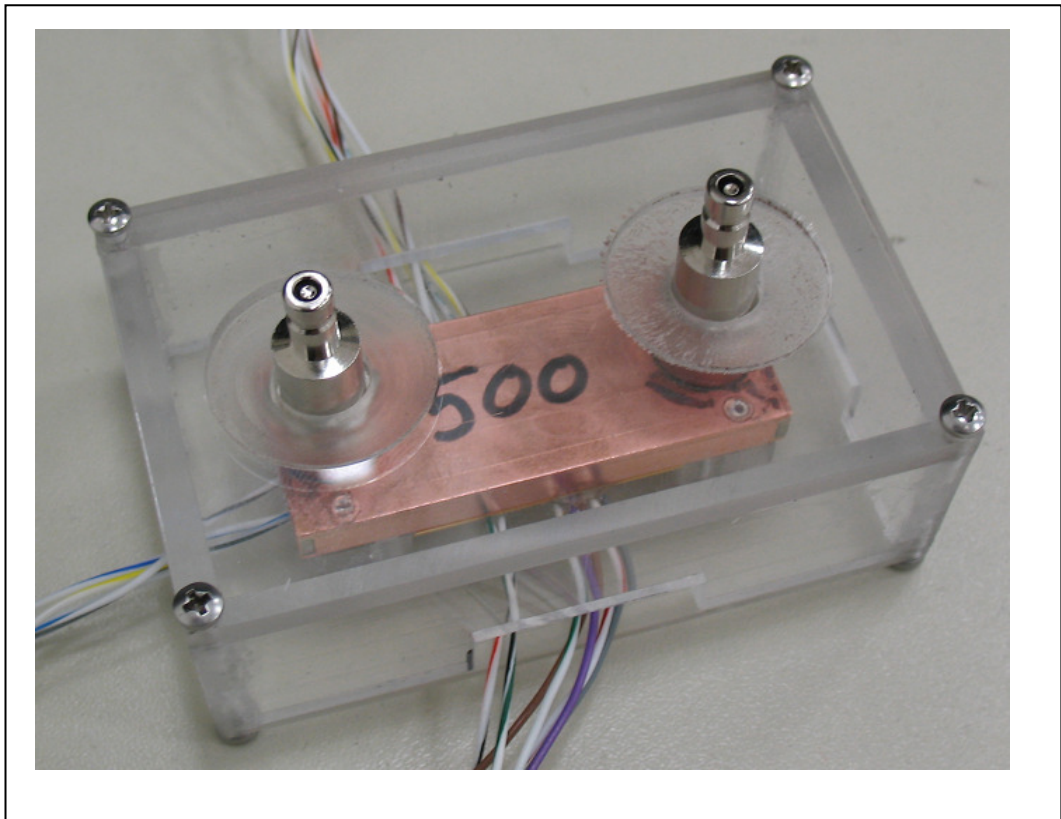


Figure 4.13: The test specimen in its protective casing

In addition to the heat load and heatsink, typical components of a liquid cooling system are a pump, filter, heat exchanger, heat exchanger fan, and expansion tank. A pump set consisting of two direct drive pumps in parallel, capable of providing 1.1 lpm flow rate against 5.2 bar system pressure, were used to drive the flow. A 12  $\mu\text{m}$  filter was included ahead of the pump to prevent blockage of the microchannels by any particles that might mix into the flow stream. The heat load applied at the heatsink base was removed from the system via the liquid-to-air heat exchanger. A simple, plastic expansion tank was employed in the cooling system cycle to remove any air bubbles trapped in the coolant stream and to maintain system pressure. The components of the cooling system described above are presented in Table 4.4.

Table 4.4: Cooling system components

COMPONENT	DESCRIPTION	PROPERTIES
	DIRECT DRIVE PUMP <b>MICROPUMP GAT23</b>	max. 0,55 lpm at 5,2 bar differential pressure
	12 MICRON FILTER <b>ASAS FUEL FILTER</b>	4 stage filter with minimum 12 $\mu\text{m}$ mesh thickness
	COPPER FIN AND TUBE HEAT EXCHANGER <b>THERMATRON 722SBP1A01</b>	20 series tube pass HX with 28 W/ $^{\circ}\text{C}$ performance at 1lpm liquid coolant flow rate
	AXIAL FAN <b>AMATEK ROTRON 3378SF</b>	28 VDC military spec. fan max. 3600 RPM, free flow rate 1300 CFM (cubic feet per minute)
	EXPANSION TANK <b>AQUARIUS III</b>	38 mm by 54 mm by 97 mm (199 $\text{cm}^3$ volume)

For the purposes of this study, the measurement facility is vital. An Agilent HP 34901 data logger and 20-channel multiplexer were used to collect all data. The digital data logger enabled the recording of all temperature, pressure, and flow rate data on a single file. In addition to the four temperature sensors integrated onto the heat load carrier, four J-type thermocouples, placed inside pipe sections close to the coolant liquid inlet and exit to the heatsink and at the air flow inlet and exit to

the heat exchanger, were included to complete the temperature measurements required. A rotary flow meter was placed between the pump and filter to accurately measure the volumetric flow rate provided by the pumps. Two pressure transducers, shown in Fig. 4.14, located at the microchannel heatsink inlet and exits, were used to measure the pressure drop across the heatsink.

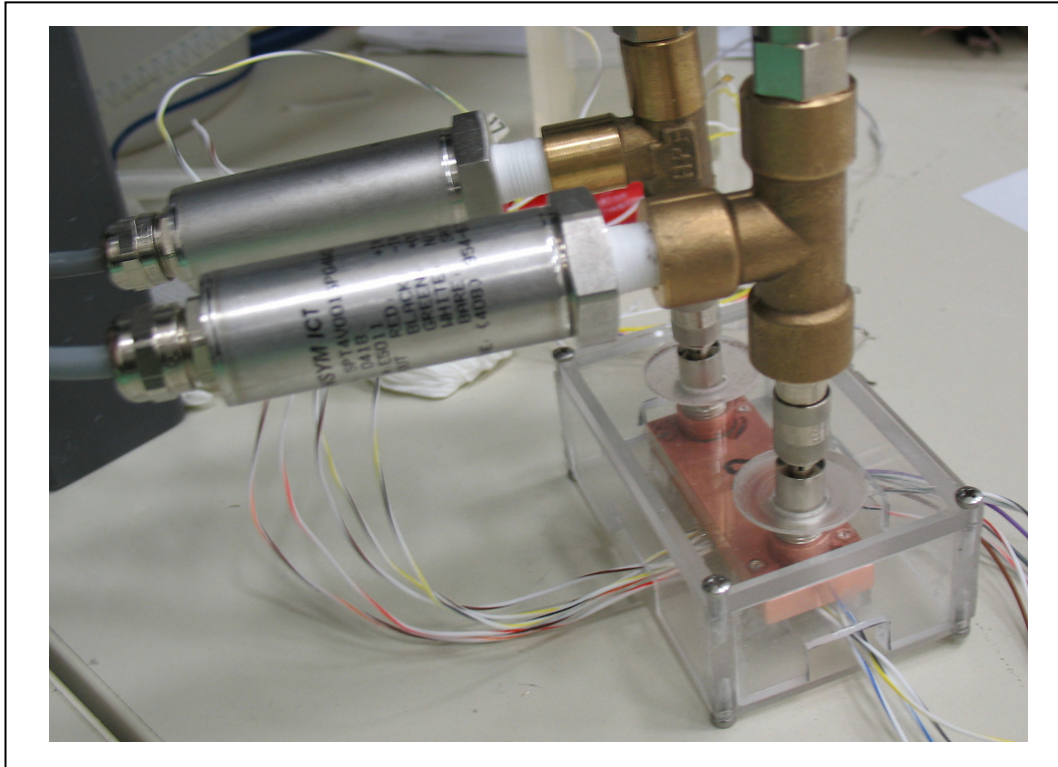


Figure 4.14: Pressure transducers at fluid inlet and outlets

The voltage output generated by all measurement instruments was converted to the appropriate reading in °C, bar, or lpm with respect to the calibration curve supplied for each instrument, and recorded at 10 second intervals by the data logger. A full data set in proper units was thus generated for each test. Properties of the measurement instruments described above are presented in Table 4.5. A schematic representation of the experimental setup is provided in Fig. 4.15. A picture of the setup in the laboratory environment, in working condition, is given in Fig. 4.16.

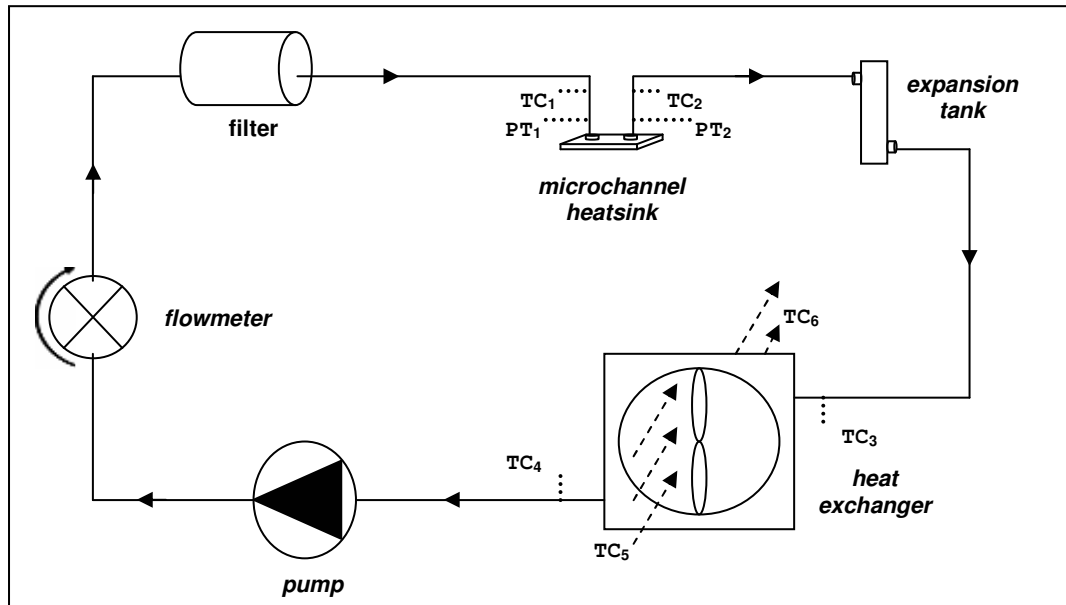


Figure 4.15: Schematic representation of the experimental setup

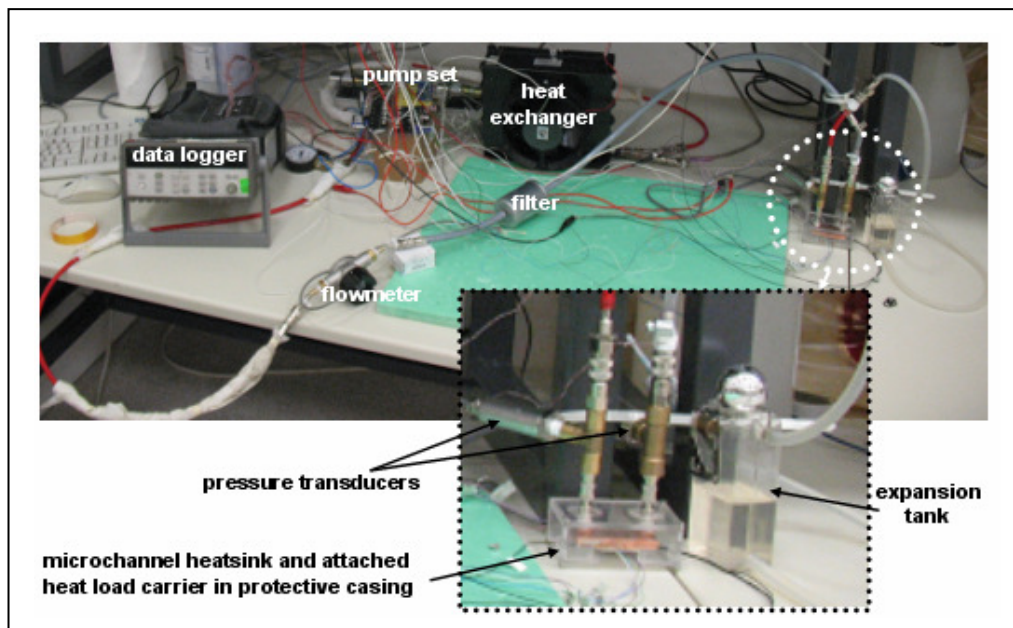




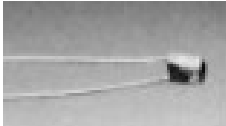


Figure 4.16: The experimental setup

Table 4.5: Measurement instruments of the experimental setup

COMPONENT	DESCRIPTION	PROPERTIES
	DIGITAL DATA LOGGER <b>AGILENT HP 34970A</b>	60 channel multiplexer and data logger capable of measuring and recording voltage, current, temperature, frequency etc. at a sampling interval of 2 seconds
	ROTARY DIGITAL FLOWMETER <b>GEMS RFO 2500</b>	RotorFlow type flowmeter with digital frequency output capable of measuring flow rates up to 5 lpm
	DIGITAL PRESSURE TRANSDUCER <b>HONEYWELL SPT4V</b>	Pressure transducer with 1-5 V output corresponding to a measured pressure of 0-15 psi
	J-TYPE THERMOCOUPLE <b>OMEGA J-32 SLE</b>	J-type thermocouple appropriate for measurements at 0-750 °C at special limits of error corresponding to 1.1 °C
	THERMISTOR HONEYWELL <b>NTC-100</b>	Chip mount thermistor rated up to 125 °C at 0.1 °C accuracy

#### 4.2.2 Measurements and Results

As described above, all measurements were recorded onto the digital data logger. During the tests, instantaneous measurements of temperature, pressure and flow rate taken at 30 second intervals were transferred from the data logger to a PC via the *Agilent Benchlink* software. The measurements were thus monitored continuously so that it could be judged easily whether or not the system reached thermal steady state conditions at each flow rate and heat load tested. Once steady state conditions were confirmed, the flow rate or heat load variable was changed to

the next test value for each microchannel heatsink. A set of data was thus obtained for the microchannel heatsinks. For each test specimen, three coolant flow rates (0.50, 0.75, 1.00 lpm) and three local heat fluxes (50, 75, 100 W/cm<sup>2</sup>) were tested. A total of 72 data sets for each of the resulting test parameter combinations, presented in Table 4.6, have thus been obtained. To clarify the points of temperature measurement on the heat load carrier, each temperature sensor has been numbered with respect to the coolant flow direction as shown in Fig. 4.17.

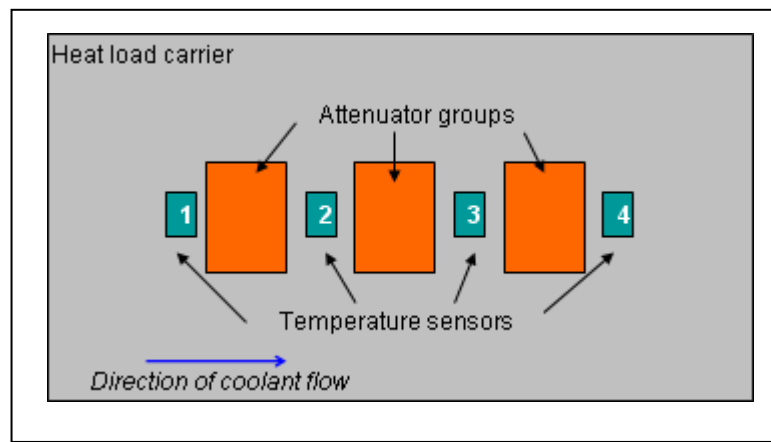


Figure 4.17: Temperature sensor enumeration convention

The temperature, pressure, and flow rate readings for each test conducted are presented in graphical form in Appendix G. Tabular summaries of the readings at steady state conditions for each test conducted are presented in Appendix H. It is observed that the highest temperature reading is consistently obtained from Sensor 3. Because the sensors are distributed among the groups of attenuators in a symmetrical fashion, the inner two sensors (Sensors 2 and 3) measure significantly higher temperatures in comparison to the outer two sensors (Sensors 1 and 4) due to the greater heat load density at the center of the heat load carrier. Due to the temperature rise of the coolant during its flow from the heatsink inlet towards the heatsink outlet, the sensor closer to the outlet, Sensor 3, measures slightly higher temperatures in comparison to Sensor 2.

Table 4.6: Test parameter combinations

Material	Channel Width ( $\mu\text{m}$ )	Coolant Flow Rate (lpm)	Local Heat Flux ( $\text{W}/\text{cm}^2$ )
Copper (CU)	300	0.50	50
			75
			100
		0.75	75
			100
			100
		1.00	50
			75
			100
	420	0.50	50
			75
			100
		0.75	75
			100
			100
		1.00	50
			75
			100
	500	0.50	50
			75
			100
		0.75	75
			100
			100
		1.00	50
			75
			100
	900	0.50	50
			75
			100
		0.75	75
			100
			100
		1.00	50
			75
			100
Aluminum (AL)	300	0.50	50
			75
			100
		0.75	75
			100
			100
		1.00	50
			75
			100
	420	0.50	50
			75
			100
		0.75	75
			100
			100
		1.00	50
			75
			100
	500	0.50	50
			75
			100
		0.75	75
			100
			100
		1.00	50
			75
			100
	900	0.50	50
			75
			100
		0.75	75
			100
			100
		1.00	50
			75
			100

Being the highest temperature measured, the readings obtained from Sensor 3 are considered to be representative of the central attenuator group, the most critical of the three attenuator groups in terms of temperature rise due to its location on the heat load carrier. In actual T/R module cooling applications, the temperature of active electronic chips are commonly monitored through temperature sensors placed on the chip carrier, the locations of which are chosen to be as close as possible to the highest heat load density on the carrier. Due to physical restrictions, it is not possible to measure the temperature of the heat source, ie. the chip, itself so the readings of temperature sensors placed right next to the critical chips are considered to be representative of the chip temperatures. This is consistent with the selection of Sensor 3 to be representative of the temperature of the central attenuator group for the present study, in which critical chips of actual T/R module applications are simulated by attenuator groups. It is therefore convenient to judge the thermal performance of the heatsinks tested with reference to the temperature rise measured by Sensor 3 with respect to the heatsink coolant inlet temperature. Graphical representations of the variation of the temperature rise at the location of Sensor 3 with varying local heat flux at the constant coolant flow rate of 1 lpm, and varying coolant flow rate at the constant local heat flux of  $100 \text{ W/cm}^2$ , based on test results conducted on all the specimens, are presented in Fig. 4.18 through Fig. 4.21. The uncertainty of  $\pm 1.1^\circ\text{C}$  due to the thermocouples measuring coolant and ambient air temperatures and the uncertainty of  $\pm 0.1^\circ\text{C}$  due to the thermistors measuring the heat load carrier temperatures are included in the graphical presentations. The measured pressure drop variation across each heatsink with respect to the coolant flow rate is given in Table 4.7. Because the pressure measurements were taken via pressure transducers connected to the heatsink inlet and outlets through T-junctions using quick-disconnect fluid fittings, as shown previously in Fig. 4.14, it was necessary to correct the pressure drop obtained from the pressure readings by subtracting the pressure drop due to the fittings. To do this, the pressure drop due to the fittings was measured at each test flow rate of 0.50 lpm, 0.75 lpm, and 1.00 lpm by connecting the two T-junctions end to end so that the pressure transducers measured the pressure at the inlet of one fitting and

eat the inlet of the other fitting. The fitting pressure drop,  $\Delta p_f$ , was measured to be 0.056 bar, 0.112 bar, and 0.189 bar for respective flow rates of 0.50 lpm, 0.75 lpm, and 1.00 lpm. Table 4.7 also presents measurement readings corrected with the fitting pressure drop by subtracting twice the fitting pressure drop (due to two fitting couples for each specimen) from the measured pressure drop. The variation of the pressure drop with coolant flow rate and channel width is presented for copper and aluminum specimens, respectively, in Fig. 4.22 and 4.23. The uncertainty of  $\pm 0.003$  bar due to the pressure transducers is included in the graphical presentations.

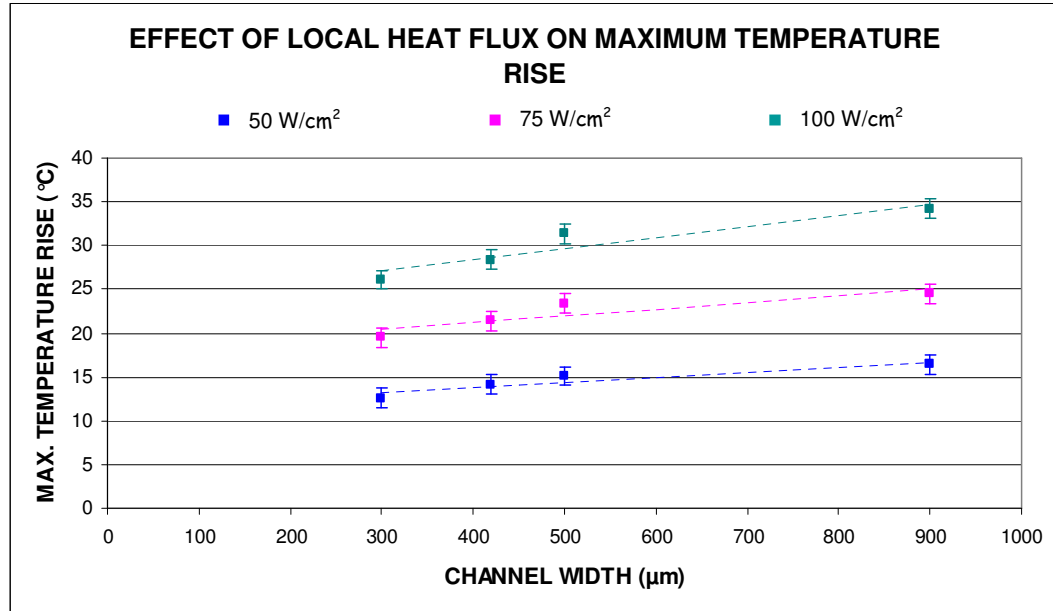


Figure 4.18: Maximum temperature rise of copper specimens at 1 lpm coolant flow rate

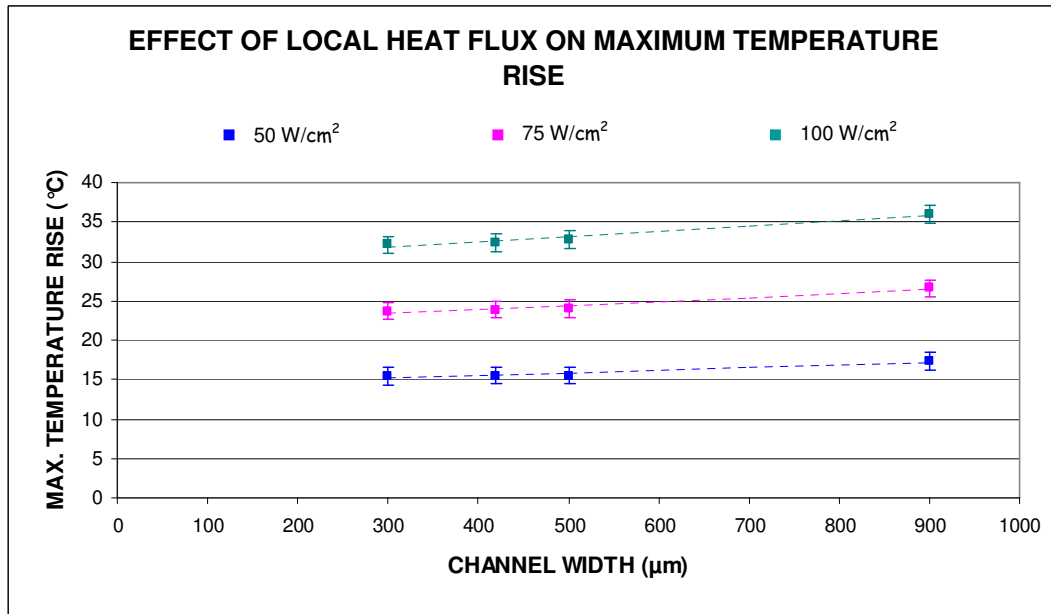


Figure 4.19: Maximum temperature rise of aluminum specimens at 1 lpm coolant flow rate

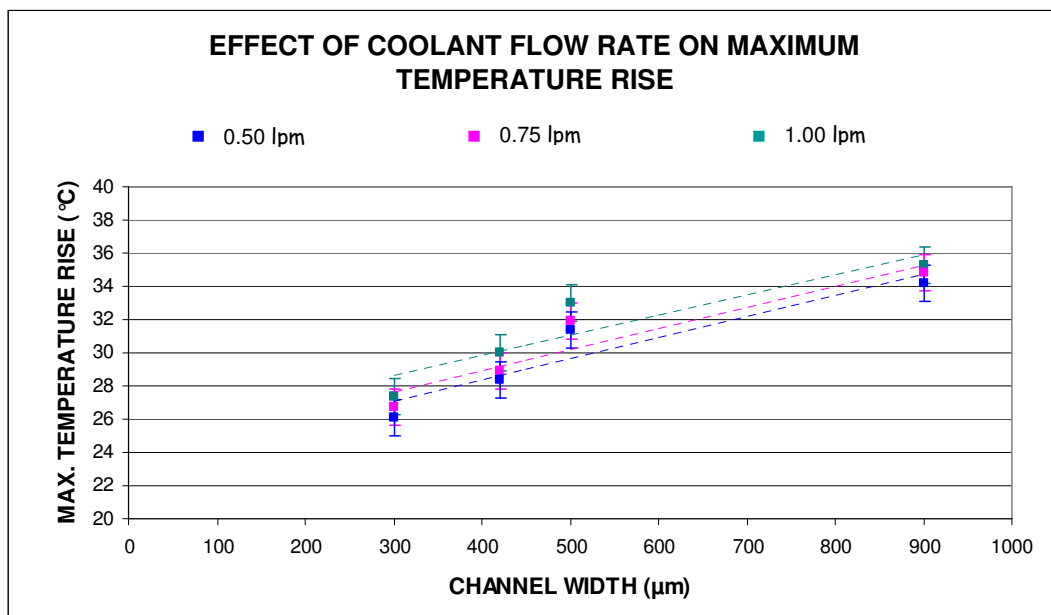


Figure 4.20: Maximum temperature rise of copper specimens at 100 W/cm<sup>2</sup> local heat flux

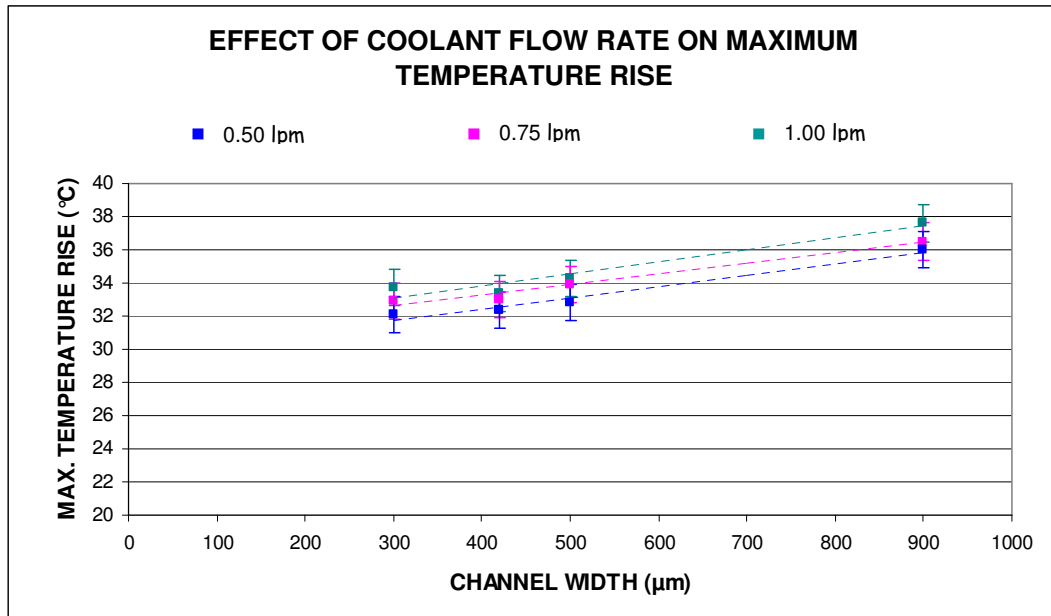


Figure 4.21: Maximum temperature rise of aluminum specimens at 100 W/cm<sup>2</sup> local heat flux

Table 4.7: Pressure drop across heatsinks

$Q$ (lpm)	$W_c$ (μm)	MATERIAL	$p_1$ (bar)	$p_2$ (bar)	$\Delta p_f$ (bar)	$\Delta p$ (bar)
0.50	300	CU	0.218	0.094	0.056	0.012
		AL	0.216	0.094		0.010
	420	CU	0.225	0.103		0.010
		AL	0.218	0.096		0.010
	500	CU	0.216	0.097		0.007
		AL	0.219	0.099		0.008
	900	CU	0.220	0.101		0.007
		AL	0.208	0.096		0.000
0.75	300	CU	0.426	0.184	0.112	0.018
		AL	0.425	0.185		0.016
	420	CU	0.422	0.187		0.011
		AL	0.425	0.190		0.011
	500	CU	0.421	0.188		0.009
		AL	0.419	0.188		0.007
	900	CU	0.416	0.185		0.007
		AL	0.408	0.187		0.000
1.00	300	CU	0.719	0.311	0.189	0.030
		AL	0.721	0.314		0.029
	420	CU	0.712	0.313		0.021
		AL	0.710	0.314		0.018
	500	CU	0.692	0.305		0.009
		AL	0.682	0.296		0.008
	900	CU	0.681	0.297		0.006
		AL	0.658	0.288		0.000

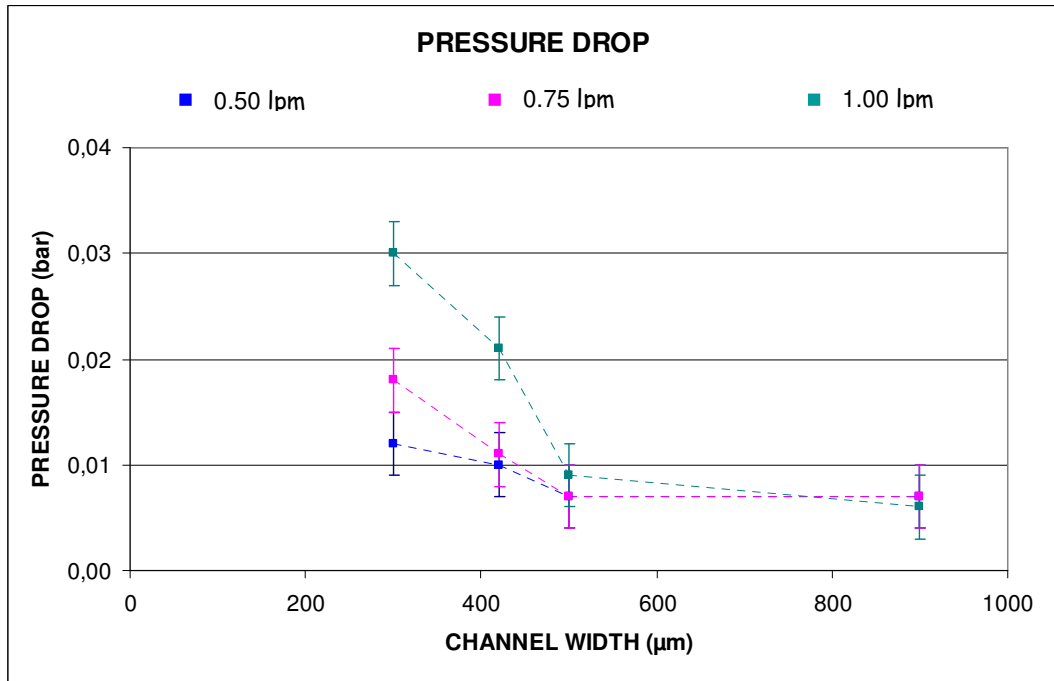


Figure 4.22: Pressure drop of copper specimens

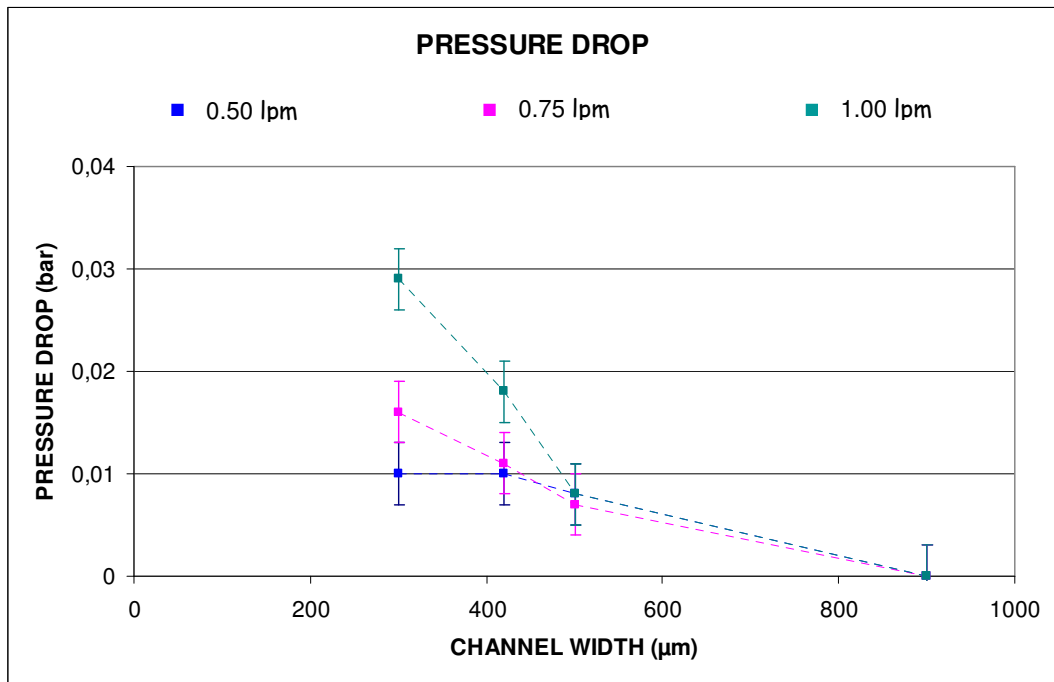


Figure 4.23: Pressure drop of aluminum specimens

### ***4.2.3 Evaluation of Results***

Preliminary inspection of the results suggests that the thermal performance of the heatsinks tested follow a linear trend with respect to the channel width. For the copper specimens at  $100 \text{ W/cm}^2$ , test results show a 31% increase in the maximum temperature rise between the minimum and maximum channel widths of  $300 \text{ }\mu\text{m}$  and  $900 \text{ }\mu\text{m}$ . The increase is 14% for the aluminum specimens. It is observed that the coolant flow rate has very little effect on the maximum temperature rise, as expected due to the constant Nusselt number predicted by laminar flow and heat transfer theory. For both the aluminum and copper specimens tested at  $100 \text{ W/cm}^2$ , doubling the coolant flow rate from 0.5 lpm to 1 lpm resulted in only a 5% reduction in the maximum temperature rise.

It is observed that the pressure drop across the heatsinks decrease smoothly with increasing channel width, as expected, with the effect of channel width being more significant at higher coolant flow rates. For the same channel width – coolant flow rate pairs, the pressure drop values of the copper and aluminum are seen to be very close, with the values for the copper specimens being consistently higher by a very small margin. This small difference is likely to be caused by the effect of material properties such as surface roughness and remnants of machining being more significant in the copper specimens. Another striking feature of the pressure drop measurements is that the measured values for the  $900 \text{ }\mu\text{m}$  specimens are inconsistently small, approaching zero for the aluminum specimen. This is attributed to the measurement range of the pressure transducers being inadequate for very small pressure measurements, and the pressure drop across the fittings being the major pressure loss term. It may be said that the pressure drop measurements are reliable only for the  $300 \text{ }\mu\text{m}$ ,  $420 \text{ }\mu\text{m}$ , and  $500 \text{ }\mu\text{m}$  specimens.

An important, yet uncontrolled, factor in evaluating the reliability of the experimental results is the amount of undesired heat loss from the heatsink to the surrounding air. As all discussions are based on the removal of the heat load

generated at the heatsink base by the coolant fluid, it is desired to keep the heat transfer to the ambient at a minimum. Due to the fragile structure of the attenuators and thin, gold wires on the heat load carrier, it was not possible to apply a thermal insulation layer at the region of heat load generation. However, with the test specimens placed inside protective containers manufactured of plexiglass as previously shown in Fig. 4.14, a stagnant volume of air was formed just under the heat load carrier. The volume of air acted as a heat insulator. In addition to this effect, the structure of the attenuators aided in preventing heat loss to the surroundings as the passive surfaces of these elements, facing the surrounding air, were of silicon. To provide an estimate of the fraction of the heat load lost to the ambient air, the simple energy balance of Eq. 2.35 was employed, with the coolant inlet and outlet temperatures measured close to the heatsink inlet and outlet sections. The calculation results, presented in Appendix I, revealed that for the tests conducted at 0.50 lpm and 0.75 lpm coolant flow rate, 90% or more of the heat load input was removed by the coolant, indicating a maximum heat loss to the surrounding air of 10%. Taking into account that the points of measurement of the heatsink coolant inlet and exit temperatures, provided by thermocouples dipped inside the plastic pipes carrying the coolant, were approximately 5 cm away from the actual inlet and outlet sections, and that the measured temperature differences in the range of 0.5 °C to 1 °C are comparable with the measurement accuracy of the thermocouples, it is likely that the actual heat loss percentages were even less.

## CHAPTER 5

### NUMERICAL ANALYSES AND RESULTS

The procedure of numerical modeling of the heatsinks and numerical results are presented in this chapter. Modeling has been done computationally using the FLUENT<sup>®</sup> finite volume CFD software, on meshes created using GAMBIT<sup>®</sup> mesh generation software.

#### 5.1 The Computational Model

The heatsinks, including coolant inlet and outlet regions, were modeled and meshed using GAMBIT<sup>®</sup>. A view of the model in GAMBIT<sup>®</sup> is given in Fig. 5.1.

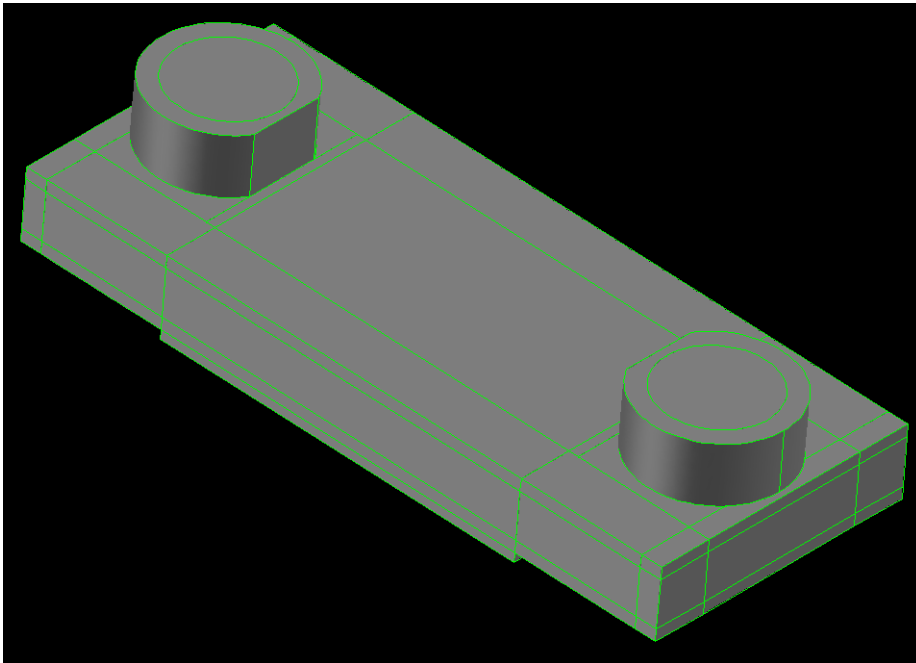


Figure 5.1: Model of the test specimens in GAMBIT<sup>®</sup>

All geometric details of the actual test specimens were included in the model to allow for the numerical analyses to resemble the experimental conditions as closely as possible. The attenuator groups were modeled as 3.49 mm x 5.24 mm, two dimensional heat sources due to their extremely small thickness of 0.01mm. Based on the results of a preliminary mesh independence study yielding satisfactory results and the availability of a powerful workstation, it was decided to make use of the maximum possible number of mesh elements.

Most of the test specimen geometry being appropriate, hexahedral cells were used in all portions of the model except for the coolant inlet and outlet regions, in which the transition of the mesh from the extremely highly density in the channels and channel walls to moderate densities in the outer surfaces was achieved through tetrahedral elements. The total number of cells, number of cells in each channel, number of cells in each channel wall, average cell width in channels, and cell width in channel walls for each of the meshes are given in Table 5.1. Various views of the meshed geometry are given in Fig. 5.2 through Fig. 5.8 to illustrate the mesh employed.

Table 5.1: Mesh statistics

$W_c$	Mesh Count	# of Elements in Channel	Average Element Width in Channel	# of Elements in Channel Wall	Element Width in Channel Wall
300 $\mu\text{m}$	6248950	12	25.00 $\mu\text{m}$	12	25.00 $\mu\text{m}$
420 $\mu\text{m}$	6227985	16	26.25 $\mu\text{m}$	12	25.00 $\mu\text{m}$
500 $\mu\text{m}$	6421885	20	25.00 $\mu\text{m}$	12	25.00 $\mu\text{m}$
900 $\mu\text{m}$	6248950	36	25.00 $\mu\text{m}$	12	25.00 $\mu\text{m}$

The mesh in all rectangular volumes of the model, such as channels, channel walls, heatsink base, side walls, and cover plate, heat load carrier, were meshed using the "quad - map" meshing scheme. The coolant inlet and outlet regions where mesh transition to larger cells were employed, and the cylindrical volumes of the inlet and outlet ports were meshed using the "cooper" scheme with "quad - map" face

meshes on the side walls and "tri - pave" face meshes on the projected base surfaces. The mesh zones are illustrated in Fig. 5.9.

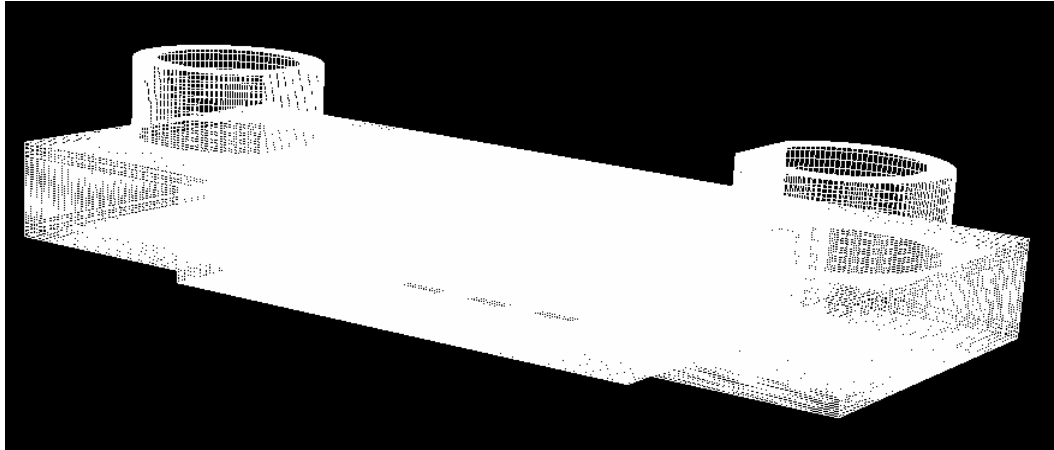


Figure 5.2: General view of the mesh on solid surfaces

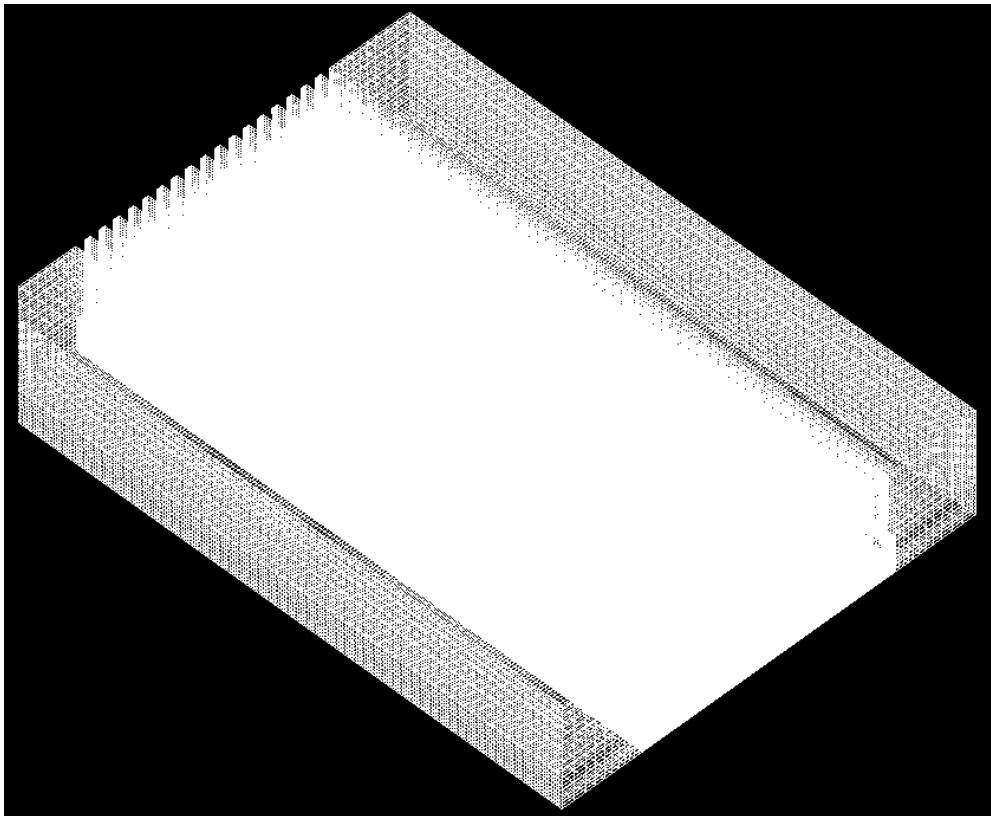


Figure 5.3: View of the mesh on outer surfaces of the heatsink

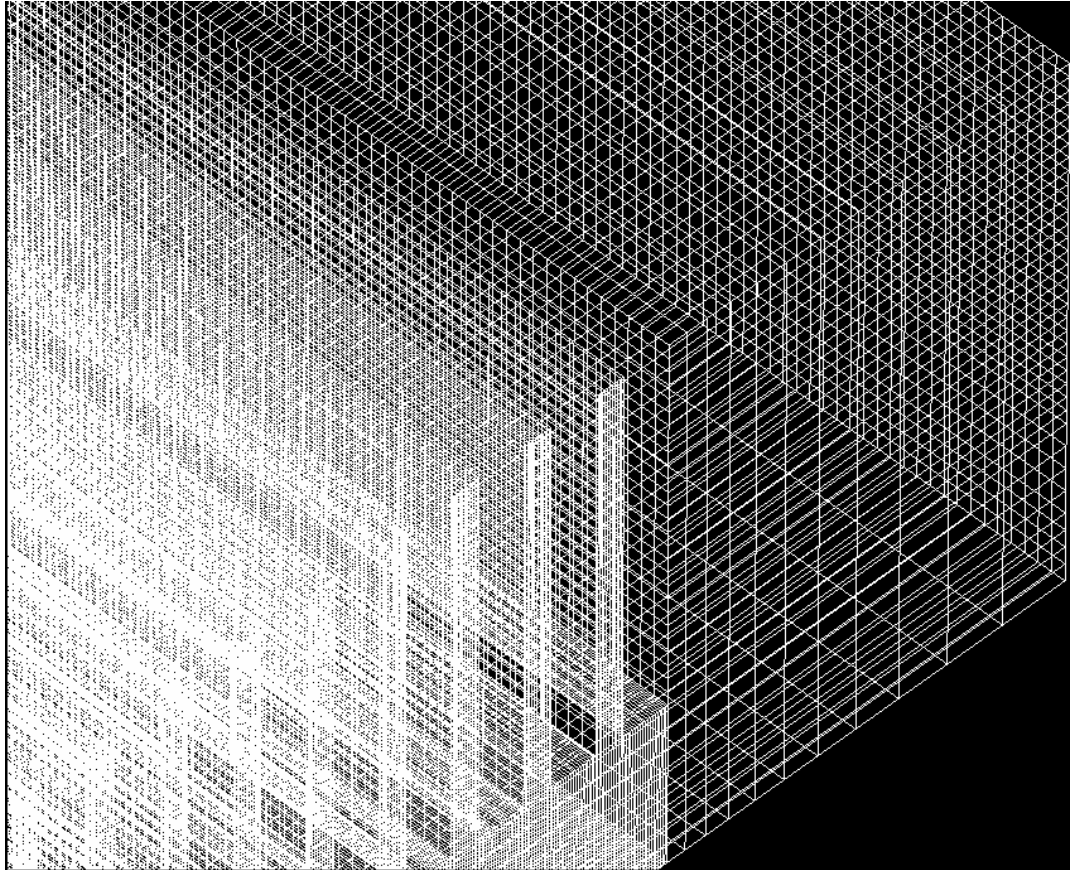


Figure 5.4: Close-up view of the mesh on outer surfaces of the heatsink

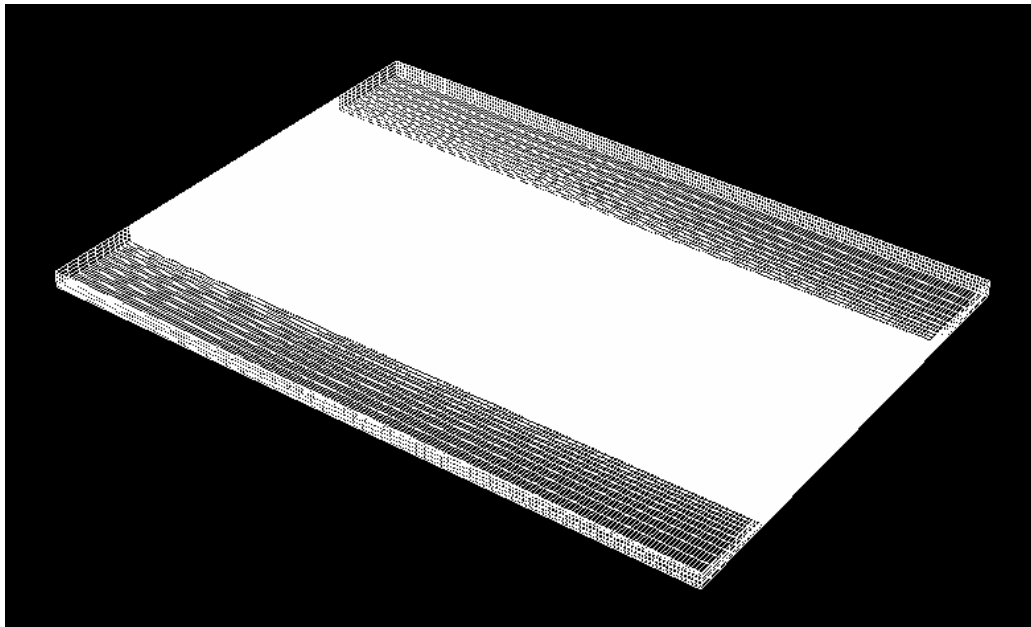


Figure 5.5: View of the mesh on outer surfaces of the heat load carrier

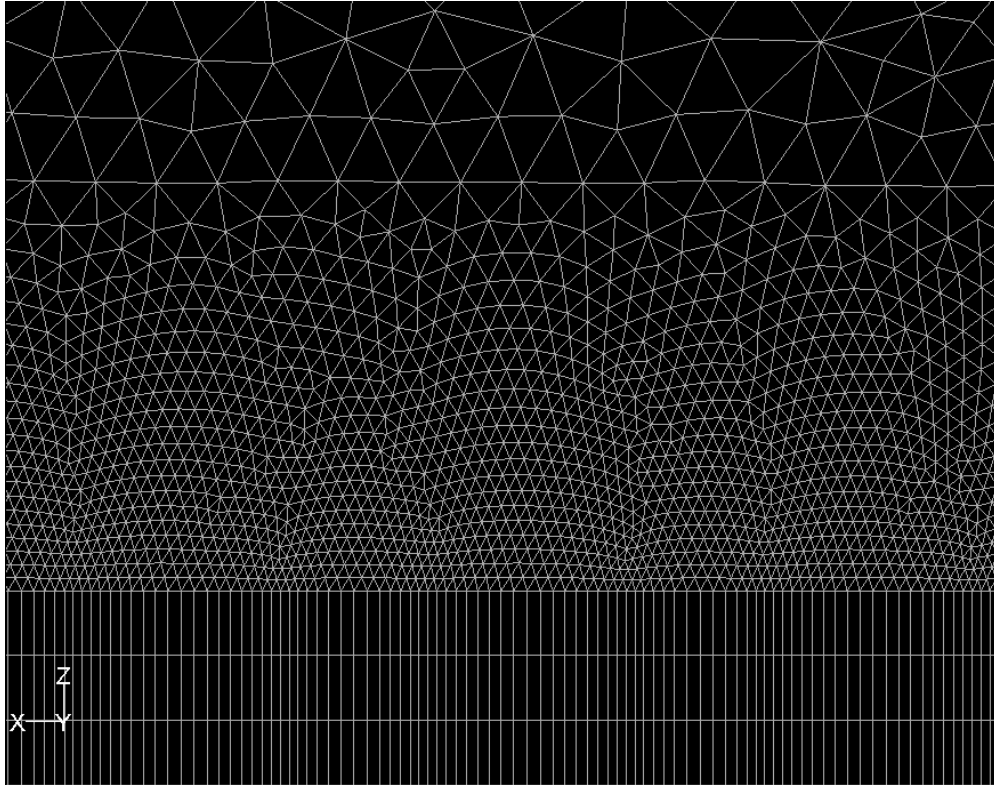


Figure 5.6: Transition of the mesh from the channels to coolant inlet-outlet regions

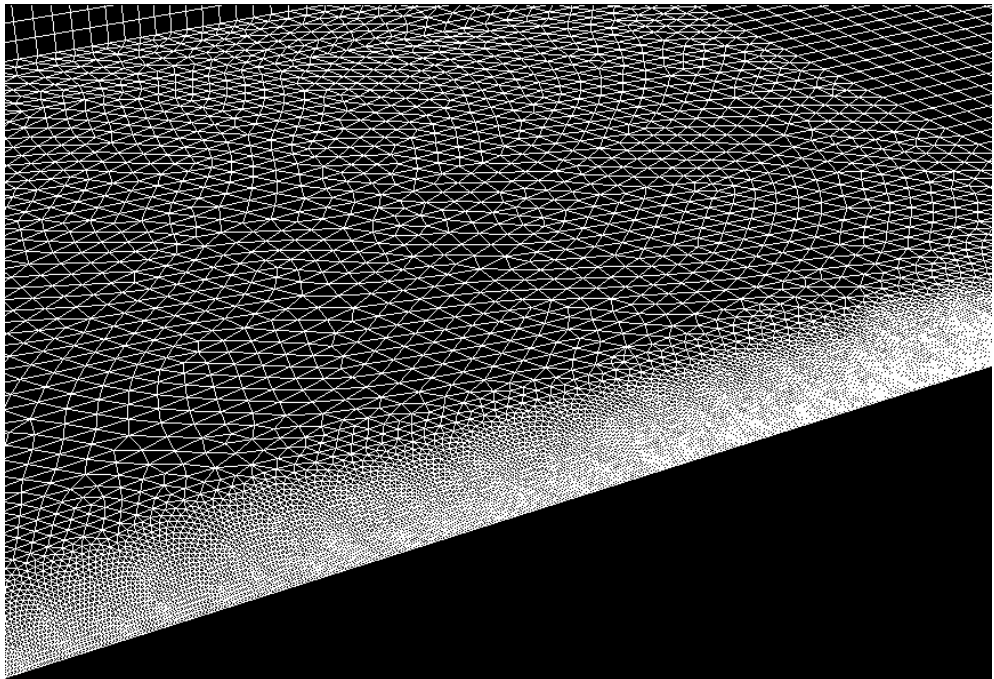


Figure 5.7: Transition of the mesh within the coolant inlet-outlet regions to smaller densities

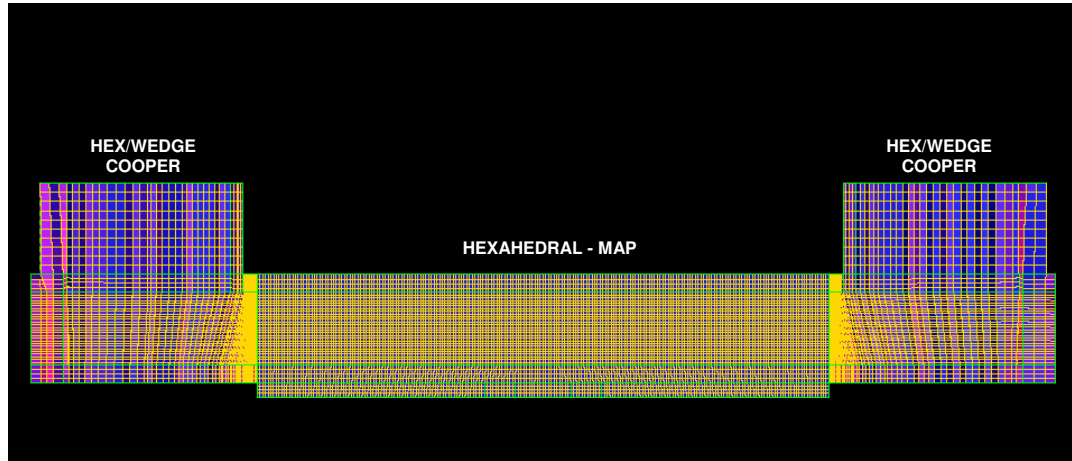


Figure 5.8: Mesh zones shown along central section

Following the completion of the mesh generation process, continuum zones and surfaces were defined. The solid regions of the model and regions of coolant flow were separated at this stage into solid and fluid volumes. The surfaces at which boundary conditions took effect, such as all external surfaces of the test specimen, interfaces between solid and fluid regions, coolant inlet and outlet sections, attenuator groups, and the location of thermal interface material (specified as the interface between the heat load carrier and heatsink base), were defined.

## 5.2 Boundary Conditions and Solver Settings

All boundary conditions were defined in FLUENT<sup>®</sup> after importing the mesh file created by GAMBIT<sup>®</sup>. The most important boundary conditions employed were those defined at the coolant inlet, at the attenuator groups, and at the thermal interface layer. Three coolant inlet velocities, in compliance with the three flow rates of 0.50 lpm, 0.75 lpm, and 1.00 lpm employed during the experiments, were specified at the inlet section (0.12 m/s, 0.18 m/s, and 0.24 m/s) calculated according to the basic flow rate relation with a circular flow cross sectional area of 9 mm diameter:

$$V_{inlet} = \frac{Q_{inlet}}{A_{flow}} \quad (5.1)$$

where  $Q_{inlet}$  is the coolant inlet flow rate, with the value in lpm divided by 60000 to obtain the value in m<sup>3</sup>/s, and  $A_{flow}$  is  $\frac{\pi}{4}(0.0094)^2 = 6.892 \cdot 10^{-5} \text{ m}^2$ .

A heat flux boundary condition was applied for each attenuator group, namely 50 W/cm<sup>2</sup>, 75 W/cm<sup>2</sup>, and 100 W/cm<sup>2</sup>, corresponding to the three local heat flux values employed during the experiments. The thermal interface (TI) boundary condition was a critical one, as it had a great impact on the temperature results. To compensate for the unknown thermal interfaces that were not modeled, such as the interfaces between the attenuator groups and the heat load carrier, and also interfaces possibly induced by impurities in the heatsink material or the remnants of the manufacturing processes, an increased effective thickness value of 0.3 mm was defined in addition to the measured thickness value of 0.2 mm. Therefore, the layer of interface material of 3 W/mK thermal conductivity was modeled as a two dimensional plane of 0.2 mm and 0.3 mm effective thickness. All numerical simulations were carried out for both effective thickness values.

In addition to the critical boundary conditions explained above that were varied during the analyses, the boundary conditions that remained the same for all simulations were the pressure outlet boundary condition at the coolant exit section set at 0 bar gauge pressure, and adiabatic walls at all external surfaces of the test specimen, heat load carrier, and attenuator groups. The fluid volumes were specified to be composed of pure water with properties at 300 K, the heat load carrier volume was specified to be composed of copper-tungsten, and all remaining solid volumes were specified to be composed of copper or aluminum. The boundary condition and volume specifications employed in the numerical simulations are presented in Tables 5.2 and 5.3.

Table 5.2: Boundary condition specifications

Boundary	Specification
Coolant Inlet	Velocity Inlet @ 300K (0.12, 0.18, 0.24 m/s )
Coolant Outlet	Pressure Outlet (0 bar Gauge Pressure)
External Surfaces	Adiabatic walls
Attenuator Groups	Heat flux (50, 75, 100 W/cm <sup>2</sup> )
Thermal Interface Layer	k = 3W/mK; 0.2, 0.3 mm effective thickness

Table 5.3: Volume specifications

Volume	Specification
Coolant	Water @ 300K
Test Specimen	Copper, Aluminum
Heat Load Carrier	Copper - Tungsten

Solver settings were selected after a number of preliminary solutions were carried out. To meet the convergence criteria of all solution residuals falling under 0.001, and monitoring of the coolant exit flow velocity and inlet pressure to a constant value, the solution required imposing of under-relaxation factors of 0.3 for pressure and 0.4 for momentum. It was observed that selection of 1<sup>st</sup> order or 2<sup>nd</sup> discretization for pressure and volume had no significant effect on the solution. This was attributed to the high mesh density. Solutions were carried out using 1<sup>st</sup> order discretization. The default pressure - momentum coupling scheme, SIMPLE, proved sufficient for the model and was employed throughout the solutions. A tabular summary of solver setting selections are given in Table 5.4.

Table 5.4: Solver settings

Setting	Selection
Flow	Laminar
Under Relaxation	Pressure: 0.3
	Momentum: 0.4
Pressure Discretization	1 <sup>st</sup> Order
Momentum Discretization	1 <sup>st</sup> Order
Pressure - Velocity Coupling	SIMPLE

### 5.3 Numerical Simulation Results

Because the numerical simulations are of complementary nature to the present study, not all of the 72 combinations of channel width, specimen material, local heat flux, and coolant flow rate employed during the experiments were simulated in FLUENT<sup>®</sup>. A representative set of simulations for both the copper and aluminum specimens sufficient to assess the effects of each variable was completed. The variation of coolant flow rate and local heat flux was confined to the specimens of 300  $\mu\text{m}$  channel width for the simulations, and the remaining channel widths were simulated using only the fixed coolant flow rate and local heat flux values of 1.00 lpm and 100  $\text{W}/\text{cm}^2$ , respectively. These maximum values of the experiments were chosen for the fixed coolant flow rate and local heat flux for the full range of channel width simulations to allow for a full comparison of the results at the limits of the parameters tested. In addition to the variables of the experiments, the effective thickness of the modeled thermal interface (TI) layer was included in the simulations as an extra variable, as described in Section 5.2, and two sets of simulation results were obtained for 0.2 mm and for 0.3 mm effective TI layer thickness ( $\text{TI}_t$ ). This was done to assess the effect of thermal interface layer thickness on the thermal performance of the microchannel heatsinks, and also to determine how well the actual behavior of the test specimens could be simulated by using an increased effective thermal interface layer thickness to compensate for other thermal interfaces in the system that could not be modeled. The set of variables for which numerical simulations were conducted are presented in Table 5.5.

Table 5.5: Simulation parameters

$Q$ (lpm)	$q''$ (W/cm <sup>2</sup> )	$W_c$ (μm)	MATERIAL	$Tl_i$ (mm)
0.50	100	300	CU	0.2
				0.3
			AL	0.2
				0.3
0.75	100	300	CU	0.2
				0.3
			AL	0.2
				0.3
1.00	50	300	CU	0.2
				0.3
			AL	0.2
				0.3
	75	300	CU	0.2
				0.3
			AL	0.2
				0.3
	100	300	CU	0.2
				0.3
			AL	0.2
				0.3
		420	CU	0.2
				0.3
			AL	0.2
				0.3
		500	CU	0.2
				0.3
			AL	0.2
				0.3
		900	CU	0.2
				0.3
			AL	0.2
				0.3

### 5.3.1 Numerical Results for Pressure Drop and Temperature Rise

To attain consistency between the numerical simulation work and experimental work, four points, corresponding to the exact locations of the four temperature sensors mounted on the heat load carrier, were defined during post-processing of the simulation results in FLUENT<sup>®</sup>. Much of the evaluation of the thermal aspect of the simulation results were based on the simulation outputs of temperature for these points. For convenience, the points in the numerical model corresponding to Sensor 1, Sensor 2, Sensor 3, and Sensor 4 of the heat load carrier will be referred to as P1, P2, P3, and P4. The CFD results for the temperatures of these points are

presented in Appendix. J. Due to the same reasons cited in Section 2.2, the simulation results for the temperature of P3 are consistently higher than the results for the remaining three points. Graphical representations of the variation of the temperature rise of P3 with respect to the heatsink coolant inlet with varying local heat flux at the constant coolant flow rate of 1 lpm, and with varying coolant flow rate at the constant local heat flux of 100 W/cm<sup>2</sup>, based on simulations conducted on the 300  $\mu$ m specimens, are presented in Fig. 5.9 and Fig. 5.10.

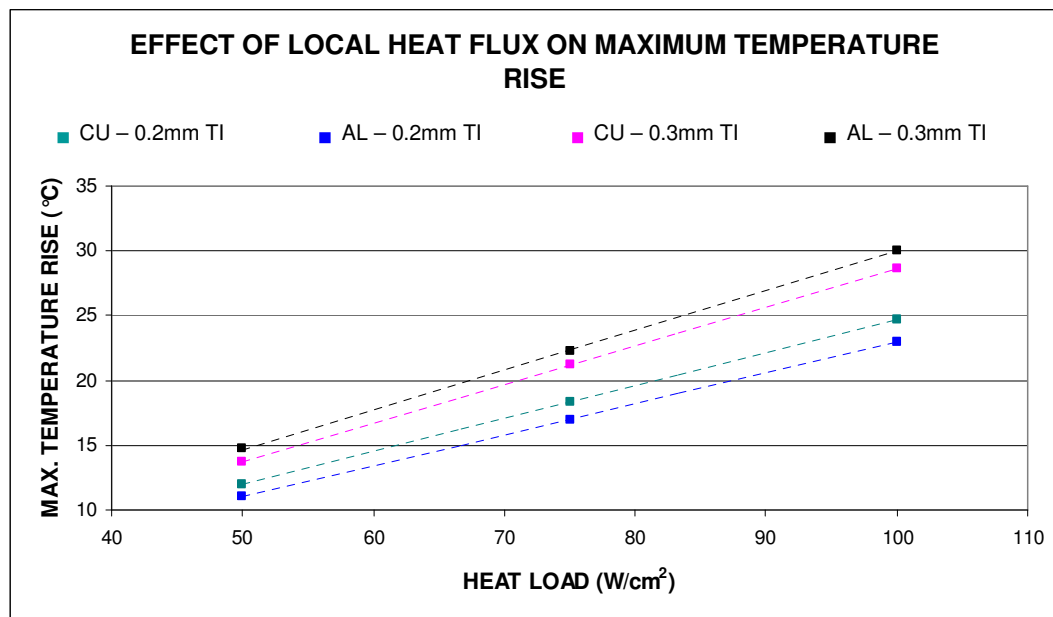


Figure 5.9: Effect of local heat flux on maximum temperature rise – 300  $\mu$ m specimens

For the 300  $\mu$ m specimens, graphical representations of the effect of coolant flow rate on maximum channel velocity and pressure drop are presented in Fig. 5.11. For the constant coolant flow rate of 1 lpm, the effect of channel width on maximum channel velocity and pressure drop are presented in Fig. 5.12

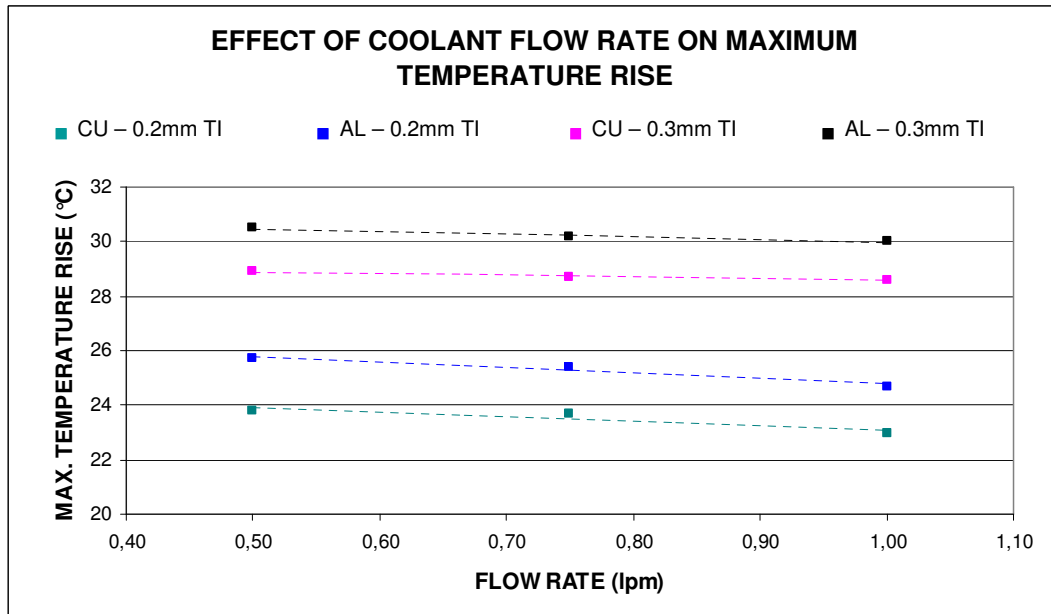


Figure 5.10: Effect of coolant flow rate on maximum temperature rise – 300  $\mu$ m specimens

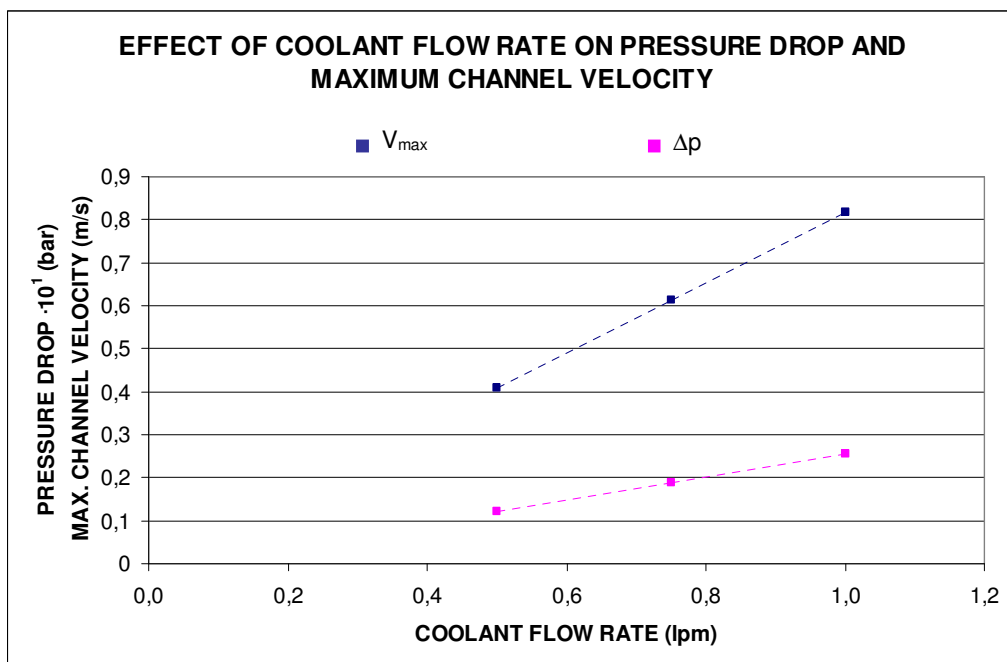


Figure 5.11 Effect of coolant flow rate on pressure drop and maximum channel velocity for the 300  $\mu$ m specimens

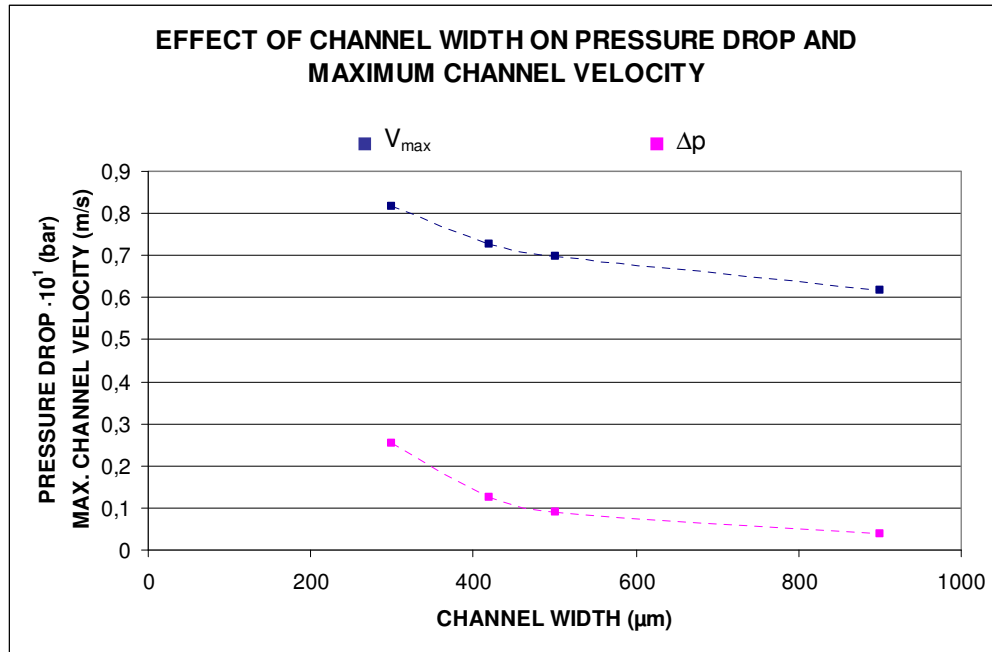


Figure 5.12 Effect of channel width on pressure drop and maximum channel velocity for the constant coolant flow rate of 1 lpm

A full discussion of the simulation results, and their comparison with experimental and analytical results, are provided in Chapter 6. A presentation of the CFD results obtained for the flow, an evaluation of heat loss effects, and an evaluation of the effects of the TI layer and localized heat source conditions are given in the following sub-sections.

### 5.3.2 CFD Results on Flow Characteristics

Pressure and velocity contours along vertical and horizontal mid-sections of the channels of the 500 μm specimen for the simulation of 1.00 lpm coolant flow rate are given in Fig. 5.13 through Fig. 5.16.

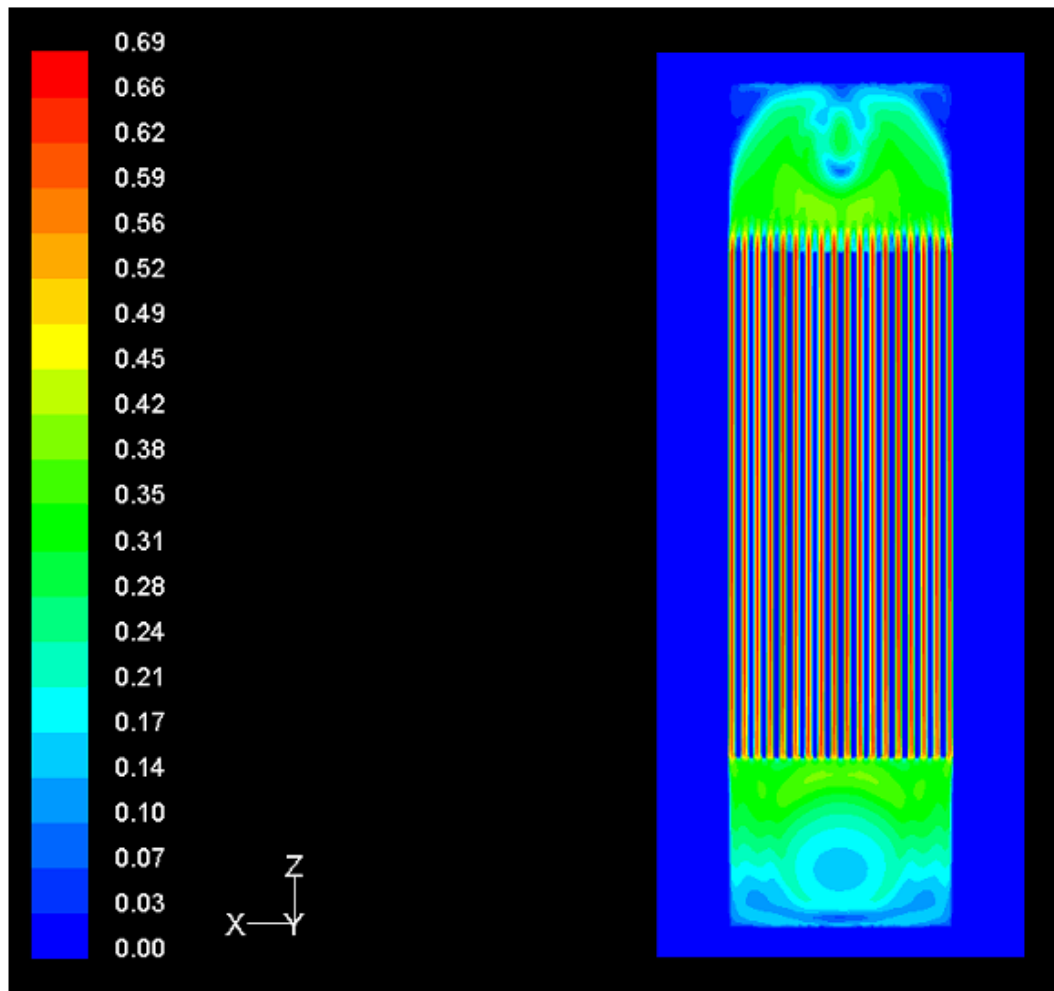


Figure 5.13 Velocity contours in (m/s) along horizontal mid-section (flow direction:  $\uparrow$ )

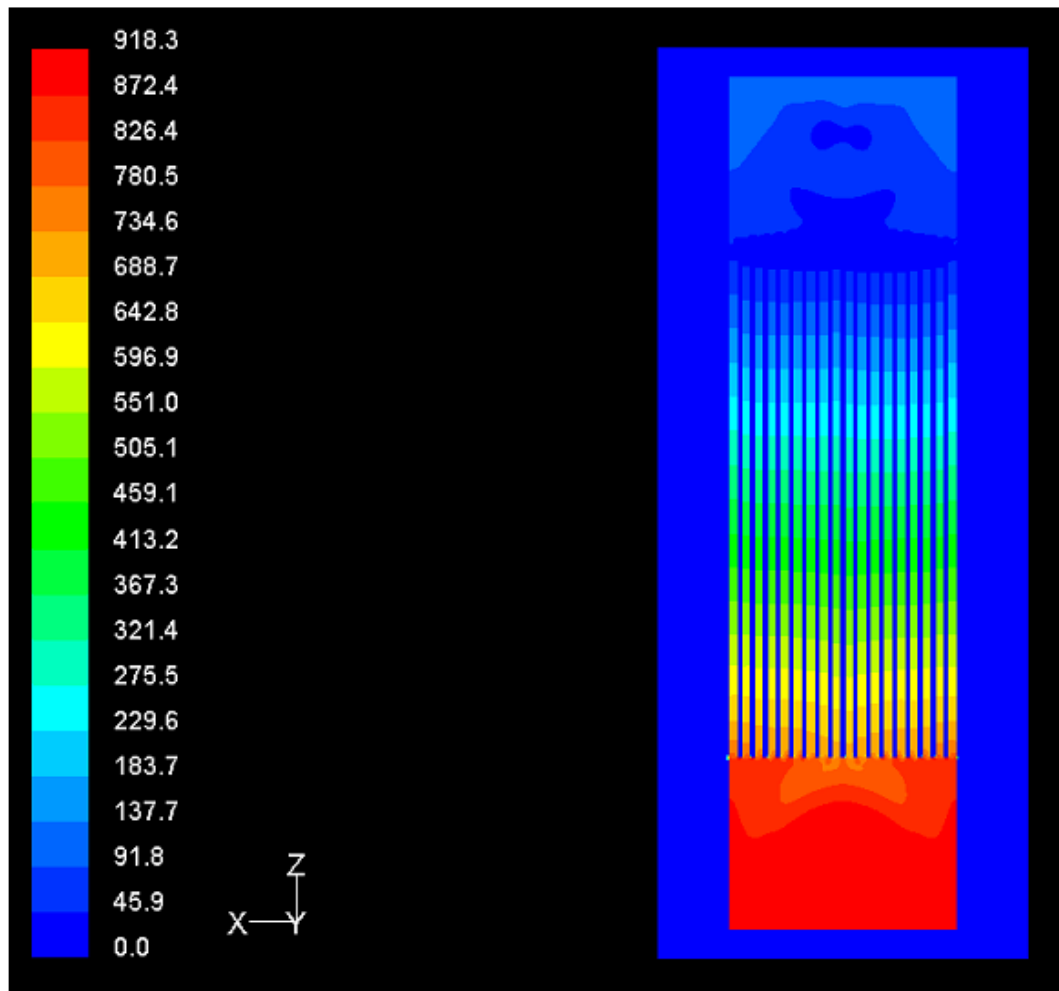


Figure 5.14 Pressure contours in (Pa) along horizontal mid-section (flow direction: ↑)

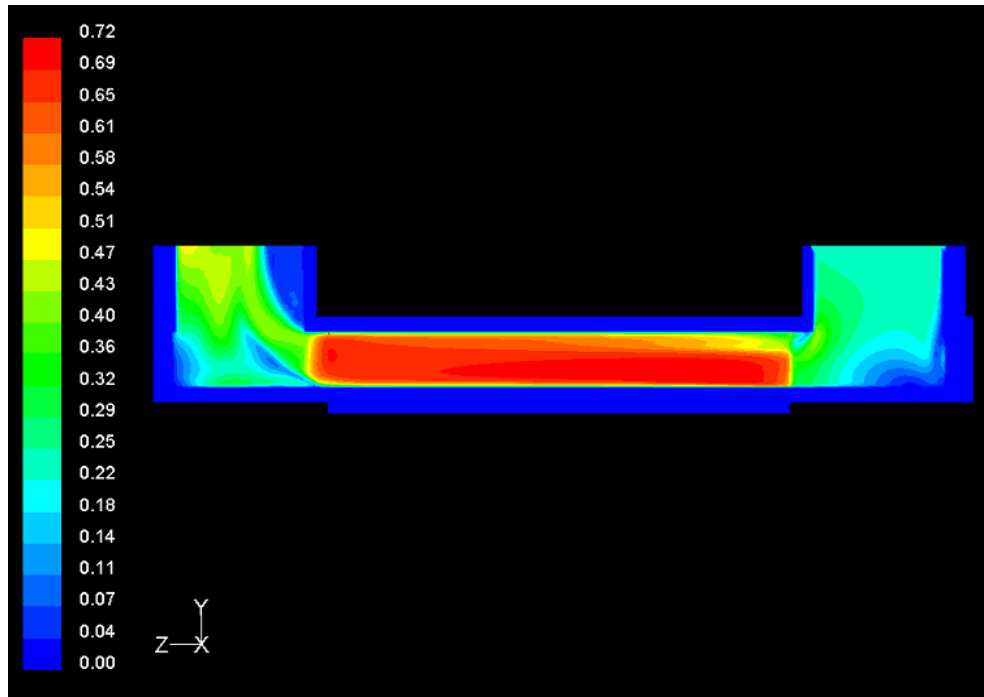


Figure 5.15 Velocity contours in (m/s) along vertical mid-section (flow direction:  $\leftarrow$ )

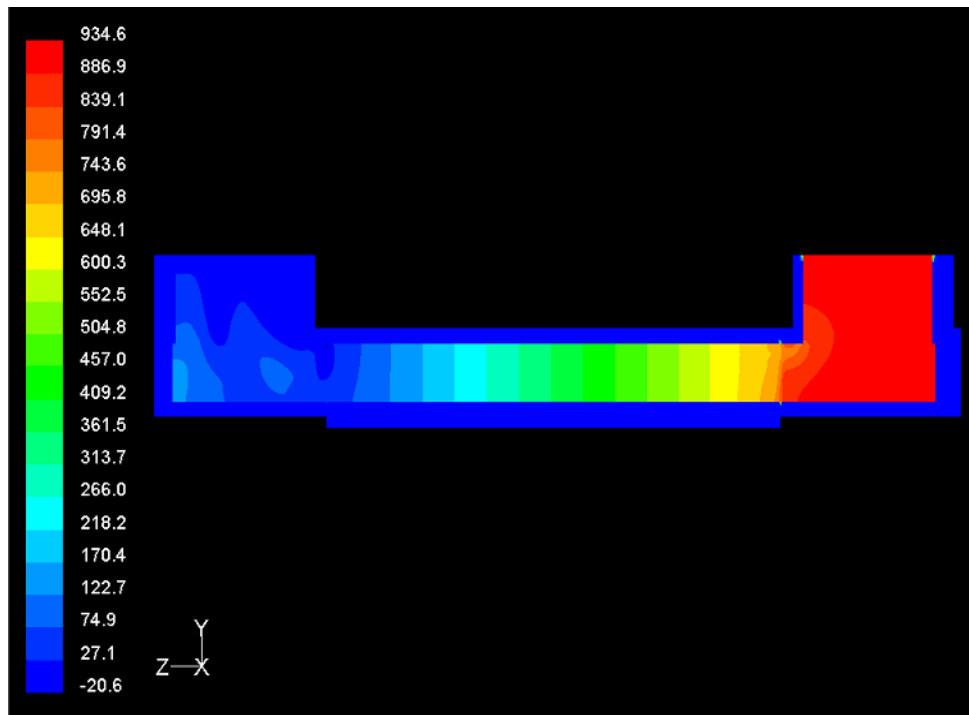


Figure 5.16 Pressure contours in (Pa) along vertical mid-section (flow direction:  $\leftarrow$ )

### 5.3.3 Heat Loss

It was stated previously in Section 4.2 that the estimated heat loss to the ambient air for coolant flow rates of 0.75 lpm and 1.00 lpm were under 10% of the total heat load input, and that actual values were expected to be even less. A view of the temperature contours of the external surfaces of the 500  $\mu\text{m}$  specimen for the simulation of 1.00 lpm coolant flow rate and 100  $\text{W}/\text{cm}^2$  local heat flux, given in Fig. 5.17, supports this result. It is seen that the top and side surfaces of the specimen remain virtually unheated in spite of the high local heat flux applied at the base. Assuming that the simulated result is representative of the actual behavior, it may be inferred that heat loss from these surfaces would be very small.

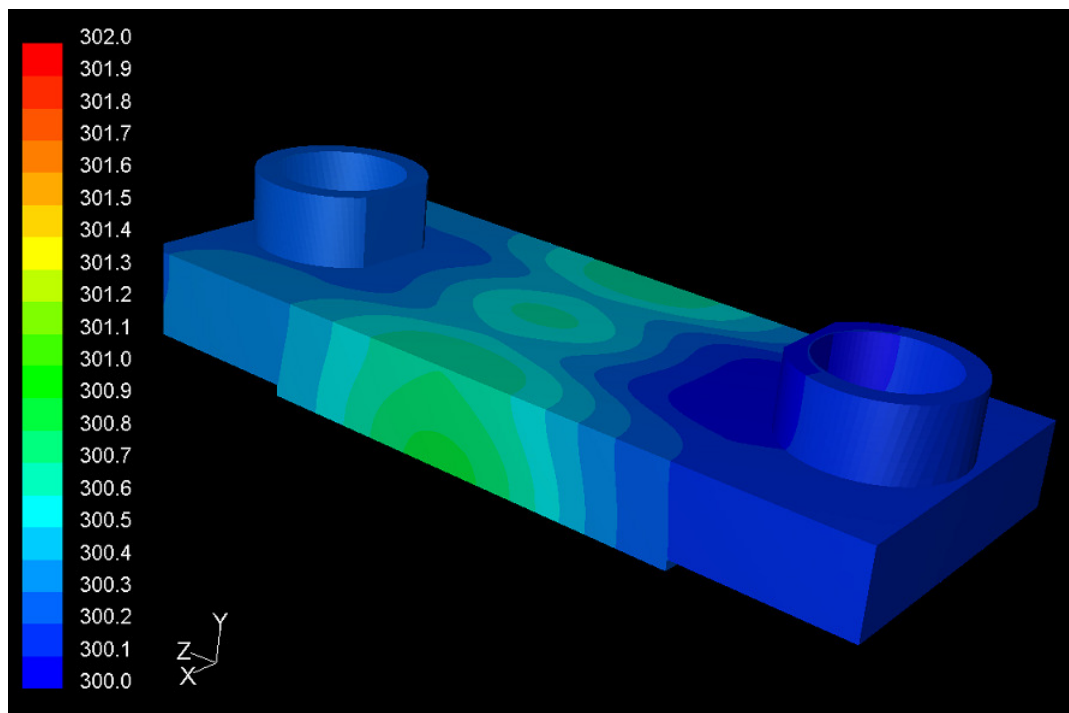


Figure 5.17 Temperature contours in (K) along external surfaces

### 5.3.4 Effect of Thermal Interface Layer

For the 500  $\mu\text{m}$  specimen simulated at 1.00 lpm coolant flow rate and  $100 \text{ W/cm}^2$  local heat flux, with a thermal interface layer of 0.3 mm, temperature contours along the vertical normal mid-section are given in Fig. 5.18. It is evident from the figure that much of the temperature rise between the heat load carrier and coolant occurs across the thermal interface layer.

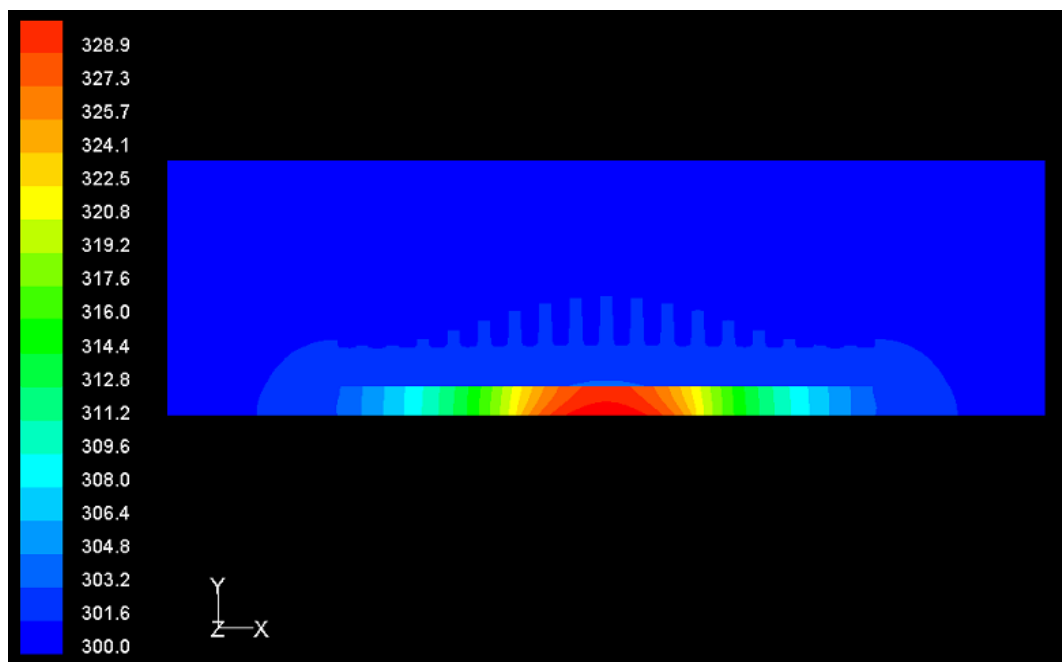


Figure 5.18 Temperature contours in (K) along vertical normal mid-section, with 0.3 mm TI

### 5.3.5 Effect of Localized Heat Load

A supplementary analysis was carried out for the 500  $\mu\text{m}$  specimen simulated at 1.00 lpm coolant flow without a thermal interface layer, but with a homogenous global heat flux of  $100 \text{ W/cm}^2$  applied evenly throughout the heat load carrier, instead of localized heat sources. Temperature contours along the vertical normal

mid-section for this simulation are given in Fig. 5.19. Comparison with Fig. 5.18 shows the lack of heat spreading along the carrier and heatsink base when the heat source is localized. Top views of the heatsinks for the two simulations without the TI layer are presented in Fig. 5.20 and 5.21 to show the difference in temperature contours along the heatsink surfaces. Fig. 5.22 shows the local concentration of high temperature regions on the heat load carrier when localized heat sources are employed.

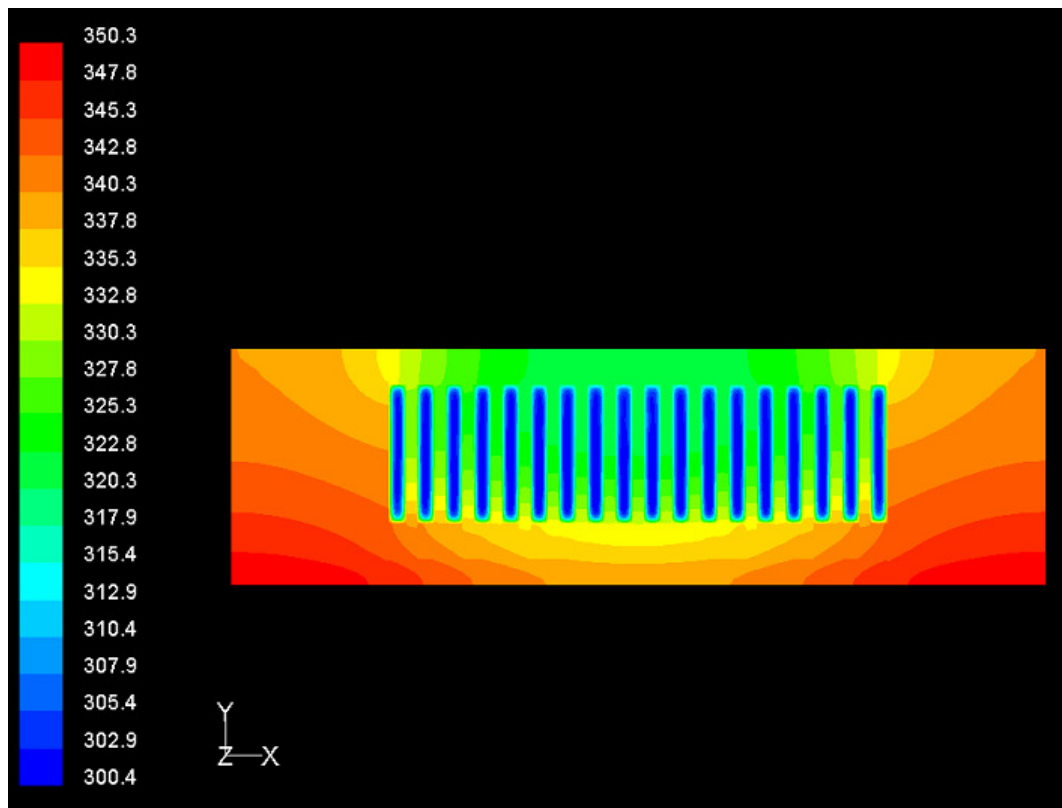


Figure 5.19 Temperature contours in (K) along vertical normal mid-section, without TI, with homogenous heat load

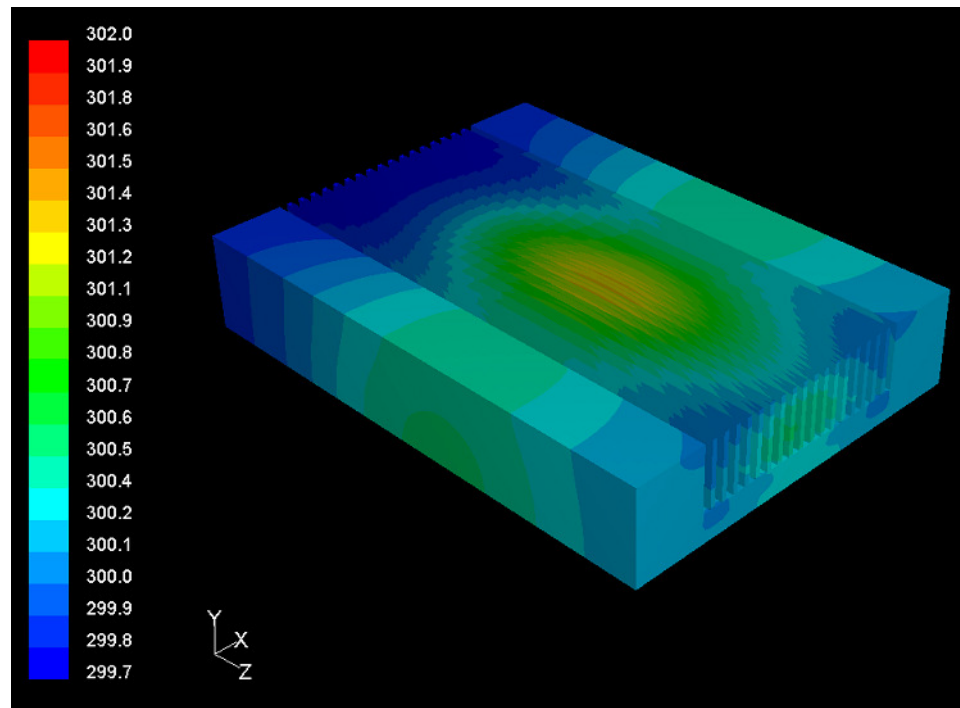


Figure 5.20 Temperature contours along heatsink surfaces, without TI, with localized heat load (K)

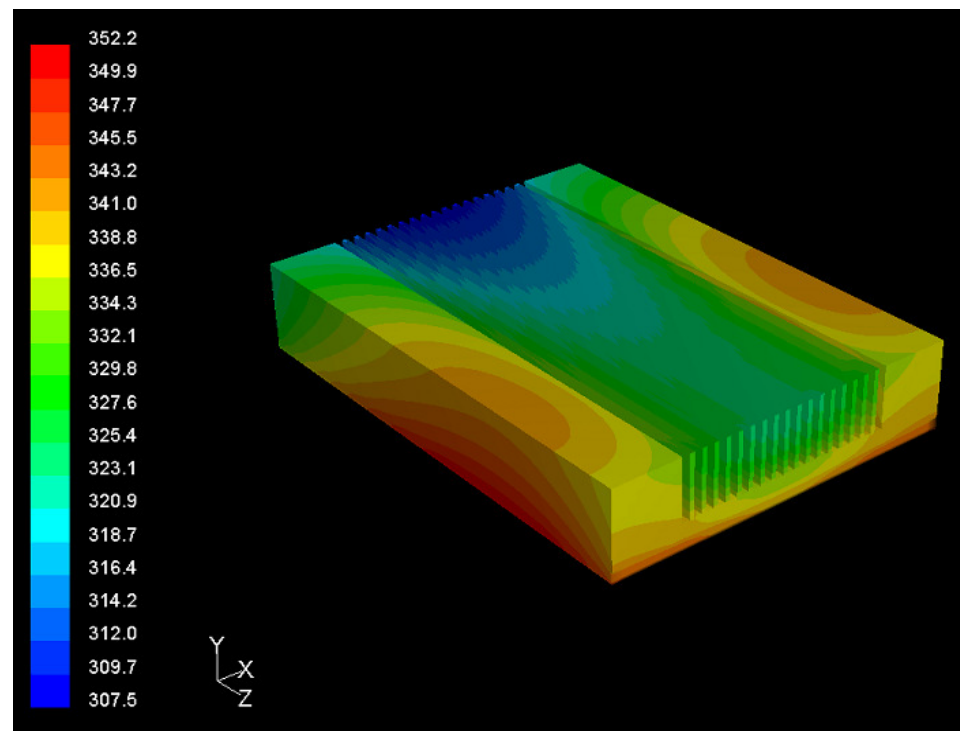


Figure 5.21 Temperature contours on heatsink surfaces, without TI, with homogenous heat load (K)

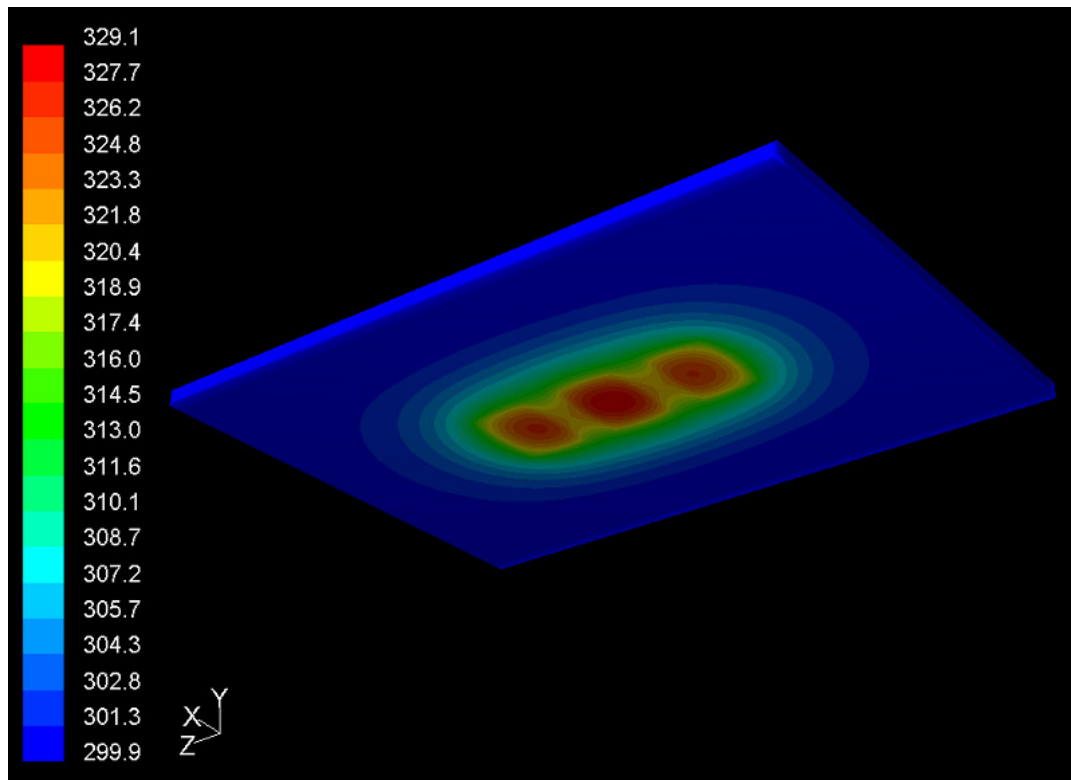


Figure 5.22 Temperature contours along heat load carrier, without TI, with localized heat load (K)

## CHAPTER 6

### DISCUSSION AND COMPARISON OF RESULTS

This chapter is devoted to the comparison of the results obtained from the experiments, numerical simulations, and analytical calculations among each other, and to the discussion of possible reasons for the particular trends observed.

#### 6.1 Comparison of Maximum Temperature Rise Results

The results obtained for Sensor 3 from experimental measurements, and the simulation results for the corresponding point obtained from CFD analyses using 0.2 mm and 0.3 mm TI effective thicknesses, are presented in graphical form for 1.00 lpm coolant flow rate and  $100 \text{ W/cm}^2$  local heat flux in Fig. 6.1 for copper specimens and in Fig. 6.2 for aluminum specimens. It is seen from Fig. 6.1 and Fig. 6.2 that there exists a striking difference in trend between the copper and aluminum specimens. The slopes of the maximum temperature rise variation trend of CFD results and experimental results for aluminum specimens are very close while the slope of the maximum temperature rise variation trend obtained from experimental results for copper specimens is significantly higher than that obtained from CFD results. This difference in behavior is attributed to the difference in material properties. Copper, being a softer material in comparison to aluminum, is more susceptible to imperfections resulting from manufacturing. Copper is also affected more greatly by the brazing operation in comparison to aluminum. It is thus suspected that the aluminum specimens have been more accurately modeled. It may be said, however, that the general linear increase trend is common for all output sets, apart from the experimental result obtained for the  $500 \text{ }\mu\text{m}$  copper specimen, which deviates markedly from the linear trend as seen in Fig. 6.1.

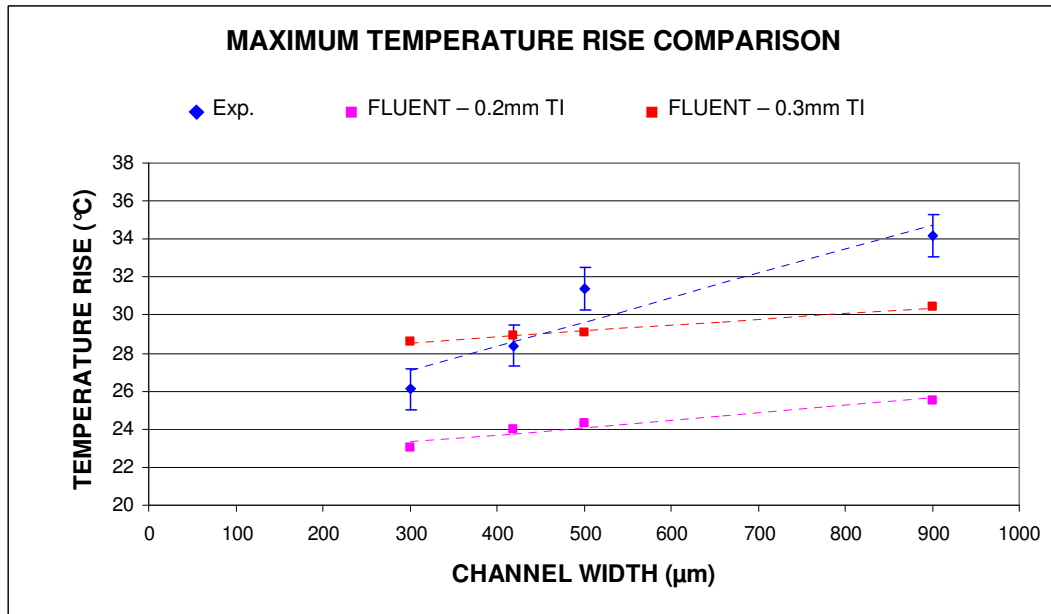


Figure 6.1: Comparison of maximum temperature rise for copper specimens

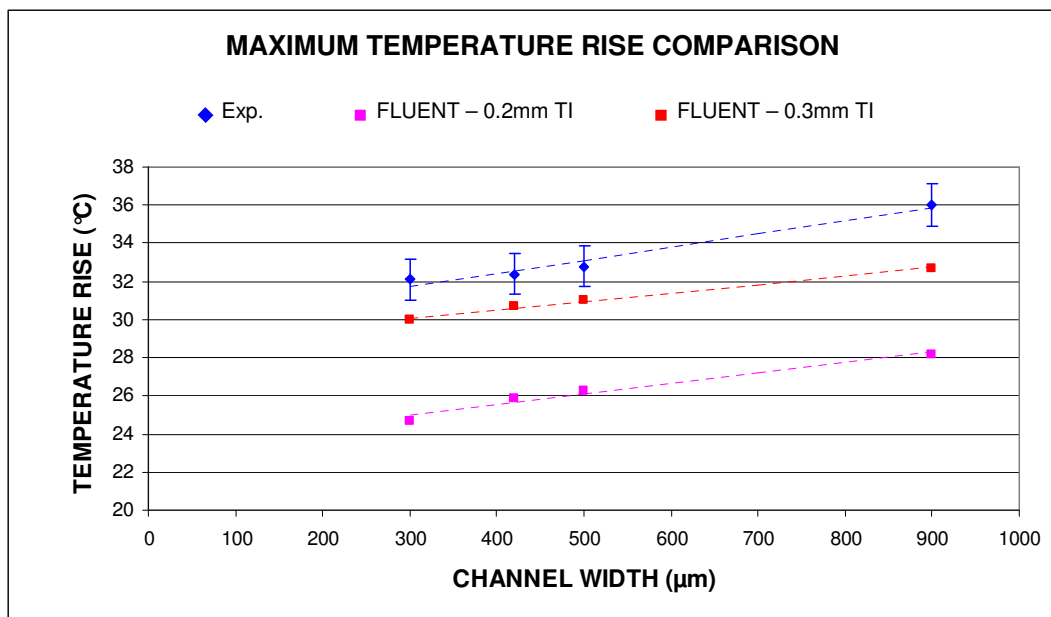


Figure 6.2: Comparison of maximum temperature rise for aluminum specimens

It is also evident from Fig. 6.1 and 6.2 that the experimental results are more closely predicted by CFD analyses incorporating the increased TI effective

thickness of 0.3 mm. This result emphasizes the importance of thermal interface layers on the thermal performance of cooling elements. It also shows that a 50% margin in the effective TI layer thickness is appropriate for the modeling of the test specimens of the present study.

## 6.2 Comparison of Average Temperature Rise Results

The average of the results obtained from all four temperature sensors from experimental measurements, and the average of the simulation results for the corresponding points obtained from CFD analyses using 0.2 mm and 0.3 mm TI effective thicknesses, are presented in graphical form for 1.00 lpm coolant flow rate and  $100 \text{ W/cm}^2$  local heat flux in Fig. 6.3 for copper specimens, and in Fig. 6.4 for aluminum specimens against the heatsink base temperature rise calculated analytically for these specimens.

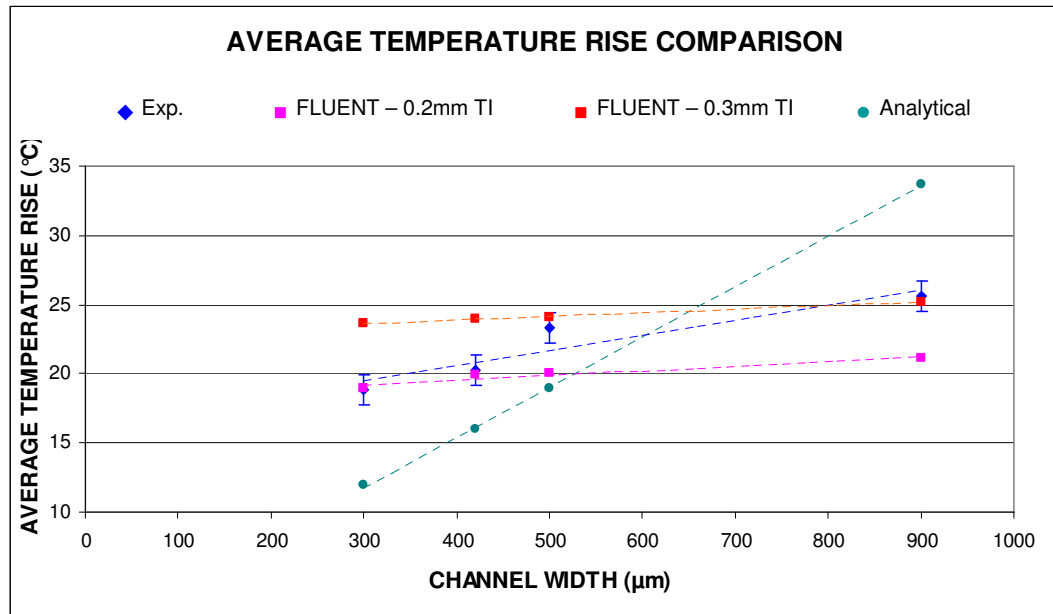


Figure 6.3: Comparison of average temperature rise for copper specimens

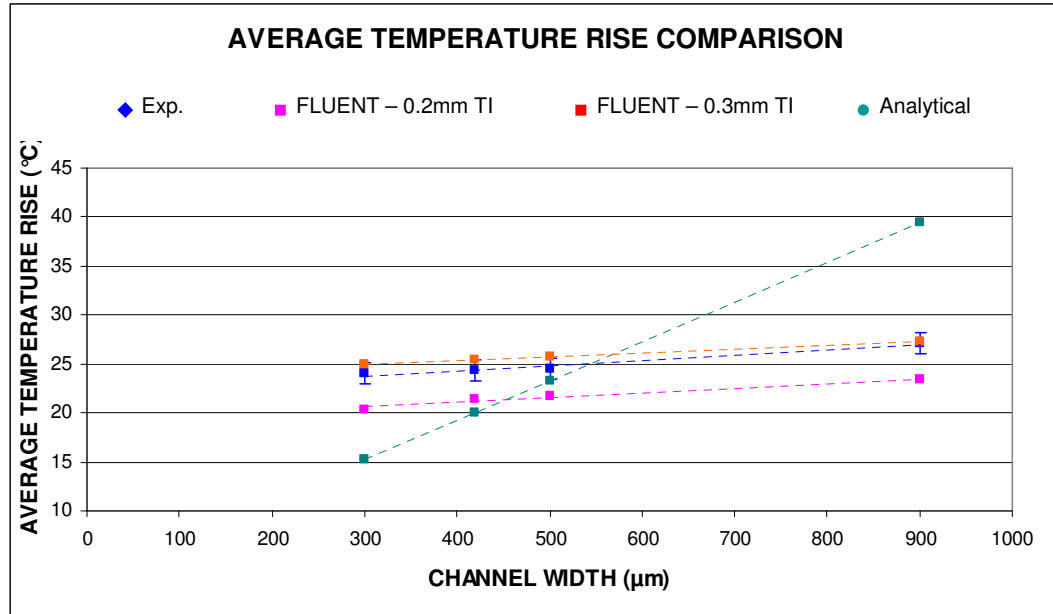


Figure 6.4: Comparison of average temperature rise for aluminum specimens

It is observed from Fig. 6.3 and Fig. 6.4 that the analytical predictions deviate very much from the CFD simulations and experimental results. This is attributed to the effect of localized heat sources. Due to the temperature rise associated with the spreading of heat from the attenuator groups along the heat load carrier, the experimental results and CFD simulations include the effect of *thermal spreading resistance* while the analytical calculation does not. Thermal spreading resistance is an agent of temperature rise that depends on the ratio of the cross sectional areas of heat generation and heat removal, and the thickness through which the change in area occurs. In the case of the test specimens, these parameters are, respectively, the surface area of the attenuator groups, the heatsink base area, and the thickness of the heat load carrier. Since these values are all the same for each of the test specimens, the temperature rise due to spreading resistance is expected to be essentially constant for all the specimens at a particular heat load and coolant flow rate. An inspection of Fig. 5.16 and 5.20 suggests that much of the temperature rise occurs within the heat load carrier and across the thermal interface layer, and that only a portion of the temperature rise occurs across the heatsink itself. Since the analytical calculation assumes only the temperature rise across the heatsink

itself, it is affected much more by the channel widths, resulting in a larger slope of the temperature rise with respect to the channel width. The quantitative deviation, on the other hand, is related also to the error due to the higher total heat power required to produce a homogenous heat flux of  $100 \text{ W/cm}^2$  along the entire heatsink base.

### 6.3 Comparison of Pressure Drop Results

A comparison of the pressure drop results for each of the specimens at 1 lpm coolant flow rate is given in graphical form in Fig. 6.5. It is seen that the CFD results and analytical calculation coincide perfectly, within an accuracy of 0.001 bar. The general trend of the experimental results is seen to agree fairly with the numerical and analytical prediction.

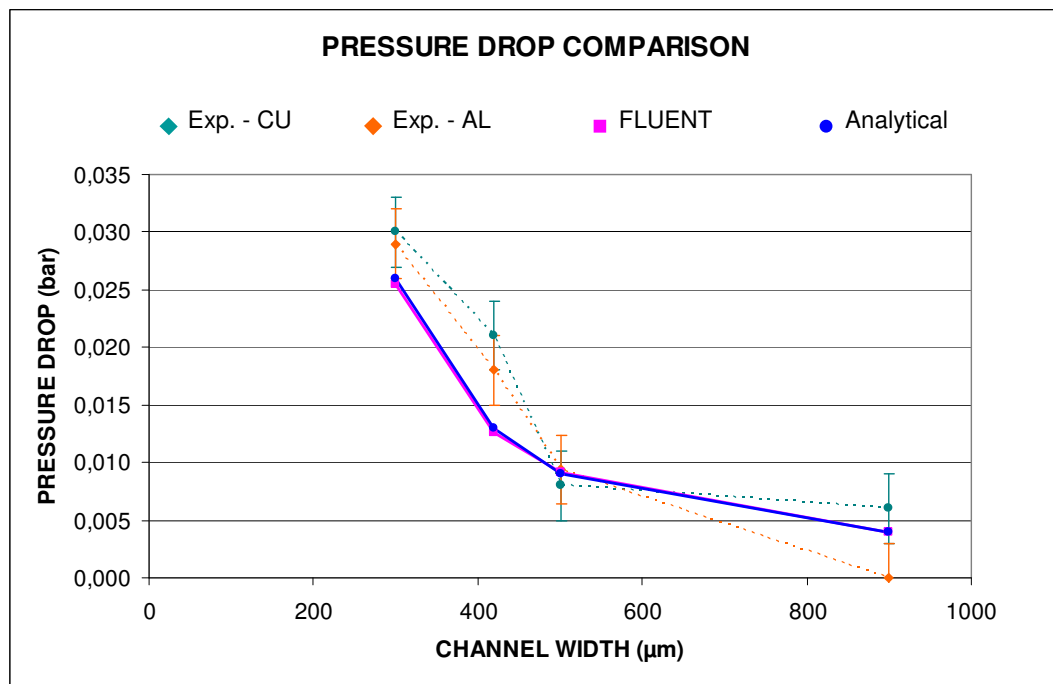


Figure 6.5: Comparison of pressure drop at 1 lpm coolant flow rate

## 6.4 Thermal Performance

The primary aim of the present study was to assess the cooling capabilities of various microchannel heatsinks for the thermal management of T/R modules in military phased array radar applications. Inspection of Table H.4 reveals that the best cooling performance obtained from the 300  $\mu\text{m}$  copper specimen at 1.00 lpm for 100  $\text{W}/\text{cm}^2$  local heat flux is characterized by a maximum temperature rise of 26.1  $^{\circ}\text{C}$ . For a military electronics cooling application, this is an acceptable temperature rise. For an ambient temperature upper limit of 55  $^{\circ}\text{C}$ , which is a commonly specified value in military application specifications, the maximum temperature of the chip carrier (corresponding to the heat load carrier of the present study) would be  $55 + 26.1 = 81.1$   $^{\circ}\text{C}$  if the 300  $\mu\text{m}$  copper specimen was employed as the cooling agent on a T/R module generating a local heat flux of 100  $\text{W}/\text{cm}^2$ , provided 1 lpm flow rate of water is available as a coolant at the ambient temperature. This would keep the T/R module surface within an acceptable safety margin of approximately 4  $^{\circ}\text{C}$  under the limit of 85  $^{\circ}\text{C}$  commonly imposed as the limit of reliable operation. Therefore, it may be said that the present study has verified a means of cooling for T/R modules generating up to 100  $\text{W}/\text{cm}^2$  within acceptable temperature limits, a capability previously not available to ASELSAN with conventional liquid cooling methods.

Another aspect worth consideration regarding thermal performance is the output of the thermally worst performing specimen, the 900  $\mu\text{m}$  aluminum specimen, in comparison to the 300  $\mu\text{m}$  copper specimen. With the maximum temperature rise given to be 36.0  $^{\circ}\text{C}$  from Table H.4, at 1.00 lpm coolant flow rate and 100  $\text{W}/\text{cm}^2$  local heat flux, it is seen that the difference in maximum temperature rise between the best and worst performing specimens is 43%, a substantial increase. Although a difference in the order of 5-10  $^{\circ}\text{C}$  in maximum temperature rise may not seem to be a very significant difference at a first glance, it is a difference that dictates whether or not a phased array radar will function reliably or not under the extreme environmental conditions required of military applications, and is a difference that

will be greatly amplified when heat loads are increased. It may be inferred from Table H.4 that among the specimens tested, copper specimens show a significant superiority compared to the aluminum specimens in terms of cooling capability, particularly for the smaller channel widths of 300  $\mu\text{m}$  and 420  $\mu\text{m}$  channel widths.

## 6.5 Comparison with Similar Studies in the Literature

A parameter commonly employed in evaluating the thermal performance of heatsinks is the concept of thermal resistance,  $R_{\text{HS}}$ , previously defined in Eq. 2.42. This parameter is useful in relating the total heat load applied to the heatsink base to the resulting temperature rise of the heatsink base with respect to the coolant fluid. However, when temperature measurements are taken on a heat load carrier supplying high local heat flux to the heatsink base, such as in the present study, the calculated value of  $R_{\text{HS}}$  will include not only the thermal resistance of the heatsink itself, but also the thermal resistance associated with the temperature rise due to heat spreading, ie., spreading resistance. The temperature rise due to the thermal interface material will also be included in this value. Therefore, due to the heating and temperature measurement methods employed in the present study in order to properly simulate an actual T/R module cooling application, it is appropriate to base thermal performance discussions on the heatsink – heat load carrier assembly, and not on the heatsink itself. To illustrate, the thermal resistance of the heatsink – heat load carrier assembly for the 300  $\mu\text{m}$  copper specimen may be calculated to be, based on Eq. 2.42,  $(26.1\text{ }^{\circ}\text{C})/(41.34\text{ W}) = 0.63\text{ }^{\circ}\text{C/W}$ . Although a one – to – one correspondence between the thermal path characteristics, and hence the implications of the  $R_{\text{HS}}$  value, does not exist between the present study and similar studies in the literature, an order – of – magnitude comparison may, nevertheless, be made. The study on cooling INTEL chips using microchannel heatsinks presented in the INTEL Technology Journal of 2005 [5] produced a thermal resistance of  $0.7\text{ }^{\circ}\text{C/W}$ , measured between the chip junction and coolant inlet, for a silicon heatsink with 25 channels of 300  $\mu\text{m}$  width, 180  $\mu\text{m}$  height, and 13 mm length. The heat load for this study was 70 W homogenous heat power on the chip

coupled with a local application of 1 W, while the water flow rate through the heatsink was 0.159 lpm. Although the measurement of thermal resistance in this study is quite different than that of the present study, being based on the chip junction temperature which includes the temperature rise due to the internal thermal resistances of the chip, it may be said that the overall output regarding thermal performance is consistent. The pressure drop of 0.06 bar for this study, however, was significantly higher than the measured value of the present study of 0.03 bar for the 300  $\mu\text{m}$  copper specimen at 1 lpm, possibly due to the much smaller channel height.

In another similar study aimed at cooling electronic packages by Zhang et al. [58], a thermal resistance of 0.59  $^{\circ}\text{C}/\text{W}$  was found between an FCPGA (Flip Chip Ball Grid Array) chip and the coolant inlet. The experimental setup was very similar to that of the present study in that water was used as the coolant at 1 lpm flow rate, the heatsink was of aluminum with 21 channels of 210  $\mu\text{m}$  width, 2 mm height and 50 mm length, a layer of thermal interface material was employed between the chip and heatsink, and the effect of heat spreading was included as the chip of 10 mm x 10 mm effective area was significantly smaller than the heatsink footprint area of 50 mm x 24 mm. The result of this study may also be said to be consistent with those of the present study in terms of thermal resistance. The pressure drop of this study, however, given to be 0.1 bar, is significantly higher than the measured value of the present study of 0.03 bar for the 300  $\mu\text{m}$  copper specimen at 1 lpm, possibly due to the smaller channel dimensions.

The study of Qu and Mudawar [48] on single phase microchannels is considered as a final example. Copper heatsinks with 21 channels of 213  $\mu\text{m}$  width, 713  $\mu\text{m}$  depth, and 10 mm length were used with water as the coolant at 0.35 lpm flow rate. An effective heat flux of 100  $\text{W}/\text{cm}^2$  was applied to the heatsink base of 10 mm x 44.8 mm base surface area by means of cartridge heaters. Temperature measurements were taken at four points along the length of the heatsink, as in the present study. Temperature rises of the measurement points with respect to the

coolant inlet were given to be between 18 °C and 31 °C. For the 300 µm copper specimen of the present study, the measured temperature rises on the heat load carrier ranged from 12 °C to 27.4 °C for 0.50 lpm coolant flow rate and 100 W/cm<sup>2</sup> local heat flux. A much higher pressure drop of 0.8 bar was measured in comparison to the value of 0.012 bar for the 300 µm copper specimen of the present study at 0.5 lpm, possibly due to the large difference in channel height.

## CHAPTER 7

### CONCLUSION

Experimental measurements and numerical simulations, using FLUENT<sup>®</sup> have been performed on copper and aluminum microchannel heatsinks of 300, 420, 500, and 900  $\mu\text{m}$  channel widths. The thermal performance characteristics of each of these specimens have been investigated experimentally and numerically at local heat fluxes as high as  $100 \text{ W/cm}^2$ , and coolant flow rates up to 1 lpm. A preliminary analytical calculation has also been performed.

#### 7.1 Agreement of Experimental, Numerical, and Analytical Results

Comparison of the results obtained show close agreement between experimental measurements and CFD simulations of temperature for the aluminum specimens, when an increased thermal interface layer effective thickness is employed in the CFD model to account for thermal interfaces that are not modeled, such as the bonding layer between the attenuators and heat load carrier, and the brazed interfaces. Fair agreement between experimental measurements and CFD simulations for the copper specimens, again for increased thermal interface layer effective thickness in the CFD model, has been observed. The larger deviations observed in copper specimens between experimental and numerical results are attributed to material properties such as greater susceptibility to imperfections and the enhanced negative effect of the brazing operation.

Analytical and numerical predictions for pressure drop are seen to coincide perfectly, as expected. It may be inferred from this result that the simplifying assumptions and choice of loss coefficients in the analytical solution are consistent

with the numerical solution of the Navier – Stokes equations using FLUENT<sup>®</sup>. Excluding the measurements for 900  $\mu\text{m}$  specimens, which were suspected to be unreliable, it may be stated that the numerical and analytical predictions for pressure drop agree fairly well with experimental measurements. It is concluded that, as long as material characteristics and uncontrolled thermal phenomena such as the temperature rise across miscellaneous thermal interfaces are properly accounted for, thermal performance of liquid cooled microchannel heatsinks may be predicted to a reasonable extent by using commercially available CFD software such as FLUENT<sup>®</sup>, while pressure drops may be predicted equally well by simple analytical calculations as well as CFD software.

The analytical calculation performed for temperature rise, assuming a homogenous heat source and not including thermal interfaces, produced results that showed significant deviation from experimental and numerical results. This deviation is attributed to the effects of localized heat sources and thermal interfaces. It is concluded that such a simplified analytical approach is not appropriate in predicting the thermal performance of microchannel heatsinks with localized, high flux heat sources and numerous thermal interfaces.

## **7.2 Effect of Thermal Interface Layer and Localized Heat Sources**

The effect of the thermal interface layer on thermal characteristics of microchannel heatsinks has been found to be very significant. Much of the temperature rise measured between the heat load carrier and coolant inlet of the test specimens occurs across the thermal interface layer. Thermal spreading resistance due to localized heat sources also adds to the total temperature rise, shadowing the enhanced cooling abilities of the microchannel heatsinks. Although the thermal performance of the microchannel heatsink specimens is greatly diminished by the temperature rise caused by thermal interface layers and thermal spreading resistance, these are unavoidable phenomena inherent in electronics cooling

applications. Presence of their effect is, therefore, required to properly simulate actual T/R module applications.

### **7.3 Critic of The Experimental Setup**

Care was taken to construct the experimental setup so as to resemble an actual T/R module cooling application as closely as possible. This was achieved by incorporating thermally active electronic components onto a copper-tungsten carrier equipped with temperature sensors to simulate the heat load, which resulted in a structure very close to actual T/R modules in which electronic chips are mounted on copper-tungsten carriers and monitored by temperature sensors placed on the carriers. Therefore, it may be said that the heat load component of the experimental setup simulated a real life electronics cooling application very well. However, this advantage also caused a number of problems. The fragility of the heat load carrier caused a frequent need of maintenance, the large currents carried by the wires made voltage measurements difficult, the grounding necessity of the circuit caused inconvenience during measurement, and the susceptibility of the temperature sensors mounted on the heat load carrier to electromagnetic interference effects (EMI) required the rotary elements of the experimental setup, such as the pump and fan, to be placed in an isolated chamber. The use of thin film resistance heaters, as is widely encountered in the literature, may have been more convenient but would have had a negative impact on the resemblance of the system to an actual T/R module cooling application.

Although the pressure transducers and thermocouples used for measuring temperature and pressure at the test specimen inlet and outlets were of high accuracy, they had to be placed a distance of approximately 4 cm away from the heatsink inlet and outlet sections due to physical restrictions. This led to some measurement error. The pressure drop caused by quick coupling fluid connectors at the heatsink inlet and outlet sections, although compensated for to some extent, also caused some measurement error.

## 7.4 Thermal Performance

The cooling capabilities of copper specimens tested are seen to be consistently superior to aluminum specimens, and should be preferred when critical heat fluxes require cooling. In terms of thermal performance, it is concluded that the 300  $\mu\text{m}$  and 420  $\mu\text{m}$  copper specimens, which provided significantly superior performance in comparison to the remaining specimens, are suitable for use in military phased array radar cooling applications with local heat fluxes as high as  $100 \text{ W/cm}^2$ . The measured maximum temperature rise of  $26.1^\circ\text{C}$  at 1 lpm coolant flow rate for the best thermally performing specimen, the 300  $\mu\text{m}$  copper specimen, at this local heat flux yields a thermal resistance of  $0.63^\circ\text{C/W}$ . The measured pressure drop across this specimen at 1 lpm coolant flow rate is 0.03 bar, a very low pressure drop that can easily be handled with a compact pump.

Comparison of the results of the present study with similar studies in the literature with respect to thermal resistances and measured temperature rises have yielded general consistency, while results of pressure drop showed significant departure, possibly due to differences in channel dimensions and flow rates employed in these studies. Unfortunately, although a large number of studies and single phase microchannel flow and heat transfer are available in the literature, very few are based on specific cooling applications such as the T/R module cooling application of the present study, while the majority of studies focus on general thermal and hydrodynamic characteristics such as channel Nusselt number and friction factor. Although these studies are very useful in understanding the thermohydraulic behavior of microchannel heatsinks, they do not provide solid output that can provide guidance for actual cooling applications. The comparison opportunities of the present study with similar studies in terms of performance have, therefore, been limited.

In general, the present study has pioneered the use of microchannel heatsinks for electronics cooling, and has enabled ASELSAN to confidently apply this

technology to coming radar projects. Especially the low pressure drops associated with the high cooling capabilities of the 300  $\mu\text{m}$  and 420  $\mu\text{m}$  copper specimens have made possible the design of long arrays of microchannel heatsinks for the cooling of phased array radars, in which hundreds of T/R modules are often packed closely together, without pushing the limits of size constraints and pressure safety margins.

## **7.5 Future Work**

Although the present study has produced satisfactory results as a pioneering study in the field of microchannel cooling technology in Turkey, much additional work is required to reach state-of-the art quality. Possible improvements regarding the experimental setup are redesigning the heat load component, possibly using thin-film deposition, to yield a simpler and more reliable component; and machining sensor taps directly into the heatsink inlet and outlet sections to allow for accurate temperature and measurements at the microchannel inlet and outlets. Smaller temperature sensors of greater accuracy may also be used to allow for better temperature measurements. Further work may include repeating the experiments with more than one sample of each specimen to judge the repeatability of the experiments, and extending the test variables to include different coolants such as ethylene-glycol and potassium-formate, repeating the whole set of experiments following completion of the suggested experimental setup improvements.

## REFERENCES

1. R.P. Feynman, "There's Plenty of Room at the Bottom", Miniaturization, H.D. Gilbert, ed., 282-296, Reinhold Publishing, New York, 1961
2. D.B. Tuckerman, R.F.W. Pease, "High-Performance Heat Sinking for VLSI", IEEE Electron Device Letters, Vol. EDL-2, No.5, 1981
3. M. Gad-el-Hak, "The Fluid Mechanics of Microdevices – The Freeman Scholar Lecture", Journal of Fluids Engineering, Vol.121, pp.5-33, 1999
4. D. Bharathan, K. Gawlik, B. Kramer, S. Rogers, T.J. Hendricks, "Advanced Power Electronics - Thermal Management", National Renewable Energy Laboratory (NREL) Publications, [http://www.nrel.gov/vehiclesandfuels/powerelectronics/pdfs/advanced\\_power\\_electronics\\_thermal\\_mgmt.pdf](http://www.nrel.gov/vehiclesandfuels/powerelectronics/pdfs/advanced_power_electronics_thermal_mgmt.pdf), 2003
5. R.S. Prasher, J. Chang, I. Sauciu, S. Narasimhan, D. Chau, D. G. Chrysler, A. Myers, S. Prstic, C. Hu, C., "Nano and Micro Technology-Based Next-Generation Package-Level Cooling Solutions", INTEL Technology Journal Vol.9, pp.285-296, 2005
6. Lytron™ Application Note and Product Catalogue, [www.lytron.com](http://www.lytron.com), 2007
7. D. Tylton, "CoolCon™ 2004 SprayCool Applications Presentation", [www.vita.com/cool/pres-2004/1430-tylton.pdf](http://www.vita.com/cool/pres-2004/1430-tylton.pdf), 2004
8. Melcor™ Product Catalogue, [www.melcor.com](http://www.melcor.com), 2007
9. F.M. White, "Viscous Fluid Flow", 2<sup>nd</sup> edition., McGraw-Hill, New York, 1991
10. R.K. Shah, A.L. London, "Laminar Flow Forced Convection in Ducts, Supplement 1 to Advances in Heat Transfer", Academic Press, New York, 1978
11. H. Herwig, S.P. Mahulikar, "Variable Property Effects in Single-Phase Incompressible Flows Through Microchannels", International Journal of Thermal Sciences Vol.45, pp.977-981, 2006
12. M.E. Steinke, S.G. Kandlikar, "Single-Phase Liquid Friction Factors in Microchannels", International Journal of Thermal Sciences, Vol.45, pp.1073-1083, 2006

13. S.G. Kandlikar, S. Garimella, D. Li, S. Colin, M.R. King, "Heat Transfer and Fluid Flow in Minichannels and Microchannels", Elsevier, Oxford, 2006
14. R.J. Philips, "Forced Convection in Liquid Cooled, Microchannel Heatsinks", MS Thesis, Department of Mechanical Engineering, Massachusetts Institute of Technology, 1987
15. O.C. Jones, "An Improvement in the Calculation of Turbulent Friction in Rectangular Ducts", Journal of Fluid Engineering, Vol.98, pp.173-181, 1976
16. B.R. Munson, D.F. Young, T.H. Okiishi, "Fundamentals of Fluid Mechanics", 5<sup>th</sup> edition, John Wiley & Sons, Indianapolis, 2006
17. W.M. Kays, A.L. London, "Compact Heat Exchangers", McGraw-Hill, New York, 1984
18. F.P. Incropera, D.P. DeWitt, "Fundamentals of Heat and Mass Transfer", 5<sup>th</sup> edition, John Wiley & Sons, Indianapolis, 2002
19. S.S Mehendale, A.M. Jacobi, R.K. Shah, "Fluid Flow and Heat Transfer at Micro- and Meso-scales with Application to Heat Exchanger Design," Applied Mechanics Reviews, Vol.53, pp.175-193, 2000
20. S.G. Kandlikar, W.J. Grande, "Evolution of Microchannel Flow Passages – Thermohydraulic Performance and Fabrication Technology", Heat Transfer Engineering, Vol.24, pp.3-17, 2003
21. N.T. Obot, "Toward a Better Understanding of Friction and Heat/Mass Transfer in Microchannels – A Literature Review", Microscale Thermophysical Engineering, Vol.6, pp.155-173, 2003
22. M. Bahrami, M.M. Jovanovich, "Pressure Drop of Fully Developed Laminar Flow in Microchannels of Arbitrary Cross-Section", Journal of Fluids Engineering, Vol.128, pp.1036-1044, 2006
23. M. Bahrami, M.M. Jovanovich, J.R. Culham, "Pressure Drop of Fully Developed, Laminar Flow in Rough Microtubes", Journal of Fluids Engineering, Vol.128, pp.632-637, 2006
24. T. Bayraktar, S.B. Pidugu, "Characterization of Liquid Flows in Microfluidic Systems", International Journal of Heat and Mass Transfer, Vol.49, pp.815-824, 2006

25. R.W. Barber, D.R. Emerson, "Challenges in Modeling Gas-Phase Flow in Microchannels: From Slip to Transition", *Heat Transfer Engineering*, Vol.27, pp.3-12, 2006
26. R.G. Deissler, "An Analysis of Second-Order Slip Flow and Temperature-Jump Boundary Conditions for Rarefied Gases", *International Journal of Heat and Mass Transfer*, Vol.7, pp.681-694, 1964
27. A. Beşkök, G.E. Karniadakis, "A Model for Flows in Channels, Pipes, and Ducts at Micro and Nano Scales", *Microscale Thermophysical Engineering*, Vol.3, pp.43-77, 1999
28. H. Xue, Q. Fan, "A New Analytic Solution of the Navier-Stokes Equations for Microchannel Flows", *Microscale Thermophysical Engineering*, Vol.4, pp.125-143, 2000
29. D. Jie, X. Diao, K.B. Cheong, L.K. Yong, "Navier Stokes Simulations of Gas Flows in Micro Devices", *Journal of Micromechanics and Microengineering*, Vol.10, pp.372-379, 2000
30. D.A. Lockerby, J.M. Reese, D.R. Emerson, R.W. Barber, "Velocity Boundary Condition at Solid Walls in Rarefied Gas Calculations", *Physical Review E*, Vol.70, 017303, 2004
31. W. Loose, S. Hess, "Rheology of Dense Fluids via Nonequilibrium Molecular Hydrodynamics: Shear Thinning and Ordering Transition", *Rheologica Acta*, Vol.28, pp.91-101, 1989
32. J.N. Israelachvili, "Measurement of the Viscosity of Liquids in Very Thin Films", *Journal of Colloid and Interface Science*, Vol.110, pp.263-271, 1986
33. M.L. Gee, P.M. McGuiggan, J.N. Israelachvili, A.M. Homola, "Liquid to Solidlike Transitions of Molecularly Thin Films under Shear", *Journal of Chemical Physics*, Vol.93, pp.1895-1906, 1990
34. W. Que, G.M. Mala, D. Li, "Pressure-Driven Water Flows in Trapezoidal Silicon Microchannels", *International Journal of Heat and Mass Transfer*, Vol.43, pp.353-364, 2000
35. J. Koo, C. Kleinstreuer, "Liquid Flow in Microchannels: Experimental Observations and Computational Analyses of Microfluidics Effects", *Journal of Micromechanics and Microengineering*, Vol.13, pp.568-579, 2003

36. J. Dirker, "Heat Eextraction from Solid-State Electronics by Embedded Solids With Application to Integrated Power Electronic Passive Modules", Ph.D thesis, University of Johannesburg
37. L.J. Missagia, J.N. Walpole, Z.L. Liao, R.J. Philips, "Microchannel Heatsinks for Two-Dimensional High-Power-Density Diode Laser Arrays", IEEE Journal of Quantum Electronics, Vol.25, pp.1988-1992, 1989
38. R.A. Riddle, R.J. Contolini, R.F. Bernhardt, "Design Claculations for the Microchannel Heatsink", Proc. National Electronic Packaging Conference – Technical Program, Vol.1, pp.161-171, 1991
39. X.F. Peng, B.X. Wang, G.P. Peterson, H.B. Ma, "Experimental Investigation of Heat Transfer in Flat Plates with Rectangular Microchannels", International Journal of Heat and Mass Transfer, Vol.38, pp.127-137, 1995
40. M.M. Rahman, F. Gui, "Experimental Measurements of Fluid Flow and Heat Transfer in Microchannel Cooling Passages in a Chip Substrate", Proc. ASME International Electronics Packaging Conference, Vol.4-2, pp.685-692, 1993
41. B.X. Wang and X.F. Peng, "Experimental Investigation on Liquid Forced Convection Heat Transfer Through Microchannels", International Journal of Heat and Mass Transfer, Vol.37, pp.73-82, 199
42. G. Hetsroni, A. Mosyak, E. Pogrebnyak, L.P. Yarin, "Fluid Flow in Microchannels", International Journal of Heat and Mass Transfer, Vol.48, pp.1982-1998, 2005
43. X.F Peng and G.P. Peterson, "The Effect of Thermofluid and Geometrical Parameters on Convection of Liquids through Rectangular Microchannels", International Journal of Heat and Mass Transfer, Vol.38, pp.755-758, 1995
44. T.M. Adams, S.I. Abdel Khalik, S.M. Jeter, Z.H. Qureshi, "An Experimental Investigation of Single-Phase Forced Convection in Microchannels", International Journal of Heat and Mass Transfer, Vol.41, pp.851-857, 1998
45. T.M. Adams, M.F. Dowling, S.I. Abdel Khalik, S.M. Jeter, "Applicability of Standard Turbulent Single Phase Forced Convection Correlations to Non-Circular Channels", International Journal of Heat and Mass Transfer, Vol.42, pp.4411-4415, 1999
46. M.N Sabry, "Scale Effects on Liquid Flow and Heat Transfer", Proc. Conference Therminice, pp.193-198, 1999

47. G.M. Mala, D. Li, "Flow Characteristics of Water in Microtubes", *International Journal of Heat and Fluid Flow* Vol.20, pp. 142-148, 1999
48. Q. Weilin, G.M. Mala and D. Li, "Pressure-Driven Water Flows in Trapezoidal Silicon Microchannels", *International Journal of Heat and Mass Transfer* Vol.43, pp.353-364, 2000
49. B. Xu, K.T Ooi, N.T. Wong, "Experimental Investigation of Flow Friction for Liquid Flow in Microchannels", *International Communications in Heat and Mass Transfer*, Vol 27, pp.1165–1176, 2000
50. D. Pfund, D. Rector, A. Shekarritz, A. Popescu, J. Welty, "Pressure Drop Measurements in a Microchannel", *Fluid Mechanics and Transport Phenomena*, Vol.46, no.8, 2000
51. W. Qu, I. Mudawar, "Experimental and Numerical Study of Pressure Drop and Heat Transfer in a Single-Phase Micro-Channel Heat Sink", *International Journal of Heat and Mass Transfer*, Vol.45, pp.2549-2565, 2002
52. P. Gao, S. Le Person, M. Favre-Marinet, "Scale Effects on Hydrodynamics and Heat Transfer in Two-Dimensional Mini and Microchannels", *International Journal of Thermal Sciences*, Vol.41, pp.1017-1027, 2002
53. D.A. Sinton, D. Li, "Microfluidic Velocimetry with Near-Wall Resolution", *International Journal of Thermal Sciences*, Vol.42, pp.847-855, 2003
54. C.Y. Yang, J.C. Wu, H.T. Chien, S.R. Lu, "Friction Characteristics of Water, R-134a, and Air in Small Tubes", *Microscale Thermophysical Engineering*, Vol.7, pp.335-348, 2003
55. H.Y. Wu, P. Cheng, "Friction Factors in Trapezoidal Silicon Microchannels with Different Aspect Ratios", *International Journal of Heat and Mass Transfer*, Vol.46, pp.2519-2525, 2003
56. H.B. Ma, G.P. Peterson, "Laminar Friction Factor in Microscale Ducts of Irregular Cross Section", *Microscale Thermophysical Engineering*, Vol.1, pp.253-265, 1997
57. D. Lelea, S. Nishio, K. Takano, "The Experimental Research on Microtube Heat Transfer and Fluid Flow of Distilled Water", *International Journal of Heat and Mass Transfer*, Vol.47, pp.2817-2830, 2004
58. P.S. Lee, S.V. Garimella, D. Liu, "Investigation of Heat Transfer in Rectangular Microchannels", *International Journal of Heat and Mass Transfer*, Vol.48, pp.1688-1704, 2005

59. S. Reynaud, F. Debray, J.P. Franc, T. Maitre, "Hydrodynamics and Heat Transfer in Two-Dimensional Minichannels", *International Journal of Heat and Mass Transfer*, Vol.48, pp.3197-3211, 2005
60. M.J. Kohl, S.I. Abdel-Khalik, S.M. Jeter, D.L. Sadowski, "An Experimental Investigation of Microchannel Flow with Internal Pressure Measurements", *International Journal of Heat and Mass Transfer*, Vol.48, pp.1518-1533, 2005
61. H.Y. Zhang, D. Pinjala, T.N. Wong, K.C. Toh, Y.K. Joshi, "Single-Phase Liquid Cooled Microchannel Heat Sink for Electronic Packages", *Applied Thermal Engineering*, Vol.25, pp.1472-1487, 2005
62. G.P. Celata, M. Cumo, S. McPhail, G. Zummo, "Characterization of Fluid Dynamic Behaviour and Channel Wall Effects in Microtube", *International Journal of Heat and Fluid Flow*, Vol.27, pp.135-143, 2006
63. M.E. Steinke, S.G. Kandlikar, J.H. Magerlein, E.G. Colgan, A.D. Raisanen, "Development of an Experimental Facility for Investigating Single-Phase Liquid Flow in Microchannels", *Heat Transfer Engineering*, Vol.27, pp.41-52, 2006
64. H. Li, M.G. Olsen, "MicroPIV Measurements of Turbulent Flow in Square Microchannels with Hydraulic Diameters from 200 $\mu\text{m}$  to 640 $\mu\text{m}$ ", *International Journal of Heat and Fluid Flow*, Vol.27, pp.123-134, 2006
65. H. Schlichting, "Boundary Layer Theory", McGraw-Hill, New York, 1955
66. Z. Li, Y.L. He, G.H. Tang, W.Q. Tao, "Experimental and Numerical Studies of Liquid Flow and Heat Transfer in Microtubes", *International Journal of Heat and Mass Transfer*, Vol.50, pp.3447-3460, 2007
67. P. Hrnjak, X. Tu, "Single Phase Pressure Drop in Microchannels", *International Journal of Heat and Fluid Flow*, Vol.28, pp.2-14, 2007
68. D. Costaschuk, J. Elsnab, S. Petersen, J.C. Klewicki, T. Ameel, "Axial Static Pressure Measurements of Water Flow in a Rectangular Microchannel", *Journal of Experimental Fluids*, Vol.10, pp. 348-360, 2007
69. Y. Mishan, A. Mosyak, E. Pogrebnyak, G. Hetsroni, "Effect of Developing Flow and Thermal Regime on Momentum and Heat Transfer in Micro-Scale Heat Sink", *International Journal of Heat and Mass Transfer*, Vol.50, pp.3100-3114, 2007
70. C.Y. Zhao, T.J. Lu, "Analysis of Microchannel Heat Sinks for Electronics Cooling", *International Journal of Heat and Mass Transfer*, Vol.45, pp.4857-4869, 2002

71. S. Belhardj, S. Mimouni, A. Saidane, M. Benzohra, "Using Microchannels to Cool Microprocessors: A Transmission Line Matrix Study", *Microelectronics Journal*, Vol.34, pp.247-253, 2003
72. T. Smy, D. Walkey, S.K. Dew, "Transient 3D Heat Flow Analysis for Integrated Circuit Devices Using the Transmission Line Matrix Method on a Quad Tree Mesh", *Solid State Electronics*, Vol.45, pp.1137-1148, 2001
73. A. Kucaba-Pietal, "Microchannels Flow Modeling with the Micropolar Fluid Theory", *Bulletin of the Polish Academy of Technical Sciences*, Vol.52, pp.209-214, 1999
74. J. Koo, C. Kleinstreuer, "Viscous Dissipation Effects in Microtubes and Microchannels", *International Journal of Heat and Mass Transfer*, Vol.47, pp.3159-3169, 2004
75. J. Judy, D. Maynes, B. Webb, "Characterization of Frictional Pressure Drop for Liquid Flows Through Microchannels", *International Journal of Heat and Mass Transfer*, Vol.45, pp.3477-3489, 2002
76. J. Koo, C. Kleinstreuer, "Analyses of Liquid Flow in Micro-Conduits", *Proc. Second International Conference on Microchannels and Minichannels*, Vol.1, pp.191-198, 2004
77. Z. Guo, Z. Li, "Size Effect on Microscale Single-Phase Flow and Heat Transfer", *International Journal of Heat and Mass Transfer*, Vol.46, pp.149-159, 2003
78. G. Gamrat, M. Favre-Marinet, D. Asendrych, "Numerical Modeling of Heat Transfer in Rectangular Microchannels", *Proc. Second International Conference on Microchannels and Minichannels*, Vol.1, pp.77-82, 2004
79. A. Bejan, E. Sciubba, "The Optimal Spacing of Parallel Plates Cooled by Forced Convection", *International Journal of Heat and Mass Transfer*, Vol.35, pp.3259-3264, 1992
80. D.P. Kulkarni, D.K. Das, "Analytical and Numerical Studies on Microscale Heat Sinks for Electronic Applications", *Applied Thermal Engineering*, Vol.25, pp.2432-2449, 2005
81. J.M. Koo, S. Im, L. Jiang, K.E. Goodson, "Integrated Microchannel Cooling for Three-Dimensional Electronic Circuit Architectures", *Journal of Heat Transfer*, Vol.127, pp.49-58, 2004
82. Z. Li, D. Du, Z. Guo, "Experimental Study on Flow Characteristics of Liquid in Circular Microtubes", *Microscale Thermophysical Engineering*, Vol.7, pp.253-265, 2003

83. P.S. Lee, S. Garimella, "Thermally Developing Flow and Heat Transfer in Rectangular Microchannels of Different Aspect Ratios", *International Journal of Heat and Mass Transfer*, Vol.49, pp.3060-3067, 2006
84. P. Wibulswas, "Laminar Flow Heat Transfer in Non-Circular Ducts", PhD Thesis, University of London, 1966
85. H. Herwig, S.P. Mahulikar, "Variable Property Effects in Single-Phase Incompressible Flows Through Microchannels", *International Journal of Thermal Sciences*, Vol.45, pp.977-981, 2006
86. D.C. Price, "A Review of Selected Thermal Management Solutions for Military Electronic Systems", *IEEE Transactions on Components and Packaging Technologies*, Vol.26, pp.26-39, 2003
87. J. Wilson, "Challenges in Thermal Control of Military Electronics Systems", *Electronics Cooling Magazine*, Vol.9, pp.18-24, February 2003
88. U.K. Revankar, K. Sreenivasulu, K.M. Veerabhadra, K.S. Beenamoie, D. Kumar, "An Experimental Active Aperture Array for L-Band High Power Active Phased Array Radar", *Trans. IEEE International Symposium on Phased Array Systems and Technology*, pp.289-294, 2003
89. C. Gillot, C. Schaeffer, "Integrated Micro Heat Sink for Power Multichip Module", *IEEE Transactions on Industry Applications*, Vol.36, pp.217-221, 2000
90. C. Chein, D. Chen, "Performances of Thermoelectric Cooler Integrated with Microchannel Heatsinks", *International Journal of Refrigeration*, Vol.28, pp.828-839, 2005
91. H. Hirshfeld, I. Silverman, A. Arenshtam, D. Kijel, A. Nagler, "High Heat Flux Cooling of Accelerator Targets with Micro-Channels", *Nuclear Instruments and Methods in Physics Research A*, Vol.562, pp.903-905, 2006
92. C. Gillot, A. Bricard, C. Schaeffer, "Single and Two Phase Heat Exchangers for Power Electronic Components", *International Journal of Thermal Sciences*, Vol.39, pp.826-832, 2000
93. G.C. Birur, T.W. Sur, A.D. Paris, P. Shakkottai, A.A. Green, S.I. Haapanen, "Micro/Nano Spacecraft Thermal Control Using a MEMS-Based Pumped Liquid Cooling System", *Trans. SPIE International Symposium on Micromachining and Microfabrication*, Vol.4560, pp.196-206, 2001
94. United States Patent No. 2003/0183368 (2003)

95. United States Patent No. 2006/0262502 (2006)

96. United States Patent No. 5099311 (1992)

97. United States Patent No. 5548605 (1996)

98. United States Patent No. 5960861 (1999)

## APPENDIX A

### RELATIONS OF VECTOR CALCULUS AND TENSOR NOTATION

For all relations of Chapter 2, the coordinate system is a Cartesian set defined by unit direction vectors  $\mathbf{i}$ ,  $\mathbf{j}$ , and  $\mathbf{k}$  in the orthogonal directions of  $x$ ,  $y$ , and  $z$ , respectively. The velocity vector,  $\mathbf{V}$ , and the gravitational acceleration vector,  $\mathbf{g}$ , are defined as follows:

$$\mathbf{V} = ui + vj + wk \quad (\text{A.1})$$

$$\mathbf{g} = -g\mathbf{k} \quad (\text{A.2})$$

Regarding the relations occurring in Chapter 2, the material derivative of a vector, the divergence of a vector, the gradient of a scalar are, the divergence of the gradient of a scalar, and the dot product of a vector with the gradient operator are, respectively,

$$\frac{D\mathbf{V}}{Dt} = \frac{\partial \mathbf{V}}{\partial t} + u \frac{\partial \mathbf{V}}{\partial x} + v \frac{\partial \mathbf{V}}{\partial y} + w \frac{\partial \mathbf{V}}{\partial z} \quad (\text{A.3})$$

$$\nabla \cdot (\mathbf{V}) = \frac{\partial u}{\partial x} + \frac{\partial v}{\partial y} + \frac{\partial w}{\partial z} \quad (\text{A.4})$$

$$\nabla \phi = \frac{\partial \phi}{\partial x} \mathbf{i} + \frac{\partial \phi}{\partial y} \mathbf{j} + \frac{\partial \phi}{\partial z} \mathbf{k} \quad (\text{A.5})$$

$$\nabla^2 \phi = \frac{\partial^2 \phi}{\partial x^2} + \frac{\partial^2 \phi}{\partial y^2} + \frac{\partial^2 \phi}{\partial z^2} \quad (\text{A.6})$$

$$\mathbf{V} \cdot \nabla = u \frac{\partial}{\partial x} + v \frac{\partial}{\partial y} + w \frac{\partial}{\partial z} \quad (\text{A.7})$$

Regarding the relation given for the compact form of the Navier-Stokes equations, the space tensor,  $x_i$ , is defined as follows:

$$x_i = (x, y, z) \quad (\text{A.8})$$

The Kronecker Delta tensor is defined as

$$\begin{aligned} \delta_{ij} &= 0 \text{ if } i \neq j \\ \delta_{ij} &= 1 \text{ if } i = j \end{aligned} \quad (\text{A.9})$$

The expansion of the tensor terms are

$$\frac{\partial}{\partial x_j} \left( \frac{\partial v_i}{\partial x_j} + \frac{\partial v_j}{\partial x_i} \right) = \left\{ \begin{array}{l} \frac{\partial^2 u}{\partial x^2} + \frac{\partial^2 u}{\partial y^2} + \frac{\partial^2 u}{\partial z^2} + \frac{\partial^2 u}{\partial x^2} + \frac{\partial^2 v}{\partial y \partial x} + \frac{\partial^2 w}{\partial z \partial x} \\ \frac{\partial^2 v}{\partial x^2} + \frac{\partial^2 v}{\partial y^2} + \frac{\partial^2 v}{\partial z^2} + \frac{\partial^2 u}{\partial x \partial y} + \frac{\partial^2 v}{\partial y^2} + \frac{\partial^2 w}{\partial z \partial y} \\ \frac{\partial^2 w}{\partial x^2} + \frac{\partial^2 w}{\partial y^2} + \frac{\partial^2 w}{\partial z^2} + \frac{\partial^2 u}{\partial x \partial z} + \frac{\partial^2 v}{\partial y \partial z} + \frac{\partial^2 w}{\partial z^2} \end{array} \right\} \quad (\text{A.10})$$

## APPENDIX B

### TECHNICAL DRAWINGS - PRELIMINARY SPECIMEN

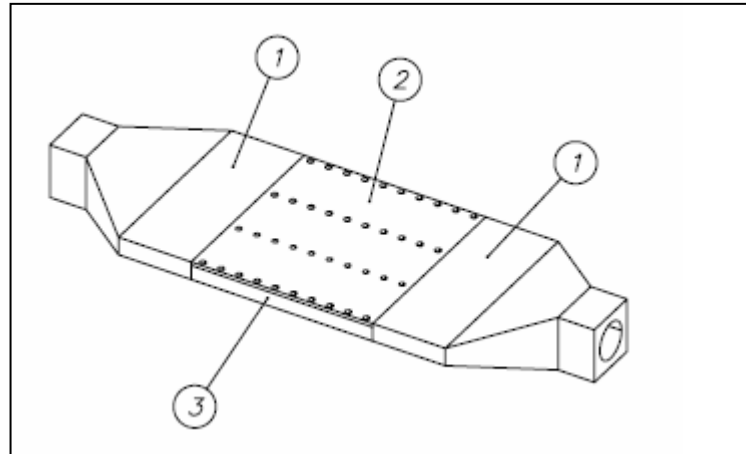


Figure B.1: Microchannel heatsink assembly

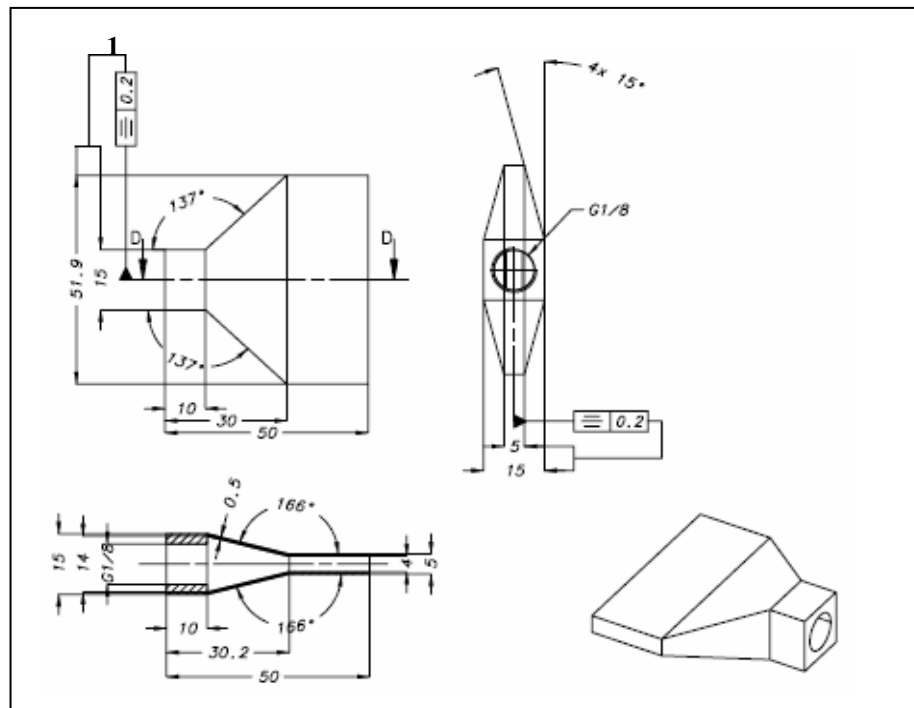


Figure B.2: Inlet - outlet parts

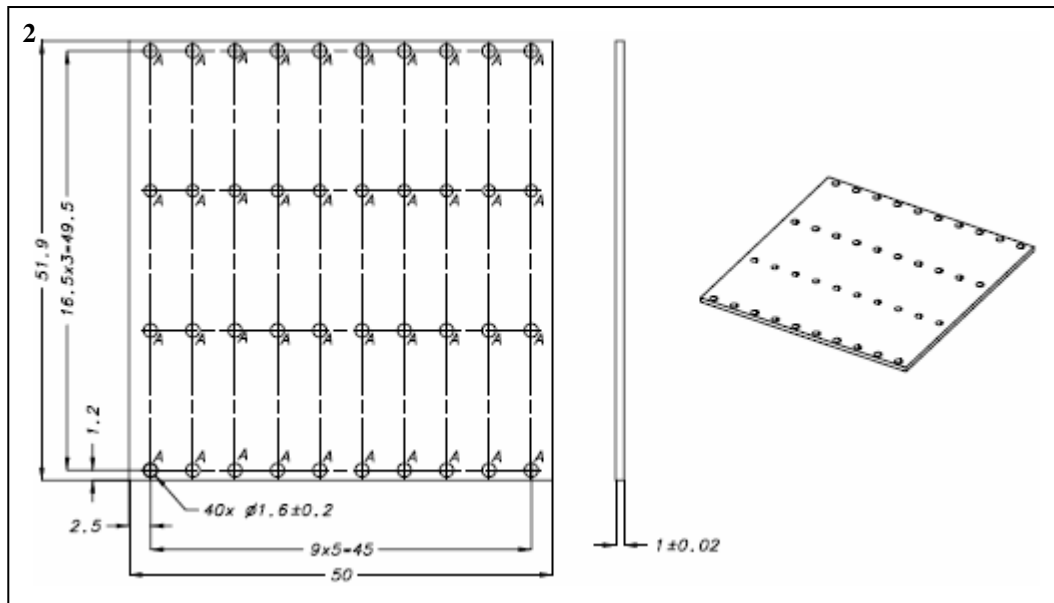


Figure B.3: Cover plate

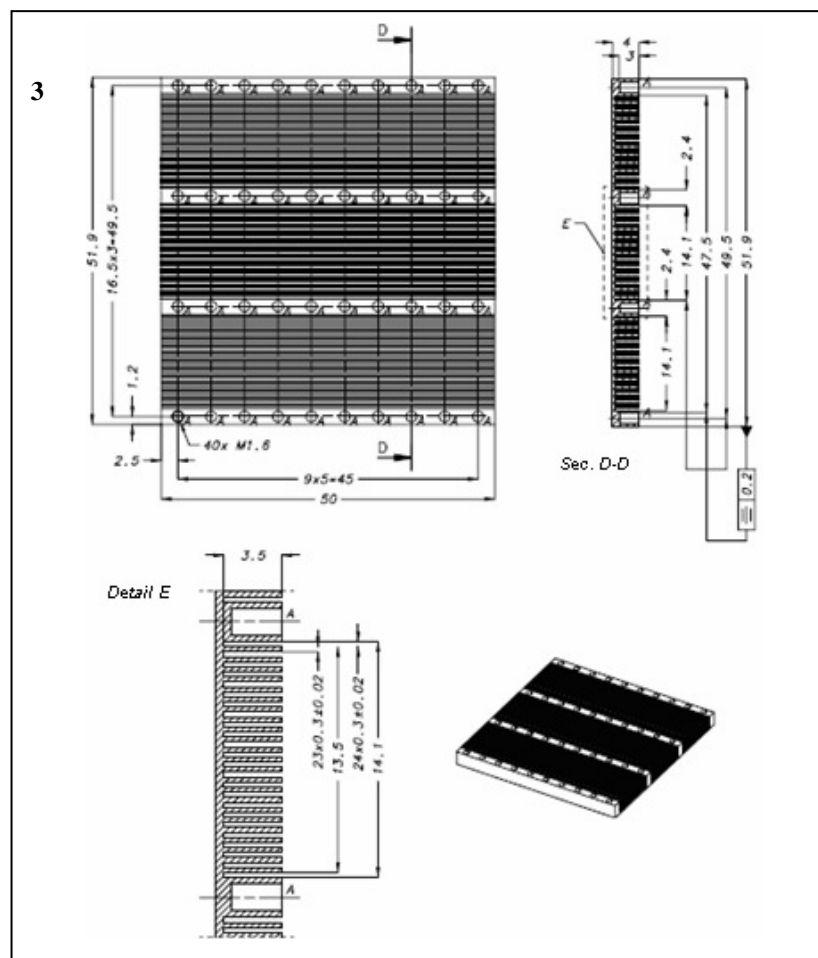


Figure B.4: Heatsink body

## APPENDIX C

### TECHNICAL DRAWINGS - TEST SPECIMENS

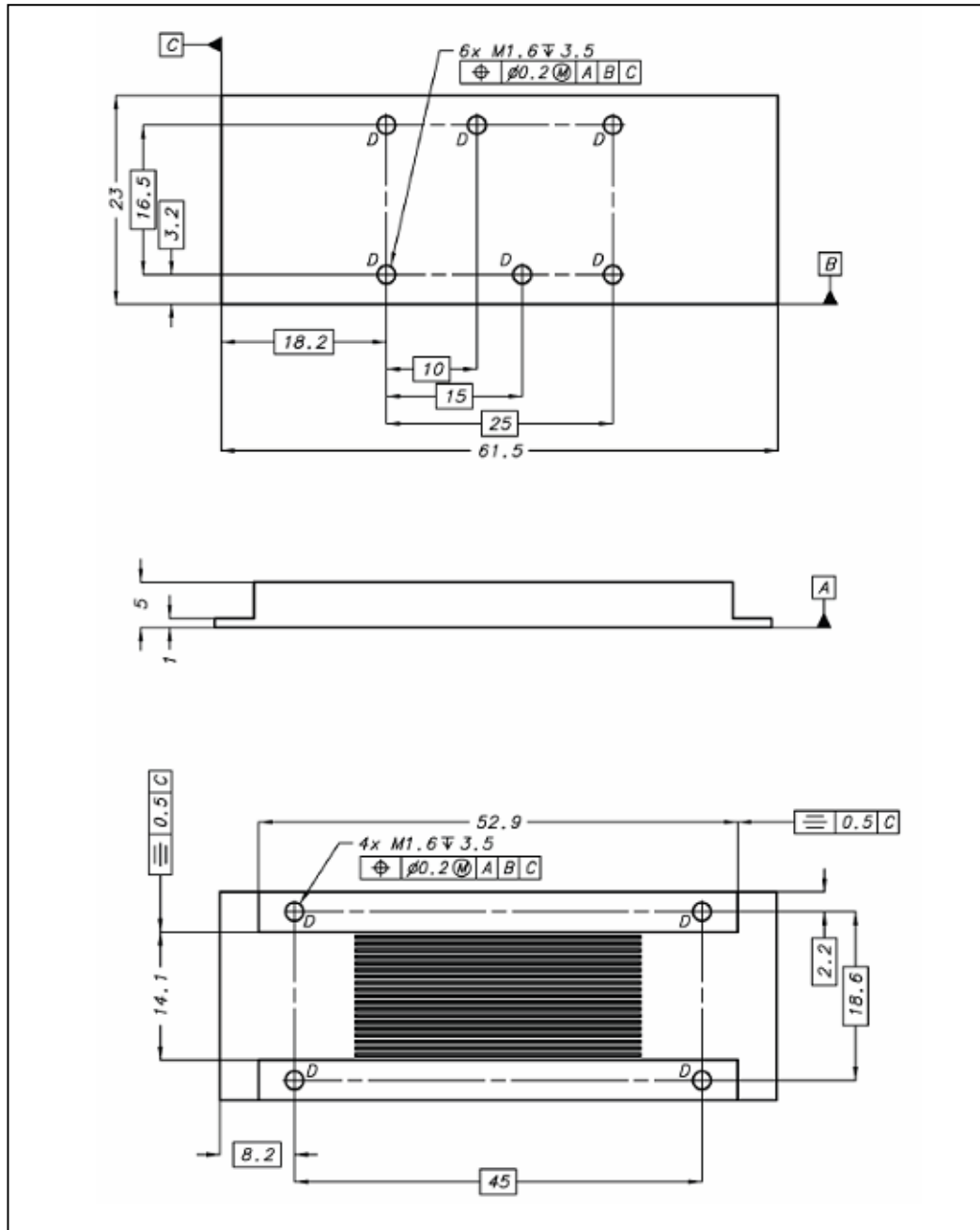


Figure C.1: 300  $\mu\text{m}$  heatsink body dimensions

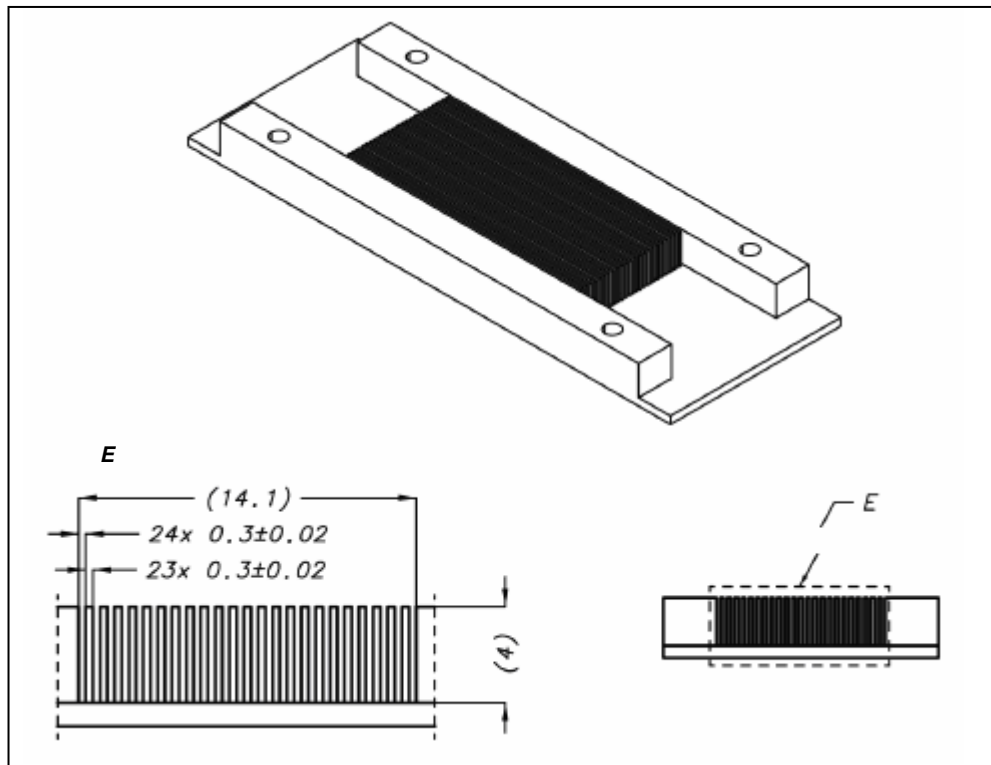


Figure C.2: 300 μm channel dimensions

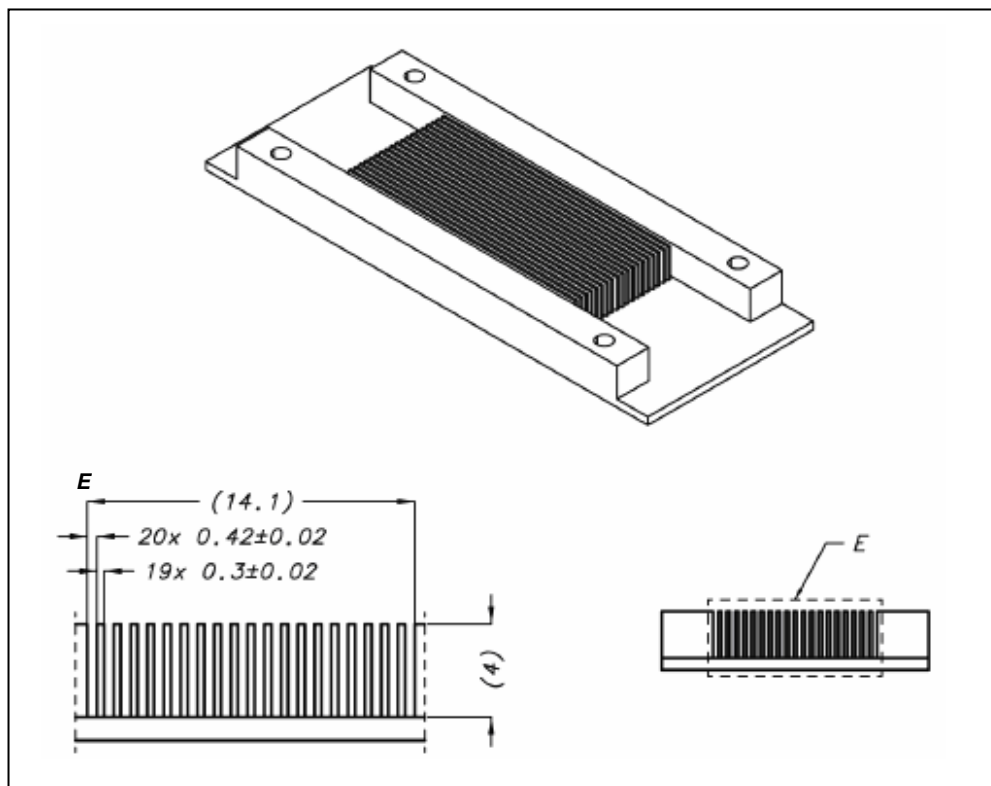


Figure C.3: 420 μm channel dimensions

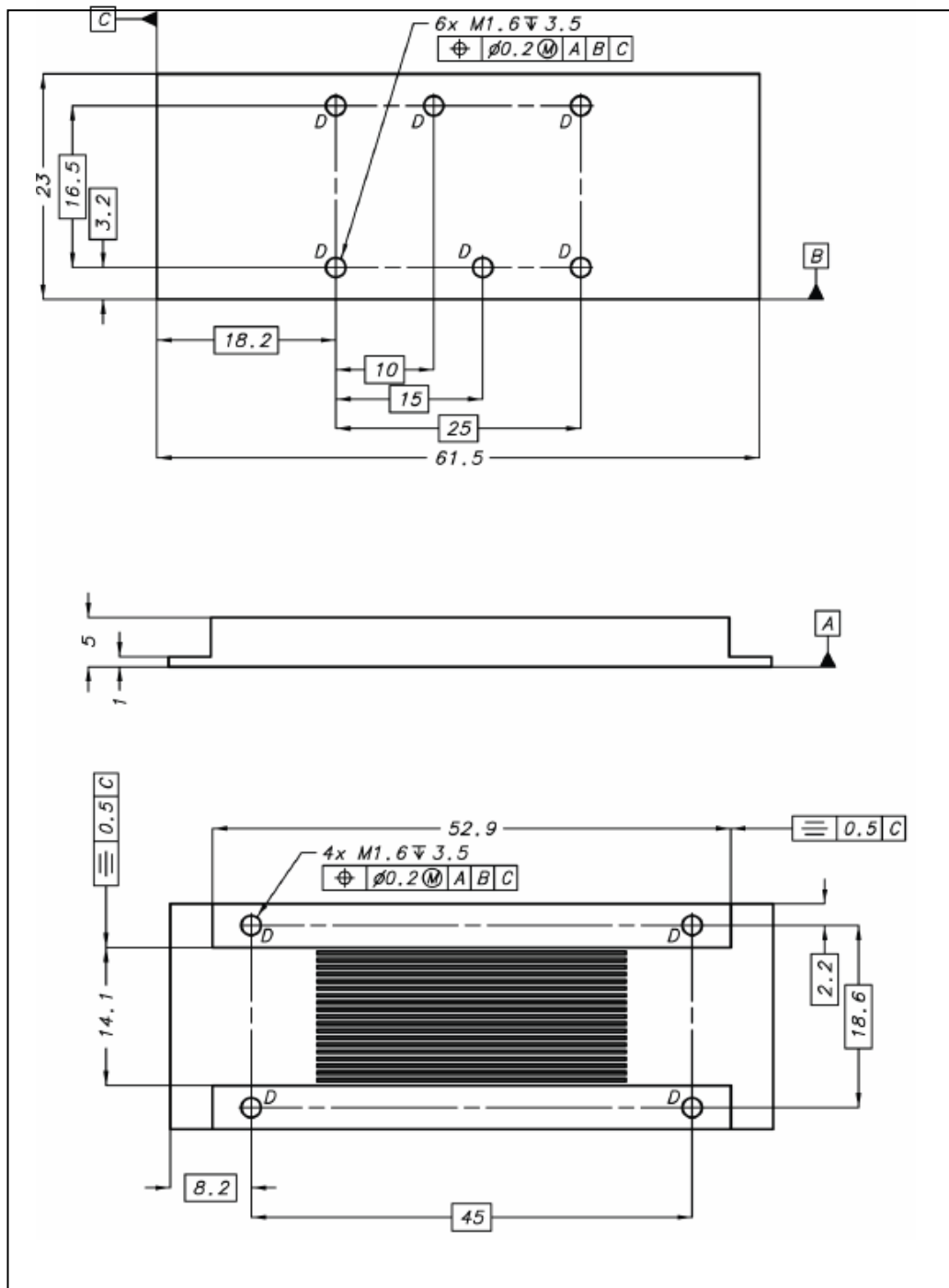


Figure C.4: 420  $\mu\text{m}$  heatsink body dimensions

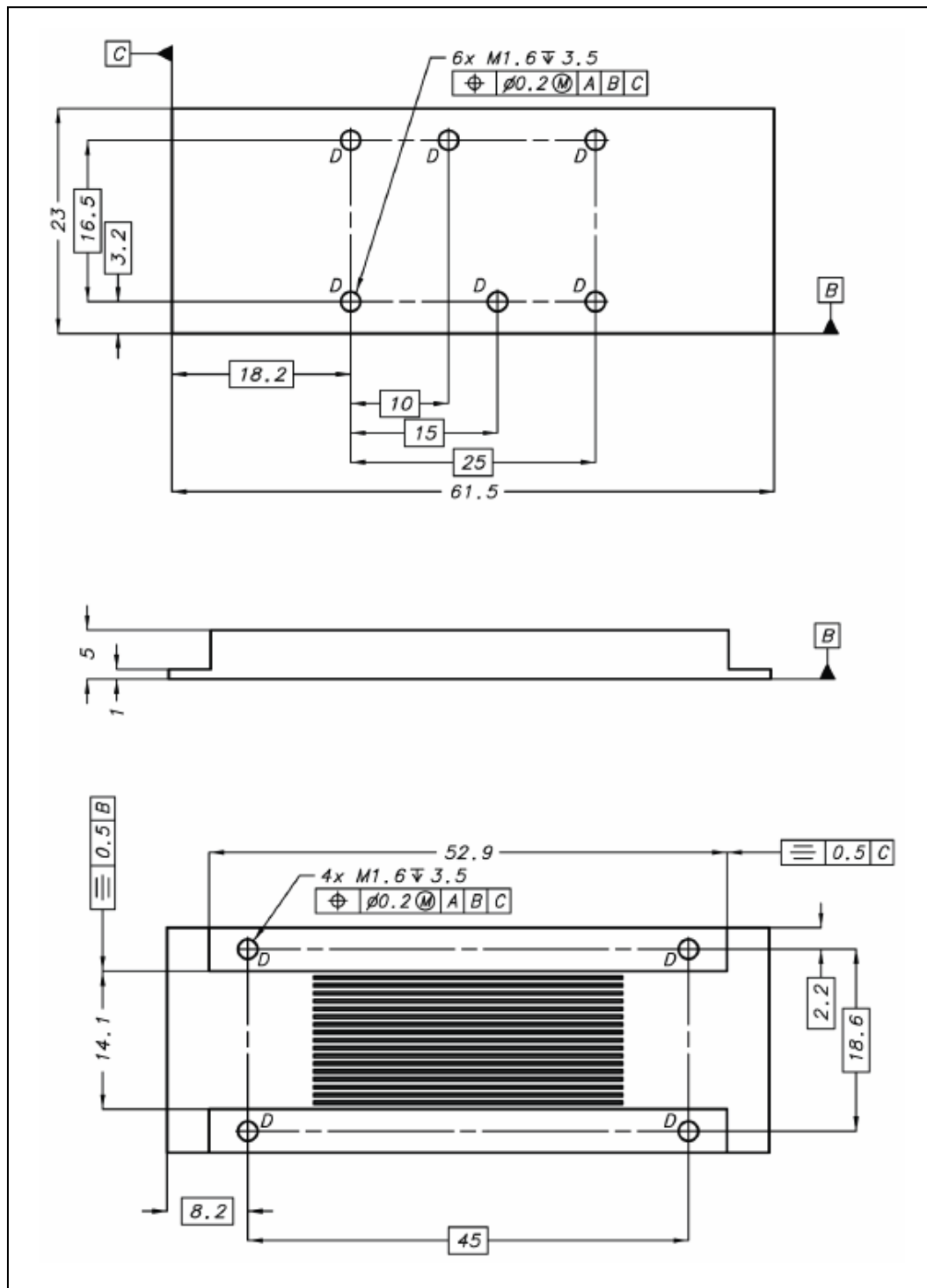


Figure C.5: 500  $\mu\text{m}$  heatsink body dimensions

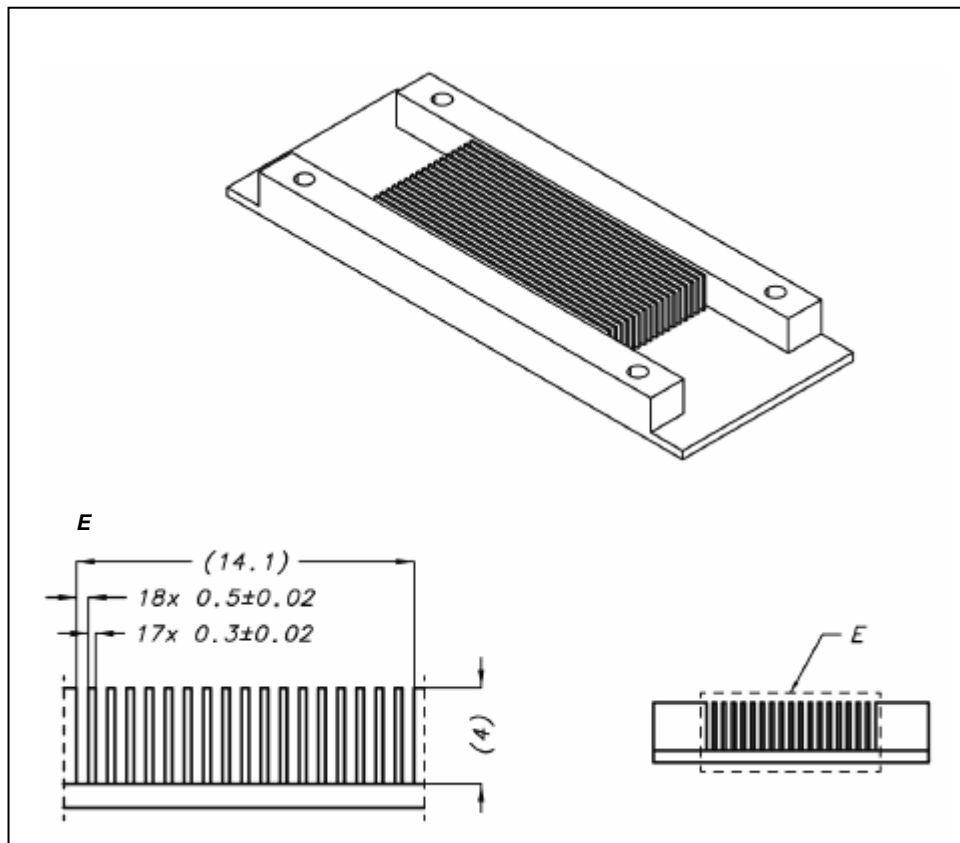


Figure C.6: 500 μm channel dimensions

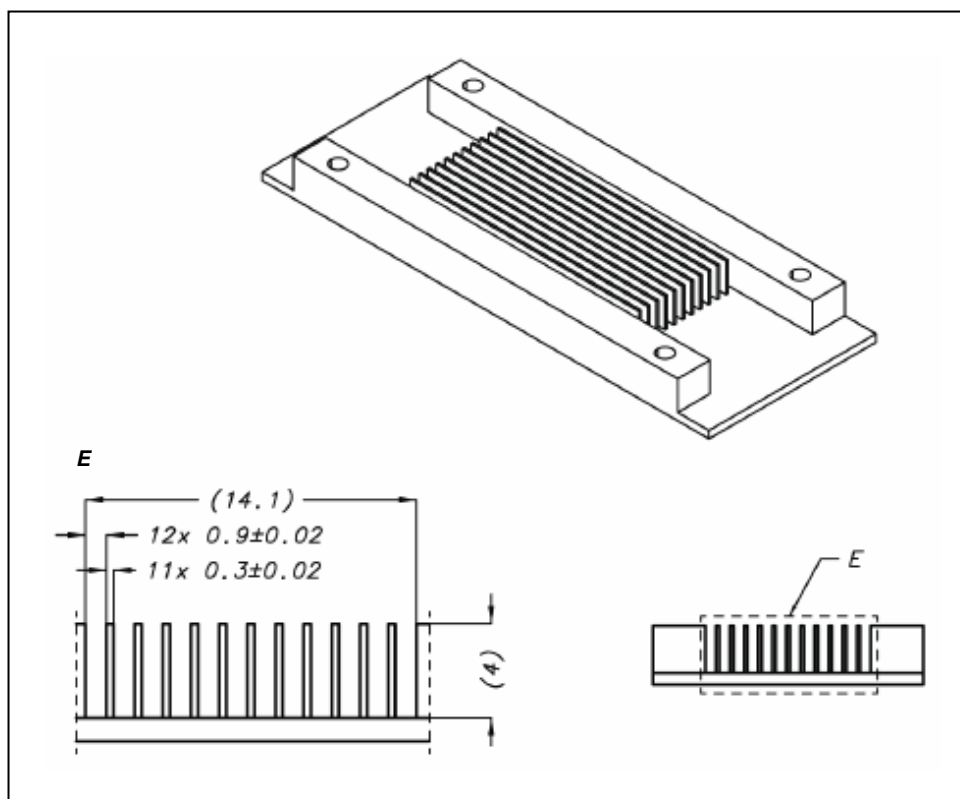


Figure C.7: 900 μm channel dimensions

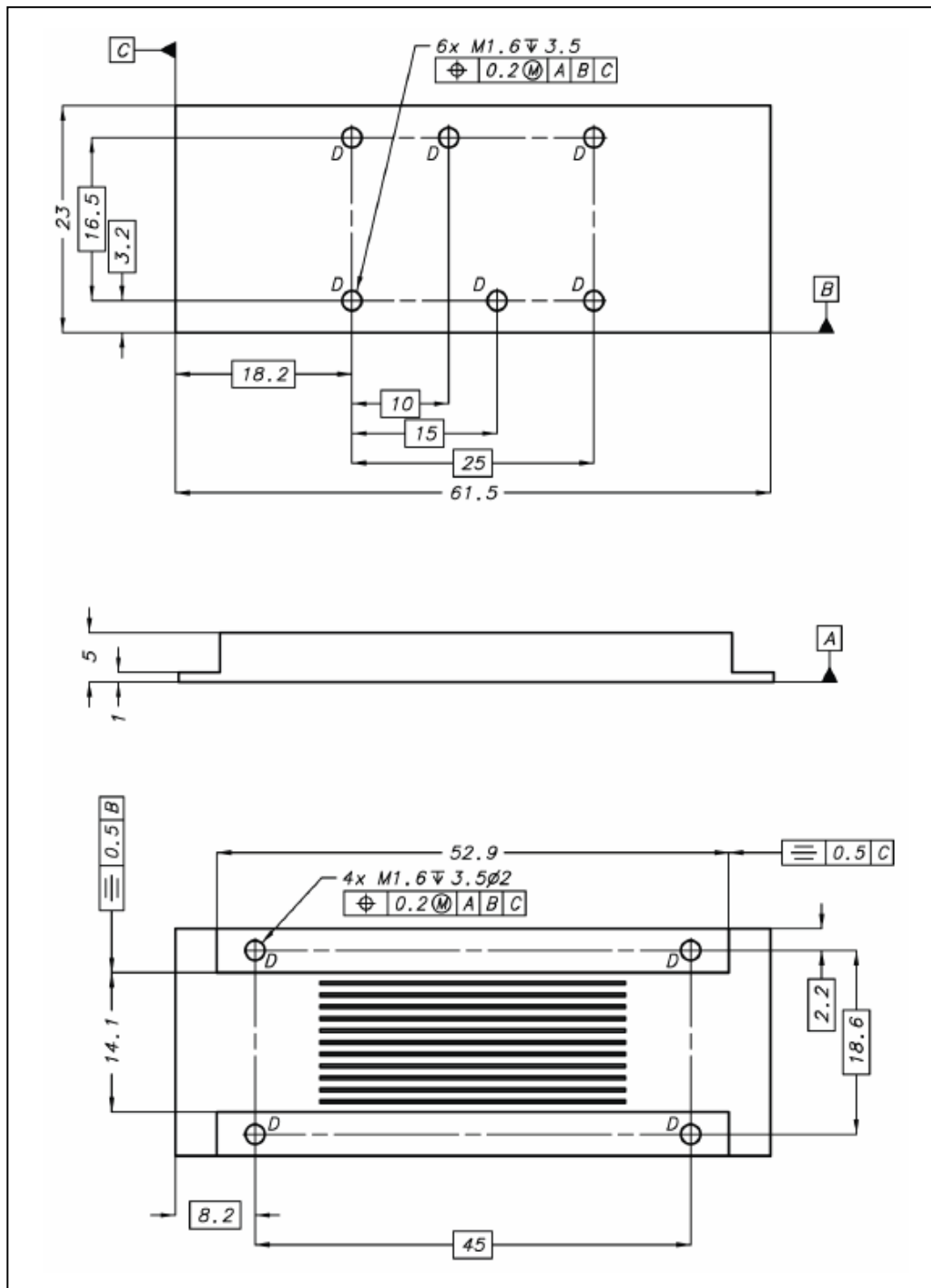


Figure C.8: 900 μm heatsink body dimensions

## APPENDIX D

### SAMPLE ANALYTICAL CALCULATION

A sample calculation for the microchannel heatsink of 300μm channel width, based on the relations presented in section 2.1, is given. Physical properties of water at 300K, on which the calculations are based, are given in Table A.B.1

Table D.1: Properties of water and ethylene glycol at 300K

PROPERTY	SYMBOL	UNIT	WATER @ 300K
Specific Heat	$C_p$	J/kg·K	4179
Dynamic Viscosity	$\mu$	N·s/m <sup>2</sup>	$8.55 \cdot 10^{-4}$
Coefficient of Conduction	$k$	W/m·K	0.613
Prandtl Number	Pr		5.83
Density	$\rho$	kg/m <sup>3</sup>	997

The set of sample calculations given below are for 300μm channel width:

$$\text{Aspect ratio: } \alpha_c = \frac{0.3mm}{4mm} = 0.075$$

$$\text{Hydraulic diameter: } D_h = \frac{(4)(4mm)(0.3mm)}{2(4mm + 0.3mm)} = 0.56 \text{ mm}$$

$$\text{Volumetric flow rate: } Q = 1 \text{ lpm} = \frac{1 \cdot 10^{-3}}{60} \text{ m}^3/\text{s}$$

$$\text{Channel flow velocity: } V_{ch} = \frac{Q}{A_{ch}} = \frac{\frac{1 \cdot 10^{-3}}{60} \text{ m}^3/\text{s}}{(24)(4 \cdot 10^{-3} \text{ m})(0.3 \cdot 10^{-3} \text{ m})} = 0.58 \text{ m/s}$$

$$\text{Reynolds number: } Re_{ch} = \frac{\rho \cdot V_{ch} \cdot D_h}{\mu} = \frac{(1058.7 \text{ kg/m}^3)(0.58 \text{ m/s})(0.56 \cdot 10^{-3} \text{ m})}{7.85 \cdot 10^{-3}}$$

$$Re_{ch} = 43.8$$

Poiseuille number:

$$Po = 1 - 1.3553\alpha + 1.9467\alpha^2 - 1.7012\alpha^3 + 0.9564\alpha^4 - 0.2357\alpha^5$$

$$Po = 1 - (1.3553)0.075 + (1.9467)0.075^2 - (1.7012)0.075^3 + (0.9564)0.075^4 - (0.2357)0.075^5$$

$$Po = 21.8$$

$$\text{Friction factor: } f = \frac{Po}{Re} = \frac{21.8}{43.8} = 0.498$$

$$\text{Entrance length: } L_h = 0.05 (Re) (D_h) = 0.05 (43.8) (0.56 \text{ mm}) = 1.23 \text{ mm}$$

$$\text{Total channel length: } L_{ch} = 31.9 \text{ mm} > 1.23 \text{ mm} = L_h$$

Hassenbach factor:

$$K(\infty) = 0.6796 + 1.2197\alpha + 3.3089\alpha^2 - 9.5921\alpha^3 + 8.9089\alpha^4 - 2.9959\alpha^5$$

$$K(\infty) = 0.6796 + (1.2197)0.075 + (3.3089)0.075^2 - (9.5921)0.075^3 + (8.9089)0.075^4 - (2.9959)0.075^5$$

$$K(\infty) = 0.786$$

$$\text{Pressure drop: } \Delta p = \frac{1}{2} \cdot \rho \cdot V_{ch}^2 \left[ \left( \frac{A_c}{A_p} \right)^2 \cdot 2K_{90} + (K_c + K_e) + \frac{4 \cdot f \cdot L_{ch}}{D_h} + K(\infty) \right]$$

$$\Delta p = \frac{1}{2} (1114.4) (0.58^2) \left[ \left( \frac{(4)(0.3)}{(4)(14.1)} \right)^2 (2)(1.1) + (0.8 + 0.98) + \frac{(4)(0.498)(31.9)}{0.56} \right]$$

$$\Delta p = 2644 \text{ Pa} = 0.026 \text{ bar}$$

Thermal entrance length:

$$L_t = c \cdot Re \cdot Pr \cdot D_h = (0.1)(43.8)(78.4)(0.56 \text{ mm})$$

$$L_t = 192.3 \text{ mm}$$

$$L = 31.9 \text{ mm} < 192.3 \text{ mm} = L_t \Rightarrow \text{thermally developing flow}$$

From Table 2.1,  $Nu_{ave} = 9.72$

$$\text{Average convection heat transfer coefficient: } h_{ave} = \frac{kNu_{ave}}{D_h}$$

$$h_{ave} = \frac{(0.613)(9.72)}{0.56 \cdot 10^{-3}} = 10675.4 \text{ W/m}^2\text{K}$$

The same calculation methodology has been carried out for the 420, 500, and 900  $\mu\text{m}$  channel heatsinks. Calculated parameters are presented in Table A.B.2.

Table D.2: Calculated flow parameters

$W_c$ ( $\mu\text{m}$ )	$\alpha_c$	$D_h$ (mm)	$V_{ch}$ (m/s)	$Re_{ch}$	$Pr$	$f$	$L_h$ (mm)	$K(\infty)$	$\Delta p$ (kPa)	$L_c$ (mm)	$Nu_{ave}$	$h_{ave}$ ( $\text{W/m}^2\text{K}$ )
300	0.075	0.56	0.58	376.6	21.8	0.058	10.5	0.79	2.638	122.6	9.72	10675.4
420	0.105	0.76	0.50	439.7	21.1	0.048	16.7	0.83	1.307	194.9	10.33	8330.0
500	0.125	0.89	0.46	479.9	20.6	0.043	21.3	0.87	0.941	248.7	10.57	7289.3
900	0.225	1.47	0.39	661.0	18.6	0.028	48.6	1.03	0.391	566.3	11.67	4868.5

For heat transfer calculations, a constant heat flux of  $100 \text{ W/cm}^2$  applied at the heatsink base has been assumed. A sample calculation for overall surface efficiency of the heatsinks has been provided below for the 300  $\mu\text{m}$  copper specimen.

$$\text{Corrected length: } L_c = L + \frac{t_f}{2} = 4 \text{ mm} + \frac{0.3 \text{ mm}}{2}$$

$$L_c = 4.15 \text{ mm}$$

$$\text{Fin efficiency: } m = \sqrt{\frac{hP_w}{kA_c}} = \sqrt{\frac{(10675.4)(64.4)}{(370)(9.57)}}$$

$$m = 597.7 \text{ m}^{-1}$$

$$\eta_f = \frac{\tanh(mL_c)}{mL_c} = \frac{\tanh\left((597.7)(4.15 \cdot 10^{-3})\right)}{(597.7)(4.15 \cdot 10^{-3})}$$

$$\eta_f = 0.52$$

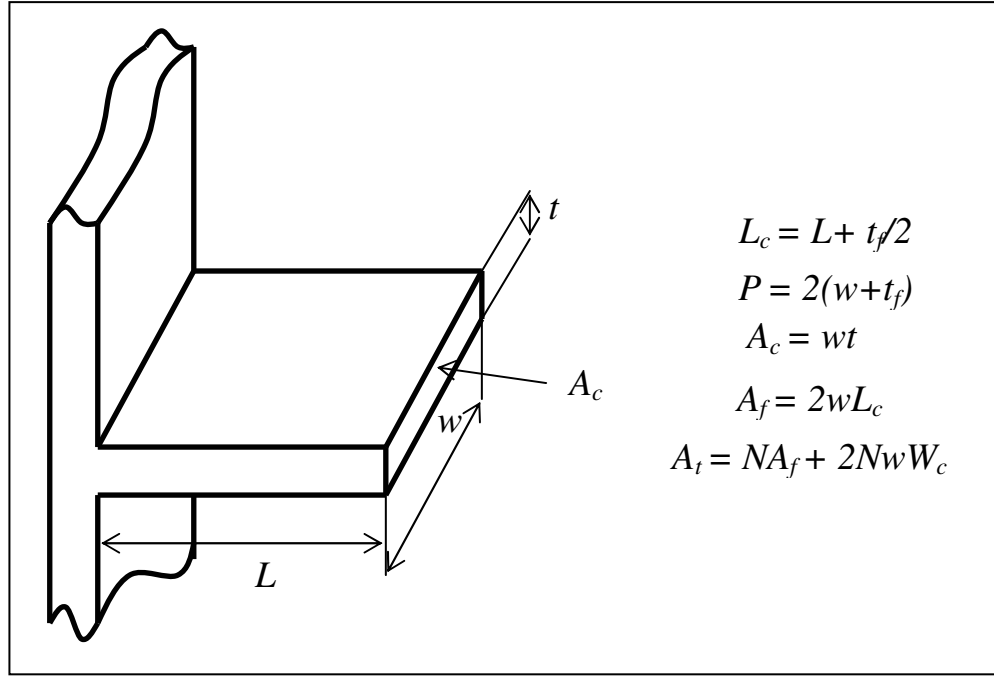


Figure D.1: Geometrical parameters

$$\text{Overall surface efficiency: } \eta_o = 1 - \frac{NA_f}{A_t}(1 - \eta_f) = 1 - \frac{(24)(264.77)}{6584.2}(1 - 0.52)$$

$$\eta_o = 0.54$$

Base temperature rise:

$$\theta_b = \frac{q_t}{\eta_o} h_{aveA_t} = \frac{\left(100 \frac{W}{cm^2}\right)(0.141cm)(0.319cm)}{0.54} (10675.4 W/m^3 K) (6584.2 \cdot 10^{-6} m^2)$$

$$\theta_b = 11.9 K$$

The fin efficiencies and heatsink temperature rise values calculated using the methodology above are presented in Table A.B.3 for the copper specimens, and in Table A.B.4 for the aluminum specimens.

Table D.3 Calculated parameters for copper specimens

$W_c$ (mm)	$A_c$ (mm <sup>2</sup> )	$A_t$ (mm <sup>2</sup> )	$A_f$ (mm <sup>2</sup> )	$m$ (m <sup>-1</sup> )	$\eta_f$	$\eta_o$	$\theta_b$ (°C)
0.30	9.57	6584.2	264.77	440.6	0.52	0.54	11.9
0.42	9.57	5639.9	264.77	389.2	0.57	0.60	16.0
0.50	9.57	5167.8	264.77	364.1	0.60	0.63	18.9
0.90	9.57	3751.4	264.77	297.6	0.68	0.73	33.6

Table D.4 Calculated parameters for aluminum specimens

$W_c$ (mm)	$A_c$ (mm <sup>2</sup> )	$A_t$ (mm <sup>2</sup> )	$A_f$ (mm <sup>2</sup> )	$m$ (m <sup>-1</sup> )	$\eta_f$	$\eta_o$	$\theta_b$ (°C)
0.30	9.57	6584.2	264.77	597.7	0.40	0.42	15.3
0.42	9.57	5639.9	264.77	528.0	0.45	0.48	20.0
0.50	9.57	5167.8	264.77	493.9	0.47	0.51	23.3
0.90	9.57	3751.4	264.77	403.6	0.56	0.62	39.4

The temperature rise between the heatsink coolant inlet and exit may readily be calculated using the energy balance relation:

$$q_t = \dot{m} c_p \Delta T$$

$$\Delta T = \frac{q_t}{\dot{m} c_p}$$

where

$$q_t = q'' A_b = \left(100 \frac{W}{cm^2}\right) (1.41 cm) (3.179 cm) = 449.8 W$$

with  $A_b$  designating heatsink base area, and

$$m = \rho Q = \left(997 \frac{kg}{m^3}\right) (1 lpm) \left(1.10^{-3} \frac{m^3}{l}\right) \left(60 \frac{s}{min}\right) = 0.0166 kg/s$$

For all specimens, the coolant temperature rise is:

$$\Delta T = \frac{q_t}{\dot{m}c_p} = 449.8 \frac{W}{\left(0.0166 \frac{kg}{s}\right) \left(4179 \frac{J}{kgK}\right)} = 6.47 \text{ }^{\circ}\text{C}$$

## APPENDIX E

### PHOTOGRAPHS OF TEST SPECIMEN BODY AND CAP

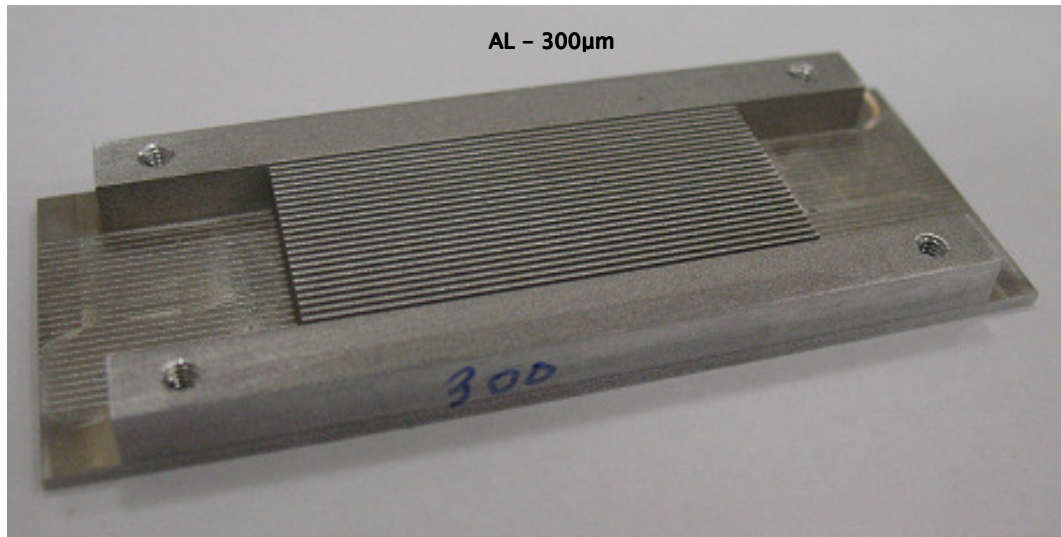


Figure E.1: AL 300 μm specimen

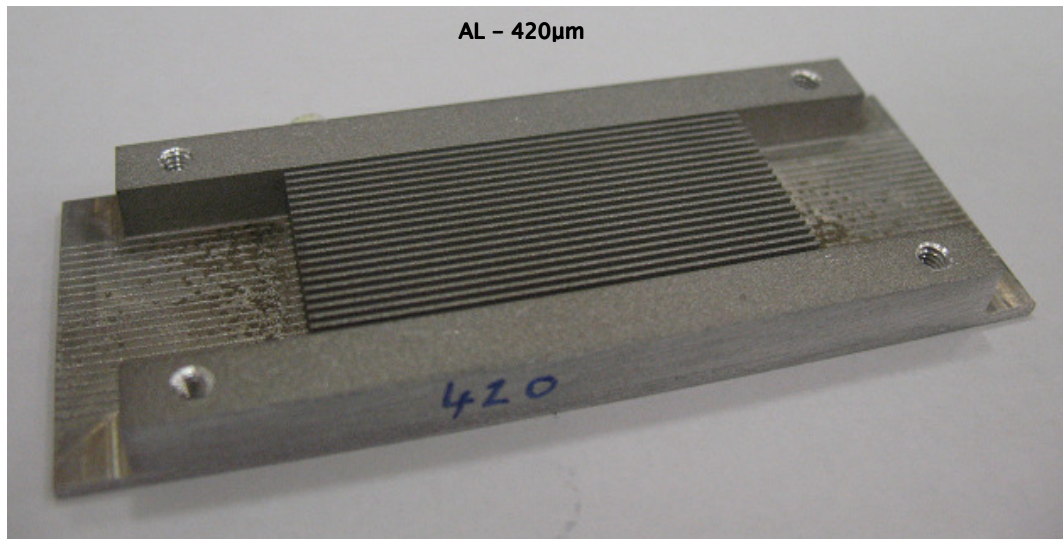


Figure E.2: AL 420 μm specimen

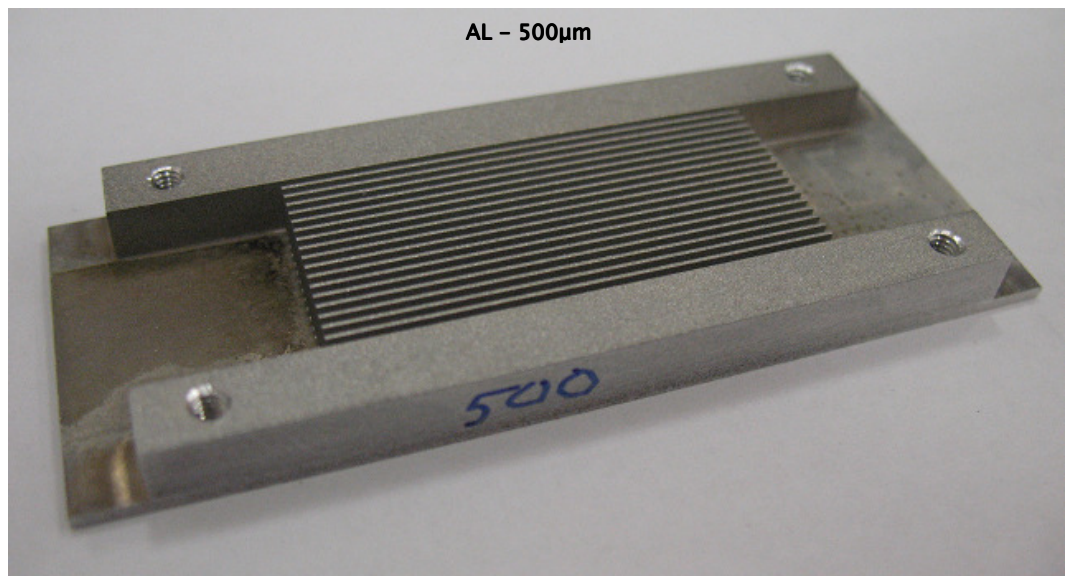


Figure E.3: AL 500 µm specimen

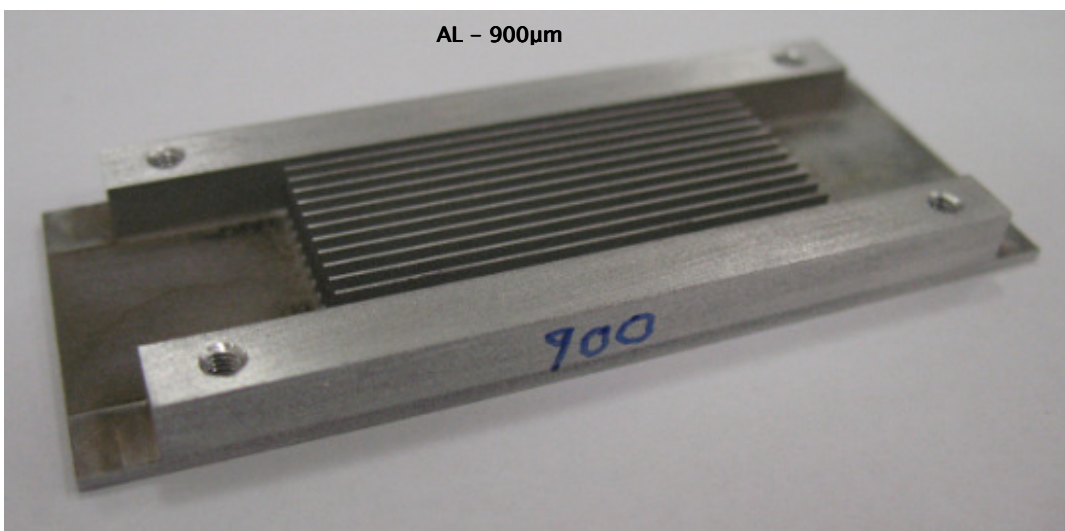


Figure E.4: AL 900 µm specimen

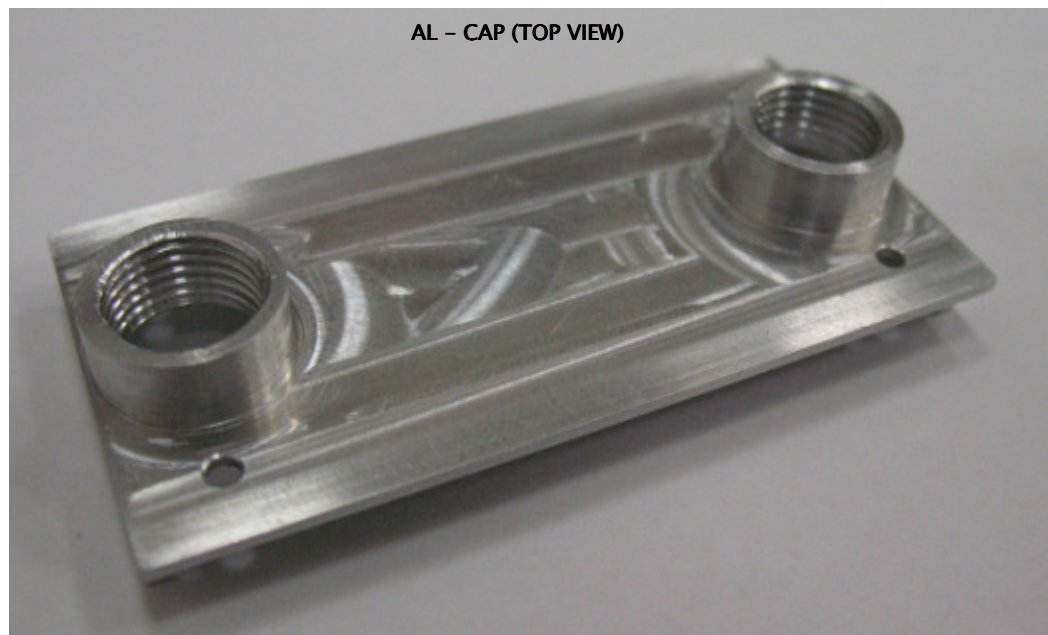


Figure E.5: AL cap – top view

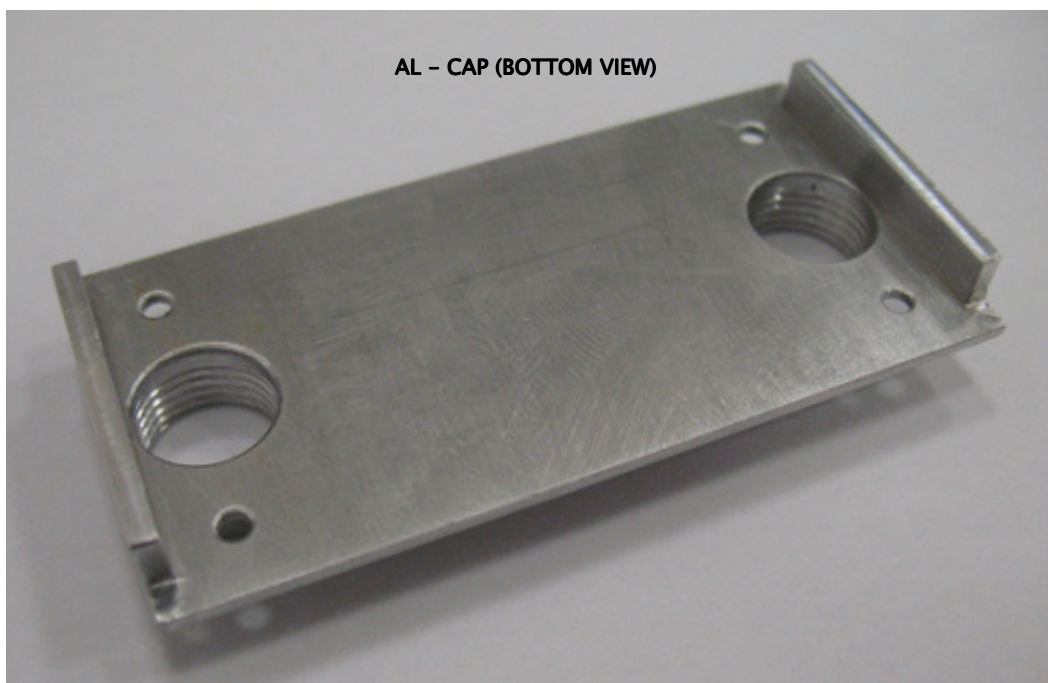


Figure E.6: AL cap – bottom view

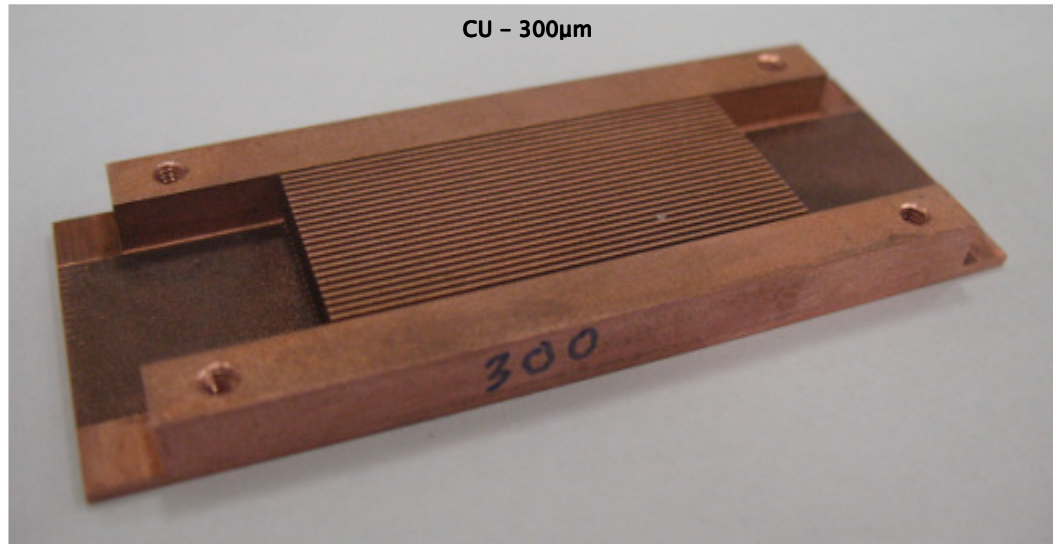


Figure E.7: CU 300  $\mu$ m specimen

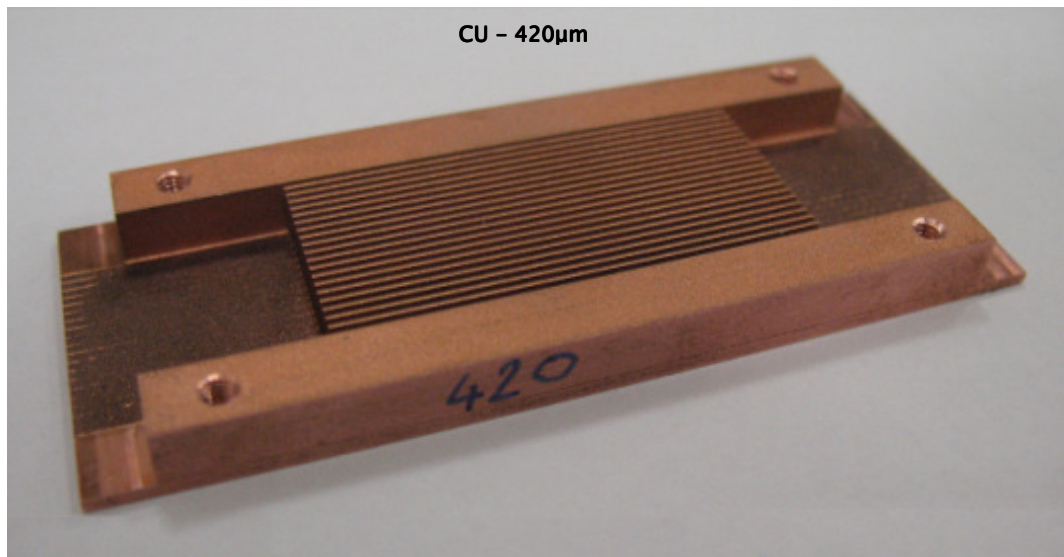


Figure E.8: CU 420  $\mu$ m specimen

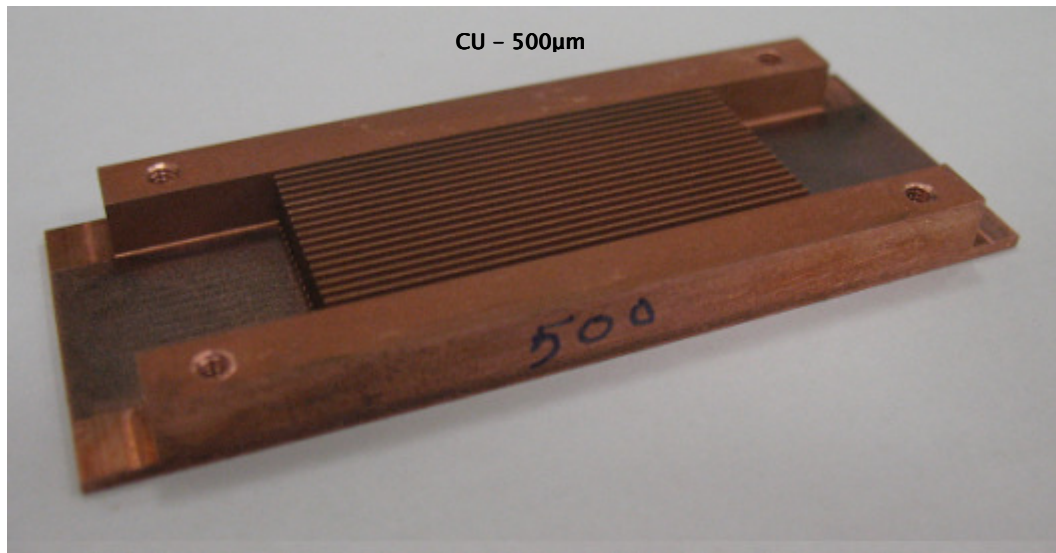


Figure E.9: CU 500  $\mu\text{m}$  specimen

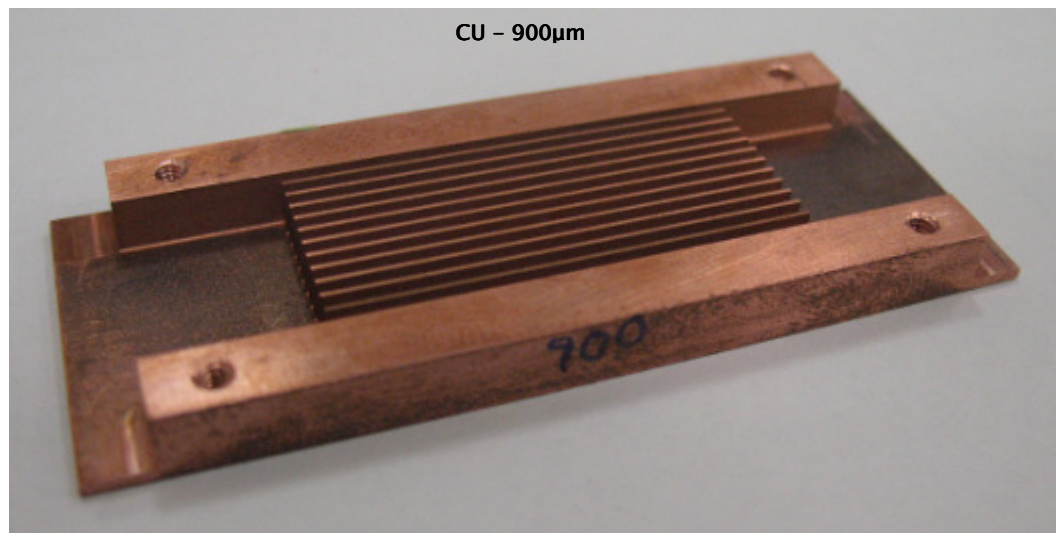


Figure E.10: CU 420  $\mu\text{m}$  specimen

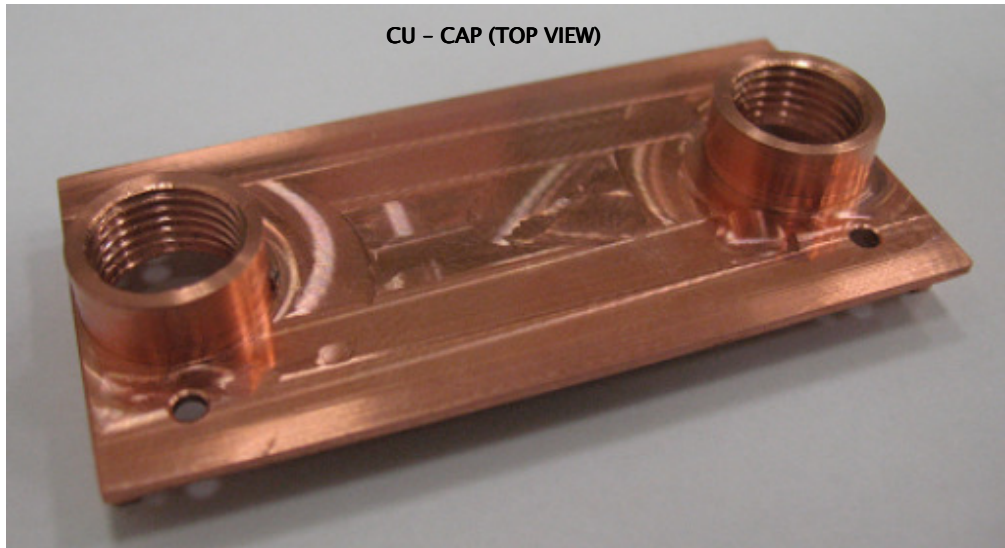


Figure E.11: CU cap – top view

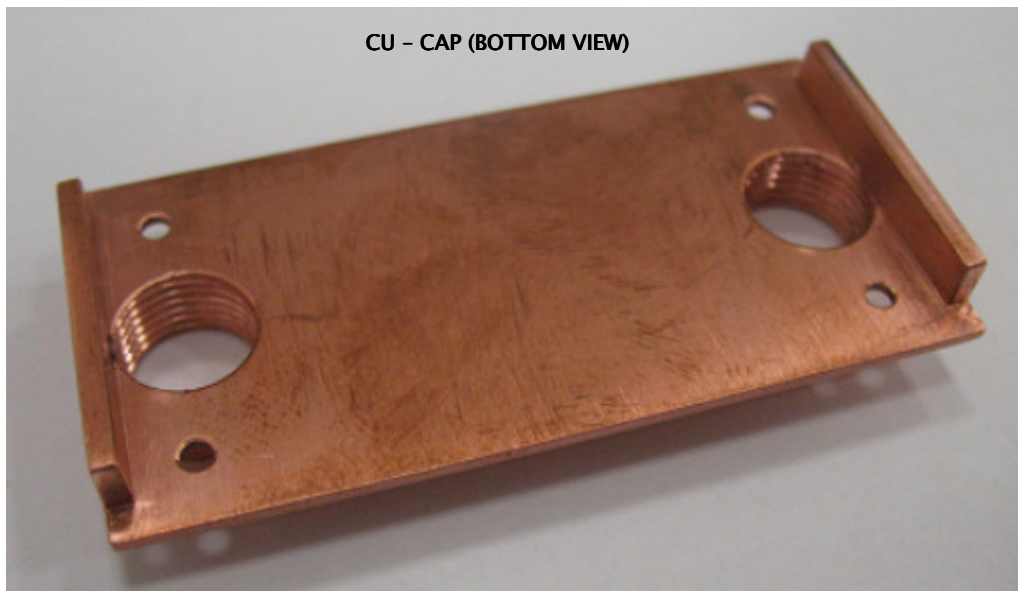


Figure E.12: CU cap – bottom view

## APPENDIX F

### MICROSCOPE VIEWS OF TEST CHANNELS

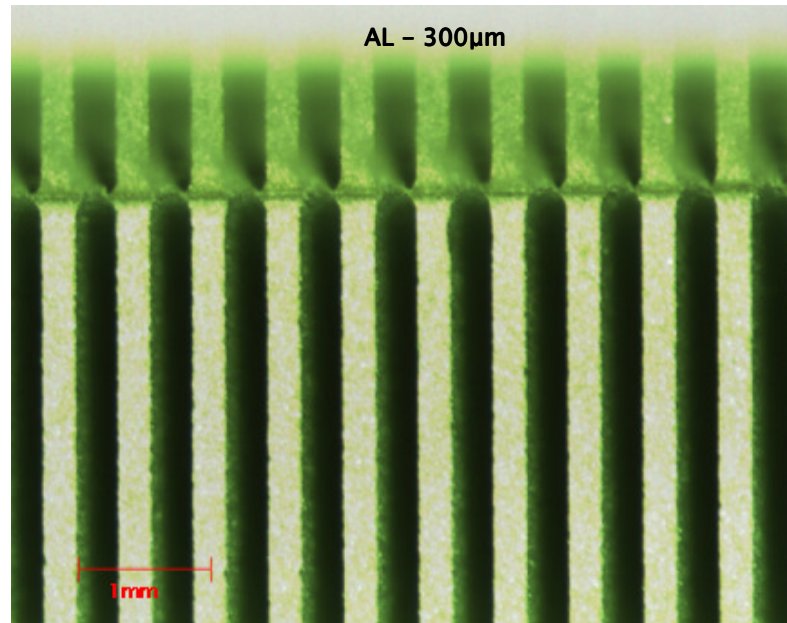


Figure F.1: AL 300  $\mu$ m specimen

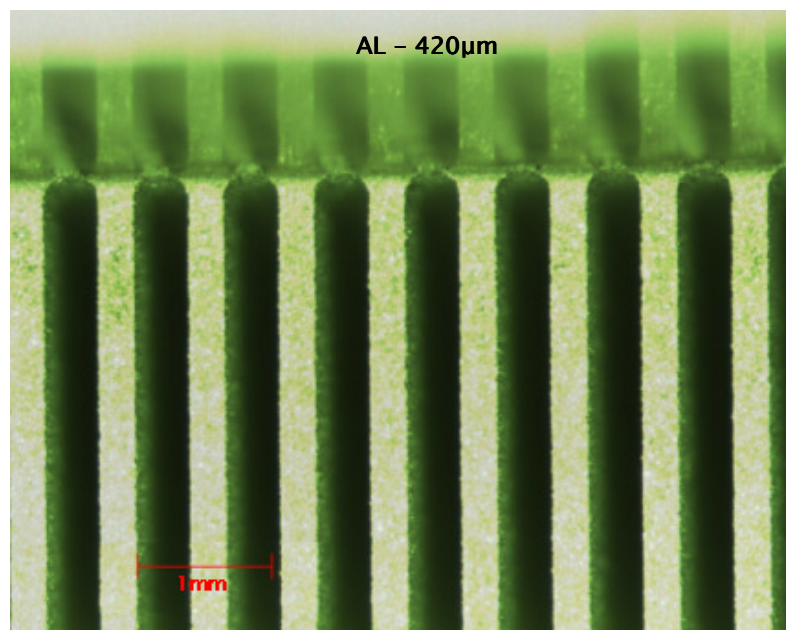


Figure F.2: AL 420  $\mu$ m specimen

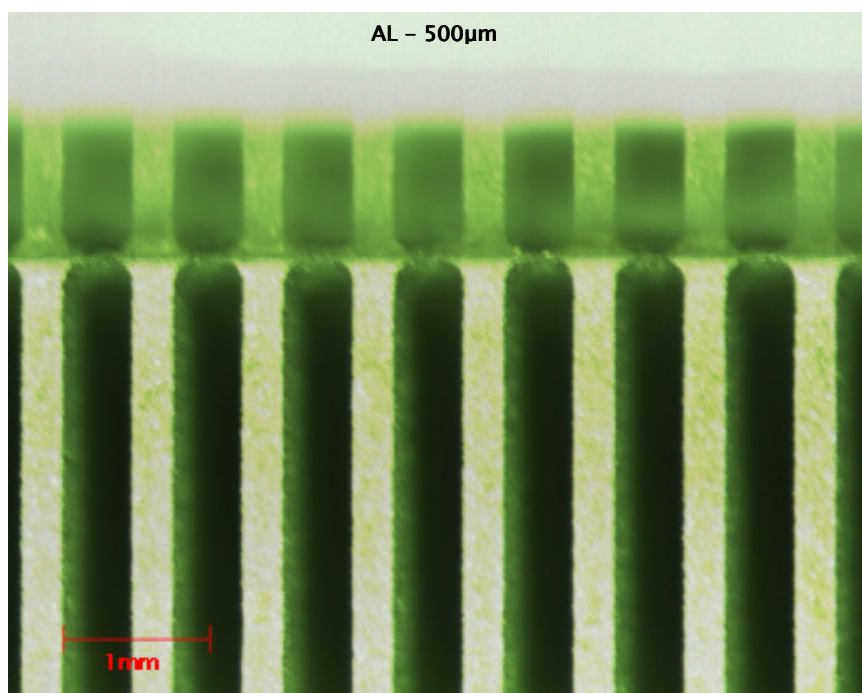


Figure F.3: AL 500  $\mu\text{m}$  specimen

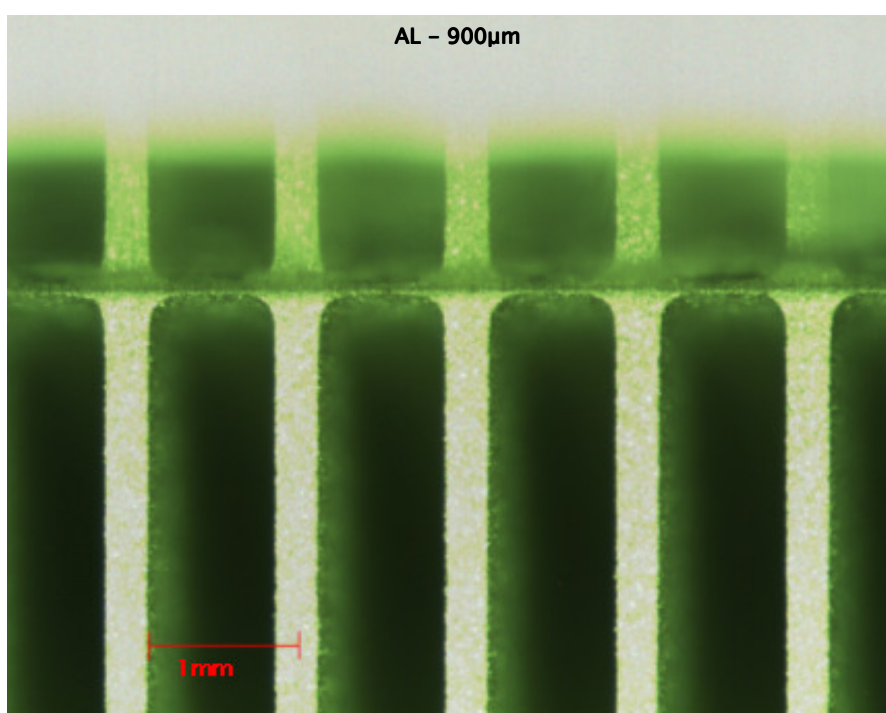


Figure F.4: AL 900  $\mu\text{m}$  specimen

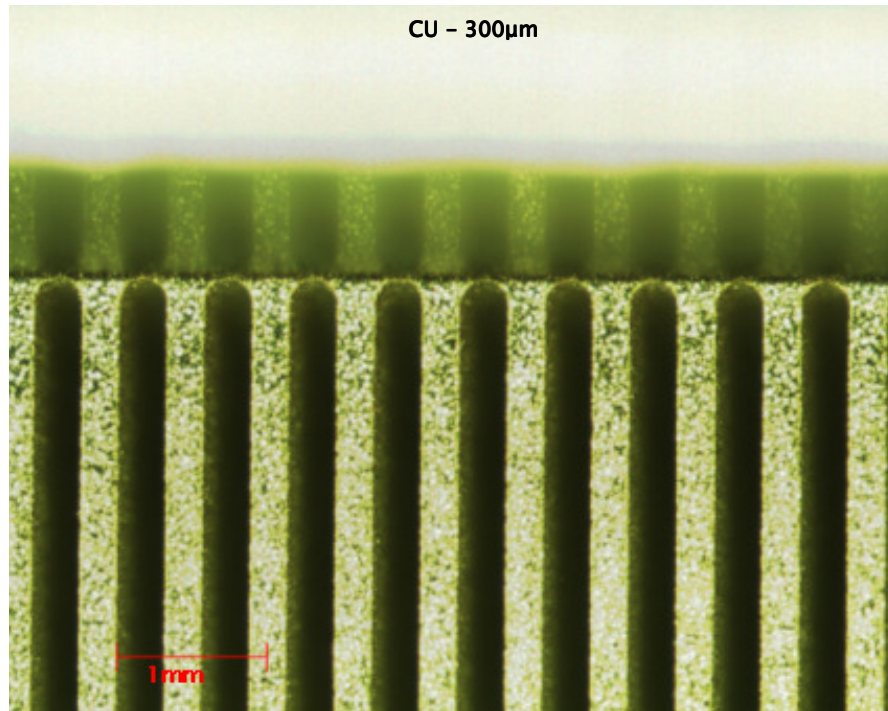


Figure F.5: CU 300 µm specimen

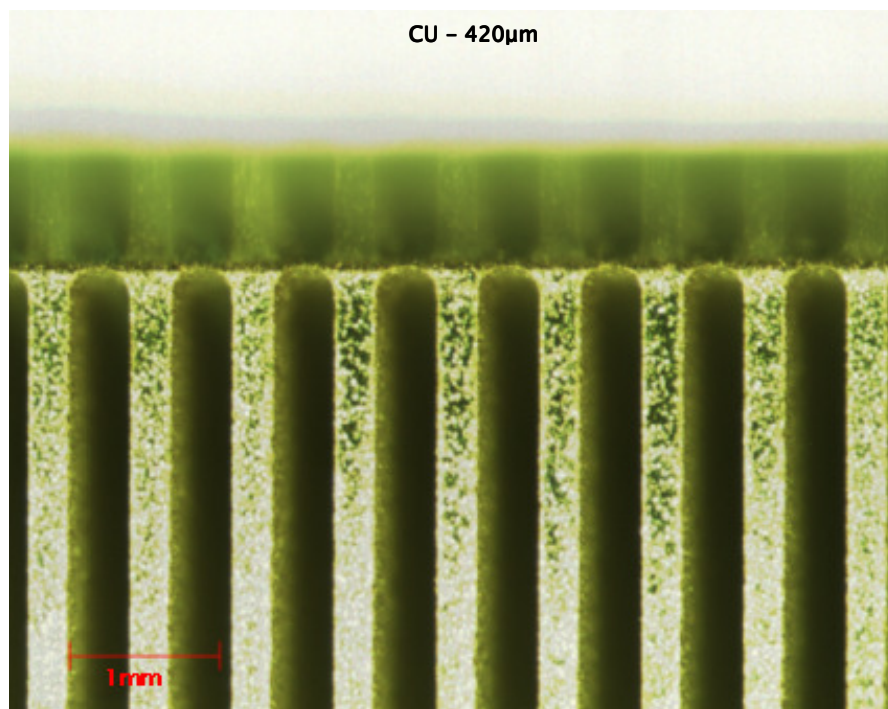


Figure F.6: CU 420 µm specimen

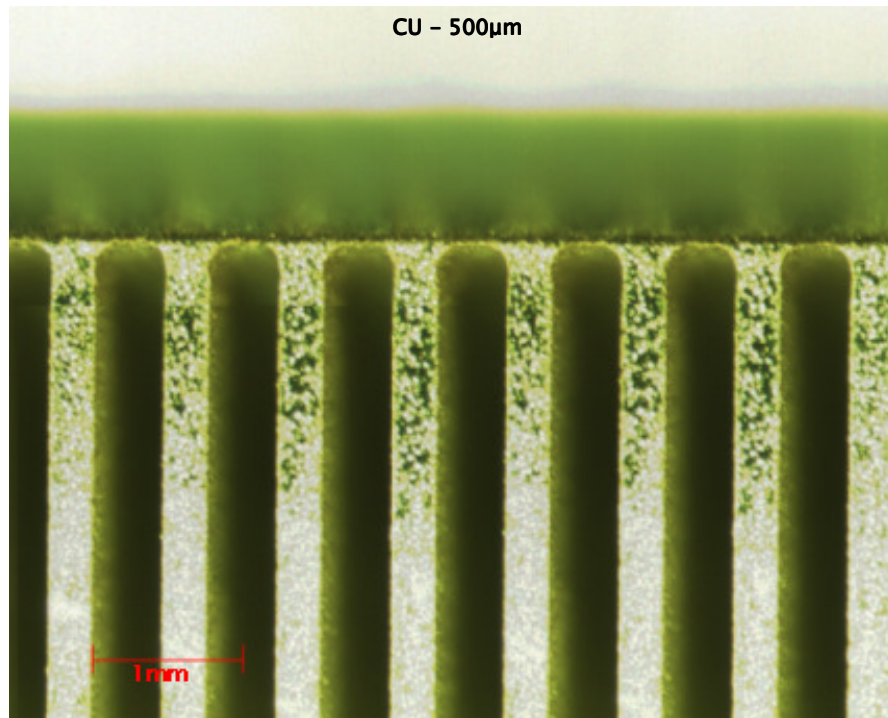


Figure F.7: CU 500  $\mu\text{m}$  specimen

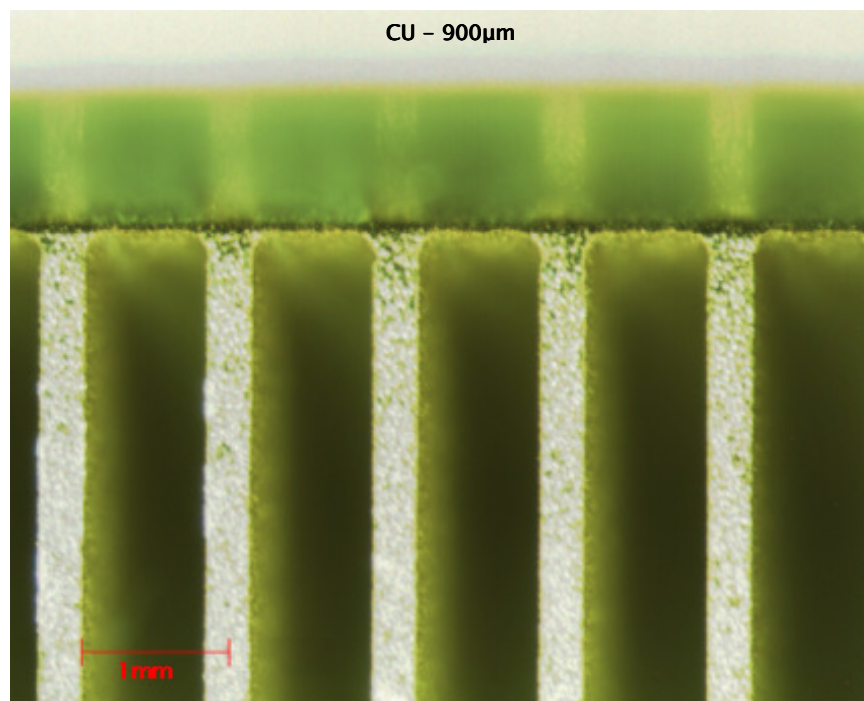


Figure F.8: CU 420  $\mu\text{m}$  specimen

## APPENDIX G

### EXPERIMENTAL RESULTS

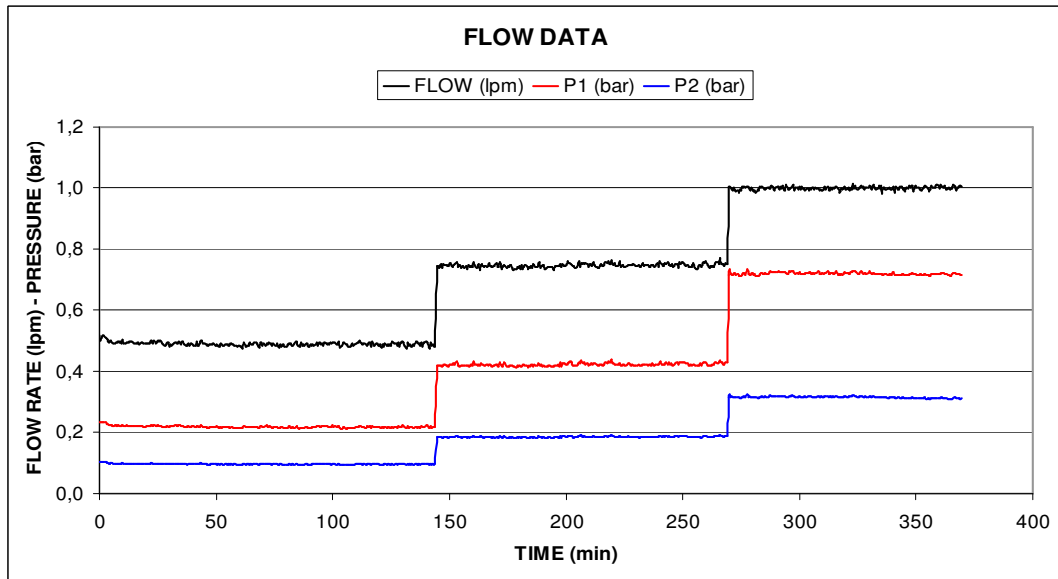


Figure G.1: Flow data – 300  $\mu$ m CU specimen

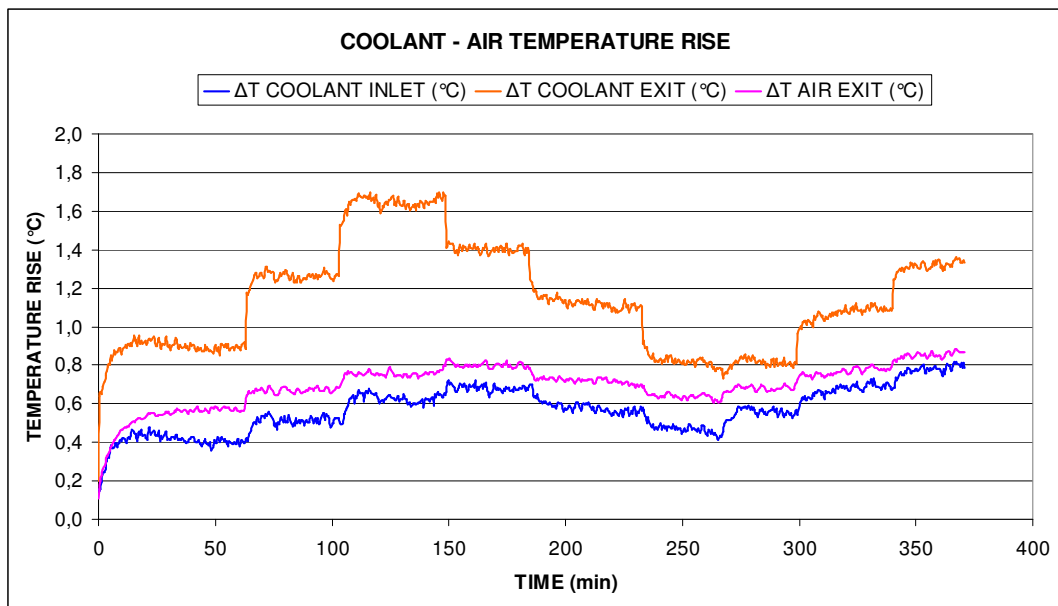


Figure G.2: Air and coolant temperature data – 300  $\mu$ m CU specimen

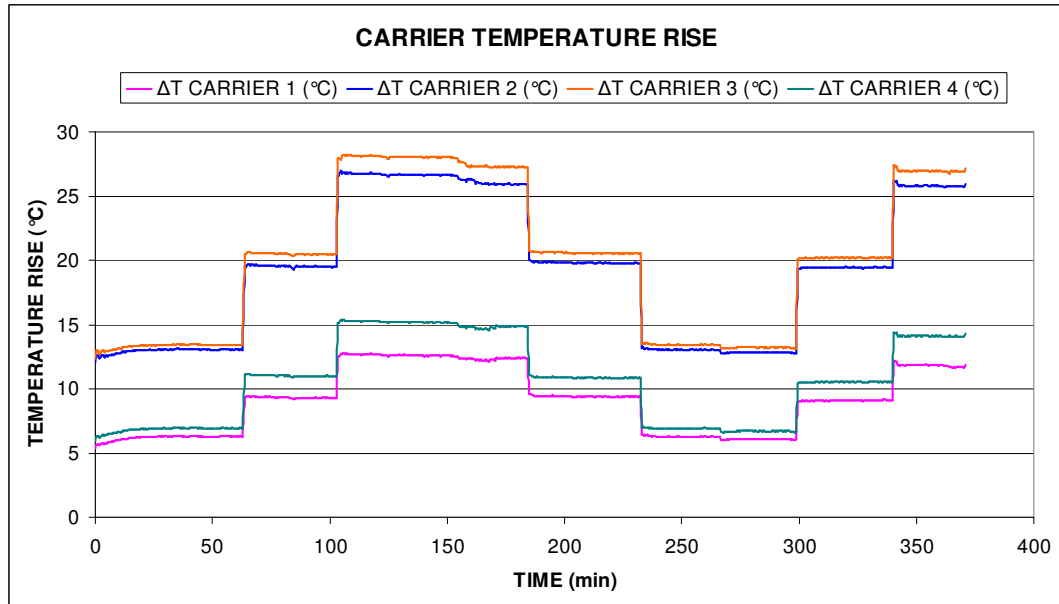


Figure G.3: Heat load carrier temperature data – 300  $\mu\text{m}$  CU specimen

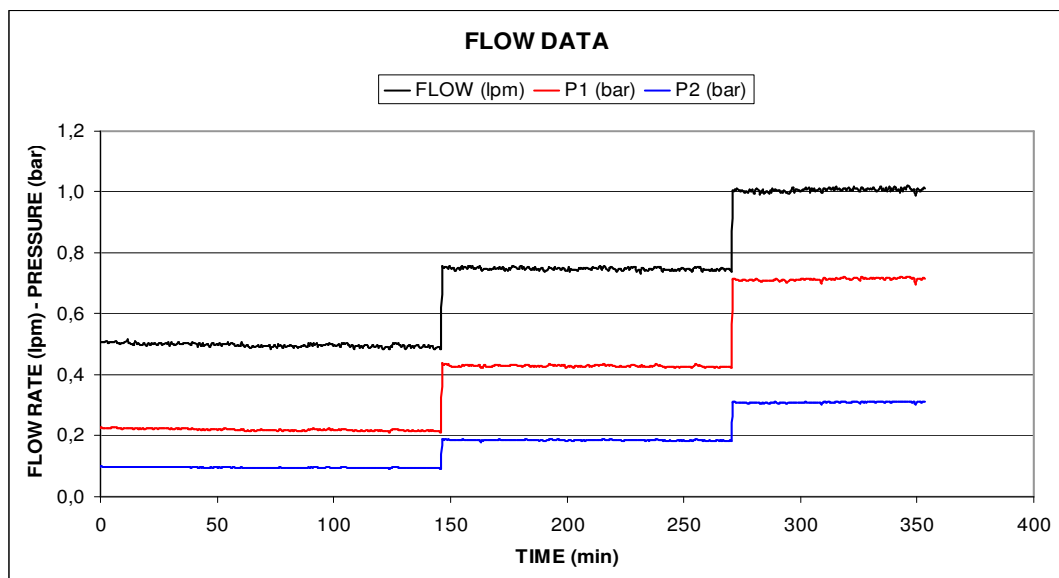


Figure G.4: Flow data – 300  $\mu\text{m}$  AL specimen

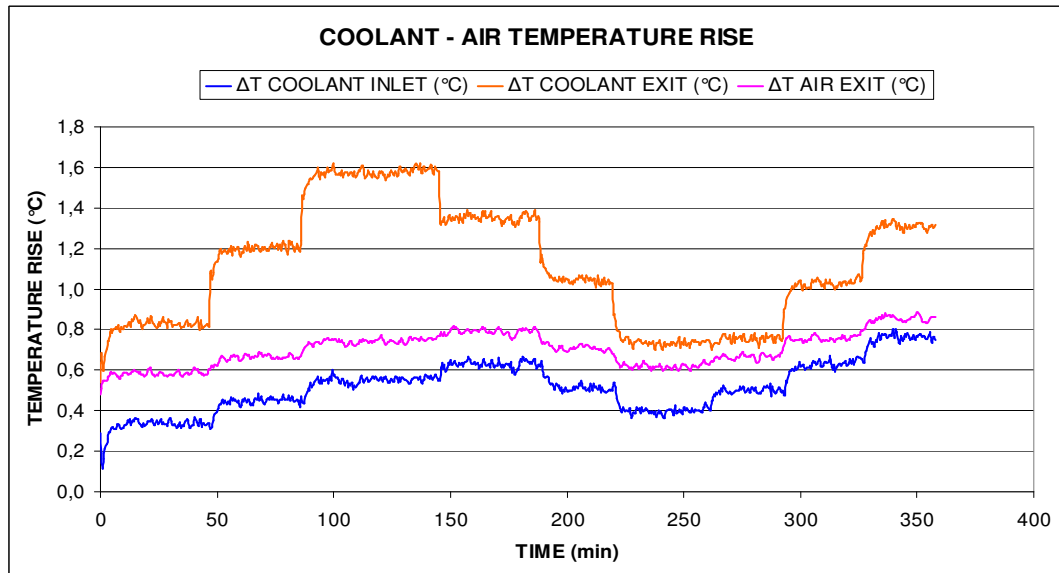


Figure G.5: Air and coolant temperature data – 300  $\mu\text{m}$  AL specimen

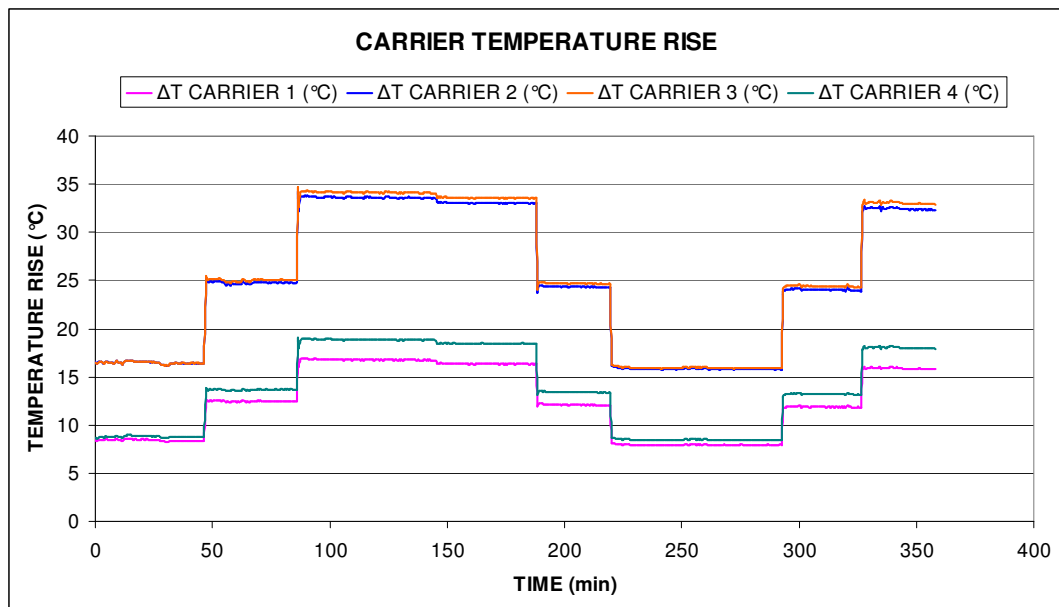


Figure G.6: Heat load carrier temperature data – 300  $\mu\text{m}$  AL specimen

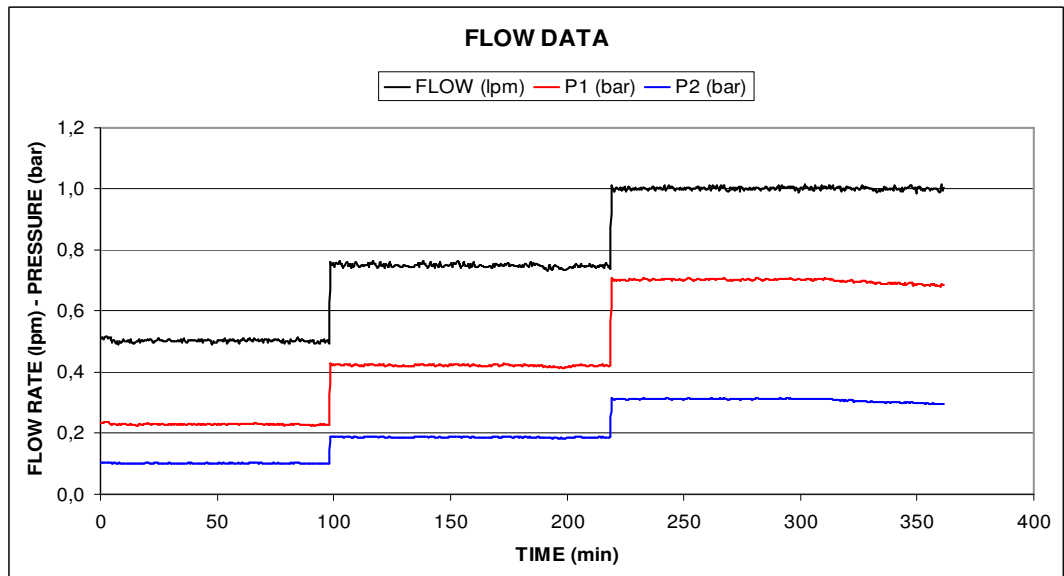


Figure G.7: Flow data – 420  $\mu$ m CU specimen

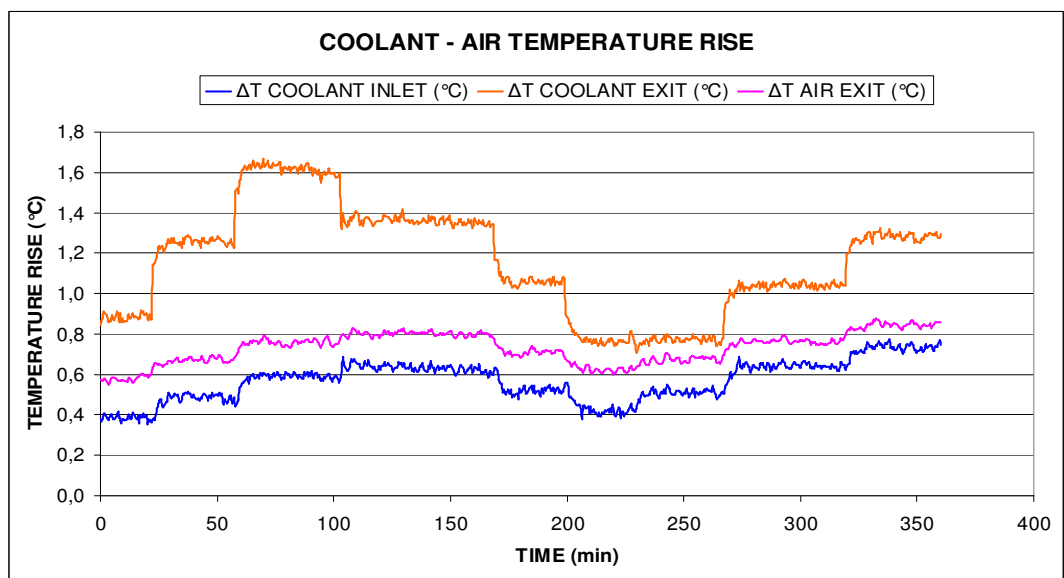


Figure G.8: Air and coolant temperature data – 420  $\mu$ m CU specimen

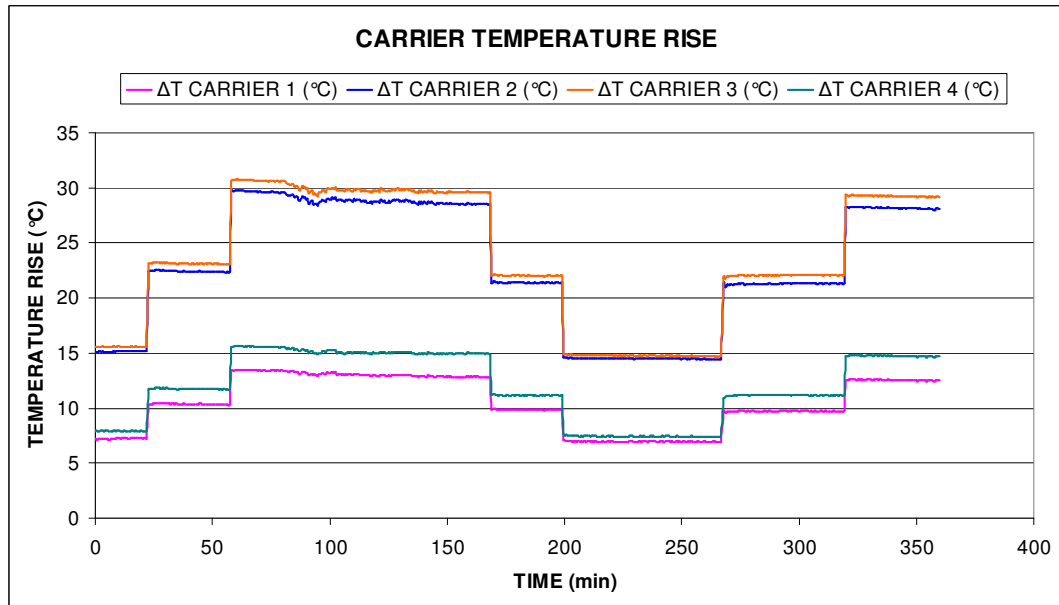


Figure G.9: Heat load carrier temperature data – 420  $\mu\text{m}$  CU specimen

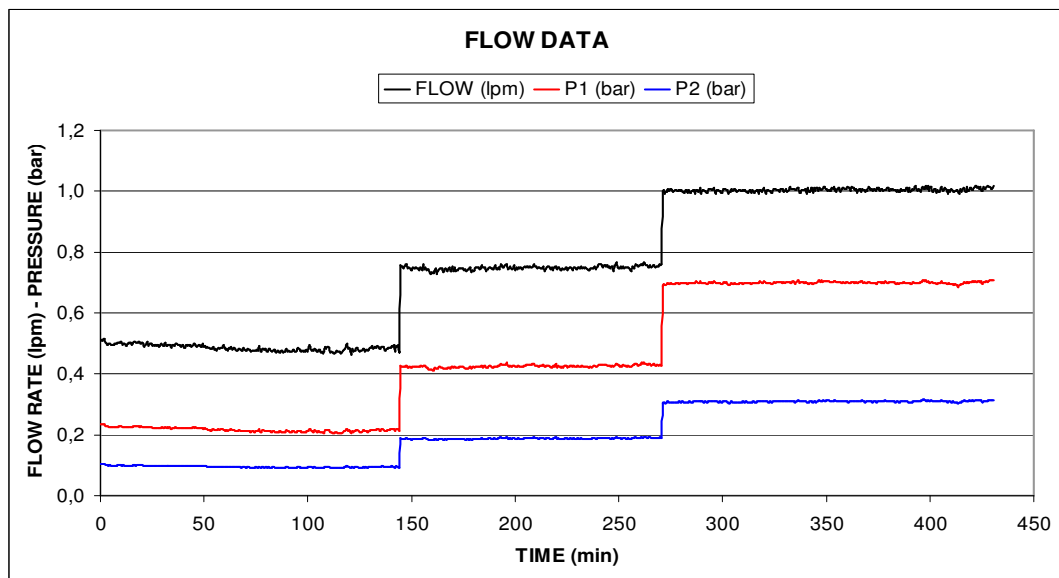


Figure G.10: Flow data – 420  $\mu\text{m}$  AL specimen

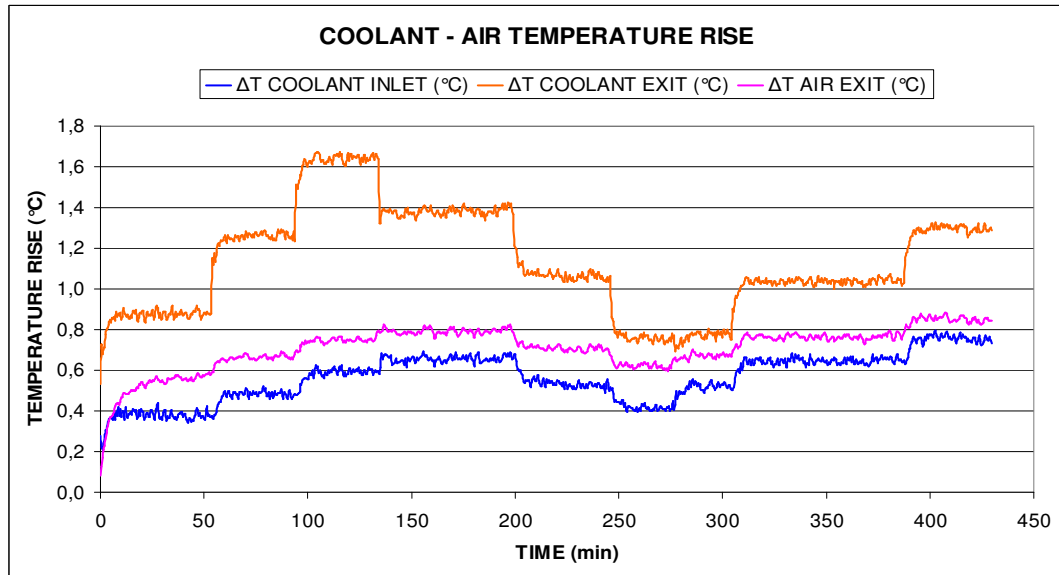


Figure G.11: Air and coolant temperature data – 420  $\mu\text{m}$  AL specimen

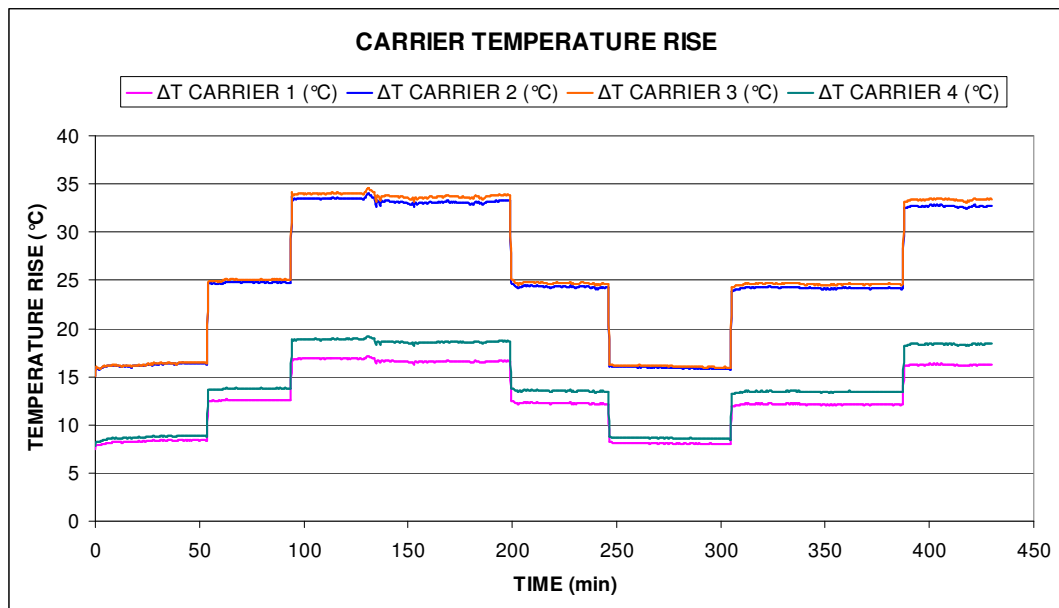


Figure G.12: Heat load carrier temperature data – 420  $\mu\text{m}$  AL specimen

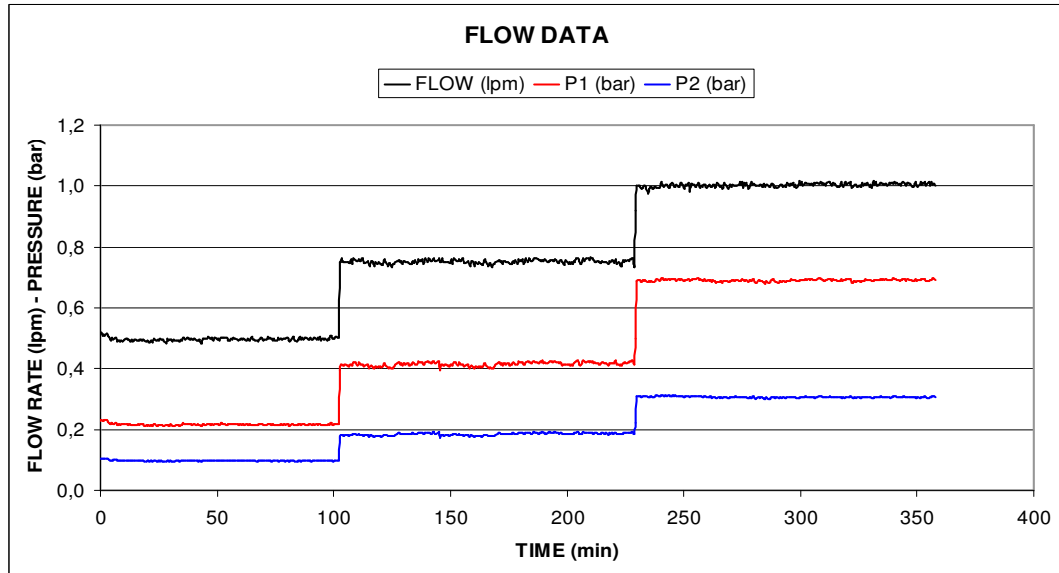


Figure G.13: Flow data – 500  $\mu\text{m}$  CU specimen

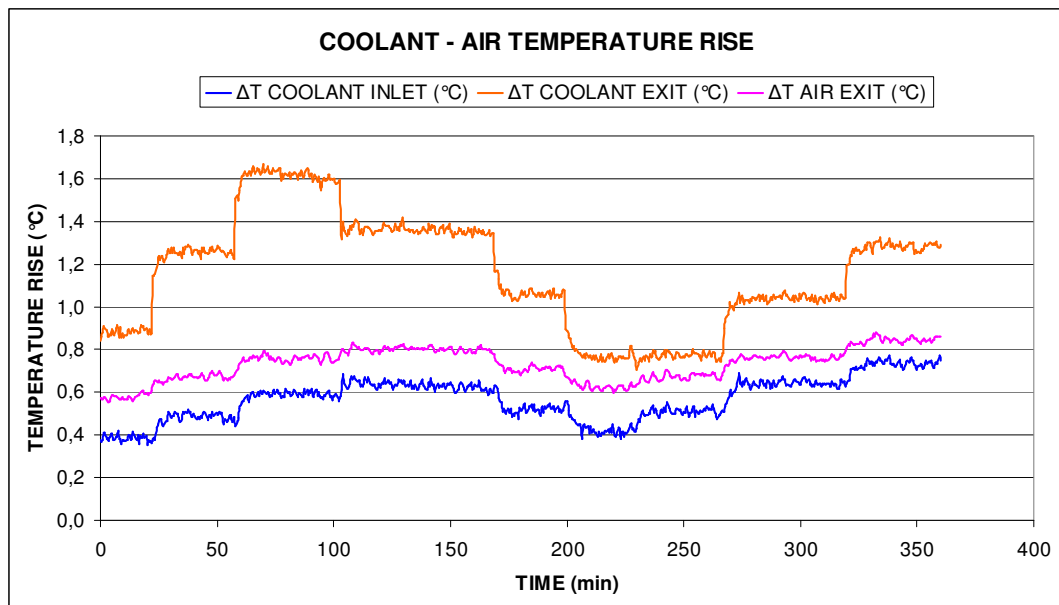


Figure G.14: Air and coolant temperature data – 500  $\mu\text{m}$  CU specimen

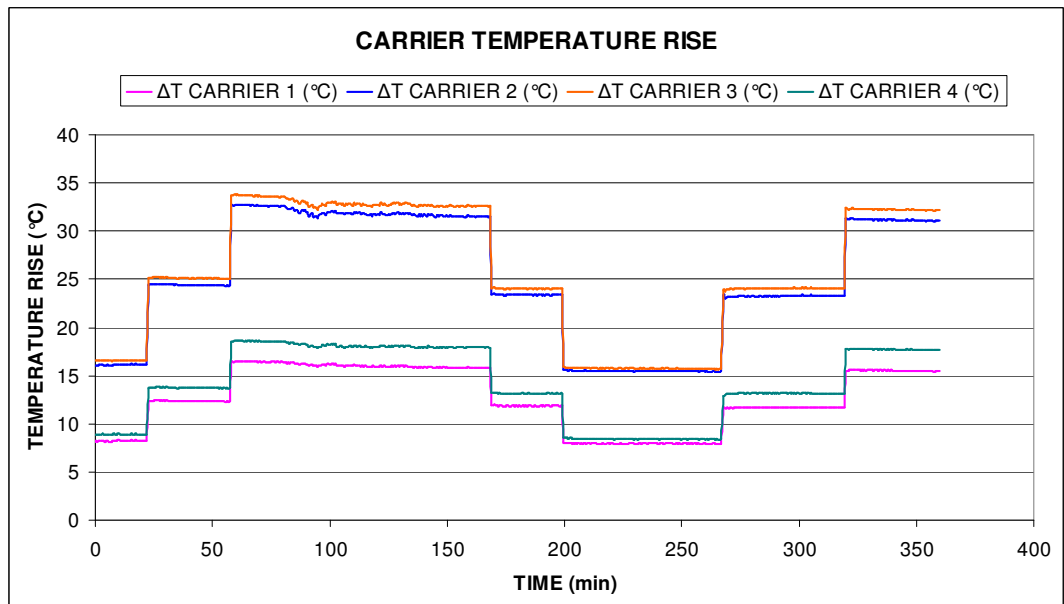


Figure G.15: Heat load carrier temperature data – 500  $\mu\text{m}$  CU specimen

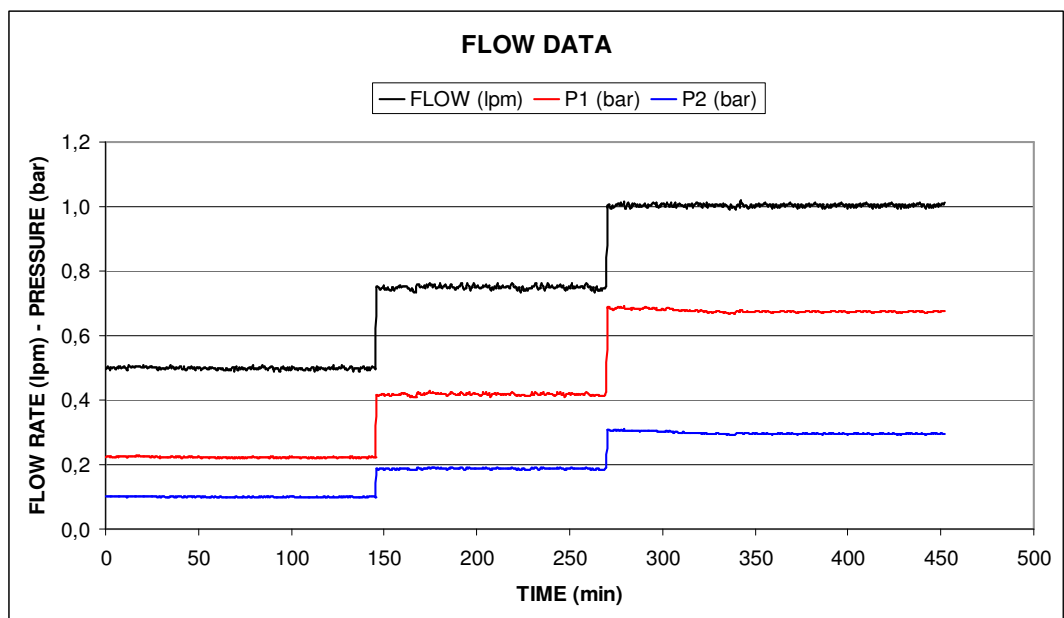


Figure G.16: Flow data – 500  $\mu\text{m}$  AL specimen

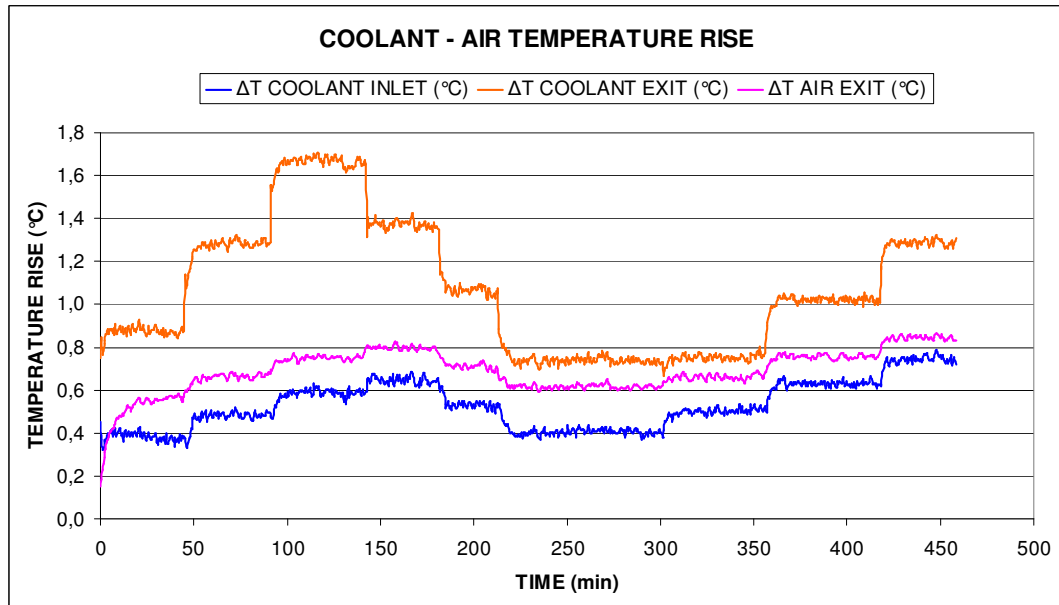


Figure G.17: Air and coolant temperature data – 500  $\mu\text{m}$  AL specimen

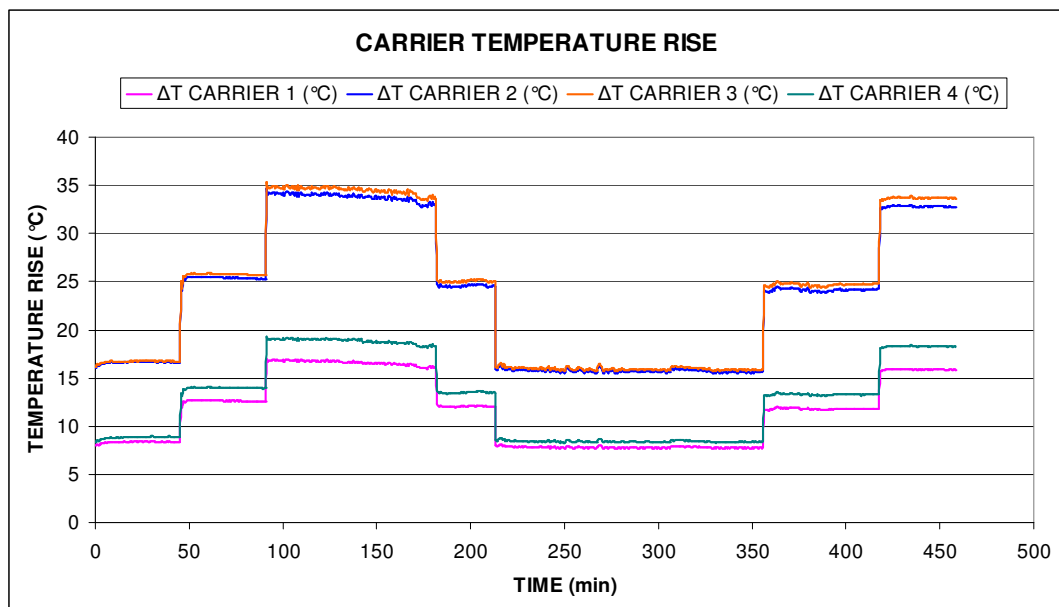


Figure G.18: Heat load carrier temperature data – 500  $\mu\text{m}$  AL specimen

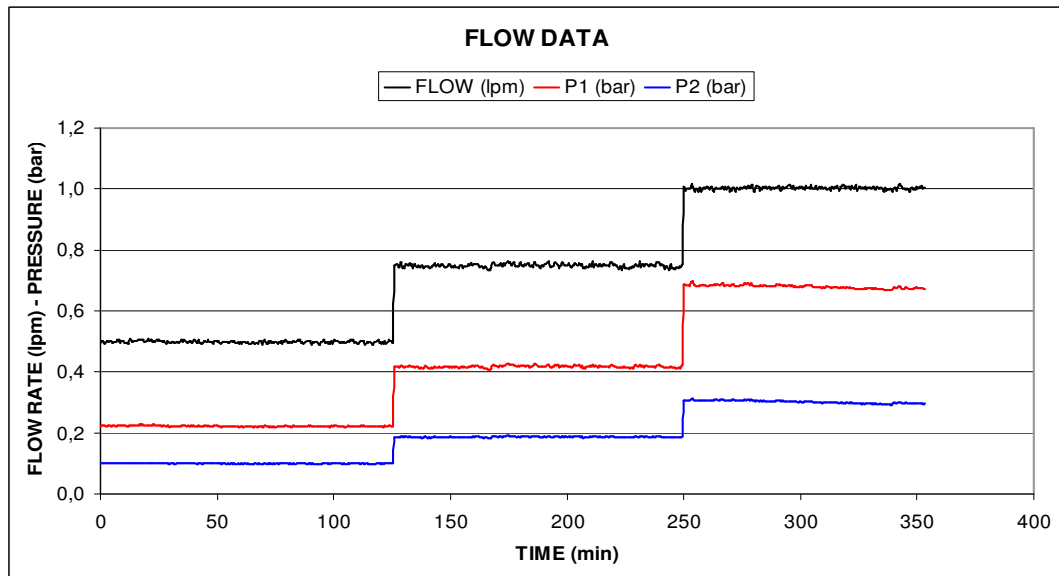


Figure G.19: Flow data – 900  $\mu\text{m}$  CU specimen

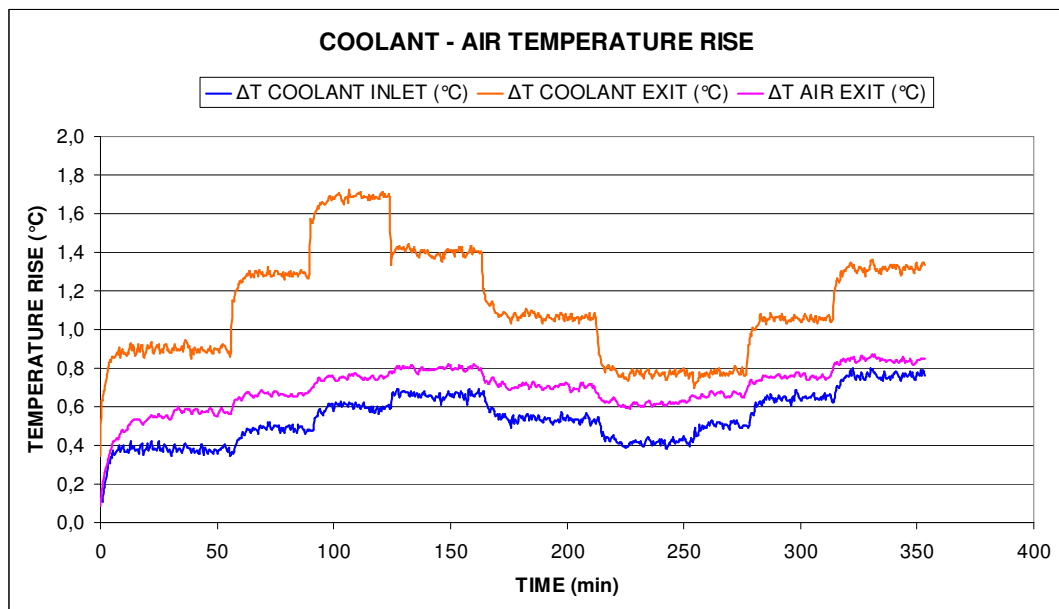


Figure G.20: Air and coolant temperature data – 900  $\mu\text{m}$  CU specimen

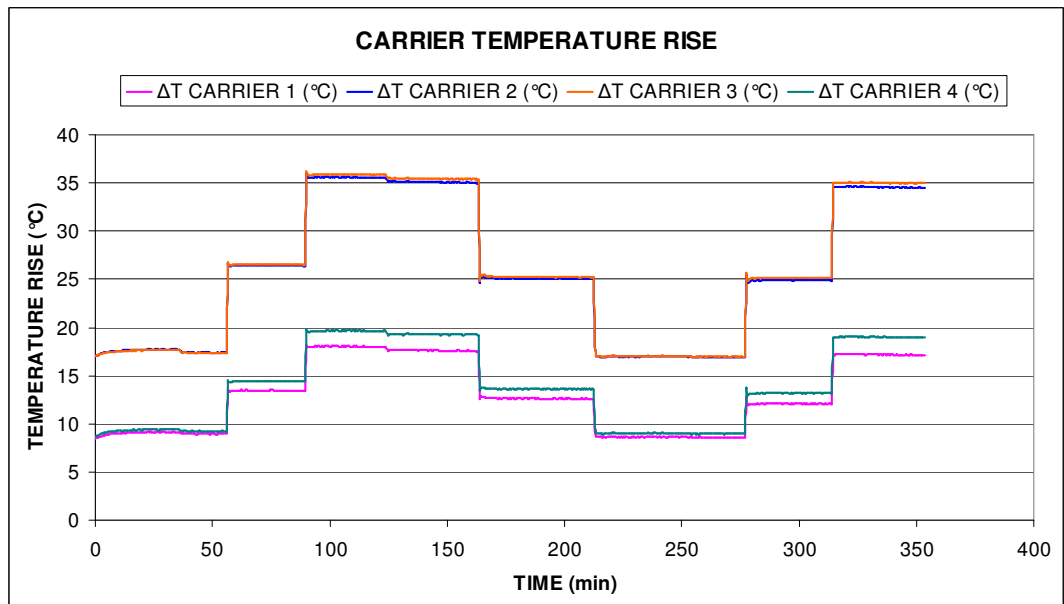


Figure G.21: Heat load carrier temperature data – 900  $\mu\text{m}$  CU specimen

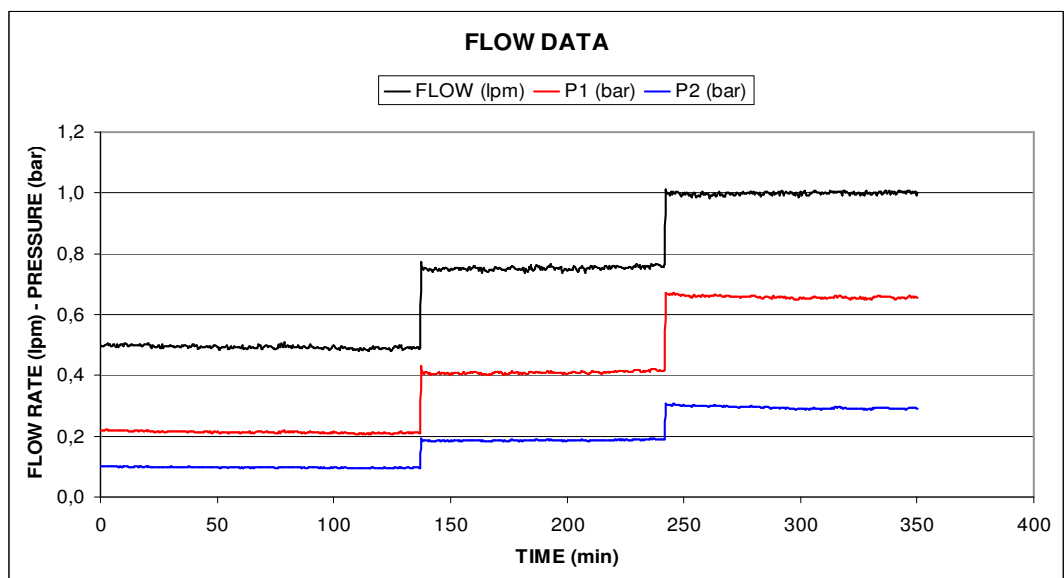


Figure G.22: Flow data – 900  $\mu\text{m}$  AL specimen

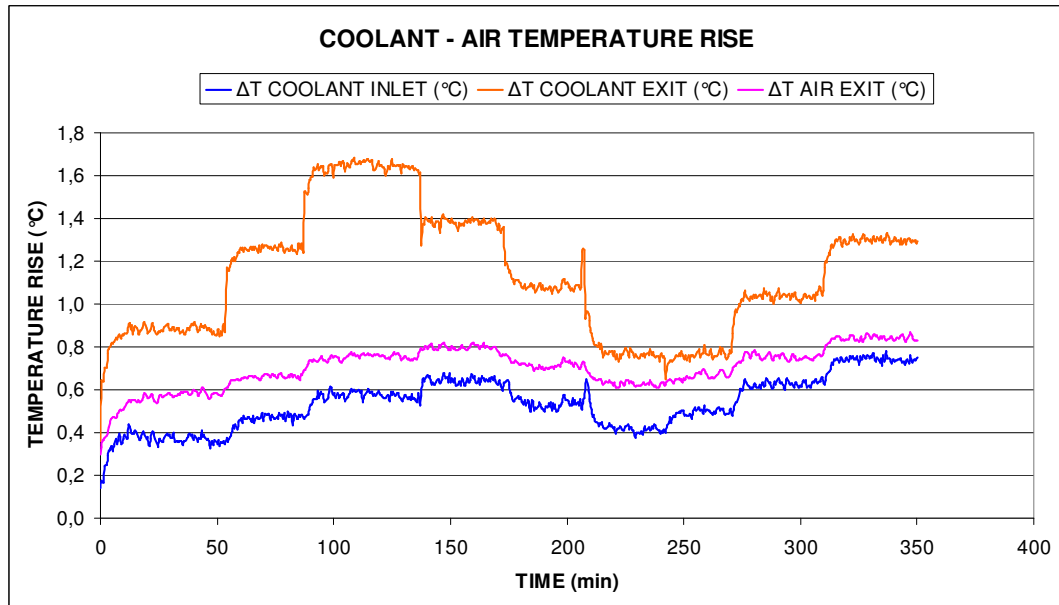


Figure G.23: Air and coolant temperature data – 900  $\mu\text{m}$  AL specimen

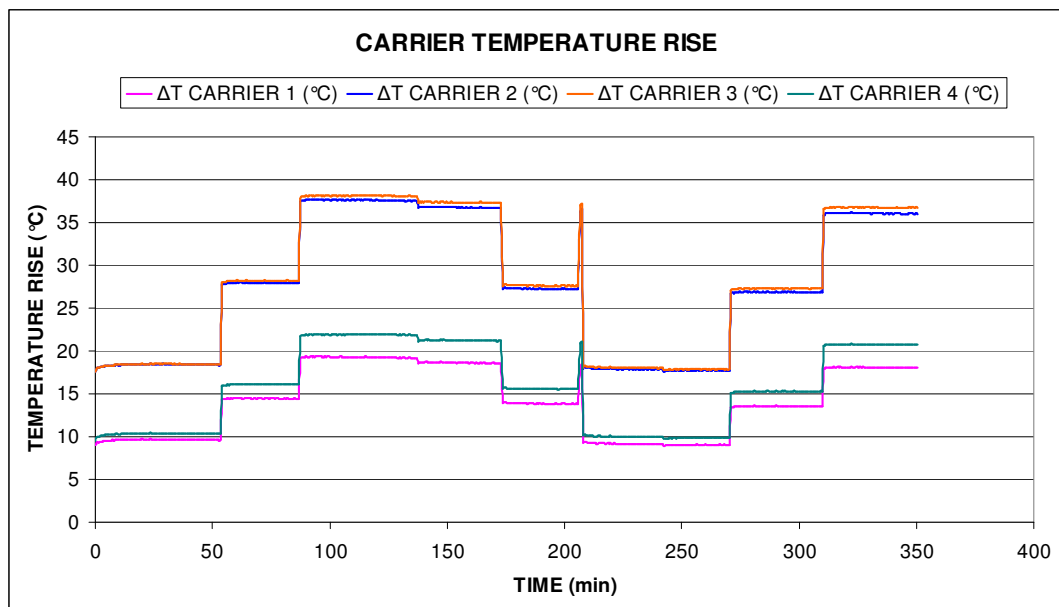


Figure G.24: Heat load carrier temperature data – 900  $\mu\text{m}$  AL specimen

## APPENDIX H

### EXPERIMENTAL RESULTS AT STEADY STATE CONDITIONS

Table H.1: Pressure readings

$Q$ (lpm)	$W_c$ ( $\mu\text{m}$ )	MATERIAL	$p_1$ (bar)	$p_2$ (bar)	$\Delta p$ (bar)
0.50	300	CU	0.218	0.094	0.124
		AL	0.216	0.094	0.122
	420	CU	0.225	0.103	0.122
		AL	0.218	0.096	0.122
	500	CU	0.216	0.097	0.119
		AL	0.219	0.099	0.120
	900	CU	0.220	0.101	0.119
		AL	0.208	0.096	0.112
0.75	300	CU	0.426	0.184	0.242
		AL	0.425	0.185	0.240
	420	CU	0.422	0.187	0.235
		AL	0.425	0.190	0.235
	500	CU	0.419	0.188	0.231
		AL	0.419	0.188	0.231
	900	CU	0.416	0.185	0.231
		AL	0.408	0.187	0.221
1.00	300	CU	0.719	0.311	0.408
		AL	0.721	0.314	0.407
	420	CU	0.712	0.313	0.399
		AL	0.710	0.314	0.396
	500	CU	0.693	0.306	0.387
		AL	0.677	0.296	0.381
	900	CU	0.679	0.302	0.377
		AL	0.658	0.288	0.370

Table H.2: Temperature readings @ 0.50 lpm coolant flow rate

Q (lpm)	$q''$ (W/cm <sup>2</sup> )	$W_c$ (μm)	MATERIAL	$\Delta T_1$ (°C)	$\Delta T_2$ (°C)	$\Delta T_3$ (°C)	$\Delta T_4$ (°C)	$\Delta T_{AVE}$ (°C)
0.50	50	300	CU	5.9	12.9	13.0	6.6	9.6
			AL	8.1	16.1	16.1	8.4	12.2
		420	CU	7.0	14.8	15.2	7.6	11.2
			AL	8.0	16.1	16.1	8.5	12.2
		500	CU	7.9	15.8	16.2	8.5	12.1
			AL	8.0	16.4	16.4	8.6	12.4
		900	CU	8.8	16.8	16.8	8.9	12.8
			AL	9.2	18.0	18.0	9.9	13.8
0.50	75	300	CU	88.0	19.0	20.0	10.5	34.4
			AL	12.0	24.5	24.6	13.3	18.6
		420	CU	9.9	21.9	22.6	11.3	16.4
			AL	12.1	15.9	16.0	13.3	14.3
		500	CU	11.8	23.9	24.6	13.2	18.4
			AL	12.1	25.2	25.3	13.5	19.0
		900	CU	13.0	27.8	27.8	13.9	20.6
			AL	14.0	27.9	27.9	14.6	21.1
0.50	100	300	CU	12.0	26.1	27.4	14.6	20.0
			AL	16.3	33.1	33.7	18.4	25.4
		420	CU	12.9	29.0	30.0	15.0	21.7
			AL	16.4	32.9	33.4	18.4	25.3
		500	CU	15.8	32.0	33.0	18.0	24.7
			AL	16.1	33.7	34.3	18.5	25.7
		900	CU	17.3	35.2	35.3	19.1	26.7
			AL	18.7	37.0	37.6	21.4	28.7

Table H.3: Temperature readings @ 0.75 lpm coolant flow rate

Q (lpm)	$q''$ (W/cm <sup>2</sup> )	$W_c$ (μm)	MATERIAL	$\Delta T_1$ (°C)	$\Delta T_2$ (°C)	$\Delta T_3$ (°C)	$\Delta T_4$ (°C)	$\Delta T_{AVE}$ (°C)
0.75	50	300	CU	5.8	12.5	12.9	6.4	9.4
			AL	7.4	15.4	15.4	8.0	11.6
		420	CU	6.4	14.0	14.3	6.9	10.4
			AL	7.6	15.6	15.6	8.2	11.8
		500	CU	7.5	15.2	15.3	8.0	11.5
			AL	7.8	15.6	15.7	8.2	11.8
		900	CU	8.2	16.6	16.6	8.5	12.5
			AL	8.7	17.5	17.6	9.5	13.3
0.75	75	300	CU	8.8	19.2	19.9	10.3	14.6
			AL	11.3	23.7	24.0	12.8	18.0
		420	CU	9.3	20.8	21.5	10.6	15.6
			AL	11.6	23.8	24.0	12.9	18.1
		500	CU	11.3	22.8	23.4	12.6	17.5
			AL	11.5	23.9	24.5	12.9	18.2
		900	CU	12.0	24.6	24.6	13.0	18.6
			AL	13.3	26.6	27.0	15.0	20.5
0.75	100	300	CU	11.7	25.2	26.7	14.2	19.5
			AL	15.6	32.3	32.9	17.8	24.7
		420	CU	12.1	27.9	28.9	14.3	20.8
			AL	15.9	32.4	33.0	17.9	24.8
		500	CU	15.1	30.9	31.9	17.2	23.8
			AL	15.9	32.7	33.9	18.0	25.1
		900	CU	16.9	34.3	34.8	18.6	26.2
			AL	17.9	36.0	36.5	20.5	27.7

Table H.4: Temperature readings @ 1.00 lpm coolant flow rate

Q (lpm)	$q''$ (W/cm <sup>2</sup> )	$W_c$ ( $\mu$ m)	MATERIAL	$\Delta T_1$ (°C)	$\Delta T_2$ (°C)	$\Delta T_3$ (°C)	$\Delta T_4$ (°C)	$\Delta T_{AVE}$ (°C)
1.00	50	300	CU	5.6	12.2	12.6	6.1	9.1
			AL	7.3	15.4	15.4	7.9	11.5
		420	CU	6.3	13.8	14.1	6.8	10.3
			AL	7.4	15.4	15.5	8.0	11.6
		500	CU	7.4	14.8	15.1	7.8	11.3
			AL	7.5	15.5	15.5	8.0	11.6
		900	CU	8.0	16.3	16.4	8.4	12.3
			AL	8.4	17.1	17.3	9.3	13.0
1.00	75	300	CU	8.4	18.7	19.5	9.8	14.1
			AL	11.2	23.3	23.7	12.5	17.7
		420	CU	9.0	20.6	21.4	11.5	15.6
			AL	11.4	23.4	23.9	12.7	17.9
		500	CU	11.0	22.6	23.4	12.5	17.4
			AL	11.4	23.5	24.0	12.8	17.9
		900	CU	11.5	24.2	24.5	12.6	18.2
			AL	12.9	26.2	26.6	14.6	20.1
1.00	100	300	CU	10.9	24.9	26.1	13.3	18.8
			AL	15.1	31.5	32.1	17.2	24.0
		420	CU	11.7	27.3	28.4	13.8	20.3
			AL	15.4	31.8	32.4	17.6	24.3
		500	CU	14.6	30.3	31.4	16.9	23.3
			AL	15.4	31.9	32.8	17.7	24.5
		900	CU	16.3	33.7	34.2	18.2	25.6
			AL	17.2	35.2	36.0	19.9	27.1

## APPENDIX I

### HEAT LOSS CALCULATION

Table I.1: Heat loss\* @ 0.50 lpm coolant flow rate

Q (lpm)	$q''$ (W/cm <sup>2</sup> )	P (W)	$W_c$ (μm)	MATERIAL	$\Delta T_{in}$ (°C)	$\Delta T_{out}$ (°C)	$\Delta T_{out/in}$ (°C)	HEAT REMOVED (W)	% LOSS
0.50	50	20.92	300	CU	0.38	0.89	0.51	17.71	15
				AL	0.35	0.85	0.50	17.36	17
			420	CU	0.39	0.89	0.50	17.36	17
				AL	0.40	0.90	0.50	17.36	17
			500	CU	0.38	0.89	0.51	17.71	15
				AL	0.38	0.90	0.52	18.05	14
	75	31.37	900	CU	0.38	0.90	0.54	18.75	10
				AL	0.37	0.89	0.52	18.05	14
			300	CU	0.50	1.25	0.75	26.04	17
				AL	0.45	1.22	0.77	26.73	15
			420	CU	0.49	1.25	0.76	26.39	16
				AL	0.51	1.28	0.77	26.73	15
	100	41.83	500	CU	0.48	1.25	0.77	26.73	15
				AL	0.48	1.27	0.79	27.43	13
			900	CU	0.51	1.30	0.79	27.43	13
				AL	0.48	1.25	0.77	26.73	15
			300	CU	0.62	1.64	1.02	35.41	15
				AL	0.58	1.55	0.99	34.37	18
	100	41.83	420	CU	0.59	1.63	1.04	36.11	14
				AL	0.62	1.65	1.03	35.76	15
			500	CU	0.61	1.65	1.04	36.11	14
				AL	0.60	1.68	1.08	37.50	10
			900	CU	0.62	1.71	1.09	37.84	10
				AL	0.59	1.67	1.08	37.50	10

Table I.2: Heat loss\* @ 0.75 lpm coolant flow rate

Q (lpm)	$q''$ (W/cm <sup>2</sup> )	P (W)	$W_c$ ( $\mu$ m)	MATERIAL	$\Delta T_{in}$ (°C)	$\Delta T_{out}$ (°C)	$\Delta T_{out-in}$ (°C)	HEAT REMOVED (W)	% LOSS
0.75	50	20.92	300	CU	0.46	0.82	0.36	18.75	10
				AL	0.38	0.76	0.38	19.79	5
			420	CU	0.39	0.76	0.37	19.27	8
				AL	0.41	0.77	0.36	18.75	10
			500	CU	0.41	0.77	0.36	18.75	10
				AL	0.40	0.76	0.36	18.75	10
	75	31.37	900	CU	0.42	0.77	0.35	18.23	13
				AL	0.41	0.77	0.36	18.75	10
			300	CU	0.56	1.10	0.54	28.12	10
				AL	0.51	1.07	0.56	29.16	7
			420	CU	0.53	1.08	0.55	28.64	9
				AL	0.51	1.05	0.54	28.12	10
0.75	100	41.83	500	CU	0.52	1.06	0.54	28.12	10
				AL	0.52	1.07	0.55	28.64	9
			900	CU	0.53	1.07	0.54	28.12	10
				AL	0.52	1.08	0.56	29.16	7
			300	CU	0.69	1.42	0.73	38.02	9
				AL	0.61	1.34	0.73	38.02	9
	100	41.83	420	CU	0.63	1.36	0.73	38.02	9
				AL	0.67	1.39	0.72	37.50	10
			500	CU	0.63	1.36	0.73	38.02	9
				AL	0.66	1.39	0.73	38.02	9
			900	CU	0.65	1.39	0.74	38.54	8
				AL	0.64	1.40	0.76	39.58	5

Table I.3: Heat loss\* @ 1.00 lpm coolant flow rate

Q (lpm)	q" (W/cm <sup>2</sup> )	P (W)	W <sub>c</sub> (μm)	MATERIAL	ΔT <sub>in</sub> (°C)	ΔT <sub>out</sub> (°C)	ΔT <sub>out-in</sub> (°C)	HEAT REMOVED (W)	% LOSS
1.00	50	20.92	300	CL	0.55	0.82	0.27	18.75	10
				AL	0.51	0.78	0.27	18.75	10
			420	CL	0.50	0.78	0.28	19.44	7
				AL	0.53	0.80	0.27	18.75	10
			500	CL	0.51	0.78	0.27	18.75	10
				AL	0.49	0.77	0.28	19.44	7
			900	CL	0.51	0.80	0.29	20.14	4
				AL	0.49	0.77	0.28	19.44	7
			300	CL	0.69	1.10	0.41	28.47	9
				AL	0.62	1.03	0.41	28.47	9
			420	CL	0.65	1.06	0.41	28.47	9
				AL	0.64	1.04	0.40	27.78	11
	75	31.37	500	CL	0.64	1.05	0.41	28.47	9
				AL	0.63	1.04	0.41	28.47	9
			900	CL	0.65	1.07	0.42	29.16	7
				AL	0.61	1.05	0.44	30.55	3
			300	CL	0.80	1.34	0.54	37.50	10
				AL	0.77	1.31	0.54	37.50	10
			420	CL	0.75	1.29	0.54	37.50	10
				AL	0.76	1.31	0.55	38.19	9
	100	41.83	500	CL	0.74	1.28	0.54	37.50	10
				AL	0.73	1.30	0.57	39.58	5
			900	CL	0.77	1.31	0.54	37.50	10
				AL	0.74	1.31	0.57	39.58	5

\* Calculation based on :  $q_{removed} = \dot{m} c_p \Delta T_{outlet - inlet}$  where  $c_p = 4179 \text{ J/kgK}$  and  $\dot{m} = \rho \cdot \text{flow rate in lpm}$   $\frac{10^{-3}}{60}$  where  $\rho = 997 \text{ kg/m}^3$

## APPENDIX J

### NUMERICAL ANALYSIS RESULTS

Table J.1: Numerical analysis results @ 0.2 mm thermal interface material thickness

Q (lpm)	q" (W/cm <sup>2</sup> )	W <sub>c</sub> (μm)	MATERIAL	ΔT <sub>1</sub> (°C)	ΔT <sub>2</sub> (°C)	ΔT <sub>3</sub> (°C)	ΔT <sub>4</sub> (°C)	ΔT <sub>AVE</sub> (°C)
0.50	100	300	CU	18.6	28.7	28.9	19.0	23.8
			AL	19.7	30.2	30.5	20.4	25.2
0.75	100	300	CU	18.5	28.6	28.7	18.8	23.7
			AL	19.6	30.0	30.2	20.1	25.0
1.00	50	300	CU	8.8	13.7	13.7	8.8	11.3
			AL	9.4	14.6	14.7	9.6	12.1
	75	300	CU	13.7	21.2	21.2	13.8	17.5
			AL	14.4	22.2	22.3	14.8	18.4
	100	300	CU	18.5	28.5	28.6	18.8	23.6
			AL	19.5	29.9	30.0	20.0	24.9
		420	CU	15.5	24.0	24.1	15.9	19.9
			AL	16.6	25.7	25.9	17.4	21.4
		500	CU	15.6	24.1	24.3	16.0	20.0
			AL	16.9	26.1	26.3	17.7	21.8
	900	900	CU	16.5	25.3	25.5	17.1	21.1
			AL	18.2	27.8	28.2	19.3	23.4

Table J.2: Numerica analysis results @ 0.3 mm thermal interface material thickness

Q (lpm)	q" (W/cm2)	W <sub>c</sub> (μm)	MATERIAL	ΔT <sub>1</sub> (°C)	ΔT <sub>2</sub> (°C)	ΔT <sub>3</sub> (°C)	ΔT <sub>4</sub> (°C)	ΔT <sub>AVE</sub> (°C)
0.50	100	300	CU	15.3	23.7	23.8	15.7	19.6
			AL	16.4	25.4	25.7	17.2	21.2
0.75	100	300	CU	15.2	23.6	23.7	15.5	19.5
			AL	16.3	25.2	25.4	17.0	21.0
1.00	50	300	CU	6.9	10.9	11.0	7.0	9.0
			AL	7.6	11.9	12.0	7.8	9.8
	75	300	CU	10.8	16.9	17.0	11.0	13.9
			AL	11.7	18.2	18.3	12.1	15.1
	100	300	CU	14.8	22.9	23.0	15.1	19.0
			AL	15.8	24.5	24.7	16.5	20.4
		420	CU	18.8	28.9	29.1	19.2	24.0
			AL	19.8	30.5	30.7	20.5	25.4
		500	CU	18.9	29.1	29.2	19.3	24.1
			AL	20.1	30.8	31.0	20.8	25.7
	900		CU	19.8	30.2	30.4	20.3	25.2
			AL	21.3	32.4	32.7	22.3	27.2